Development and characterization of a haemostatic patch from various natural resources

Thesis Submitted
by
Pranabesh Kumar Sasmal

Doctor of Philosophy (Engineering)
Department of Mechanical Engineering
FACULTY COUNCIL OF ENGINEERING & TECHNOLOGY
JADAVPUR UNIVERSITY
KOLKATA, INDIA
2025

JADAVPUR UNIVERSITY

KOLKATA-700032, INDIA

INDEX NO. (135/19/E)

1. **Title of the thesis:**

“Development and characterization of a haemostatic patch from various natural resources”

2. **Name, Designation & Institution of Supervisor/s:**

Dr. Abhijit Chanda

Professor

Department of Mechanical Engineering

Jadavpur University

Kolkata-700032

And

Dr. Pallab Datta

Assistant Professor

Department of Pharmaceutics

National Institute of Pharmaceutical Education and Research - Kolkata

Kolkata-700054

Publications

3. Journal Articles

I. P.K. Sasmal, S. Dasgupta, S Samanta, K.P. Reddy, S. Hoque, S. Nandi, A. Chanda, and P. Datta, "Dual drug-loaded self-wearable electrospun nanofiber for synergistic pharmacological intervention through tertiary hemostasis in prehospital trauma care,". Biomed Mater. 2025 May 30;20(4). doi: 10.1088/1748-605X/addbb6. PMID: 40398445.

II. P.K. Sasmal, S. Samanta, S. Dasgupta, S. Nandi, A. Chanda, and P. Datta, "Oyster shell powder reinforced chitosan-poly(vinyl alcohol) freeze-dried composite sponge for on-site hemorrhage control," Journal of Biomaterials Applications, 24May 2025. doi:10.1177/08853282251347348

III. P.K. Sasmal, S. Dasgupta, J. Kubacki, S. Hoque, S. Nandi, A. Chanda, and P. Datta, "Biogenic calcium mineral- chitosan composite nanofiber dressing for control of traumatic hemorrhage," Journal of Biomedical Materials Research: Part B- Applied Biomaterials. 09 June 2025, **doi.org/10.1002/jbm.b.35601**

IV. P.K. Sasmal and P. Datta, "Tranexamic acid-loaded chitosan electrospun nanofibers as drug delivery system for hemorrhage control applications," *J Drug Deliv Sci Technol*, vol. 52, pp. 559–567, Aug. 2019, doi: 10.1016/j.jddst.2019.05.018.

Other Publication:

V. S. Mukherjee, P.K. Sasmal, K.P. Reddy, A. Pal, D. Pal, S.K. Nandi, A. Chanda, S. Ahmed, and P. Datta, "Spatiotemporally Controlled Release of Etamsylate from Bioinspired Peptide-Functionalized Nanoparticles Arrests Bleeding Rapidly and Improves Clot Stability in a Rabbit Internal Hemorrhage Model," Acs Biomaterials Science and Engineering, July 2024 https://doi.org/10.1021/acsbiomaterials.4c00743.

4. Patents - NIL

5. Presentations in National/ International / Conference / Workshops

- P.K.Sasmal, A. Chanda, and P. Datta, "Development and Characterization of low cost hemostatic film with marine shell waste," in INCOM2024: Proceedings of 2nd International Conferences on Mechanical Engineering, Jadavpur University, Kolkata,India. January 5& 6, 2024. Paper No. INCOM2024-0733

Book chapter

- P.K.Sasmal, A. Chanda, and P. Datta, "Development and characterization of an inexpensive hemostatic film with oyster shell waste", Advances in Materials, Manufacturing and Design, Lecture Note in Mechanical Engineering Springer Nature Notebook. Published on 4th January 2025. https://doi.org/10.1007/978-981-97-6667-3_18

~~12/06/2025~~
4/12/25

Dr. Pallab Datta
Assistant Professor
National Institute of Pharmaceutical
Education and Research Kolkata
168, Ma[illegible] Road
Kolkata- 700054.

Abhijit Chanda
~~12/6/25~~
4/12/25

Professor
Dept. of Mechanical Engineering
Jadavpur University, Kolkata-32

"Statement of Originality"

I, Pranabesh Kumar Sasmal registered on 14.06.2019 do hereby declare that this thesis entitled "Development and characterization of a haemostatic patch from various natural resources" contains literature survey and original research work done by the undersigned candidate as part of Doctoral studies.

All information in this thesis has been obtained and presented in accordance with existing academic rules and ethical conduct. I declare that, as required by these rules and conduct, I have fully cited and referred all materials and results that are not original to this work.

I also declare that I have checked this thesis as per the "Policy on Anti Plagiarism, Jadavpur University, 2019", and the level of similarity as checked by iThenticate software is ~~9~~ 7%.

Pranabesh kumar Sasmal

Signature of Candidate:

Date: ~~12.06.2025~~ 4/12/25

Certified by Supervisor(s):

(Signature with date, seal)

1. Abhijit Chanda ~~12/6/25~~ 4/12/25

Professor
Dept. of Mechanical Engineering
Jadavpur University, Kolkata-32

2. P Datta ~~12/06/2025~~ 4/12/25

Dr. Pallab Datta
Assistant Professor
National Institute of Pharmaceutical
Education and Research Kolkata.
168, Manik[illegible] Road
Kolkata- 700054.

CERTIFICATE FROM THE SUPERVISOR/S

This is to certify that the thesis entitled "**Development and characterization of a haemostatic patch from various natural resources**" submitted by Pranabesh Kumar Sasmal, who got his name registered on 14/06/2019 for the award of Ph.D.(Engineering) degree of Jadavpur University, is absolutely based upon his own work under the supervision of **Dr. Abhijit Chanda and Dr. Pallab Datta**, and that neither his thesis nor any part of the same has been submitted for any degree / diploma or any other academic award anywhere before.

Abhijit Chanda
12/6/25
4/12/25

Dr. Abhijit Chanda
Professor
Department of Mechanical Engineering
Jadavpur University
Kolkata-700032

Professor
Dept. of Mechanical Engineering
Jadavpur University, Kolkata-32

PDatta
12/06/2025
4/12/25

Dr. Pallab Datta
Assistant Professor
Department of Pharmaceutics
NIPER- Kolkata
Kolkata-700054

Dr. Pallab Datta
Assistant Professor
National Institute of Pharmaceutical
Education and Research Kolkata.
168, Maniktala Main Road
Kolkata- 700054.

Acknowledgement

First and foremost, I would like to express my deepest regards and respect to the most important person in my thesis advisor **Dr. Abhijit Chanda**, Dept. of Mechanical Engineering, Jadavpur University, for his esteemed guidance, invaluable suggestions, constant encouragement and affection at every stage of my work. Without him, conceiving this study would have been impossible. My heart will always bear respectful gratitude to him. My deepest gratitude goes to my guide **Dr. Pallab Datta**, Assistant Professor, Department of Pharmaceutics, NIPER-Kolkata, Kolkata-700054. I am very much grateful for his tremendous help and kind support in this research. He has not only been my guide but more like a friend to me. He has educated me on different characterization part of this thesis work. The thesis work would never be possible without his help.

I acknowledge the Zoological Survey of India, Prani Bigyan Bhavan, under the Ministry of Environment, Forest and Climate Change, Government of India, for the identification of Marine Shell.

I express my gratefulness to HOD, Department of Mechanical Engineering, Jadavpur University, Kolkata, and the Director, Niper-Kolkata & IIEST-SHIBPUR and Honourable Vice Chancellor, Jadavpur University & West Bengal University of Animal and Fishery Sciences for providing me the facilities to do this research work. Further I express my indebtedness to Director, ESI (MB) Scheme, for giving me opportunities to go with this research work at Jadavpur University. I would like to give my sincere thanks to **Dr. Samit Kumar Nandi**, Department of Veterinary Surgery & Radiology, West Bengal University of Animal & Fishery Science, Kolkata, for his kind help in in vivo animal experiment. I would also like to express my appreciation to **Dr. Ananya Barui**, HOD, Centre for Healthcare Science and Technology, IIEST-SHIBPUR, for extending her help in nanofiber fabrication, characterization and in vitro studies. My sincere regards to **Prof. Amit Roy Chowdhury**, IIEST-SHIBPUR and **Dr. Sujan Krisna Samanta,** Associate Professor, Netaji Subhash Engineering College, Techno City,Garia,Kolkata, for giving my journey a shape. I express my warm regards to **K. Prasanth Reddy**, NIPER-K for SEM, FTIR, XRD characterization. I also like to express my special gratitude to **Debdeep Sikder**, **Debasis Dewanjee**, for their kind help in the initial part to choose the area of the work. I would like to acknowledge **Dr. Howa Begom, Sudipta, Rajdeep, Shalini, Srijini** for being more like a family members to me during my entire research work. Last but certainly not the least, I would like to thank my father **Dhirendra Nath Sasmal**, mother **Karuna Sasmal**, my beautiful wife **Moumita** and twin daughters **Shreenika & Shanveeka**, my father-in-law **Prafulla Adhikary** and mother-in-law **Rina Adhikary,** for their immense mental support, caring and constant enthusiasm, whenever I tried to tread a lesser-walked lane. They always manage to bring a smile to my face. Without their help, I could have never achieved anything in any sphere of life.

May, 2025

(Pranabesh Kumar Sasmal)

Department of Mechanical Engineering, JU

Abstract

Uncontrolled haemorrhage remains a critical challenge in wartime and civilian trauma care emergencies, necessitating the development of effective haemostatic materials to reduce rebleeding during patient transportation. The unmet clinical need has led to exploring drug loaded haemostat dressings, providing mechanical haemostasis and drug delivery to the bleeding site to stabilize clots. It is desirable to employ sustainable biomaterials for fabrication of the patches. This thesis specify that such biomaterials were successfully produced and evaluated in different forms: nanofiber sheets, freeze-dried sponges etc. Simultaneously, oyster shell waste presents an emerging ecological concern. Also, this research explores the development of novel haemostatic biomaterials by repurposing oyster shell waste as a functional component in bleeding control applications. Various formulations were investigated, including: calcium-enriched chitosan nanofibers derived from *Magallana cuttackensis* shells marine shell waste nanofiber (MSWNF); dual-drug loaded polyvinyl alcohol/chitosan nanofibers incorporating tranexamic acid and ethamsylate (PVA/CS/TXA-E); chitosan sponges reinforced with oyster shell powder (PVA/CS/MSW-O); and haemostatic films combining polyvinyl alcohol, chitosan, and oyster shell powder.

Comprehensive characterization using XRD, EDX, XPS, Raman spectroscopy, FTIR, and SEM confirmed the presence of calcium compounds (CaO, $Ca(OH)_2$, $CaCO_3$) from the marine shell waste. Calcined MSW at 1200°C (MSW-T) showed a large zone of inhibition surrounded it and had an excellent antibacterial activity against *Staphylococcus Aureus*. In vitro assays demonstrated significant improvements in haemostatic performance across all formulations, with reductions in clotting time (CT), prothrombin time (PT), activated partial thromboplastin time (aPTT), and plasma recalcification time (PRT). The in vitro clotting time (CT) under (PVA/CS/TXA-E) and MSWNF nanofibers were 230 ± 11 s and 168 ± 4 s, which, along with other parameters- prothrombin times (27 ± 0.4 s and 22 ± 0.6 s), and plasma recalcification time (76 ± 4s and 47 ± 1 s), indicated enhancement in hemostasis performance by MSWNF over (PVA/CS/TXA-E). The PVA/CS/TXA-E nanofiber patches comprised fiber strands with a 347±22 nm average diameter and showed a swelling ratio of 459%. The nanofiber possessed intermittent hydrophilicity (water contact angle 32). Drug release through the nanofiber followed a non-Fickian diffusion model. Dual-drug loaded nanofibers showed a decrease in the clotting time by 24%, while activated partial thromboplastin time (aPTT), Prothrombin time (PT), and Platelet recalcination time (PRT) decreased by 6%, 20% & 15% over the single-drug loaded nanofibers. The PVA/CS/MSW-O sponge demonstrated superior performance in controlling both oozing and pressurized bleeding.

In vivo studies using rabbit models verified enhanced haemostatic efficacy, with MSWNF showing a 22% improvement in haemorrhage control. After evaluation in the rabbit incision model, the bleeding time of the control group (274 ± 6 s) was longer than (PVA/CS/TXA-E) (97 ± 8 s) or MSWNF (75 ± 5 s). Blood oozing until haemostasis was 0.380 g, 0.354 g, and 0.121 g under control gauge, (PVA/CS/TXA-E), and MSWNF, respectively, demonstrating enhancement in haemostasis performance by MSWNF. Histopathological examination confirmed biocompatibility and wound healing progression, evidenced by epithelialization, capillary formation, and granulation tissue development after 7 days of scaffold application. Gene expression analysis in RT-PCR revealed upregulation of key wound healing markers (VEGF-A, PDGF, IGF-1).

These findings demonstrate that natural biomaterials can be effectively employed to enhance haemostatic efficacy. Calcium-based compounds extracted from marine waste products substantially boost the ability of different biomaterial formulations to stop bleeding, offering promising, sustainable, and cost-effective alternatives for managing severe haemorrhage while addressing ecological concerns associated with oyster shell waste. The novel utilization of Magallana Cuttackensis shells, a specific marine ecological waste material, as a high-value functional biomaterial for biogenic calcium represents a significant and innovative contribution that effectively bridges the fields of biomaterials science, hemostasis management, and sustainable bioeconomy.

Keywords: Marine ecological hazard, Bioeconomy, nanofiber, haemostasis, biomaterial, Drug release, in-vivo.

Table of Contents

Contents **Page**

Chapter 1: INTRODUCTION

References

Chapter 2: LITERATURE REVIEW

Chapter 3: SCOPE OF THE WORK AND OBJECTIVES OF THE THESIS

Chapter 4: MATERIALS AND METHODS: SYNTHESIS AND CHARACTERIZATION

References

Chapter 5: RESULTS AND DISCUSSION

References

Chapter 6 : CONCLUSION AND FUTURE PROSPECTS OF WORK

List of Tables

Table **Page**

List of Figures

Figure **Page**

LIST OF ABBREVIATIONS

PVA	Poly vinyl alcohol
CS	Chitosan
TXA	Tranexamic acid
E	Ethamsylate
MSW	Marine Shell Waste
OS	Oyster Shell
MSWNF	Marine Shell Waste Nanofiber
CNF	Control nanofiber
UTS	Ultimate Tensile Strength
EB	Elongation at break
PBS	Phosphate buffered saline
WBCT	Whole blood clotting time
APTT	Activated partial thromboplastin time
PT	Prothombin Time
PRT	Platelet Recalcination Time
PPP	Platelet Poor Plasma
MTT	(3-(4,5-dimethylthiazol-2-yl)-2,5-diphenyltetrazolium bromide) assay
DMEM	Dulbecco’s modified Eagle’s medium
HADF	Human adult dermal fibroblast
OD	Optical Density
PT-PCR	Reverse transcription polymerase chain reaction
VEGF-A	Vascular endothelial growth factor A
PDGF	Platelet derived growth factor
IGF-1	Interleukin growth factor 1
GADPH	Glyceraldehyde-3-phosphate dehydrogenase
PC32	Poly vinyl alcohol and Chitosan 3:2 volume ratio (v/v)
PC11	Poly vinyl alcohol and Chitosan 1:1 ratio (v/v)
PS	Protein S

Chapter 1

INTRODUCTION

1. Introduction

Post-traumatic bleeding represents the second prominent cause of death from trauma injuries, following cardiac arrest, and is responsible for approximately 15% of trauma-related fatalities. In a healthy human body, blood volume remains constant and accounts for about 7-8% of total body weight. 20% blood loss experiences initial symptoms like dizziness and decreased urine output emerge. These are early signs of improper circulation. When blood loss escalates to 40% within a short period, life-threatening conditions rapidly develop and immediate medical intervention is needed. The body's natural haemostatic response to minor wounds is a complex, multi-stage process that includes vasoconstriction, platelet thrombosis and secondary haemostasis to seal wound surfaces and prevent excessive blood loss. Understanding these bodily responses is essential for developing useful approaches in trauma management and haemorrhage control to reduce the mortality risks associated with traumatic blood loss.

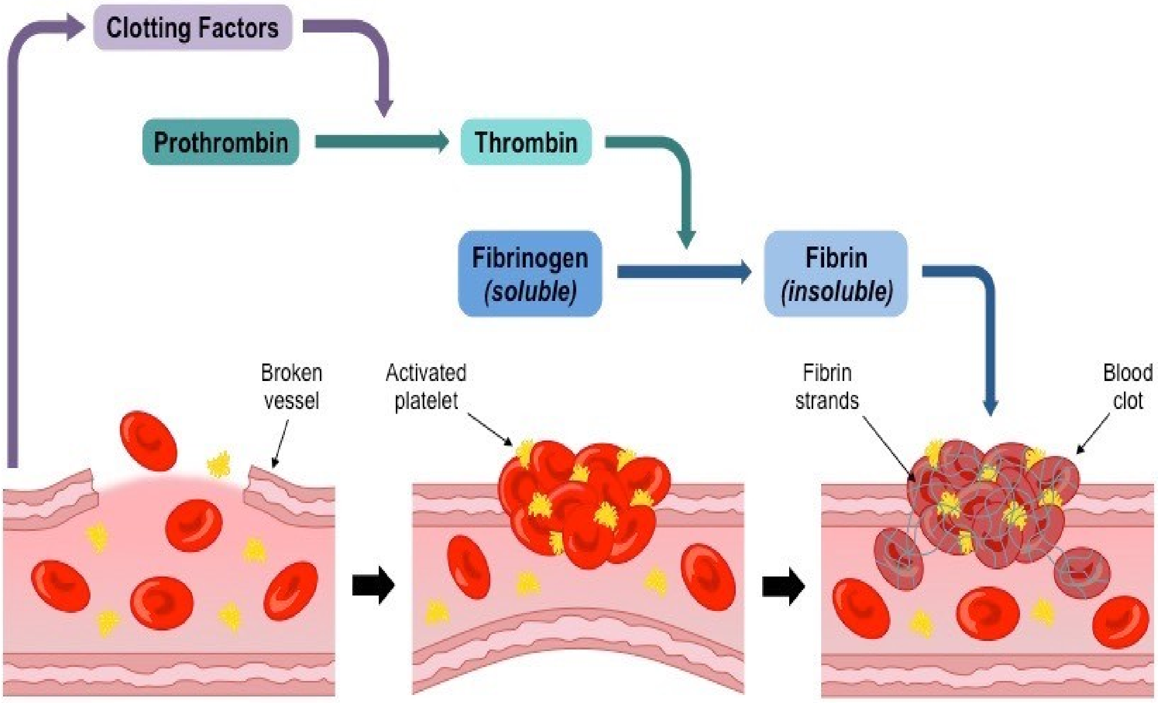

Figure 1.1 The general mechanism of blood clotting.

Haemostasis is a complex physiological process initiated by blood vessel rupture, involving multiple intricate mechanisms to stop bleeding. When injury occurs, vasoconstriction first reduces blood flow, while haemostatic agents like thromboxane A2 promote local arterial constriction. Platelets are activated by thrombin and adenosine diphosphate (ADP), while exposed subendothelial collagen causes platelet adhesion. During primary haemostasis, activated platelets release chemicals (ADP, TXA2) to attract more platelets and form clots. Meanwhile, blood coagulation occurs through internal and external mechanisms that combine to turn dissolved fibrinogen into solid fibrin threads, creating a stronger clot in the presence of calcium ion.

Thus, it is critical to produce haemostatic scaffolds that are convenient, safe, and effective. Current haemostasis research investigates various active bleeding-control agents that fall into four main categories namely natural polymers, synthetic polymers, inorganic materials, and metal-based compounds. These materials are designed into various innovative forms to treat bleeding and wound healing requirements, such as nanofibers, gels, sponges, and nanoparticles. The versatility of dressing materials extends beyond traditional wound management, finding significant applications in specialized medical interventions such as surgical procedure and traumatic injury.

It is important to understand haemorrhage and haemostasis before exploring haemostatic agents.

1.1 Haemorrhage

Haemorrhage following traumatic injuries is a significant reason of fatalities in both civilian and battlefield environments. It also remains the leading cause of death in cases of postpartum haemorrhage (PPH) and major road accidents. Postpartum haemorrhage is the prime cause of maternal death in both developed and developing countries, accounting for approximately 30% of all global maternal deaths [1]. Most countries in sub-Saharan Africa and Southern Asia have maternal mortality rates exceeding 1,000 women per 100,000 live births. According to more recent data from organizations like the World Health Organization (WHO) and UNICEF (2023), global maternal mortality is approximately 800 women per day, which translates to about one death every 2 minute worldwide [2]. The majority of PPH-related deaths occur within 4 hour following delivery, indicating inadequate management of the third stage of labour, with bleeding exceeding 1000 ml in early PPH.

Road traffic accidents represent the primary cause of mortality for among people aged 15 - 29 years. [3]. According to the report "Road Accidents in India," 150,000 people died and 380,000 were injured during 2021-22. All states and union territories of India reported a total of 461,312 accidents from 2022 to 2023, claiming 168,491 lives and causing injuries to 443,366 persons [4]. The death toll is projected to exceed 250,000 in 2025, as estimated by Singh S.K. [5]. A primary factor contributing to fatalities in traffic accidents is the failure to get victims to appropriate medical facilities quickly enough, coupled with substantial blood loss at the time of the accident.

1.2. Haemostasis

Haemostasis is the physiological process that maintains blood within blood vessels, minimizes excessive bleeding, and stops blood flow from damaged vessels by creating a haemostatic plug. This process is accelerated by local vasoconstriction, primary haemostasis, secondary haemostasis, and coagulation.

When an injury occurs, the process unfolds as follows:

1.2.1. Local vasoconstriction

Vascular spasms brought on by injury or damage to blood vessels result in vasoconstriction. This process initiates the cessation of blood flow. This response is localized to the site of injury and can persist for up to thirty minutes. The vasoconstriction is primarily mediated by endothelin-1, a powerful vasoconstrictor produced by the injured endothelium. Simultaneously, the damaged endothelium releases several components such as sub-endothelial collagen, von Willebrand factor (vWF), adenosine triphosphate (ATP) and various inflammatory mediators. Von Willebrand Factor (vWF) is not only released by the damaged endothelium but is also synthesized by megakaryocytes and stored in platelet α-granules. The inflammatory mediators attract macrophages to the site of injury. Exposed collagen fibers adhere to the damaged endothelium of the injured blood vessel. The increased thrombogenicity of the extracellular matrix (ECM) is particularly important as it promotes both platelet adhesion and aggregation, which are crucial steps in the formation of a haemostatic plug.

1.2.2. Primary haemostasis

Primary haemostasis is the initial phase of blood clotting that occurs immediately after blood vessel injury. It begins with vasoconstriction, where damaged blood vessels narrow to reduce blood flow. The injury exposes collagen fibers, which trigger a three-step platelet response i.e, adhesion, activation, and aggregation. Platelets first adhere to the exposed collagen, then become activated, changing shape and releasing chemicals. This activation attracts more platelets, which aggregate at the injury site. The culmination of this process is the formation of a platelet plug, effectively sealing the damaged area and completing primary haemostasis.

1.2.2.1. Platelet formation

Human platelets, also known as thrombocytes, are small biconvex disc-shaped structures measuring 2-3 μm in diameter. These cellular fragments are present in healthy individuals at a concentration of 150-450 x 10^9/L in whole blood, approximately ten times less frequent than red blood cells. Platelets are primarily produced by megakaryocytes in the bone marrow, with a healthy adult generating about 10^11 platelets daily. They have an average lifespan of 8-9 days before being destroyed by phagocytosis in the spleen and liver. In circulation, about 70% of platelets are mobile while the remainder are stored in the spleen. Interestingly, rheological forces from red blood cells push platelets towards vessel walls, creating a 3-5fold platelet enrichment at the vessel boundary. This positioning allows platelets to continually monitor the vascular wall for damage. Abnormal platelet counts can lead to thrombocytopenia (count below 150,000/μL) that can cause inadequate clotting and increased bleeding risk, while thrombocythemia (count above 600,000/μL) may increase the risk of thrombotic events such as stroke or myocardial infarction.

1.2.2.2. Platelet reorganization and attachment to areas of vascular damage

In ordinary state the total life span of platelets is uneventful so there are some transient stimuli evoke an explosive response as a result turning a powerful haemostatic agent within a matter of second at a stage of vascular injury. The dramatic interface is made possible through a number of interactions between the receptor aligned over the platelets and the extracellular ligands at the site of vascular injury.

1.2.2.3. Platelet accumulate at the site of injury to form haemostatic plug

Platelets build up at the wound site to create a mesh that seals it off. The platelets become spiky instead of spherical, and they release chemicals and proteins that trap other platelets and clotting proteins in the expanding plug that develops into a blood clot.

1.2.2.4. Platelet activation

Platelets can be activated by a wide range of events. Moreover, stimulation of the biomaterial surface might activate platelet cells. Following degranulation, adhered platelets release cytoplasmic granules containing ADP, platelet activation factors, and serotonin. A key physiological agonist called ADP is kept in the dense bodies of platelets and is crucial for maintaining proper thrombosis and hemostasis. As soon as the platelets adhere to the wounded area, they become activated and take on the shape of a pseudopodal, which triggers the release of GpIIbIIIa, a collagen receptor on their surface membrane [6]. A critical stage in platelet aggregation and endothelium adhesion is the GpIIbIIIa complex, which is arranged by the calcium-dependent interaction of GpIIb and GpIIIa. Concurrently, platelets often produce and release thromboxane A2 (TXA2), which promotes platelet aggregation and vasoconstriction. Furthermore, to facilitate platelet aggregation, GpIIbIIIa integrins and P-selectin migrate from the α-granule membrane to the platelet membrane. These receptors also have the potential to serve as a catalytic surface and speed up the hemostasis process.

Following platelet activation, the GpIIbIIIa receptor (50–100/platelets) attaches to vWF or Fib, initiating platelet aggregation. Pseudopods extend from each stimulated platelet, forming clumps and becoming aggregated. The production of thrombin through the hemostasis process amplifies these activations even further. A main platelet plug is promoted by platelet aggregation. The ADP receptor interacts with the P2Y1 and P2Y12 ADP receptor family, which may be found on platelets and contribute to aggregation. P2Y1 receptors have a role in inducing the first platelet aggregation and shape alterations. P2Y12 is a crucial mediator for blood clotting at the same time. In order to finish the aggregation process, P2Y12 dramatically rises in response to ADP. Fibrin development should eventually stabilize by the formation of platelet plug [7].

1.2.3. Secondary haemostasis

The secondary haemostasis phase involves the formation of fibrin clots at the location of initial haemostatic plug, including intrinsic pathway, extrinsic pathway and common pathway.

1.2.3.1. Intrinsic pathway

The intrinsic pathway is initiated by the activation of factor XII after tissue injury. These activations are facilitated by two proteins namely high-molecular-weight prekallikrein and kininogen. The transformation of factor XI into factor XIa is catalysed by factor XIIa. Factor XIa catalyses the transformation of factor IX into factor IXa by the presence of calcium ions. Factor IXa forms a complex (factor IXa–factor VIII complex) with factor VIII and calcium is needed to maintain stability and preserve the membrane-binding domains on these proteins. Factor Xa becomes activated when factor X binds to the factor IXa–factor VIII complex. Factor Xa and factor V join together on membrane surfaces to create a complex in the presence of calcium ion. Reacting with the factor Xa–factor V complex, prothrombin transforms into thrombin, that breaks down fibrinogen into fibrin monomer. Then the fibrin monomer polymerize to form long fibres. Subsequently, factor XIIIa promotes more bonding between the polymer and stabilizing the newly formed clot.

The activated partial thromboplastin time is a straightforward laboratory test that can be used to measure the intrinsic blood coagulation activity. Using citrate buffer, blood plasma is collected and anticoagulated. It is impossible to form a fibrin clot in these circumstances. The plasma is mixed with a negatively charged substance, kaolin. Factor XII is activated by Kaolin into factor XIIa, an enzyme, which activates factor XI. Insufficient calcium ions prevent the process from continuing to activate further since they are necessary for activating factor IX. After adding calcium ions and a phospholipid preparation, the clot formation time was recorded. Depending on the chemical composition utilized, activated partial thromboplastin time is 25 to 50 sec. The test plasma clotting times are compared to normal plasma clotting times. A prolonged partial thromboplastin time indicates delayed clotting, which can be caused by a pharmacological inhibitor of blood coagulation or a deficit in the action of one or more blood-clotting components.

1.2.3.2. Extrinsic pathway

The extrinsic pathway of blood coagulation is initiated by tissue factor. Although tissue factor is present in many body cells, it is especially prevalent in the brain, lungs, placenta and abundant to the extracellular membrane of injured tissue. Factor X is activated more easily when tissue factor and factor VII work together as cofactors. On the other hand, factor VII has the ability to activate factor IX, which can then activate factor X. After activation, prothrombin is converted to thrombin by factor X, a step that requires factor V. Fibrinogen is converted into fibrin by the thrombin. All elements of the extrinsic pathway are also elements of the intrinsic pathway, with the exception of factor VII.

The prothrombin time (PT) test is a straightforward test that may be used in the lab to measure the activity of extrinsic blood clotting pathway. Tissue factor-rich animal tissues are used to obtain tissue extract, also known as tissue thromboplastin. After anticoagulating plasma with citrate buffer, phospholipid, calcium, and thromboplastin are added at the same time, allowing the plasma to clot. The prothrombin time, which is the amount of time until clot formation, is typically 10 to 12 seconds. In real-world applications, test plasma clotting times are contrasted with normal plasma clotting times. Prolonged prothrombin time, which is a measure of delayed clotting, can be caused by a pharmacological inhibitor of the extrinsic blood clotting pathway.

1.2.3.3. Common pathway

The common pathway represents the ultimate route of blood coagulation. Calcium ions in the blood cause clotting according to this mechanism. Factor VII and Factor XII cannot be activated without calcium ions. Additionally, they contribute to the activation of both factor X and factor IX. When factor XII (FXII) is triggered by contact with foreign surface, the common route gets started. After that, this FXII triggers FXI, which triggers FIX. Prothrombin is then activated by FX, which is activated by FIX. FVIIa then changes prothrombin into thrombin, and thrombin changes fibrinogen into fibrin. After then, the fibrin polymerizes to create a clot.

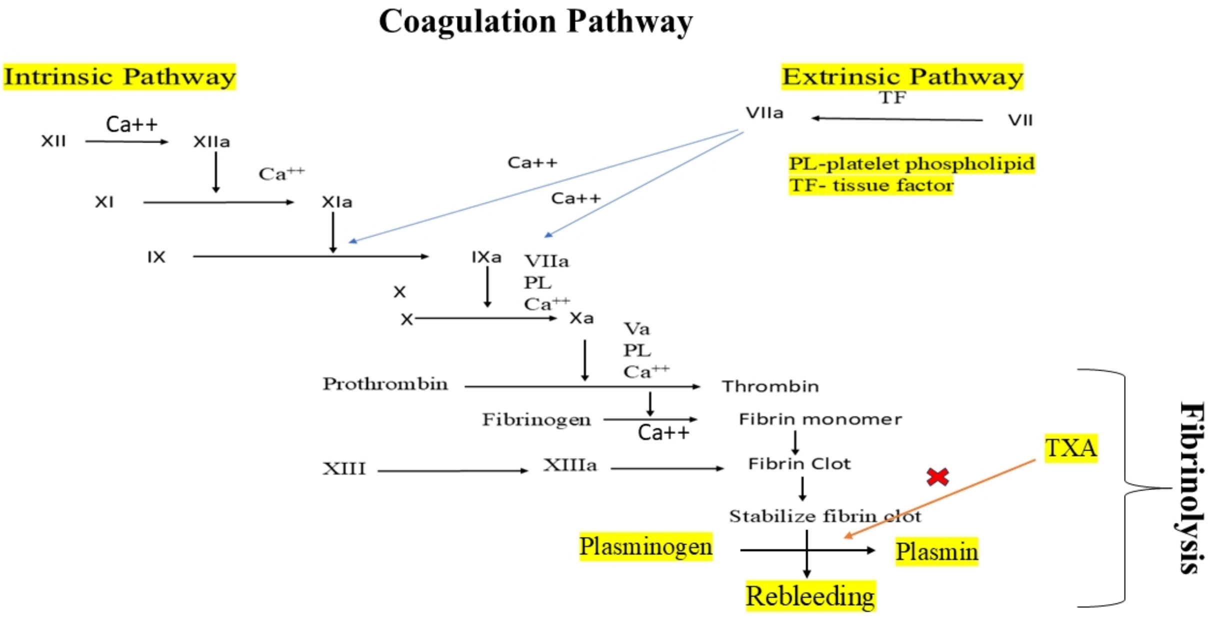

Figure 1. 2 The role of Ca^{++} and fibrinolysis in blood coagulation pathway.

1.2.4. Tertiary haemostasis

The tertiary haemostasis system operates alongside the blood clotting cascade as a regulatory mechanism to control clot size. This system involves an enzyme-driven process called fibrinolysis, where plasmin breaks down fibrin clots into smaller fragments known as fibrin degradation products (FDPs). The plasmin enzyme comes from plasminogen that was bound to fibrin and produced in the liver. This breakdown reaction is facilitated by tissue plasminogen activator (tPA) or urokinase plasminogen activator (u-PA) from the endothelium of blood vessels. The secretion of tPA is triggered by various factors including blocked blood flow, thrombin presence, adrenaline, vasopressin, and intense physical activity. Following clot formation, plasminogen transforms into plasmin, which is an enzyme that degrades the fibrin structures within the clot, eventually breaking it apart and restoring proper blood flow through the injured or obstructed vessels. Simultaneously, when platelets become activated, they contract the actin and myosin protein fibers within their cellular structure, causing the blood clot to shrink in size [8].

1.3. Clot retraction and fibrinolysis

Clot retraction is the process in which the clot shrinks and draws the wound edges closer together. During clot retraction, actin and myosin in the platelets of the platelet plug contract. The fibrinogen-connected platelet web starts to retract and condense as these proteins tighten. As a result, the associated fibrin retracts and condenses the blood clot. Therefore, by pulling the injured ends of the blood vessel, clot retraction reduces the size of the cut. Both epithelial and fibroblast cells proliferate within and around the clot. Meanwhile, the body begins the process of tissue repair and regeneration to fully heal the injured blood vessel.

After the injured blood vessel has healed, the clot is no longer needed. Fibrinolysis is the process by which the clot is broken down and removed, primarily through the action of an enzyme called plasmin. Plasmin is the active form of plasminogen. Plasminogen is synthesized and released by the liver and is converted to plasmin by tissue plasminogen activator (tPA). tPA is produced in endothelial cells. The process of clot breakdown is sparked by tPA, which significantly speeds up its enzymatic function to convert plasminogen to plasmin in the presence of fibrin. Fibrin starts its own breakdown by activating tPA.

Hemostasis maintains the balance between clot formation and clot dissolution. Disruption of this balance can lead to bleeding disorders or thrombotic disorders, where blood clots form inappropriately within blood vessels. Though achieving rapid haemostasis is long recognized as a crucial step in disease management, this objective has still remained a critical challenge. Haemorrhage is also of prime importance during several surgical procedures including laparoscopic surgeries, where internal haemorrhage raises concerns for post-operative complications. In addition, menorrhagia is another syndrome associated with huge amount of blood loss. All these clinical conditions have driven extensive interest in the development of biomaterials and tissue sealants for haemorrhage control. An ideal haemostatic system should provide rapid control of bleeding, be infection-resistant, have no cytotoxicity, not produce any inflammation-triggering degradation products or thromboembolic complications and not adversely affect the wound healing cascade [9], [10].

Thus, haemostatic dressing becomes very beneficial to stop bleeding and reach a hospital within golden hours [11]. The well-known idea of the "golden hours" holds that reducing the amount of time between an accident and receiving decisive care is crucial for improving the prognosis of trauma patients. The data were not backed up by any proven proof. The haemostatic material should have rapid haemostasis capability with a significant antimicrobial effect meant for use during the prehospitalization period. Rapid haemostasis is accomplished by constricting blood vessels, accelerating the formation of clotting factors, activating platelets, and shortening the coagulation cascade reaction [12].

1.4. Haemostatic materials

Currently, haemostatic materials are made from natural polymers, synthetic polymers, inorganic and metal-containing materials.

1.4.1. Natural polymers

Polysaccharides and collagens are the most extensively used natural polymeric haemostatic compounds. These are histocompatibility, naturally degradable, non-irritating, non-immunogenic, and non-haemolytic. Polysaccharides are monosaccharide-based biomaterials with significant haemostatic potential. Glycans like chitosan, cellulose, alginate and hyaluronic acid offer exceptional wound healing properties due to biodegradability, biocompatibility, and tissue-mimicking structures [13], [14]. Their inherent characteristics enable superior blood coagulation and minimal immune response, positioning them as promising advanced medical biomaterials for haemostatic interventions.

Chitosan has developed as a versatile biomaterial by its non-immunogenicity, antimicrobial characteristics, exceptional biocompatibility, and biodegradability [15]. Its haemostatic capabilities collectively promote blood coagulation through three mechanisms. The first mechanism involves red blood cell (RBC) aggregation, where the positively charged glucosamine in chitosan attracts negatively charged RBCs, inducing agglutination and facilitating coagulation cascade [16]. The second mechanism focuses on platelet stimulation, platelet adhesion and aggregation by chitosan effectiveness and enhancing the expression of the GPIIb/IIIa complex on platelet surfaces [17]. The third haemostatic effect of chitosan relates to its molecular weight (Mw) and degree of deacetylation (DDA) [18]. Research indicates that chitosan nanofibers typically have an Mw of 8.6-247 kDa and a DDA of 75–88% [19].

Several FDA-approved chitosan dressing such as HemCon® Bandage, utilizing freeze-dried chitosan, achieves haemostasis within 2 minutes through compression and intrinsic properties. Its stiffness makes it difficult to apply to deep wounds, and it must be removed within 48 hours.

Celox®, composed of chitosan particles, improves the rigidity of HemCon® Bandage and offers improved haemostatic effects. TraumaStat®, created from chitosan, silicon dioxide, and polyethylene, offers a greater surface area, improved wound contact, and increased flexibility, making it appropriate for various types of wounds.

Cellulose is a remarkable natural polymer derived from plants and bacteria. It possesses non-cytotoxicity, biocompatibility, biodegradability, and high absorption capacity. Cellulose physically compresses bleeding sites and contains carboxyl functional groups that bind with Fe^{3+} ions of hemoglobin, forming brown gels that seal capillary ends [20]. Additionally, it can activate platelets, accelerating the haemostasis process [21]. By combining cellulose with inorganic materials like kaolin and halloysite nanoclay, scientists have developed advanced nanocomposite materials with superior blood clotting performance. For instance, Ca^{2+} cross-linked nano fibrillated cellulose/kaolin hydrogels efficiently trigger thrombin generation, while halloysite nanocomposite fibers demonstrate enhanced clotting activity [22]. Oxidized cellulose (OC) represents another significant advancement, improving biosolubility and tissue compatibility. Its negatively charged surface interacts with thrombin, facilitating haemostasis through physical adsorption and physiological mechanisms [23].

Hyaluronic acid (HA) is a naturally occurring acidic mucopolysaccharide well known for its exceptional biocompatibility within the human body [24]. Due to rich in hydroxyl groups, it enables remarkable water absorption and hydrogen bonding that helps concentrate platelets and coagulation factors at wound sites [25]. It actively participates in inflammatory responses by mediating the release of cytokines like TNF-α, IL-1β, and IL-8. Moreover, HA facilitates fibroblast invasion and proliferation, thereby promoting tissue regeneration and wound closure [26]. HA-tyrosine (HA-Tyr) hydrogels have demonstrated improved haemostasis and increased cell adhesion capabilities [27]. Bagheri et al. specifically investigated phenolic hydroxy HA (HA-Ph) hydrogels, examining their impact on cell adhesion and proliferation properties [28].

Alginate has absorption capabilities and ability to concentrate platelets and coagulation factors. Rong et al. have developed microspheres consist of brown seaweed and thrombin that provide promising results in haemorrhage treatment. Thrombin-loaded alginate-calcium microspheres (TACMs) have proven particularly effective in managing blunt trauma and arterial bleeding with specific ratios like G/M = 0.38 [29].

Collagen stimulates platelet activation and ADP and TXA2, that lead to irreversible platelet aggregation [30], [31]. The adverse effects include allergic reactions, demonstrates poor adhesion, and resists easy degradation. To address these challenges, researchers have converted collagen into gelatin by partial hydrolysis [32]. Park et al. conducted a comparative study using Hemoblast®, and Floseal® in a porcine liver haemorrhage model with superior bleeding reduction capabilities [33]. Wang et al. developed functionalized gelatin sponges using gold/silver clusters to enhance antibacterial properties [34].

1.4.2. Synthetic polymers

Synthetic Polymers also used as haemostatic material for their easy synthesis and fabrication compared to natural polymers. Poly(ethylene glycol) (PEG) demonstrates tissue adhesion and is used as a drug carrier in controlled release form [35], [36]. PEG-based hydrogels can concentrate platelets and coagulation factors around wound sites, making them particularly suitable for haemostatic closure of traumatic organ injuries [37]. PEG and acrylic acid can participate in esterification reactions, producing poly(ethylene glycol) diacrylate (PEGDA) [38]. This hydrogel can be rapidly formed through a photoinitiator and ultraviolet (UV) light at room temperature and used for quick wound closure.

Polyurethane (PU) foams can effectively induce coagulation cascades and platelet aggregation [39]. A notable example is NasoPore®, a PU-based foam that demonstrated improved hemostasis and received positive patient feedback in clinical trials, particularly in nasal caulking following endoscopic sinus surgery [40].

Poly(vinyl alcohol) (PVA)-based hemostatic sponges offer exceptional hydrophilic and liquid-absorbing properties, coupled with strong biocompatibility and chemical stability [41]. Kim et al. promoted mucosal healing by using PVA-based nanocellulose sponges in a rabbit model with nasal mucosal defects [42].

Similarly, Deineka et al. utilized nanofiber mats composed of poly(ethylene oxide) (PEO) and chitosan in a rat liver injury model, that reduced bleeding time with improved degradability and tissue repair [43]. Cheng et al. developed PCL/collagen fibers using phage incorporation and electrostatic spinning, demonstrating excellent antimicrobial effects and rapid hemostasis in rabbit injury models [44].

However, most synthetic polymers fundamentally lack the biological activity to promote blood clotting. They primarily serve as cross-linking agents for haemostatic materials. By combining synthetic polymers with natural polymers, scientists aim to create materials that integrate the strengths for haemostatic medical treatments.

1.4.3. Inorganic materials and metal-containing materials

Inorganic materials have become novel haemostatic agents. Zeolites and kaolin are notable examples of materials that accelerate blood coagulation. These haemostats are derived from natural minerals and have several strong benefits in haemorrhage. They are abundant, inexpensive, porous, very absorbent, and carry minimal risk of blood-transmitted diseases, but most are not biodegradable and require disposal after application.

Zeolites are a crystalline microporous minerals composed of $[SiO4]^{4-}$ and $[AlO4]^{5-}$ structural units. These materials improved the clotting process by drawing water from blood and concentrating blood cells, platelets, and coagulation factors at injury sites. QuikClot, the first-generation product, demonstrated rapid water absorption and haemostatic properties but was characterized by an undesirable exothermic reaction that limited in vivo application. Recognizing this limitation, researchers developed QuikClot ACS (Advanced Clotting Sponge), a second-generation haemostat that generates less heat and provides more effective haemostasis. For instance, Yu and colleagues pioneered a groundbreaking approach by creating a zeolite-infused cotton T-shirt capable of achieving rapid haemostasis [45]. This development holds particular promise for emergency scenarios where conventional first aid resources may be limited, potentially saving lives in critical situations by providing an immediate haemostatic intervention.

Kaolin binds to Factor XII and starts the blood clotting process, which activates Factor XI and forms a clot in intrinsic pathway. The commercial products of kaolin are promoted as QuikClot Combat Gauze™, QuikClot Combat Gauze XL, QuikClot Combat Gauze TraumaPad, and QuikClot® Interventional™. Kheirabadi et al. assessed the effectiveness of QuikClot Combat Gauze™ in pig model of arterial bleeding and found it to be the primary treatment for severe hemorrhage in combat situations [46].

1.4.4 Biomaterial sustainability

In recent years, materials derived from renewable sources have opened new possibilities for creating innovative and sustainable approaches. The sustainability of biomaterials centres on creating and utilizing substances sourced from renewable biological origins as alternatives to conventional materials, while reducing their environmental footprint. This area presents a significant, intricate challenge that spans social and technical domains, necessitating comprehensive evaluation from ecological, social, and technological perspectives. Various biomass and waste materials, including collagen-like biopolymers, are being utilized to create biocompatible nanocomposite materials. Catalina and colleagues focused on recovering bio-collagen from abattoir waste and converting leather waste into valuable products [47]. Hapkin's research team examined the mechanical properties and biochemical characteristics of silk-based hydrogels derived from silk fibroin proteins for applications in nerve tissue repair [48]. Jan and their group developed an environmentally friendly and adaptable method using crosslinked polysaccharide hydrogels as frameworks for silica formation [49]. These silica-peptide hydrogels exhibited strong mechanical strength, demonstrated good biocompatibility, and facilitated cellular attachment and multiplication for tissue engineering scaffold purposes. Scaling up the cost-effective and environmentally sustainable production of bio-based materials from natural sources represents a current challenge. Materials derived from biomass and waste offer diverse applications across adsorption processes, energy conversion technologies, and biomedical fields.

Table 1. 1 The Composition, advantages and disadvantages of some of the commonly-employed commercial haemostatic agents.

Year	Haemostatic Agent	Composition	Advantage/Disadvantage
1940	Gelfoam®[50]	Gelatin based Thrombin.	For haemostasis in tubeless percutaneous nephrolithotomy. There is a risk of nerve compression due to excessive swelling. Gelatin is derived from animal source, so there is a risk of antigenicity.
1949	Superglue®[51]	Cyanoacrylates	Surgical adhesives for tympanic membrane repair in battle field, wound adhesive.
1960	Surgicel®[52]	Oxidised cellulose	Control surgical bleeding during partial nephrectomy. Concerning for abscess.
1970	Avitene®, Halistat®, Instat®[53]	Microfibrillar Collagen based.	Strong adhesion to the injured tissues as form of fine fiber and sponge. Activate the intrinsic pathway of coagulation cascade. Promotes platelet clumping and protein release to create fibrin, leading to blood clotting. Exothermic polymerization reaction, slow degradation rate, toxicity and increased

			tissue inflammations.
1998	Tisseel®, Hemaseel®[54]	Bovine thrombin and fibrin sealant	Improving skin graft survival and adhesion in the grafting of soldiers with several burn injuries.
1998	Dermabond®	2-Octyl-Cyanoacrylate	A good adhesive with antimicrobial properties.
1999	Floseal®[55]	Flowable bovine based gelatin matrices with human derived thrombin granules.	It is absorbable and tolerated in invasive surgery. Applied focally at the target site of bleeding to provide fast, effective bleeding control. Rare reports of abscess formation or granuloma formation.
2000	Avitene Ultrafoam Collagen	Composed of non-woven web material as well as sponge with thrombin.	Readymade sponge enhances platelet aggregation and the release of proteins to form fibrin. Active, absorbable collagen hemostat helps accelerate clot formation. Soft and pliable. No soaking necessary
2002	Quickclot®[56]	Gauge impregnated with Zeolite.	Absorb water molecules inside the blood, leaving bigger platelets and clotting factor molecules. Exhibit exothermic reaction to produce tissue damage.
2002	HemCon®[57]	Chitosan based haemostatic agent	Function by causing blood vessel constriction and quickly binding to red blood cells, platelets, and clotting factors. Also, it can absorb fluid to the wound site by aggregating clotting factor, making a gel like matrix over the wounds.
2003	Crosseal®	Human fibrinogen with thrombin	Utilized for topical delivery of antibiotics, chemotherapies and analgesics.
2005	Surgiflo®	Flowable porcine based-gelatin matrices with	Used in laproscopic surgery to control oozing and prevent bleeding.

		human derived thrombin.	
2007	Evithrom®[51]	Human thrombin	Used to arrest oozing blood and minor bleeding from capillaries and small venules is accessible but control of bleeding by standard surgical techniques is ineffective.
2008	Recothrom®	Recombinant human thrombin	A topical thrombin indicated to aid hemostasis whenever oozing blood and minor bleeding from capillaries and small venules.
2014	Quickclot Combat Gauge[58]	Gauge impregnated with keolin.	Keolin activates factor XII and assists in the initiation of the coagulation cascade that promote blood clotting.
2017	Hemoblast™[59]	Powdered surgical hemostat consist of highly purified porcine collagen with bovine chondroitin sulfate and human pooled plasma derived thrombin.	Effective on moderate bleeding including pooling and flowing bleeding. May be risk of allergic-anaphylactoid reaction and thromboembolic events.

References:

[1] Mathai M, Gülmezoglu AM, Hill S. Saving womens lives: evidence-based recommendations for the prevention of postpartum haemorrhage. Bull World Health Organ. 2007 Apr;85(4):322-3. doi: 10.2471/blt.07.041962. PMID: 17546315; PMCID: PMC2636323.

[2] Ekwuazi EK, Chigbu CO, Ngene NC. Reducing maternal mortality in low- and middle-income countries. Case Rep Womens Health. 2023 Sep 9;39:e00542. doi: 10.1016/j.crwh.2023.e00542. PMID: 37954228; PMCID: PMC10636262.

[3] F. Li *et al.*, "A Review on Injury Mechanism of Intracerebral Hemorrhage in Vehicle Accidents," *Curr Pharm Des*, vol. 23, no. 15, Jun. 2017, doi: 10.2174/1381612823666161118144829.

[4] G Gotkari et al. "ROAD ACCIDENTS IN INDIA 2022." road safety report 2022, Government of india, Page no1-238.

[5] S. K. Singh, "Road Traffic Accidents in India: Issues and Challenges," in *Transportation Research Procedia*, Elsevier B.V., 2017, pp. 4708–4719. doi: 10.1016/j.trpro.2017.05.484.

[6] Periayah MH, Halim AS, Mat Saad AZ. Mechanism Action of Platelets and Crucial Blood Coagulation Pathways in Hemostasis. Int J Hematol Oncol Stem Cell Res. 2017 Oct 1;11(4):319-327. PMID: 29340130; PMCID: PMC5767294..

[7] R. T. Dorsam and S. P. Kunapuli, "Central role of the P2Y12 receptor in platelet activation," *Journal of Clinical Investigation*, vol. 113, no. 3, pp. 340–345, Feb. 2004, doi: 10.1172/jci200420986.

[8] Palta S, Saroa R, Palta A. Overview of the coagulation system. Indian J Anaesth. 2014 Sep;58(5):515-23. doi: 10.4103/0019-5049.144643. PMID: 25535411; PMCID: PMC4260295.

[9] Hickman DA, Pawlowski CL, Sekhon UDS, Marks J, Gupta AS. Biomaterials and Advanced Technologies for Hemostatic Management of Bleeding. Adv Mater. 2018 Jan;30(4):10.1002/adma.201700859. doi: 10.1002/adma.201700859. Epub 2017 Nov 22. PMID: 29164804; PMCID: PMC5831165..

[10] Peng T. Biomaterials for hemorrhage control. Trends Biomater Artif Organs. 2010;24(1):27-68.

[11] K. Okada, H. Matsumoto, N. Saito, T. Yagi, and M. Lee, "Revision of 'golden hour' for hemodynamically unstable trauma patients: An analysis of nationwide hospital-based registry in Japan," *Trauma Surg Acute Care Open*, vol. 5, no. 1, Mar. 2020, doi: 10.1136/tsaco-2019-000405.

[12] Periayah MH, Halim AS, Mat Saad AZ. Mechanism Action of Platelets and Crucial Blood Coagulation Pathways in Hemostasis. Int J Hematol Oncol Stem Cell Res. 2017 Oct 1;11(4):319-327. PMID: 29340130; PMCID: PMC5767294.

[13] T. Zhu *et al.*, "Recent Progress of Polysaccharide-Based Hydrogel Interfaces for Wound Healing and Tissue Engineering," Sep. 01, 2019, *Wiley-VCH Verlag*. doi: 10.1002/admi.201900761.

[14] M. Naseri-Nosar and Z. M. Ziora, “Wound dressings from naturally-occurring polymers: A review on homopolysaccharide-based composites,” Jun. 01, 2018, *Elsevier Ltd.* doi: 10.1016/j.carbpol.2018.02.003.

[15] S. B. Rao and C. P. Sharma, “Use of chitosan as a biomaterial: Studies on its safety and hemostatic potential,” *J Biomed Mater Res*, vol. 34, no. 1, pp. 21–28, Jan. 1997, doi: 10.1002/(SICI)1097-4636(199701)34:1<21::AID-JBM4>3.0.CO;2-P.

[16] E. P. Rondon *et al.*, “Evidence supporting the safety of pegylated diethylaminoethyl-chitosan polymer as a nanovector for gene therapy applications,” *Int J Nanomedicine*, vol. 15, pp. 6183–6200, 2020, doi: 10.2147/IJN.S252397.

[17] T. C. Chou, E. Fu, C. J. Wu, and J. H. Yeh, “Chitosan enhances platelet adhesion and aggregation,” *Biochem Biophys Res Commun*, vol. 302, no. 3, pp. 480–483, Mar. 2003, doi: 10.1016/S0006-291X(03)00173-6.

[18] Y. Huang *et al.*, “Hemostasis mechanism and applications of N-alkylated chitosan sponge,” *Polym Adv Technol*, vol. 28, no. 9, pp. 1107–1114, Sep. 2017, doi: 10.1002/pat.4003.

[19] H. Hattori and M. Ishihara, “Changes in blood aggregation with differences in molecular weight and degree of deacetylation of chitosan,” *Biomedical Materials (Bristol)*, vol. 10, no. 1, Feb. 2015, doi: 10.1088/1748-6041/10/1/015014.

[20] K. Parikka *et al.*, “Functional and anionic cellulose-interacting polymers by selective chemo-enzymatic carboxylation of galactose-containing polysaccharides,” *Biomacromolecules*, vol. 13, no. 8, pp. 2418–2428, Aug. 2012, doi: 10.1021/bm300679a.

[21] L. P. Soares, M. G. De Oliveira, A. L. B. Pinheiro, B. R. Fronza, and M. E. S. Maciel, “Effects of laser therapy on experimental wound healing using oxidized regenerated cellulose hemostat,” *Photomed Laser Surg*, vol. 26, no. 1, pp. 10–13, Feb. 2008, doi: 10.1089/pho.2007.2115.

[22] A. Basu, J. Hong, and N. Ferraz, “Hemocompatibility of Ca2+-Crosslinked Nanocellulose Hydrogels: Toward Efficient Management of Hemostasis,” *Macromol Biosci*, vol. 17, no. 11, Nov. 2017, doi: 10.1002/mabi.201700236.

[23] H. Li *et al.*, “Manufacturing and physical characterization of absorbable oxidized regenerated cellulose braided surgical sutures,” *Int J Biol Macromol*, vol. 134, pp. 56–62, Aug. 2019, doi: 10.1016/j.ijbiomac.2019.05.030.

[24] A. Fallacara, S. Manfredini, E. Durini, and S. Vertuani, “Hyaluronic Acid Fillers in Soft Tissue Regeneration,” *Facial Plastic Surgery*, vol. 33, no. 1, pp. 87–96, Feb. 2017, doi: 10.1055/s-0036-1597685.

[25] K. L. Aya and R. Stern, “Hyaluronan in wound healing: Rediscovering a major player,” *Wound Repair and Regeneration*, vol. 22, no. 5, pp. 579–593, Sep. 2014, doi: 10.1111/wrr.12214.

[26] A. G. Tavianatou, I. Caon, M. Franchi, Z. Piperigkou, D. Galesso, and N. K. Karamanos, “Hyaluronan: molecular size-dependent signaling and biological functions in inflammation and cancer,” 2019, *Blackwell Publishing Ltd.* doi: 10.1111/febs.14777.

[27] C. Loebel *et al.*, “Cross-Linking Chemistry of Tyramine-Modified Hyaluronan Hydrogels Alters Mesenchymal Stem Cell Early Attachment and Behavior,” *Biomacromolecules*, vol. 18, no. 3, pp. 855–864, Mar. 2017, doi: 10.1021/acs.biomac.6b01740.

[28] S. Bagheri *et al.*, “Control of cellular adhesiveness in hyaluronic acid-based hydrogel through varying degrees of phenol moiety cross-linking,” *J Biomed Mater Res A*, vol. 109, no. 5, pp. 649–658, May 2021, doi: 10.1002/jbm.a.37049.

[29] J. jing Rong *et al.*, “Thrombin-loaded alginate-calcium microspheres: A novel hemostatic embolic material for transcatheter arterial embolization,” *Int J Biol Macromol*, vol. 104, pp. 1302–1312, Nov. 2017, doi: 10.1016/j.ijbiomac.2017.03.020.

[30] R. W. Farndale, “Collagen-induced platelet activation,” *Blood Cells Mol Dis*, vol. 36, no. 2, pp. 162–165, Mar. 2006, doi: 10.1016/j.bcmd.2005.12.016.

[31] T. Manon-Jensen, N. G. Kjeld, and M. A. Karsdal, “Collagen-mediated hemostasis,” *Journal of Thrombosis and Haemostasis*, vol. 14, no. 3, pp. 438–448, Mar. 2016, doi: 10.1111/jth.13249.

[32] L. Zhang *et al.*, “Potentials of sandwich-like chitosan/polycaprolactone/gelatin scaffolds for guided tissue regeneration membrane,” *Materials Science and Engineering C*, vol. 109, Apr. 2020, doi: 10.1016/j.msec.2019.110618.

[33] S. M. Park *et al.*, “Efficacy and Safety of a Thrombin-Containing Collagen-Based Hemostatic Agent in Spinal Surgery: A Randomized Clinical Trial,” *World Neurosurg*, vol. 154, pp. e215–e221, Oct. 2021, doi: 10.1016/j.wneu.2021.07.012.

[34] X. Wang *et al.*, “Gelatin sponge functionalized with gold/silver clusters for antibacterial application,” *Nanotechnology*, vol. 31, no. 13, Jan. 2020, doi: 10.1088/1361-6528/ab59eb.

[35] F. Lasowski, T. Rambarran, V. Rahmani, M. A. Brook, and H. Sheardown, “PEG-containing siloxane materials by metal-free click-chemistry for ocular drug delivery applications,” *J Biomater Sci Polym Ed*, vol. 32, no. 5, pp. 581–594, 2020, doi: 10.1080/09205063.2020.1851558.

[36] D. B. Kaldybekov, S. K. Filippov, A. Radulescu, and V. V. Khutoryanskiy, “Maleimide-functionalised PLGA-PEG nanoparticles as mucoadhesive carriers for intravesical drug delivery,” *European Journal of Pharmaceutics and Biopharmaceutics*, vol. 143, pp. 24–34, Oct. 2019, doi: 10.1016/j.ejpb.2019.08.007.

[37] E. Lih, J. S. Lee, K. M. Park, and K. D. Park, “Rapidly curable chitosan-PEG hydrogels as tissue adhesives for hemostasis and wound healing,” *Acta Biomater*, vol. 8, no. 9, pp. 3261–3269, 2012, doi: 10.1016/j.actbio.2012.05.001.

[38] Z. Stillman, B. M. Jarai, N. Raman, P. Patel, and C. A. Fromen, “Degradation profiles of poly(ethylene glycol)diacrylate (PEGDA)-based hydrogel nanoparticles,” *Polym Chem*, vol. 11, no. 2, pp. 568–580, Jan. 2020, doi: 10.1039/c9py01206k.

[39] H. T. Beaman *et al.*, “Hemostatic shape memory polymer foams with improved survival in a lethal traumatic hemorrhage model,” *Acta Biomater*, vol. 137, pp. 112–123, Jan. 2022, doi: 10.1016/j.actbio.2021.10.005.

[40] P. K. Burduk, M. Wierzchowska, B. Grześkowiak, W. Kaźmierczak, and K. Wawrzyniak, “Desfecho clínico e satisfação do paciente com o uso de tampão biodegradável (NasoPore) e não biodegradável: estudo prospectivo, duplo-cego e randomizado,” *Braz J Otorhinolaryngol*, vol. 83, no. 1, pp. 23–28, Jan. 2017, doi: 10.1016/j.bjorl.2016.01.001.

[41] T. M. Tamer *et al.*, “Development of polyvinyl alcohol/kaolin sponges stimulated by marjoram as hemostatic, antibacterial, and antioxidant dressings for wound healing promotion,” *Int J Mol Sci*, vol. 22, no. 23, Dec. 2021, doi: 10.3390/ijms222313050.

[42] J. W. Kim *et al.*, “Effect of expanding nanocellulose sponge on nasal mucosal defects in an animal model,” *Regen Biomater*, vol. 7, no. 1, pp. 47–52, Oct. 2019, doi: 10.1093/rb/rbz054.

[43] V. Deineka *et al.*, “Hemostatic and tissue regeneration performance of novel electrospun chitosan-based materials,” *Biomedicines*, vol. 9, no. 6, 2021, doi: 10.3390/biomedicines9060588.

[44] W. Cheng *et al.*, “Incorporation of bacteriophages in polycaprolactone/collagen fibers for antibacterial hemostatic dual-function,” *J Biomed Mater Res B Appl Biomater*, vol. 106, no. 7, pp. 2588–2595, Oct. 2018, doi: 10.1002/jbm.b.34075.

[45] L. Yu, X. Shang, H. Chen, L. Xiao, Y. Zhu, and J. Fan, “A tightly-bonded and flexible mesoporous zeolite-cotton hybrid hemostat,” *Nat Commun*, vol. 10, no. 1, Dec. 2019, doi: 10.1038/s41467-019-09849-9.

[46] B. S. Kheirabadi, M. R. Scherer, J. S. Estep, M. A. Dubick, and J. B. Holcomb, “Determination of efficacy of new hemostatic dressings in a model of extremity arterial hemorrhage in swine,” *Journal of Trauma - Injury, Infection and Critical Care*, vol. 67, no. 3, pp. 450–459, Sep. 2009, doi: 10.1097/TA.0b013e3181ac0c99.

[47] M. Catalina, J. Cot, A. M. Balu, J. C. Serrano-Ruiz, and R. Luque, “Tailor-made biopolymers from leather waste valorisation,” *Green Chemistry*, vol. 14, no. 2, pp. 308–312, Jan. 2012, doi: 10.1039/c2gc16330f.

[48] A. M. Hopkins *et al.*, “Silk hydrogels as soft substrates for neural tissue engineering,” *Adv Funct Mater*, vol. 23, no. 41, pp. 5140–5149, Nov. 2013, doi: 10.1002/adfm.201300435.

[49] J. S. Jan, P. S. Chen, P. L. Hsieh, and B. Y. Chen, “Silicification of genipin-cross-linked polypeptide hydrogels toward biohybrid materials and mesoporous oxides,” *ACS Appl Mater Interfaces*, vol. 4, no. 12, pp. 6865–6874, Dec. 2012, doi: 10.1021/am302016c.

[50] C. Schonauer, E. Tessitore, G. Barbagallo, V. Albanese, and A. Moraci, “The use of local agents: Bone wax, gelatin, collagen, oxidized cellulose,” Oct. 2004. doi: 10.1007/s00586-004-0727-z.

[51] Lew WK, Weaver FA. Clinical use of topical thrombin as a surgical hemostat. Biologics. 2008 Dec;2(4):593-9. doi: 10.2147/btt.s2435. PMID: 19707440; PMCID: PMC2727895

[52] Paulo, Danika & Semonche, Alexa & Choudhry, Osamah & Almufti, Fawaz & Prestigiacomo, Charles & Roychowdhury, Sudipta & Nanda, Anil & Gupta, Gaurav. (2018). History of Hemostasis in Neurosurgery. World Neurosurgery. 124. 10.1016/j.wneu.2018.12.015.

[53] Wagner WR, Pachence JM, Ristich J, Johnson PC. Comparative in vitro analysis of topical hemostatic agents. J Surg Res. 1996 Dec;66(2):100-8. doi: 10.1006/jsre.1996.0379. PMID: 9024819.

[54] Doria C, Vaccino S. Topical hemostasis: a valuable adjunct to control bleeding in the operating room, with a special focus on thrombin and fibrin sealants. Expert Opin Biol Ther. 2009 Feb;9(2):243-7. doi: 10.1517/14712590802689258. PMID: 19236254.Feb. 2009.

[55] M. C. Oz, J. F. Rondinone, and N. S. Shargill, "Floseal Matrix: New Generation Topical Hemostatic Sealant," in *Journal of Cardiac Surgery*, Nov. 2003, pp. 486–493. doi: 10.1046/j.0886-0440.2003.00302.x.

[56] Seyednejad H, Imani M, Jamieson T, Seifalian AM. Topical haemostatic agents. Br J Surg. 2008 Oct;95(10):1197-225. doi: 10.1002/bjs.6357. PMID: 18763249.

[57] M. A. Brown, M. R. Daya, and J. A. Worley, "Experience with Chitosan Dressings in a Civilian EMS System," *Journal of Emergency Medicine*, vol. 37, no. 1, pp. 1–7, Jul. 2009, doi: 10.1016/j.jemermed.2007.05.043.

[58] B. S. Kheirabadi *et al.*, "Safety evaluation of new hemostatic agents, smectite granules, and kaolin-coated gauze in a vascular injury wound model in swine," *Journal of Trauma - Injury, Infection and Critical Care*, vol. 68, no. 2, pp. 269–277, Feb. 2010, doi: 10.1097/TA.0b013e3181c97ef1.

[59] Seyednejad H, Imani M, Jamieson T, Seifalian AM. Topical haemostatic agents. Br J Surg. 2008 Oct;95(10):1197-225. doi: 10.1002/bjs.6357. PMID: 18763249.."

Chapter 2
LITERATURE REVIEW

2. Literature Review

Wounds are a leading cause of fatalities, particularly in military conflicts, traumatic injuries, surgical procedures, and disaster accidents. The primary concern is haemorrhage that is closely tied to the body's haemostasis process. In India alone, over 1.4 million fatal accidents were reported in 2021-2022, with an extensive bleeding leading to hypovolemic shock [1]. Delayed medical intervention following traumatic injuries significantly increases mortality rates, with approximately 80% of total deaths attributed to prolonged blood loss [2]. Research indicates that rapid haemorrhage control within the initial minutes after injury could potentially reduce mortality by 20-30%, highlighting the critical importance of immediate medical response and blood loss management. Excessive bleeding can prolong surgical times, delay wound healing, and increase infection risk. Uncontrolled haemorrhage from traumatic injuries is a major cause of death, especially for those under 45 [3]. Prompt control of bleeding through compression, tourniquets, and haemostatic agents are needed. Effective haemostatic dressings require a multifaceted design approach, focusing on rapid blood clotting, ease of application, bacterial infection prevention, and high biocompatibility. The primary challenge lies in developing advanced wound management materials that can swiftly control bleeding while minimizing the risk of bacterial resistance. Therefore, innovative haemostatic dressing must prioritize immediate blood loss intervention without compromising long-term clinical complication.

2.1. Material structural properties

Surface topography plays a crucial role in biomaterial-blood interactions, fundamentally influencing protein adsorption, platelet adhesion, and blood coagulation through complex surface characteristics. The intricate interplay between surface properties like charge density, molecular weight, roughness, and porosity determines the hemocompatibility of material. Anionic surfaces adsorb less protein, while cationic surfaces activate complement systems, with flexible molecules more readily attaching to cell membranes. Rougher surfaces, particularly those under 2 micrometres, enhance platelet attachment, whereas smooth surfaces have minimal impact. The nanoscale and microscale topographical features critically govern protein adsorption and biological responses, suggesting that future biomaterial research must focus on understanding protein interactions at these microscopic levels.

2.1.1. Chitosan Based Systems

Derived from chitin through alkaline deacetylation, chitosan is a versatile biopolymer characterized by its unique molecular structure connecting N-acetyl-D-glucosamine and D-glucosamine units [4]. Chitosan possesses valuable biomedical properties including biocompatibility, biodegradability, and multiple biological activities such as antimicrobial [5], antioxidant [6], and antitumor capabilities [7].

Chitosan exhibits haemostatic capabilities through its unique electrostatic interactions with blood elements, facilitating effective wound healing processes. By attracting negatively charged blood cells and facilitating platelet activation, chitosan demonstrates remarkable capabilities in sealing wound surfaces. The positive charge of chitosan initiates an intricate blood clotting cascade by attracting negatively charged red blood cells and stimulating platelets to activate [8]. This intricate electrostatic interaction enables effective haemostasis, with potential applications in various medical procedures including endoscopic sinus surgery, parenchymal bleeding management, and urinary extravasation treatment [9], [10].

Research reveals that haemostatic capabilities of chitosan are intricately linked to its molecular weight (Mw) and degree of deacetylation (DDA) [11]. Broad-range chitosan with molecular weight between 8.6–275 kDa and degree of deacetylation 35–85% demonstrates superior whole blood aggregation compared to uniform molecular variants. Optimal haemostatic performance is observed with chitosan having Mw of 50–247 kDa and DDA of 75–88%, effectively interacting with erythrocytes, platelets, and plasma proteins. Complete deacetylation with low molecular weight inhibits aggregation, suggesting a delicate balance in molecular characteristics. Interestingly, yang et al. showed that low DDA (64.4–71.8%) and higher Mw (380–2240 kDa) as more efficient in initiating haemostasis but coagulation factors might not be activated by them [12].

The physiological state of chitosan greatly affects its haemostatic process. Solid-state chitosan absorbs platelets without erythrocyte aggregation, while acetic acid solutions can cause erythrocyte deformation and aggregation [13]. The binding process depends on interactions between positively charged chitosan molecules and negatively charged blood platelets. Numerous chitosan and its derivatives have been studied as blood-clotting materials, including hydrogels, films, powders, membranes, scaffolds, and sponges for wound treatment.

2.1.1.1. Physically modified chitosan-based haemostatic scaffold

The limited storage stability and biosafety concerns of blood clotting factors (BCF) have historically constrained their pre-hospital applications. Integrating BCF such as thrombin [14], fibrin, and fibrinogen with chitosan presents an innovative strategy to enhance haemostatic performance [15]. Lan et al. demonstrated that chitosan-based materials enriched with gelatin exhibit remarkable efficacy, characterized by significantly reduced clotting time and minimized blood loss, particularly in managing pressured and oozing bleeding without requiring external compression. Their studies showed better haemostatic effects compared to chitosan and gelatin sponge alone in rabbit ear and liver injury models [16].

Chen et al. created trilayer nanofibrous membranes of chitosan and PVA with nano-bioglass that had haemostatic properties. These membranes also showed effective biological properties in encouraging fibroblast cell growth and increasing the expression of genes related to healing growth factors. Animal studies using rat full-thickness skin wounds and mouse diabetic wounds demonstrated their significant effectiveness in enhancing recovery [17].

Atmospheric pressure plasma offers an innovative approach to surface modification without altering material structure, with Ar/O_2 and non-thermal nitrogen gas plasma treatments effectively enhancing surface properties of chitosan. These modifications improve red blood cell absorption through enhanced electrostatic interactions [18], [19].

Innovative surface treatments, such as marine mussel-derived catechol-coating and polydopamine coating, demonstrate remarkable hemostatic potential. These advanced chitosan-based materials create self-sealing membranes through rapid protein complexation, showing promising results in diabetic rat models and potential applications for hemophilia patients [20], [21].

Chan et al. developed chitosan-based gauze with polySTAT, a polymer modified with fibrin-binding peptides, to improve blood clotting and resist increasing arterial pressure [22]. This approach shows better clot stability than Celox® rapid and improves survival in rabbit femoral artery models. Similarly, Ouyang et al. fabricated tilapia peptide with chitosan microspheres to develop a composite sponge with improved biostability, broadening its potential applications in wound dressings [23].

2.1.1.2. Chemically modified chitosan-based haemostatic scaffold

In wound management, chitosan has developed innovative haemostatic derivatives by its hydroxyl and amino groups. Upon contact with blood it transforms into a three-dimensional gel that accelerates coagulation. Liu et al. developed a polysulfone membrane material grafted with sulfonated hydroxypropyl chitosan via a Schiff-base reaction, designed for hemodialysis with anticoagulant properties similar to heparin [24]. Chen et al. formulated N-acetyl chitosan with different alkane chain by sodium boron tetra hydride (NaBH4) and latter freeze drying

[25]. The acceleration of coagulation by N-acetyl chitosan may be associated with its effect on erythrocytes but is not favourable for the activation of coagulation factors or platelet adhesion. Wang et al. further developed N-acetyl chitosan nanofibers with diameters of 175-240 nm capable of highest surface area, contact angle, and blood absorption compared to chitosan nanofibers. These nanofibers induced the adherence, aggregation, and activation of platelets, but this process was not initiated by the flux of intracellular Ca^{2+}. By strategically modifying chitosan through N-alkylation and incorporating graphene oxide, researchers have engineered a biomaterial that rapidly transforms liquid blood into gel, effectively controlling bleeding across injury severities [26]. Hydrophobically synthesized chitosan by Dowling et al. that extends beyond traditional wound dressings, offering solutions for challenging truncal region bleeding in critical organs like the liver, kidneys, and spleen, without requiring external compression [27]. Saporito et al. developed sponge-like dressings based on chitosan and glycosaminoglycan loaded with tranexamic acid that demonstrated both hemostatic and proliferative properties. These dressings showed promise in controlling bleeding and promoting healing in wounds as well as in abdominal surgery [28], [29]. These advanced biomaterials combine insights from materials science, biochemistry, and medical engineering to create targeted haemostatic treatments that improve wound care by addressing multiple needs at once.

2.1.1.3. Chitosan-based composite haemostatic scaffold

Chitosan-based composite materials have received considerable interest for blood-clotting uses because of their beneficial characteristics, including excellent water absorption, biocompatibility, safety, and biodegradability. Shi et al. explored combining carboxymethyl chitosan, sodium alginate, and collagen. When chitosan is crosslinked with alginate and collagen, it creates microspheres with many tiny pores. The extensive surface area of microsphere enhances blood clotting by absorbing water from blood, concentrating clotting factors, and facilitating the conversion of fibrinogen to fibrin [30].

When chitosan nanoparticles are combined with gelatin and carrageenan, they demonstrate impressive porosity and ability to generate thrombin and absorb blood, making them effective for coagulation. Zhang et al. developed chitosan nanoparticles with a specific peptide sequence glycine-arginine-glycine-aspartic acid-serine (GRGDS) to enhance blood clotting activity when administered intravenously for internal bleeding treatment [31].

To enhance the hemostatic efficiency, zinc alginate (ZnAlg) was added to chitosan to make porous CS@ZnAlg microspheres on the surface by successive steps of micro-emulsion, polyelectrolyte adhesion, and thermally induced phase separation [32] [33]. For instance, researchers developed a haemostatic kit incorporating light-activated chitosan hydrogel and calcium alginate, that demonstrates strong tissue adhesion and accelerated clotting through platelet aggregation triggered by calcium ions. This composite achieves complete hemostasis in just 3 min, compared to 10 min for traditional chitosan gauze and CELOX [34].

To achieve complete blood clotting in diabetic rats, Karahaliloglu et al. created a nano/microbilayer haemostatic dressing with a porous sublayer made of chitosan, bacterial cellulose (BC) as the basement, and active agents in the coagulation cascade like vitamin K, protamine sulphate, and kaolin as a filler. The upper layer is made of silk fibroin and phosphatidylcholine blend. This enhanced blood clotting by reducing both clotting time and blood loss through electrostatic interactions of red blood cell and platelets [35]. Wang et al. combined calcium, chitosan with materials like alginate, cellulose, silk and Bletilla striata polysaccharide has been shown to enhance blood clotting by reducing both clotting time and blood loss due to calcium release from microsphere [36].

2.1.2. Cellulose Derivatives

Cellulose is a remarkable natural polymer derived from plants and bacteria. It has non-cytotoxicity, biocompatibility, biodegradability, and high absorption capacity. It provides various medical uses, including blood-clotting agents, wound coverings, tissue engineering, and medication delivery. The cellulose contains carboxyl functional groups that compresses bleeding sites and bind with Fe^{3+} ions of hemoglobin, forming brown gels which seal capillary ends. Additionally, it can activate platelets and accelerating the haemostasis process.

Basu et al. have investigated haemostatic property of nanofibrillated cellulose (NFC) hydrogel as base cross linked with Ca^{2+}, kaolin and collagen for advanced wound care and made a conclusion all of them efficiently trigger thrombin generation [37]. Oxidized cellulose (OC) represents another significant advancement, improving biosolubility and tissue compatibility due to oxidation of hydroxyl groups to carboxyl groups. Its negatively charged surface interacts with thrombin, facilitating haemostasis through physical adsorption and physiological mechanisms. The carboxyl group content plays a crucial role in its haemostatic effectiveness, enabling rapid platelet attraction and blood concentration. The OC-based commercial haemostatic product Surgicel® is utilized to control minor arterial bleeding during surgical procedures.

2.1.3. Advanced alginate formulations

Alginate is a remarkable biomaterial characterized by its exceptional absorption capabilities through cross-linking with metal ions, particularly calcium and ability to concentrate platelets and coagulation factors. In diabetic foot ulcer models, alginate oligomers can combine with calcium to generate gels that accelerate the clotting process. Algosteril ®, the alginate based commercial product has been approved clinically for wound care dressing. Hi et al. developed polycaprolactone alginate composite fibers crosslinked with nano silver, showing enhanced antimicrobial properties alongside haemostatic function [38].

For instance, Xuan et al. have developed microspheres derived from brown seaweed and loaded with thrombin in haemorrhage treatment. Thrombin-loaded alginate-calcium microspheres (TACMs) have proven particularly effective in managing blunt trauma and arterial bleeding as an embolic agent [39].

2.1.4. Synthetic polymer

Synthetic Polymers have a significant attention as haemostatic material due to their ease of synthesis and fabrication compared to natural polymers. Poly(ethylene glycol) (PEG) showed excellent tissue-binding properties and used as controlled medication release. Its applications extend to enzyme immobilization, and inhibit bleeding by creating physical barriers. PEG-based hydrogels take up water and gather platelets and clotting factors at injury sites to control bleeding in damaged organs. For instance, PEG and acrylic acid can undergo esterification reactions, resulting in poly(ethylene glycol) diacrylate (PEGDA) for quick wound closure [40].

Poly(vinyl alcohol) (PVA)-based haemostatic sponges offer exceptional hydrophilic and liquid-absorbing properties, coupled with strong biocompatibility and chemical stability. These sponges swell upon water absorption, enabling localized compression and physical haemostasis. Kim et al. enhanced tissue regeneration using PVA-based nanocellulose sponges in a rabbit nasal tissue defect model [41].

Similarly, Deineka et al. utilized nanofiber mats composed of poly(ethylene oxide) (PEO) and chitosan in a rat liver injury model, achieving significantly reduced bleeding time with improved degradability and tissue repair [42]. Cheng et al. developed PCL/collagen fibers using phage incorporation and electrostatic spinning, demonstrating excellent antimicrobial effects and rapid haemostasis in rabbit injury models [43].

By combining synthetic polymers with bioactive natural polymers, researchers seek to develop materials that integrate the strengths and haemostatic properties.

2.1.5. Inorganic and metal loaded haemostatic scaffold

Modern haemostatic biomaterials demand multifunctional capabilities encompassing blood clotting, antimicrobial activity, and tissue regeneration. Blending chitosan with components like calcium, zinc, silica and silver nanoparticles creates highly porous composites with superior blood absorption and antimicrobial properties.

Quick Clot®, Combat Gauge™ (Z-medica corporation) composed of kaolin clay, zeolite, and bioactive glass demonstrate remarkable capabilities in enhancing blood clotting mechanisms [44]. These materials improve haemostatic effectiveness through enhanced water absorption, procoagulant activation, and concentrated blood component interactions. Zeolite, a porous crystalline aluminosilicate, particularly stands out with its ability to absorb water, concentrate platelets, and activate coagulation factors. The strategic incorporation of calcium-based zeolites has shown efficient prothrombin activation while minimizing thromboembolic events by Shang et al. [45]. Li et al. created a strongly bonded and flexible porous zeolite-cotton hybrid blood-clotting agent to prevent zeolite particles from entering the patient's body [46].

Calcium ($Ca^{2+)}$ plays a crucial role in physiological coagulation, activating Factor X and facilitating prothrombin complex formation [47], [48]. Silver (Ag^+) ions provide potent antimicrobial properties [49], while zinc (Zn^{2+}) serves as an effective platelet modulator [50]. Copper (Cu^{2+}) ions contribute to antimicrobial defence and cellular response stimulation. These metal ions can be strategically integrated into chitosan, cellulose, and other polymer matrices to enhance haemostatic performance, improve mechanical properties, and reduce infection risks. The precipitation of metal ions on biomaterial surfaces can accelerate platelet activation, shorten haemostasis time, and create more effective wound management solutions.

2.1.6. Drug loaded haemostatic scaffold

The pharmacological augmentation of haemostatic biomaterials through anti-fibrinolytic and clot-strengthening drugs remains significantly underexplored. Several anti-fibrinolytic agents, including tranexamic acid (TXA), aprotinin, and aminocaproic acid, have been commonly utilized during trauma surgery, demonstrating reduced transfusion requirements and improved patient survival rates. Aprotinin has raised toxicity apprehensions, while aminocaproic acid has exhibited potential negative impacts on wound healing processes. Conversely, tranexamic acid has demonstrated promising effects on wound healing and therapeutic potential.

Benoni et al. indicates that intravenous TXA reaches minimum therapeutic plasma levels approximately 3 hours after administration [51]. While there are concerns about possible blood clot formation and blockage of blood vessels (thromboembolism), meta-analyses of clinical data suggest overall safety. Notably, direct topical application emerges as a preferred approach for managing severe bleeding conditions, particularly in surgical procedures like total knee arthroplasty.

Ethamsylate enhances platelet adhesion and restores capillary resistance, while TXA simultaneously inhibits plasmin formation. This dual-action approach addresses multiple aspects of the blood clotting process. Baser et al. provided compelling evidence in paediatric cardiac surgery [52]. Their study revealed that the simultaneous activation of platelets and plasma-initiated blood coagulation through the overlapping enzymatic interactions of ethamsylate and TXA yields superior results. Specifically, the combined treatment proved more effective in reducing postoperative blood loss compared to TXA administration alone.

2.2. Fabrication of haemostatic patches

The right choice of the material formulation is as important to the efficacy of haemostatic materials as chemically active. Common types of haemostatic materials include nanofibers, hydrogels, and sponges.

2.2.1. Nanofibers

Nanofibers possess a distinctive surface area that enables exceptional adsorption and surface activity properties. These interwoven materials are characterized by significantly small lattice and film pore sizes, high porosity, and superior surface adsorption capabilities. Researchers classify nanofibers based on spinning methods namely electrostatic spinning [53], solution blowing, and centrifugal spinning techniques [54].

Electrospinning is the most common nanofiber production method because it is easy to perform and widely applicable across different fields. This innovative approach utilizes high-voltage electric field conditions to generate electrostatic force that enables the extrusion of polymer solution from a syringe needle [55]. Under these conditions, surface tension is overcome, allowing the creation of a charged polymer jet that stretches and forms continuous ultra-fine fibers collected at the receiving end.

Multiple research studies have demonstrated the remarkable potential of nanofibers in biomedical applications. For instance, Biranje et al. successfully created chitosan nanofibrous membranes by electrospinning chitosan/polyvinyl alcohol (CH/PVA) blends in aqueous solutions under 20-25 kV electric field [56]. Using CH/PVA mass ratios from 10/90 to 40/60, they produced uniform nanofibers with diameters ranging from 80-300 nm, where lower chitosan concentrations yielded finer fibers (~100 nm) with spindle-like structures, while higher concentrations produced thicker fibers (~300 nm with bead-like formations **Figure 2. 1**.

Additionaly, Sardou et al. developed PCL/gelatin nanofibers containing 1% w/v lawsone that effectively enhanced fibroblast attachment and growth [57]. Likewise, Ahmed et al. created chitosan/PVA/ZnO nanofibers that showed powerful antioxidant effects in diabetic wound models, effectively inhibiting local inflammation and supporting wound healing [58]. Daristotle et al. further explored the haemostatic potential of nanofibers by preparing poly lactic glycolic acid (PLGA), poly ethylene glycol (PEG), and silicon di oxide (SiO_2) nanoparticle mixtures that demonstrated significant haemostatic effects to porcine liver wound models [59].

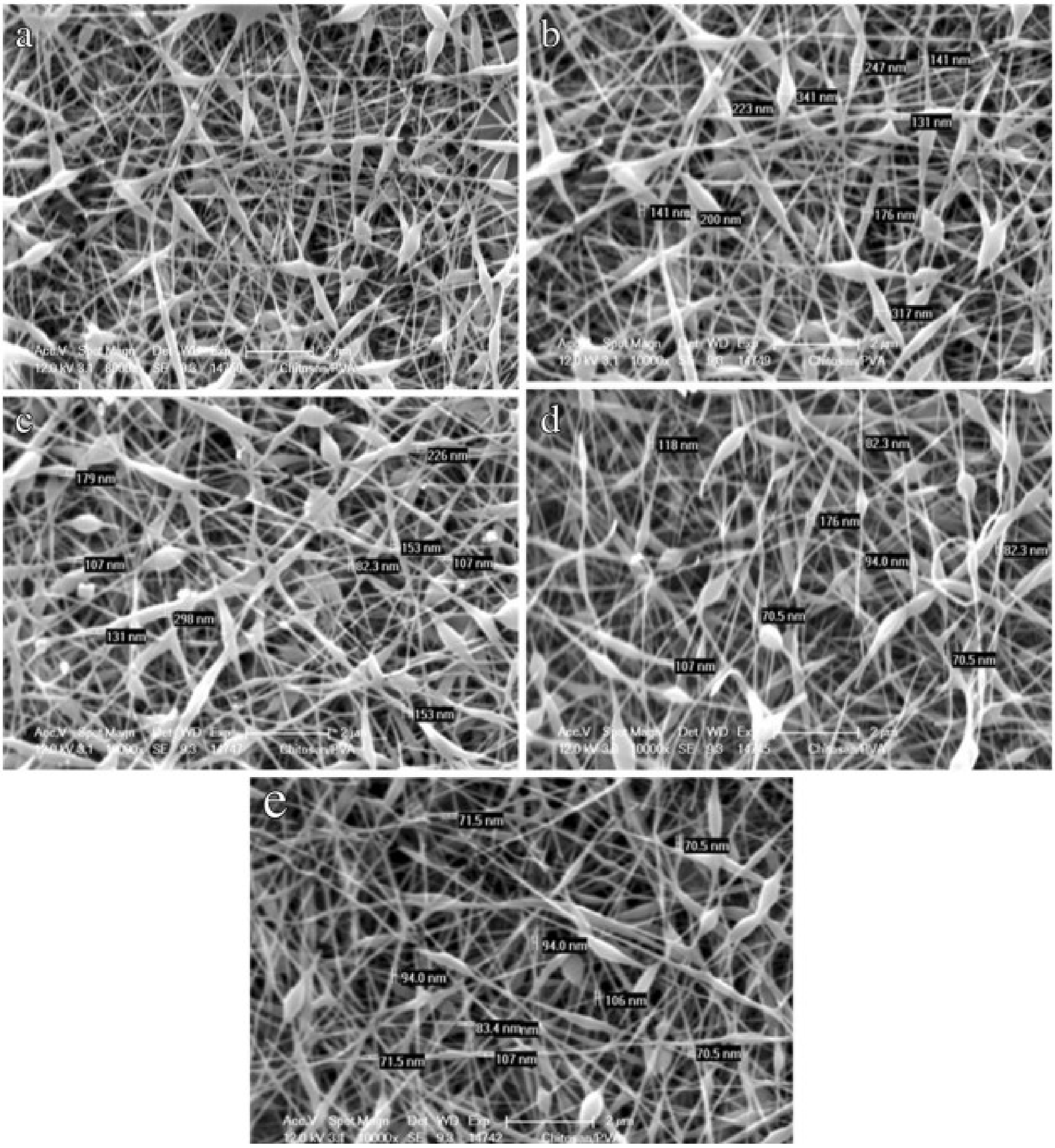

Figure 2. 1 SEM micrographs of chitosan/Poly vinyl alcohol nanofibrous membranes demonstrate a progressive reduction in fiber diameter as the chitosan content decreases within the blend composition: (**a**) CS/PVA ratio of 50/50, (**b**) CS/PVA ratio of 40/60, (**c**) CS/PVA ratio of 30/70, (**d**) CS/PVA ratio of 20/80, and (**e**) CS/PVA ratio of 10/90. Reproduced with permission from Biranjee et al (56).

2.2.2. Hydrogels

Hydrogels are sophisticated macromolecular structures featuring a three-dimensional network with hydrophilic and hydrophobic side chains, capable of absorbing and retaining substantial water quantities through their cross-linked configuration. In wound healing and haemostasis, this form of materials reduced clotting time increasing local platelet and clotting factor concentration. Their unique structural properties enable effective tissue adhesion, maintaining wound site moisture to halt bleeding and accelerate healing.

Yu et al. created the NB–CMC composite by using amide bonds to attach O-nitrobenzyl alcohol (NB) units to the structure of water-soluble carboxymethyl chitosan (CMC) [60]. This has outstanding coagulation and blood cell adhesion properties and can be employed to produce great haemostatic effects both in vitro and in vivo. Bohm et al. added cyclized succinate groups to a tetra-PEG hydrogel [61]. According to experimental findings, the tetra-PEG hydrogel demonstrated substantial haemostatic effects on a pig spleen haemorrhage model and could tolerate pressures of ≤294 ± 27 mmHg.

2.2.3. Sponges

Sponges provide dense porous structure to absorb wound moisture, strategically increasing platelet and clotting factor concentration. Under these conditions, platelets stick together and clump, creating a blood clot that effectively stops bleeding. The negative effects of gelatin sponges include breaking apart when exposed to blood in large wounds due to damage fragile blood cells and platelets. Researchers have developed advanced sponge technologies by using freeze-drying to create lyophilized, porous structures. Composite sponges containing modified chitosan enhances blood clotting by interacting with blood cell surface. The sponges combined with silica form a porous composite that can swell and compress the local wound area through water absorption [62].

Goncharuk et al. created porous poly(vinyl formal) (PVF) sponges by combining poly(vinyl alcohol) (PVA) with formaldehyde through a freeze-drying method [63]. In the mouse tail break model, the haemostatic effectiveness of the PVF sponge was 92.7% greater than that of Celoxin®.

2.3. In-vivo model study

Achieving effective haemostasis in challenging medical scenarios like battlefield injuries, accidents, or surgical interventions is often complicated by the presence of friable tissues and coagulopathy. Traditional methods such as applying additional sutures can potentially worsen bleeding instead of controlling it. To address these critical situations, topical haemostatic agents have been developed specifically for emergency prehospital and post-surgical bleeding management to control haemorrhage. To evaluate the effectiveness of various haemostatic agents, researchers applied the topical haemostatic agent with moderate digital pressure. Wounded animals treated with standard surgical gauze served as the control group, allowing for a comparative assessment of the haemostatic agents against a baseline intervention. The efficacy of haemostatic agent in in-vivo animal experimental study was conducted through rat-tail bleeding model and liver bleeding study.

Ziheng et al. developed an innovative adhesive hydrogel by combining polyethylene glycol, alginic acid extracted from brown algae, tannic acid, and an iron solution [64]. To evaluate its biocompatibility, they applied the hydrogel to rats' dorsal skin, creating 1 cm incisions. The results confirmed the biocompatible properties, with no significant fibrosis observed. The researchers further tested the haemostatic performance of hydrogel by applying it to rat tail bleeding wounds and rabbit injured livers. The mean blood loss for injured livers was 30 ± 27 mg whereas the rat tail bleeding showed a significantly lower blood loss of 2.77 ± 1.74 mg.

In a comparative study, X.K. Ouyang et al. developed innovative freeze-dried porous microspheres composed of sodium alginate, cellulose nanocrystals, and polylysine [65]. Their comprehensive haemostatic evaluation involved tail bleeding, hepatic haemorrhage, and femoral artery haemorrhage models of mouse. The research revealed promising hemostatic performance across these models in **figure 2.2**. For tail bleeding, they observed a bleeding volume of approximately 43 mg and a haemostasis time of 81 sec. The liver bleeding model demonstrated more efficient results, with a bleeding volume of 13 mg and a haemostasis time of 36 sec. It was showed a bleeding volume of 1607 mg and a haemostasis time of 71 sec in femoral artery haemorrhage.

A bilayered foam was designed and prepared by S. Indrakumar et al. with silk fibroin, chitosan and silica nano particles [66]. The time to stop bleeding was determined by puncturing the major femoral artery of rat. The clotting time was reported of 31±4s and minimal blood loss with no occurrence of rebleeding.

Younas et al. innovatively developed a multifunctional microneedle patch utilizing chitosan and fucoidan as the base, and loaded with lidocaine hydrochloride monohydrate, thrombin, and moxifloxacin at the needle tips [67]. The microneedle patch demonstrated a coagulation time of 208 ± 2 sec on full-thickness excisional wounds in mice.

Q. Xu et al. developed a hemostatic patch (PCMC/CCS) with a two-layer structure, composed of partly carboxymethylated cotton (PCMC) and catechol-grafted chitosan (CCS). [68]. The patch formed blood clots in 42 sec for liver bleeding and 72 sec in a femoral artery model of mice.

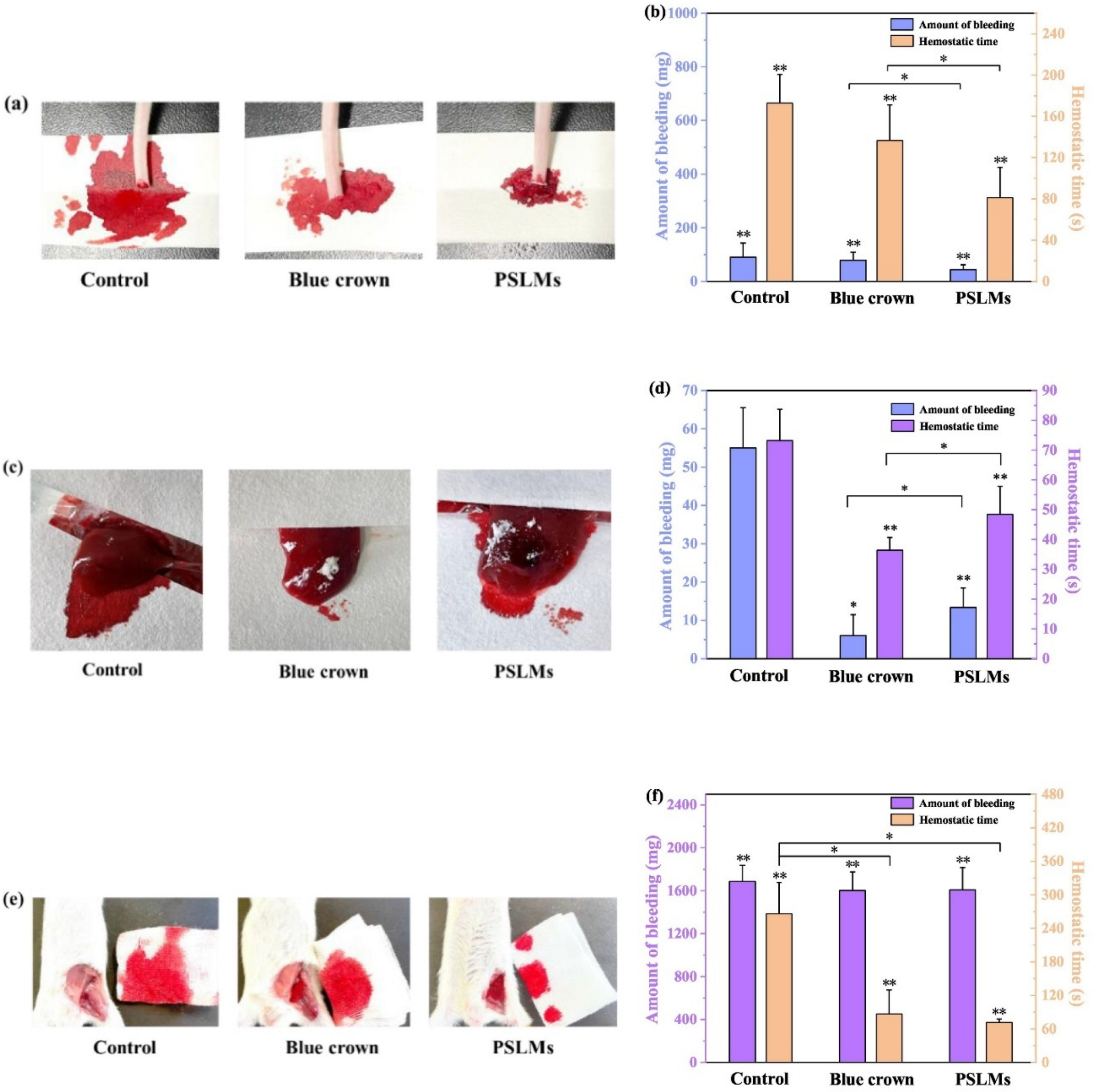

Figure 2. 2 ‘The bleeding volume and hemostasis time of control group (without hemostatic treatment), blue crown (commercial CS powder), and PSLMs (SA/CNC self-assembly with the antibacterial polymer ε-polylysine) in the mouse tail bleeding model (a), liver bleeding model (c), and femoral artery bleeding model (e), and bleeding volume and hemostasis time for censoring hemostasis (b), liver rupture hemostasis (d), and femoral artery hemostasis (f).’ Reproduced with permission from Ouyang et al (65).

A hydrophilic anti-adhesive chitosan/graphene oxide composite sponge was developed by F. Du et al [69]. The blood-clotting effectiveness was evaluated using rat models with liver puncture wounds and femoral artery injuries. The sponge successfully stopped bleeding within 32 sec for the liver wound and 66 sec for the femoral artery injury, with blood loss measured at 0.20 g and 1.03 g, respectively. Additionally, the researchers reported that the sponge could be safely peeled off from the wound without causing rebleeding.

L.W. Chan et al. investigated the haemostatic potential of PolySTAT/chitosan gauzes using a rat femoral artery injury model [70]. Their research explored on mechanical stabilization of red blood cell aggregates through fibrin cross-linking to gauze surfaces.

G. Patil et al. developed a haemostatic solution by synthesizing a chitosan-gelatin xerogel [71]. In a rat model with femoral artery injury, the xerogel achieved blood clotting in 2.5 min, which was quicker than Celox (3.3 min) and regular gauze (4.6 min). In another study, V. Deineka et al. reported that a chitosan electrospun membrane successfully stopped bleeding in 84.53 ± 4.88 sec in a rat liver bleeding model [72].

2.4. Definition of the problem and rationale of study

Recent innovations in tissue engineering are transforming haemostatic technologies, enabling more sophisticated and adaptable solutions for healthcare applications. Advanced manufacturing techniques like 3D printing and electrospinning are revolutionizing haemostatic material development by allowing precise customization of size, shape, structure, and internal porosity.

Advanced technologies provide superior material properties, enabling the precise and controlled delivery of medications, proteins, and blood coagulation factors. By enabling sophisticated structural design and precise manipulation of chemical components, researchers can now create haemostats with morphological precision and functionality. Nanomaterials have grown much attention in tissue engineering and wound healing. Their high surface area and porous structure provide exceptional capacity for adsorbing red blood cells, cellular components, and clotting factors in the haemostasis process. These innovations offer more effective platelet activation, better adhesion, and improved coagulation processes in wound healing treatments [73].

Electrospinning is a fabrication technique distinguished by process simplicity and material customization capabilities. By utilizing an external electric field, this method generates continuous fibers ranging from sub-micrometer to nanometer dimensions. The nanofiber offers high surface-to-volume ratios, microscopic pore sizes, high porosity. These unique properties enable nanofibres to create optimal wound healing environments by maintaining moisture, promoting cell adhesion, and facilitating proliferation [74]. The electrospinning technology permits the smooth integration of medications and coagulation agents for precise therapeutic applications. The technology creates smooth wound surfaces with little scarring, showing great promise for skin repair, wound healing, and quick blood clotting [75]. However, high-voltage requirements pose challenges with surgical instruments and electronic devices in traditional electrospinning. To address these limitations, researchers have developed gas-blowing spinning—an electricity-free alternative that uses high-speed gas streams to generate and deposit nanofibres rapidly [76]. This novel method delivers quicker fiber placement, greater ease of use, and better integration with surgical environments [77]. Despite significant advances, future research needs to concentrate on creating suitable solvents and processing methods to improve nanofiber stability while maintaining biocompatibility and biodegradability.

3D printing technology has emerged an approach in tissue engineering and to create patient-specific medical implants, products, and equipment in biomedical applications. These advanced hemostats integrate proteins, blood cells, clotting factors, and creating highly effective for sealing wounds. The porous structure of 3D-printed materials provides exceptional cell compatibility, facilitating strong platelet and red blood cell attachment critical for efficient hemostasis. Polysaccharide-based hemostats produced through 3D printing offer remarkable versatility in functionalization, enabling rapid incorporation of properties like antibacterial and antioxidant capabilities. The physical and chemical precision of 3D printing allows for the creation of materials with optimized strength, adhesive stability, and structural integrity, capable of managing excessive bleeding across diverse medical scenarios. This technology enables the design of hemostatic materials with size, shape, and internal porosity, offering strategic advantages for wound healing. By maintaining an appropriate environment and preventing thrombosis lysis, 3D-printed hemostats can effectively manage bleeding with minimize complications.

Future research should focus on innovative 3D structures that integrate advanced optical biosensors and responsive materials, enabling the hemostatic material to monitor wound conditions and dynamically release therapeutic agents. The final objective is to develop an advanced three-dimensional hemostatic device that could decrease hospital costs, reduce bleeding, and improve wound healing. While pursuing these technological advancements, researchers must also consider the economic feasibility to ensure these innovative hemostatic solutions can be practically implemented in clinical settings.

The development of hemostatic agents from natural resources presents a highly promising approach to addressing bleeding control in resource-limited settings. By combining chitosan derived from seafood industry waste with naturally abundant clay minerals like kaolin and bentonite, a dual-mechanism hemostatic agent emerges with significant advantages. This hybrid approach synergistically leverages both the positive charge of chitosan to attract blood components and the negative charge of clay minerals to activate the coagulation cascade. The manufacturing process remains straightforward, utilizing basic techniques like acid dissolution, freeze-drying, air-drying, and nanofiber preparation methods. This strategy not only transforms waste materials into valuable medical products but also provides a sustainable, cost-effective solution for emergency hemorrhage control with minimal infrastructure.

References:

[1] G Gotkari et al. “ROAD ACCIDENTS IN INDIA 2022.”road safety report 2022, Government of india, Page no1-238.

[2] Katzenell U, Ash N, Tapia AL, Campino GA, Glassberg E. Analysis of the causes of death of casualties in field military setting. Mil Med. 2012 Sep;177(9):1065-8. doi: 10.7205/milmed-d-12-00161. PMID: 23025136.

[3] E. E. Moore *et al.*, “Trauma-induced coagulopathy,” *Nat Rev Dis Primers*, vol. 7, no. 1, Dec. 2021, doi: 10.1038/s41572-021-00264-3.

[4] I. Younes and M. Rinaudo, “Chitin and chitosan preparation from marine sources. Structure, properties and applications,” Mar. 01, 2015, *MDPI AG*. doi: 10.3390/md13031133.

[5] M. Ghannadnia and I. Rasaee, “Antibacterial properties of biologically formed chitosan nanoparticles using aqueous leaf extract of Ocimum basilicum,” 2016, doi: 10.7508/nmj.2016.03.001.

[6] M. Guo, Y. Ma, C. Wang, H. Liu, Q. Li, and M. Fei, “Synthesis, anti-oxidant activity, and biodegradability of a novel recombinant polysaccharide derived from chitosan and lactose,” *Carbohydr Polym*, vol. 118, pp. 218–223, Mar. 2015, doi: 10.1016/j.carbpol.2014.11.027.

[7] H. Ravi, N. Kurrey, Y. Manabe, T. Sugawara, and V. Baskaran, “Polymeric chitosan-glycolipid nanocarriers for an effective delivery of marine carotenoid fucoxanthin for induction of apoptosis in human colon cancer cells (Caco-2 cells),” *Materials Science and Engineering C*, vol. 91, pp. 785–795, Oct. 2018, doi: 10.1016/j.msec.2018.06.018.

[8] N. Howe and B. Cherpelis, “Obtaining rapid and effective hemostasis: Part I. Update and review of topical hemostatic agents,” 2013, *Mosby Inc.* doi: 10.1016/j.jaad.2013.07.014.

[9] H. Xie, L. Lucchesi, J. S. Teach, and R. Virmani, “Long-term outcomes of a chitosan hemostatic dressing in laparoscopic partial nephrectomy,” *J Biomed Mater Res B Appl Biomater*, vol. 100 B, no. 2, pp. 432–436, Feb. 2012, doi: 10.1002/jbm.b.31966.

[10] J. chun Zhou, J. jing Zhang, W. Zhang, Z. yang Ke, and B. Zhang, “Efficacy of chitosan dressing on endoscopic sinus surgery: a systematic review and meta-analysis,” Sep. 01, 2017, *Springer Verlag*. doi: 10.1007/s00405-017-4584-x.

[11] N. S. M., U. Mony, and R. Jayakumar, “Chitin and Chitosan as Hemostatic Agents,” in *Encyclopedia of Polymer Science and Technology*, Wiley, 2016, pp. 1–12. doi: 10.1002/0471440264.pst647.

[12] J. Yang, F. Tian, Z. Wang, Q. Wang, Y. J. Zeng, and S. Q. Chen, “Effect of chitosan molecular weight and deacetylation degree on hemostasis,” *J Biomed Mater Res B Appl Biomater*, vol. 84, no. 1, pp. 131–137, Jan. 2008, doi: 10.1002/jbm.b.30853.

[13] Q. He *et al.*, “Positive charge of chitosan retards blood coagulation on chitosan films,” *J Biomater Appl*, vol. 27, no. 8, pp. 1032–1045, May 2013, doi: 10.1177/0885328211432487.

[14] X. F. Huang, J. W. Jia, Z. K. Wang, and Q. L. Hu, “A novel chitosan-based sponge coated with self-assembled thrombin/tannic acid multilayer films as a hemostatic dressing,” *Chinese Journal of Polymer Science (English Edition)*, vol. 33, no. 2, pp. 284–290, Feb. 2015, doi: 10.1007/s10118-015-1580-8.

[15] C. M. Han, L. P. Zhang, J. Z. Sun, H. F. Shi, J. Zhou, and C. Y. Gao, “Application of collagen-chitosan/fibrin glue asymmetric scaffolds in skin tissue engineering,” *J Zhejiang Univ Sci B*, vol. 11, no. 7, pp. 524–530, Jul. 2010, doi: 10.1631/jzus.B0900400.

[16] G. Lan *et al.*, “Chitosan/gelatin composite sponge is an absorbable surgical hemostatic agent,” *Colloids Surf B Biointerfaces*, vol. 136, pp. 1026–1034, Dec. 2015, doi: 10.1016/j.colsurfb.2015.10.039.

[17] Q. Chen *et al.*, “Electrospun chitosan/PVA/bioglass Nanofibrous membrane with spatially designed structure for accelerating chronic wound healing,” *Materials Science and Engineering C*, vol. 105, Dec. 2019, doi: 10.1016/j.msec.2019.110083.

[18] J. Jaifu, K. Thunsiri, S. Udomsom, D. Boonyawan, and W. Wattanutchariya, “Blood absorption improvement of a naturally derived hemostatic agent by atmospheric pressure plasma jet,” 2019. [Online]. Available: www.sciencedirect.comwww.materialstoday.com/proceedings

[19] K. Walczak, J. Thiele, D. Geisler, K. Boening, and M. Wieckiewicz, “Effect of chemical disinfection on chitosan coated PMMA and PETG surfaces-An in vitro study,” *Polymers (Basel)*, vol. 10, no. 5, May 2018, doi: 10.3390/polym10050536.

[20] J. H. Ryu, Y. Lee, W. H. Kong, T. G. Kim, T. G. Park, and H. Lee, “Catechol-functionalized chitosan/pluronic hydrogels for tissue adhesives and hemostatic materials,” *Biomacromolecules*, vol. 12, no. 7, pp. 2653–2659, Jul. 2011, doi: 10.1021/bm200464x.

[21] M. Shin *et al.*, “Hemostatic Swabs Containing Polydopamine-like Catecholamine Chitosan-Catechol for Normal and Coagulopathic Animal Models,” *ACS Biomater Sci Eng*, vol. 4, no. 7, pp. 2314–2318, Jul. 2018, doi: 10.1021/acsbiomaterials.8b00451.

[22] L. W. Chan, C. H. Kim, X. Wang, S. H. Pun, N. J. White, and T. H. Kim, “PolySTAT-modified chitosan gauzes for improved hemostasis in external hemorrhage,” *Acta Biomater*, vol. 31, pp. 178–185, Feb. 2016, doi: 10.1016/j.actbio.2015.11.017.

[23] Q. Ouyang *et al.*, “Construction of a composite sponge containing tilapia peptides and chitosan with improved hemostatic performance,” *Int J Biol Macromol*, vol. 139, pp. 719–729, Oct. 2019, doi: 10.1016/j.ijbiomac.2019.07.163.

[24] T. M. Liu, J. J. Xu, and Y. R. Qiu, “A novel kind of polysulfone material with excellent biocompatibility modified by the sulfonated hydroxypropyl chitosan,” *Materials Science and Engineering C*, vol. 79, pp. 570–580, Oct. 2017, doi: 10.1016/j.msec.2017.05.103.

[25] Z. Chen *et al.*, “Blood coagulation evaluation of N-alkylated chitosan,” *Carbohydr Polym*, vol. 173, pp. 259–268, Oct. 2017, doi: 10.1016/j.carbpol.2017.05.085.

[26] X. Wang *et al.*, “Exploration of Blood Coagulation of N -Alkyl Chitosan Nanofiber Membrane in Vitro,” *Biomacromolecules*, vol. 19, no. 3, pp. 731–739, Mar. 2018, doi: 10.1021/acs.biomac.7b01492.

[27] M. B. Dowling *et al.*, “Sprayable Foams Based on an Amphiphilic Biopolymer for Control of Hemorrhage Without Compression,” *ACS Biomater Sci Eng*, vol. 1, no. 6, pp. 440–447, Dec. 2015, doi: 10.1021/acsbiomaterials.5b00067.

[28] F. Saporito *et al.*, “Freeze dried chitosan acetate dressings with glycosaminoglycans and traxenamic acid,” *Carbohydr Polym*, vol. 184, pp. 408–417, Mar. 2018, doi: 10.1016/j.carbpol.2017.12.066.

[29] J. Bartley, “Should chitosan and tranexamic acid be combined for improved hemostasis after sinus surgery?,” *Med Hypotheses*, vol. 81, no. 6, pp. 1036–1038, Dec. 2013, doi: 10.1016/j.mehy.2013.09.027.

[30] J. Jin *et al.*, “Microspheres of Carboxymethyl Chitosan, Sodium Alginate, and Collagen as a Hemostatic Agent in Vivo,” *ACS Biomater Sci Eng*, vol. 4, no. 7, pp. 2541–2551, Jul. 2018, doi: 10.1021/acsbiomaterials.8b00453.

[31] P. Zhang *et al.*, “GRGDS-functionalized chitosan nanoparticles as a potential intravenous hemostat for traumatic hemorrhage control in an animal model,” *Nanomedicine*, vol. 14, no. 8, pp. 2531–2540, Nov. 2018, doi: 10.1016/j.nano.2018.08.007.

[32] M. Pan *et al.*, “Porous chitosan microspheres containing zinc ion for enhanced thrombosis and hemostasis,” *Materials Science and Engineering C*, vol. 85, pp. 27–36, Apr. 2018, doi: 10.1016/j.msec.2017.12.015.

[33] J. Li *et al.*, “Porous chitosan microspheres for application as quick in vitro and in vivo hemostat,” *Materials Science and Engineering C*, vol. 77, pp. 411–419, Aug. 2017, doi: 10.1016/j.msec.2017.03.276.

[34] H. Hattori, Y. Amano, Y. Nogami, B. Takase, and M. Ishihara, “Hemostasis for severe hemorrhage with photocrosslinkable chitosan hydrogel and calcium alginate,” *Ann Biomed Eng*, vol. 38, no. 12, pp. 3724–3732, Dec. 2010, doi: 10.1007/s10439-010-0121-4.

[35] Z. Karahaliloğlu, M. Demirbilek, İ. Ulusoy, B. Gümüşkaya, and E. B. Denkbaş, “Active nano/microbilayer hemostatic agents for diabetic rat bleeding model,” *J Biomed Mater Res B Appl Biomater*, vol. 105, no. 6, pp. 1573–1585, Aug. 2017, doi: 10.1002/jbm.b.33696.

[36] C. Wang *et al.*, “Preparation and evaluation of chitosan/alginate porous microspheres/Bletilla striata polysaccharide composite hemostatic sponges,” *Carbohydr Polym*, vol. 174, pp. 432–442, Oct. 2017, doi: 10.1016/j.carbpol.2017.06.112.

[37] A. Basu, J. Hong, and N. Ferraz, “Hemocompatibility of Ca2+-Crosslinked Nanocellulose Hydrogels: Toward Efficient Management of Hemostasis,” *Macromol Biosci*, vol. 17, no. 11, Nov. 2017, doi: 10.1002/mabi.201700236.

[38] W. W. Hu and Y. T. Lin, “Alginate/polycaprolactone composite fibers as multifunctional wound dressings,” *Carbohydr Polym*, vol. 289, Aug. 2022, doi: 10.1016/j.carbpol.2022.119440.

[39] F. Xuan *et al.*, “Biocompatibility and Effectiveness Evaluation of a New Hemostatic Embolization Agent: Thrombin Loaded Alginate Calcium Microsphere,” *Biomed Res Int*, vol. 2017, 2017, doi: 10.1155/2017/1875258.

[40] Z. Stillman, B. M. Jarai, N. Raman, P. Patel, and C. A. Fromen, “Degradation profiles of poly(ethylene glycol)diacrylate (PEGDA)-based hydrogel nanoparticles,” *Polym Chem*, vol. 11, no. 2, pp. 568–580, Jan. 2020, doi: 10.1039/c9py01206k.

[41] J. W. Kim *et al.*, “Effect of expanding nanocellulose sponge on nasal mucosal defects in an animal model,” *Regen Biomater*, vol. 7, no. 1, pp. 47–52, Oct. 2019, doi: 10.1093/rb/rbz054.

[42] V. Deineka *et al.*, “Hemostatic and tissue regeneration performance of novel electrospun chitosan-based materials,” *Biomedicines*, vol. 9, no. 6, 2021, doi: 10.3390/biomedicines9060588.

[43] W. Cheng *et al.*, “Incorporation of bacteriophages in polycaprolactone/collagen fibers for antibacterial hemostatic dual-function,” *J Biomed Mater Res B Appl Biomater*, vol. 106, no. 7, pp. 2588–2595, Oct. 2018, doi: 10.1002/jbm.b.34075.

[44] Basadonna G. QuikClot combat gauze for hemorrhage control. Prehosp Disaster Med. 2012 Apr;27(2):217. doi: 10.1017/S1049023X12000490. Epub 2012 May 16. PMID: 22588520.

[45] X. Shang *et al.*, “Unusual zymogen activation patterns in the protein corona of Ca-zeolites,” *Nat Catal*, vol. 4, no. 7, pp. 607–614, Jul. 2021, doi: 10.1038/s41929-021-00654-6.

[46] L. Yu, X. Shang, H. Chen, L. Xiao, Y. Zhu, and J. Fan, “A tightly-bonded and flexible mesoporous zeolite-cotton hybrid hemostat,” *Nat Commun*, vol. 10, no. 1, Dec. 2019, doi: 10.1038/s41467-019-09849-9.

[47] T. Subramaniam, M. B. Fauzi, Y. Lokanathan, and J. X. Law, “The role of calcium in wound healing,” Jun. 02, 2021, *MDPI*. doi: 10.3390/ijms22126486.

[48] T. Koklic, R. Majumder, and B. R. Lentz, “Ca2+ switches the effect of PS-containing membranes on Factor Xa from activating to inhibiting: Implications for initiation of blood coagulation,” *Biochemical Journal*, vol. 462, no. 3, pp. 591–601, Sep. 2014, doi: 10.1042/BJ20140130.

[49] M. Zienkiewicz-Strzałka, A. Deryło-Marczewska, Y. A. Skorik, V. A. Petrova, A. Choma, and I. Komaniecka, “Silver nanoparticles on chitosan/silica nanofibers: Characterization and antibacterial activity,” *Int J Mol Sci*, vol. 21, no. 1, Jan. 2020, doi: 10.3390/ijms21010166.

[50] N. S. Ahmed, M. E. Lopes-Pires, and N. Pugh, “Zinc: an endogenous and exogenous regulator of platelet function during hemostasis and thrombosis,” 2021, *Taylor and Francis Ltd.* doi: 10.1080/09537104.2020.1840540.

[51] G. P. Georgiev, P. P. Tanchev, Z. Zheleva, and P. Kinov, “Comparison of topical and intravenous administration of tranexamic acid for blood loss control during total joint replacement: Review of literature,” Apr. 01, 2018, *Elsevier (Singapore) Pte Ltd*. doi: 10.1016/j.jot.2017.12.006.

[52] I. I. Abd El Baser, H. M. ElBendary, and A. ElDerie, “The synergistic effect of tranexamic acid and ethamsylate combination on blood loss in pediatric cardiac surgery,” *Ann Card Anaesth*, vol. 24, no. 1, pp. 17–23, Jan. 2021, doi: 10.4103/aca.ACA_84_19.

[53] A. D. Juncos Bombin, N. J. Dunne, and H. O. McCarthy, “Electrospinning of natural polymers for the production of nanofibres for wound healing applications,” Sep. 01, 2020, *Elsevier Ltd*. doi: 10.1016/j.msec.2020.110994.

[54] Y. Gao *et al.*, “Recent progress and challenges in solution blow spinning,” Feb. 01, 2021, *Royal Society of Chemistry*. doi: 10.1039/d0mh01096k.

[55] J. Xue, J. Xie, W. Liu, and Y. Xia, “Electrospun Nanofibers: New Concepts, Materials, and Applications,” *Acc Chem Res*, vol. 50, no. 8, pp. 1976–1987, Aug. 2017, doi: 10.1021/acs.accounts.7b00218.

[56] S. Biranje, P. Madiwale, and R. V. Adivarekar, “Electrospinning of chitosan/PVA nanofibrous membrane at ultralow solvent concentration,” *Journal of Polymer Research*, vol. 24, no. 6, May 2017, doi: 10.1007/s10965-017-1238-z.

[57] M. Adeli-Sardou, M. M. Yaghoobi, M. Torkzadeh-Mahani, and M. Dodel, “Controlled release of lawsone from polycaprolactone/gelatin electrospun nano fibers for skin tissue regeneration,” *Int J Biol Macromol*, vol. 124, pp. 478–491, Mar. 2019, doi: 10.1016/j.ijbiomac.2018.11.237.

[58] R. Ahmed *et al.*, “Novel electrospun chitosan/polyvinyl alcohol/zinc oxide nanofibrous mats with antibacterial and antioxidant properties for diabetic wound healing,” *Int J Biol Macromol*, vol. 120, pp. 385–393, Dec. 2018, doi: 10.1016/j.ijbiomac.2018.08.057.

[59] J. L. Daristotle *et al.*, “Improving the adhesion, flexibility, and hemostatic efficacy of a sprayable polymer blend surgical sealant by incorporating silica particles,” *Acta Biomater*, vol. 90, pp. 205–216, May 2019, doi: 10.1016/j.actbio.2019.04.015.

[60] Y. Ma *et al.*, “Liquid Bandage Harvests Robust Adhesive, Hemostatic, and Antibacterial Performances as a First-Aid Tissue Adhesive,” *Adv Funct Mater*, vol. 30, no. 39, Sep. 2020, doi: 10.1002/adfm.202001820.

[61] S. Böhm, C. Strauß, S. Stoiber, C. Kasper, and V. Charwat, “Impact of source and manufacturing of collagen matrices on fibroblast cell growth and platelet aggregation,” *Materials*, vol. 10, no. 9, Sep. 2017, doi: 10.3390/ma10091086.

[62] X. Sun *et al.*, “A composite sponge based on alkylated chitosan and diatom-biosilica for rapid hemostasis,” *Int J Biol Macromol*, vol. 182, pp. 2097–2107, Jul. 2021, doi: 10.1016/j.ijbiomac.2021.05.123.

[63] O. Goncharuk *et al.*, “Hemostatic dressings based on poly(vinyl formal) sponges,” *Materials Science and Engineering C*, vol. 129, Oct. 2021, doi: 10.1016/j.msec.2021.112363.

[64] Y. Zheng *et al.*, “Hemostatic patch with ultra-strengthened mechanical properties for efficient adhesion to wet surfaces,” *Biomaterials*, vol. 301, Oct. 2023, doi: 10.1016/j.biomaterials.2023.122240.

[65] X. kun Ouyang, L. Zhao, F. Jiang, J. Ling, L. Y. Yang, and N. Wang, “Cellulose nanocrystal/calcium alginate-based porous microspheres for rapid hemostasis and wound healing,” *Carbohydr Polym*, vol. 293, Oct. 2022, doi: 10.1016/j.carbpol.2022.119688.

[66] S. Indrakumar, S. Ghosh, T. K. Dash, V. Mishra, B. Tandon, and K. Chatterjee, “Silk composite interfacial layer eliminates rebleeding with chitosan-based hemostats,” *Carbohydr Polym*, vol. 304, Mar. 2023, doi: 10.1016/j.carbpol.2022.120479.

[67] A. Younas, Z. Dong, Z. Hou, M. Asad, M. Li, and N. Zhang, “A chitosan/fucoidan nanoparticle-loaded pullulan microneedle patch for differential drug release to promote wound healing,” *Carbohydr Polym*, vol. 306, Apr. 2023, doi: 10.1016/j.carbpol.2023.120593.

[68] Q. Xu *et al.*, “Catechol-chitosan/carboxymethylated cotton-based Janus hemostatic patch for rapid hemostasis in coagulopathy,” *Carbohydr Polym*, vol. 315, Sep. 2023, doi: 10.1016/j.carbpol.2023.120967.

[69] F. Du *et al.*, “Hydrophilic chitosan/graphene oxide composite sponge for rapid hemostasis and non-rebleeding removal,” *Carbohydr Polym*, vol. 316, Sep. 2023, doi: 10.1016/j.carbpol.2023.121058.

[70] L. W. Chan, C. H. Kim, X. Wang, S. H. Pun, N. J. White, and T. H. Kim, “PolySTAT-modified chitosan gauzes for improved hemostasis in external hemorrhage,” *Acta Biomater*, vol. 31, pp. 178–185, Feb. 2016, doi: 10.1016/j.actbio.2015.11.017.

[71] G. Patil, A. Torris, P. R. Suresha, S. Jadhav, M. V. Badiger, and V. Ghormade, “Design and synthesis of a new topical agent for halting blood loss rapidly: A multimodal chitosan-gelatin xerogel composite loaded with silica nanoparticles and calcium,” *Colloids Surf B Biointerfaces*, vol. 198, Feb. 2021, doi: 10.1016/j.colsurfb.2020.111454.

[72] V. Deineka *et al.*, “Hemostatic performance and biocompatibility of chitosan-based agents in experimental parenchymal bleeding,” *Materials Science and Engineering C*, vol. 120, Jan. 2021, doi: 10.1016/j.msec.2020.111740.

[73] M. F. Matus, C. Vilos, B. A. Cisterna, E. Fuentes, and I. Palomo, “Nanotechnology and primary hemostasis: Differential effects of nanoparticles on platelet responses,” Feb. 01, 2018, *Elsevier Inc.* doi: 10.1016/j.vph.2017.11.004.

[74] S. Biranje, P. Madiwale, and R. V. Adivarekar, “Electrospinning of chitosan/PVA nanofibrous membrane at ultralow solvent concentration,” *Journal of Polymer Research*, vol. 24, no. 6, May 2017, doi: 10.1007/s10965-017-1238-z.

[75] P. Zahedi, I. Rezaeian, S. O. Ranaei-Siadat, S. H. Jafari, and P. Supaphol, “A review on wound dressings with an emphasis on electrospun nanofibrous polymeric bandages,” Feb. 2010. doi: 10.1002/pat.1625.

[76] S. C. Xu *et al.*, “A battery-operated portable handheld electrospinning apparatus,” *Nanoscale*, vol. 7, no. 29, pp. 12351–12355, Aug. 2015, doi: 10.1039/c5nr02922h.

[77] Y. Gao *et al.*, “A portable solution blow spinning device for minimally invasive surgery hemostasis,” *Chemical Engineering Journal*, vol. 387, May 2020, doi: 10.1016/j.cej.2020.124052.

Chapter 3

SCOPE OF THE WORK AND OBJECTIVES OF THE THESIS

3. Scope of the work and Objectives of the thesis

3.1 Scope of the work

Numerous studies have been conducted on the development of an ideal haemostatic material. Research in haemostatic materials has extensively focused on chitosan-based formulations due to its inherent blood-clotting properties. The critical aspect identified through the literature survey is the issue of rebleeding, which is vital for achieving sustained haemostasis.

Calcium plays a pivotal role in the blood clotting pathway, as it is essential for activating critical factors in the haemostatic process. During bleeding, the urgent and immediate availability of calcium in suitable form at the wound site is crucial. However, the naturally available calcium in the body may prove insufficient to meet the urgent demand, especially in cases of excessive blood loss.

Haemostatic materials with varying hydrophilic/hydrophobic properties present distinct challenges: hydrophobic materials exhibit insufficient wound residence time for effective clotting, while hydrophilic materials may promote bacterial growth due to prolonged adhesion, highlighting the need for balanced material properties.

This current research aims to develop advanced chitosan-based haemostatic materials through innovative approaches, focusing on several key objectives including design optimization of electrospun nanofiber structures with enhanced structural integrity and controlled drug release properties. The study integrates novel components such as tranexamic acid, ethamsylate, and calcium-rich marine shell powder, while addressing critical performance aspects like rebleeding prevention through improved structural design, optimized calcium/drug release at wound sites, and balanced hydrophilic/hydrophobic properties for optimal wound retention and antimicrobial effectiveness. Through comprehensive evaluation involving in-vitro haemostatic parameters, in-vivo animal studies, analysis of clotting time, histopathological observations, biocompatibility testing, and healing potential assessment, the current study seeks to bridge existing gaps in haemostatic material development by combining innovative material design with thorough performance validation under biological conditions.

3.2 Objectives of the thesis

The objective of the thesis has been framed to reflect the synergistic approach established through experimental results. Instead of evaluating drug- loaded patches and biogenic- calcium- based patches as separate strategies, findings demonstrate that the most effective system is the combined formulation integrating both mechanisms.

Thus, the objectives are:

1. To develop hemostatic scaffolds using natural polymers, pharmacological agents (TXA and Ethamsylate), and biogenic calcium (MSW-T) derived from marine shell waste.

2. To compare the hemostatic, mechanical, and biological performance of drug- loaded, biogenic- calcium- loaded, and combined hybrid scaffolds.

3. To identify the optimal scaffold configuration—demonstrated to be the MSWNF nanofiber—which integrates drug delivery with Ca^{2+}- mediated hemostatic and regenerative enhancement.

Chapter 4

MATERIALS AND METHODS: SYNTHESIS AND CHARACTERIZATION

Formulation acronyms:

The “control nanofiber” (CNF) is composed of PVA, CS, Tranexamic acid and ethamsylate by electrospinning process whereas ‘MSWNF’ was composed of PVA, CS, Tranexamic acid and ethamsylate with calcined marine shell waste at 1200℃ by electrospinning process.

S0 or MSW-O	Marine shell waste dried and crushed at 100℃. Both are same.
S1200 or MSW-T	Marine shell waste particles, calcined and crushed at 1200℃. Both are same.
AD1	Air dried film using poly vinyl alcohol, chitosan by solvent casting method.
AD2	Air dried film using poly vinyl alcohol, chitosan and marine shell waste at 100℃ by solvent casting method.
FD1	Freeze dried sponge consist of PVA and chitosan by lyophilisation techniques.
FD2 or (PVA/CS/MSW-O)	Freeze dried sponge consist of PVA and chitosan and MSW at 100℃ by lyophilisation techniques.
CNF or PVA/CS/TXA-E	Control nano fiber was composed of PVA,CS, Tranexamic acid and ethamsylate by electrospinning process. Both are same.
MSWNF or PVA/CS/TXA-E/MSW-T	Nano fiber was composed of PVA,CS, Tranexamic acid and ethamsylate with calcined marine shell waste at 1200℃ by electrospinning process. Both are same.

4. Materials and Methods: Synthesis and Characterization

In this chapter, details of the haemostatic scaffold fabrication, descriptions of materials and methods as well as characterization of the patches have been discussed.

4.1. Materials

Poly vinyl alcohol (PVA) 98% hydrolised with (M.W. 89,000-98,000) was obtained from Sigma-Aldirch, USA. Chitosan (CS, with a molecular weight range of approximately 190-310 kDa and a deacetylation degree of 75-85%) was procured from Sigma-Aldirch, USA. Marine shell waste (MSW) was collected from the exoskeleton of *Magallana cuttackensis*, a species of the Ostreidae family, from Sundarbans delta, West Bengal, India. For the extraction of calcium carbonate particles from MSW, sodium hydroxide (≥97% assay) and glacial acetic acid (≥99.5% assay) were obtained from Thermo Fisher Scientific India Pvt. Ltd, Mumbai, India. Blood coagulation reagents, Liquicelin-E and Uniplastin, were sourced from Tulip Diagnostics (P) Ltd., Goa, India. An anticoagulant, 3.8% sodium citrate solution, was acquired from Clinichem Enterprises, Kolkata, India. For spectrophotometric analysis, Ninhydrin (MW 178.14, spectrophotometric grade) was obtained from Spectrochem Pvt. Ltd., Mumbai, India.

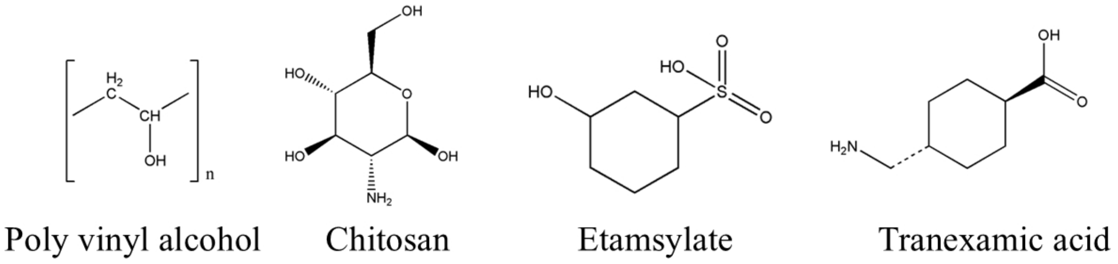

Figure 4. 1 Chemical components used for fabrication of nanofibers depicted by molecular structures of the components.

4.2. Extraction of calcium compound from Marine Shell waste

Extraction of calcium compound was performed as per the scheme shown in **Figure 4.2(a)**. Initially, MSW was thoroughly cleaned with plain water followed by boiled water to remove debris. The shells were then treated with a 10% sodium hydroxide solution, followed by 1% glacial acetic acid to maintain appropriate acidity/alkalinity. After rinsing with deionized water, the shells were dried at 100°C in a hot air furnace for 3-4 h and then crushed to obtain particles (MSW-O) depicted in **Figure 4.2(b)**. The crushed marine shell waste (MSW) particles were subjected to calcination at three different temperatures (800, 1000, and 1200°C) for 2 h in a muffle furnace (SICCO, Kolkata, India), with a heating rate of 5°C per minute. Among the calcined samples, MSW-T demonstrated the largest zone of inhibition, indicating superior antimicrobial activity compared to other temperatures (Figure 5.A.5). Furthermore, MSW-T showed the most significant reduction in coagulation time when compared to all extracted and calcined MSW samples (Figure 5.A.6). Therefore, 1200°C was selected as the optimal calcination temperature, and the resulting product was designated as MSW-T (Figure 4.2(c)) for use in membrane fabrication.

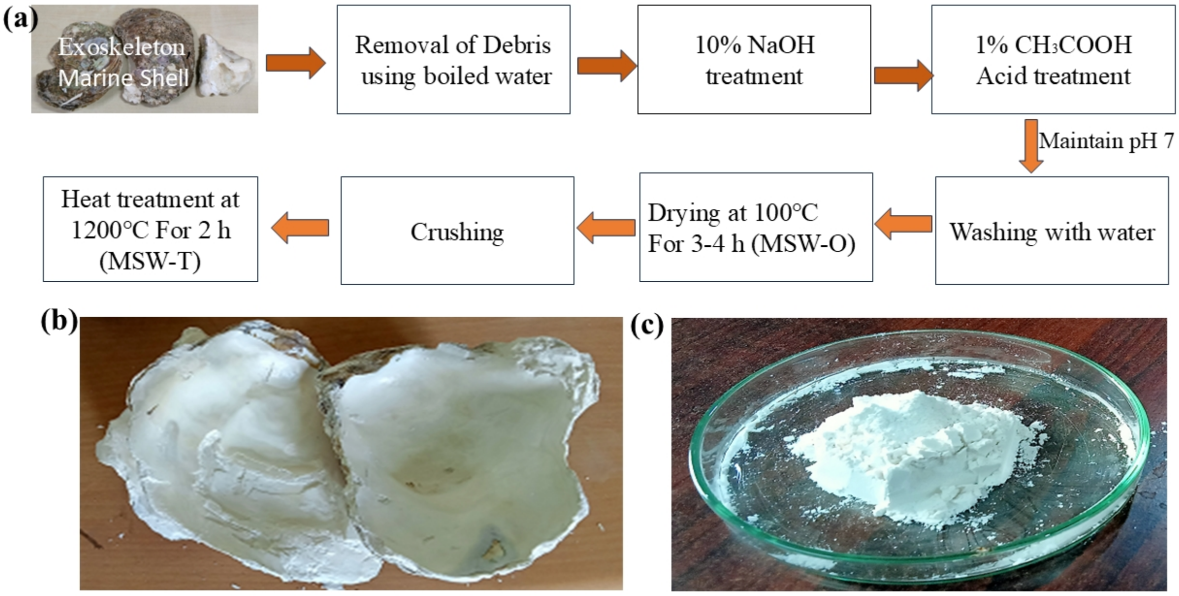

Figure 4. 2 Processing of marine shell waste represented by (a) procedural scheme adopted for extraction, (b) physical appearances of marine shell waste and (c) physical appearance of calcined marine shell waste powder

4.3. Fabrication of haemostatic patches from various natural resources chitosan (CS) and marine shell waste (MSW)

4.3.1. Fabrication of haemostatic flim and sponges

The fabrication of haemostatic patches was accomplished through two distinct drying techniques: air drying and freeze drying methods. These processes utilized chitosan and marine shell waste as sustainable, naturally-derived raw materials. Chitosan, known for its biocompatibility and haemostatic properties, was combined with processed marine shell waste to create composite patches. The air drying method involved controlled ambient temperature dehydration, while the freeze drying technique employed sublimation under vacuum conditions to remove moisture. Both approaches aimed to preserve the structural integrity and biological activity of the natural components while creating effective haemostatic materials for medical applications.

4.3.1.1. Fabrication of haemostatic flim by air drying method

12% PVA (98% hydrolised, 89-98 KDa molecular weight Sigma-Aldrich, USA) and 3% CS (medium molecular weight, Sigma-Aldrich, USA) were prepared in deionized water and mixed in a 20:80 ratio for preparation of the film. This mixture was homogenized in Ultrasonic Probe Sonicator, (PCI Analytics, Thane, India) for 10 minutes and poured into a glass Petri dish and air dried at 37°C for 3 days to get film by using a simple solvent casting method. This film was named as AD1. Another type of film AD2 was prepared by mixing MSW-O powder (5mg/mL) in PVA/CS solution. The pictorial images of the flims are shown in the **Figure. 4.3**.

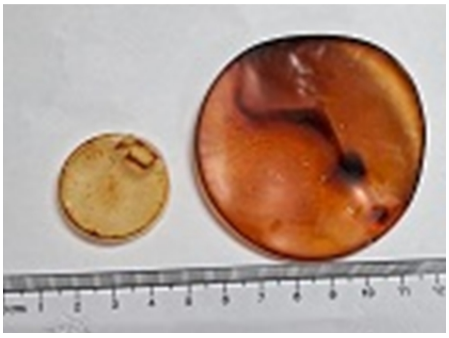

Figure 4. 3 The pictorial images of airdried films

4.3.1.2. Preparation of haemostatic sponge by freeze drying method

To prepare the haemostatic sponges, chitosan (CS) was dissolved in 1% acetic acid and stirred at 800 rpm for 24 h. Similarly, a 12% (w/v) PVA solution was developed by solubilising PVA in deionized water under vigorous agitation (400 rpm) at 80°C for 8 h. To prepare control sponges (PVA/CS) 20% of CS solution (3% w/v in 1% acetic acid) was mixed with 80% of PVA solution (12% w/v). For the oyster shell incorporated chitosan sponges (PVA/CS/MSW-O), oyster shell (MSW-O) powder (5mg/mL) was added to the mixture consisting of 80% polyvinyl alcohol (PVA, 12% w/v) and 20% chitosan (CS, 3% w/v dissolved in 1% acetic acid). The mixture was continuously agitated at 500 rpm for 24 h. Both the solution was stored at -20°C for 24 h and subsequently lyophilized at -50°C for 8 h (depicted in **Figure.4.4 & 4.5**).

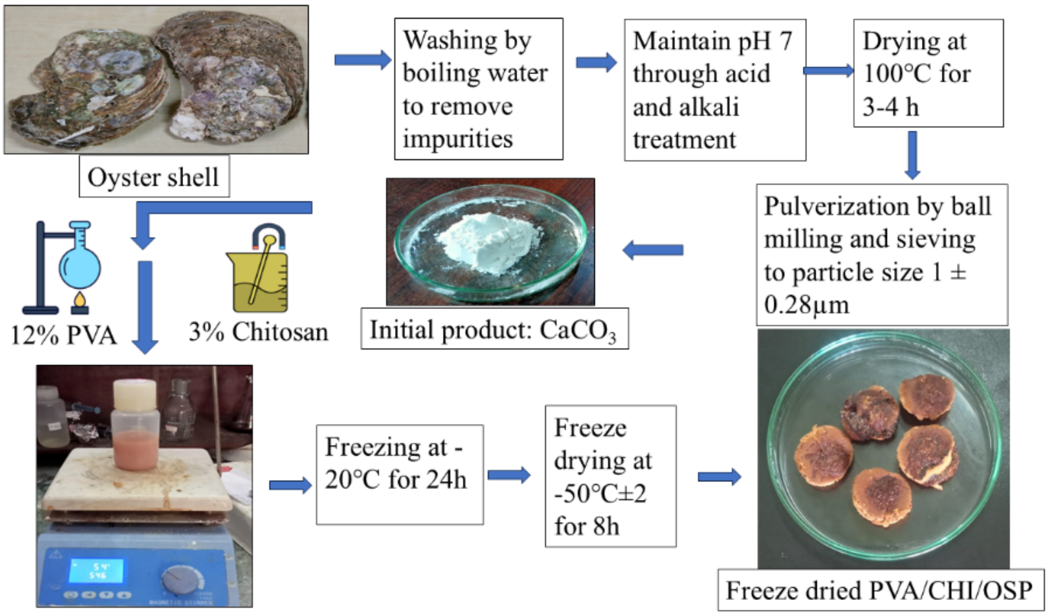

Figure 4. 4 Fabrication of oyster shell incorporated freeze died sponge shown by method of preparation

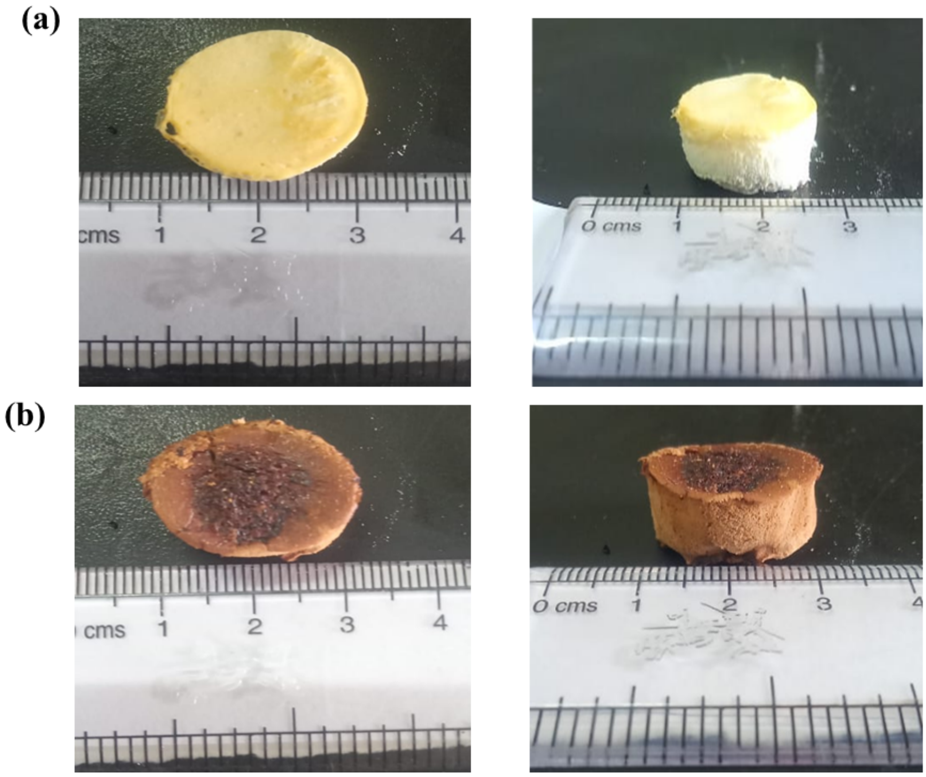

Figure 4. 5 Physical appearances of (a) PVA-chitosan sponge (PVA/CS) and (b) PVA-chitosan OS derived Ca mineral composite sponges (PVA/CS/MSW-O).

4.3.2. Fabrication of nanofibers

The fabrication of haemostatic nanofibers was accomplished through the electrospinning technique, which utilizes high voltage to create ultrafine fibers from polymer solutions. This process incorporated chitosan as the primary biocompatible polymer matrix, known for its natural haemostatic and antimicrobial properties. The nanofiber composition was further enhanced with antihemorragic drugs, specifically tranexamic acid and ethamsylate, which serve as potent bleeding control agents. Tranexamic acid functions by inhibiting fibrinolysis and stabilizing blood clots, while ethamsylate helps reduce capillary bleeding and improve platelet adhesion. Additionally, calcined marine shell waste was integrated into the formulation, providing calcium carbonate content that can promote coagulation and serve as a sustainable, cost-effective reinforcing agent. This combination of natural polymers, therapeutic agents, and processed marine waste created a multifunctional nanofiber system designed for rapid bleeding control and wound management applications.

4.3.2.1. Fabrication of haemostatic nanofiber by electrospinning method

The preparation of nanofiber membranes involved three distinct formulations, all utilizing chitosan (CS) and polyvinyl alcohol (PVA) as base polymers placed in the electrospinning machine (E-spin Nanotech, Kanpur, India) using copper plate or aluminium foil as the collector depicted in **Figure.4.6, 4.7** & **4.8.** The solutions were prepared by dissolving CS in acetic acid and PVA in distilled water or deionized water, with same PVA:CS ratios (8:2) depending on the formulation.

Figure 4. 6 Electrospinning Machine used for nanofiber fabrication (E-spin Nanotech, Kanpur, India)

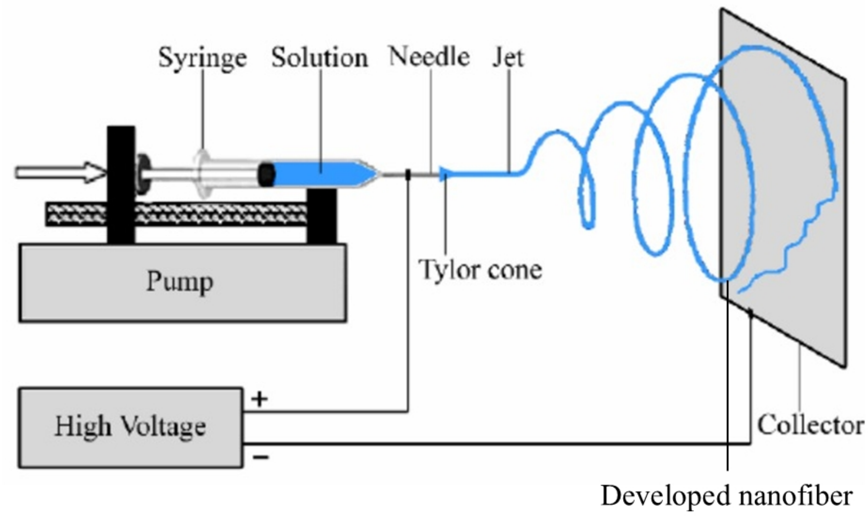

Figure 4. 7 Schematic outline of Electrospinning Setup

Various therapeutic agents were incorporated, including tranexamic acid (TXA, 30mg/mL), ethamsylate (E, 30mg/mL), and calcined marine shell waste (MSW-T, 5mg/mL). The electrospinning process was conducted under similar conditions across all formulations: feed rates of 0.4-0.5 mL/h, collector distance of 12 cm, and applied voltage ranging from 20-27 KV. Solutions were loaded into 24G syringes and electrospun onto aluminium foil-covered collectors. The resulting nanofiber membranes were carefully peeled off and stored in vacuum desiccator or dust-free polyethylene bags at room temperature for further use. Electrospinning was performed repeatedly to get membranes of a final thickness of 0.2 mm.

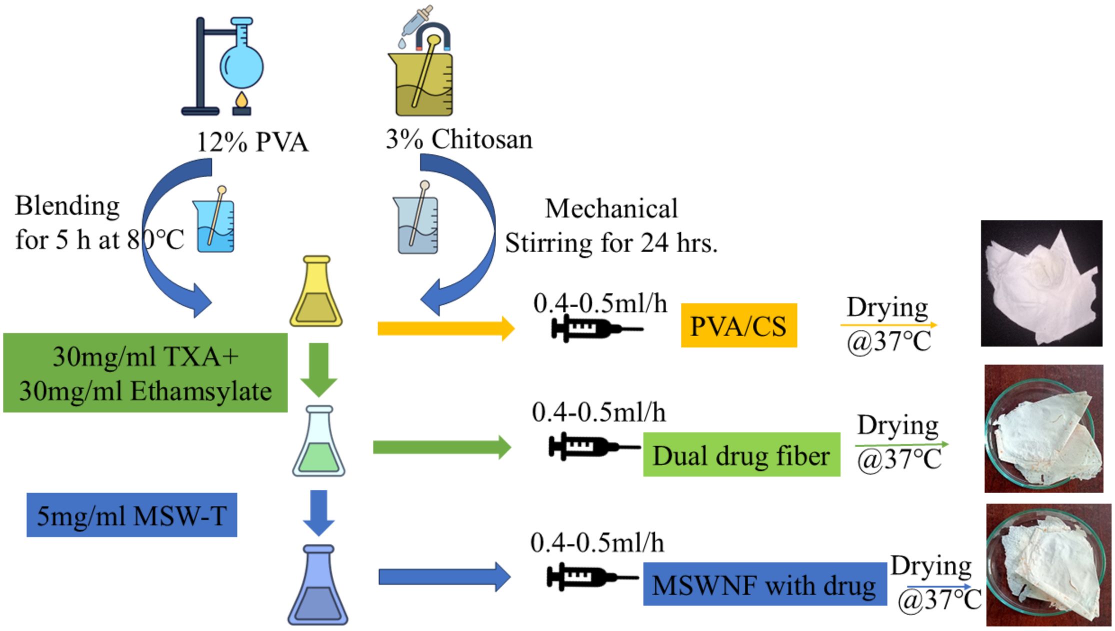

Figure 4. 8 Preparation of nanofiber membranes by utilizing chitosan (CS) and polyvinyl alcohol (PVA) as base polymers with tranexamic acid, ethamsylate and marine shell waste.

4.4. Characterization

4.4.1. Vibrational Spectroscopy

An infrared spectrum represents a fingerprint of a sample with absorption peaks which correspond to the frequencies of vibrations between the bonds of the atoms making up the material. Because each different material is a unique combination of atoms, no two compounds yield the exact identical infrared spectrum. The chemical characterization was performed following standard procedures [1] [2]. Briefly the functional group analysis of the developed scaffold was performed by using an attenuated total reflection (ATR) mode Fourier transform infrared spectrophotometer (IRAffinity-1S, SHIMADZU, Japan) with a resolution of 4 cm^{-1}. Theall spectrum was documented over 4000-400 cm^{-1} as an average of 32 scans.

Further examination of surface functional groups was performed by Raman spectroscopy (alpha 300 Access WITEC, Germany) at an excitation wavelength of 784 nm and class 3B laser power of 1 Mw. Spectra were acquired at 50 s integration time with 10 number of accumulations. Post processing of data was done with the help of Control S1X software with 6.0.5.115 version.

4.4.2. X-ray diffraction analysis

X-ray Diffraction analysis was used to define the structure and composition of the synthesized powder (MSW-O) and MSW-T from MSW using an X-ray diffractometer (Malvern PANalytical Empyrean Series III model). The instrument operated with Cu Kα radiation (λ = 1.540 Å) at 40 keV and 40 mA, scanning from 10° to 90° 2θ with a 0.02° step size. Diffraction peaks were collected using a data collector and subsequently analysed using High Score Plus Interpretation software.

4.4.3. Energy dispersive X-ray analysis

Elemental analysis of synthesized and calcined marine shell waste (MSW) powder was performed by using Gemini SEM 360 ZEISS microscope equipped with EDX-APEX microprobe software. The spectrum was acquired at an acceleration voltage of 15kV EHT and a current of 1.5nA.

4.4.4. X-ray photoelectron Spectroscopy of MSW-T powder

The chemical composition of the MSW-T powder sample was obtained by utilize the X-ray photoelectron spectroscopy method. The XPS spectra were measured at room temperature on the PHI 5700/660 spectrometer (Physical Electronics Inc., Eden Prairie, MN, USA) with used to monochromatized Al Kα radiation ($h\omega$ = 1486.6 eV). The survey spectra and the high resolution Cu2p, C1s and O1s core lines were measured with the energy step resolution of 0.400 eV and 0.100eV, respectively. In order to neutralize the surface positive charge effect, the flood gun was used. The position of the C1s peak at 285 eV was chosen as the reference. Deconvolution Cl2p, Sr3d, Mg1s, Na1s, Ca2p, C1s and O1s core lines as well as the atomic and weight concentration calculation were obtained by MultiPak software (ver. 9.8.0.19).

4.4.5. Scanning electron microscopy of scaffold

The scaffolds (freeze-dried sponges and electrospin nanofiber) underwent scanning electron microscopy (SEM) analysis using Gemini SEM 360 ZEISS microscope at an acceleration voltage of 5 kV. Sample preparation followed a standard protocol involving alcohol degradation and gold sputter coating (approx. 2.5 nm thickness of coating) [3] . ZEISS Smart SEM software was used to measure inter-porosity distances and pore size distributions from the SEM images. The fiber diameter was calculated at 50 different portions of the nanofiber by Image J® software [4].

4.4.6. Mechanical Properties

Uniaxial compression tests were performed of PVA/CS and PVA/CS/MSW-O sponges (monoliths of 10 mm diameter and 8 mm height) using a 250N load cell attached to a universal testing machine (Tinius Olsen 5KS, UK) at a compression rate of 1 mm/min.

Stress-strain curves of the membranes (CNS, MSWNF) were obtained under tensile loading and used for calculating the elastic modulus (E), ultimate strength (UTS) and percentage of elongation (EB) using a 25 N load cell attached to a universal testing machine (Tinius Olsen 5KS, UK). Specimens (n=4) of dimension 20 mm × 10 mm × 0.05 mm (L×W×H) were used for testing. The crosshead speed was kept at 0.1 mm/min. The compressive stress and the strain data were calculated by a horizon software attached to the machine.

4.4.7. Swelling and degradation of the patches

All the nanofiber patches were cut into specified dimension of 10 mm×10 mm, immersed into phosphate buffered saline (PBS) at room temperature, and observed for 48 h. Each specimen was removed from the PBS at different times, the surface was gently soaked using filter paper, and weight was taken. The swelling ratio of the electrospun patches was measured using **equation (1).**

$$\text{Swelling ratio} = \frac{W_w - W_d}{W_d} \text{ --———— } (1)$$

Where W_w and W_d are wet weight and dry weight of the scaffolds. The results are reported based on average of five measurements.

The degradation of patches in PBS was studied by continuing incubation upto 4 days after completion of swelling was observed followed by intermittent observations every 5th day were taken for the next 20 day. After gentle soaking with filter paper, the patches were dried in a furnace for 10 min at 40℃ to remove interfacial water molecules, and finally, the weight of the patches was taken. The procedure was performed in triplicate and mass remaining was calculated by **equation (2).**

$$\text{Remaining Mass \%} = \frac{W_i - W_s}{W_i} \times 100 \text{-------} (2)$$

W_i=initial weight, W_s= weight after swelling

4.4.8. Contact angle

This angle is a guide of the wettability of a solid surface. A smaller contact angle proposes that the material is water lovable and high-energy surface qualities. But a higher contact angle indicates that the material is water repellent and low-energy surface characteristics. The contact angle of the films was measured by SURFECTENS 4.5 surface tensiometer (OEG GmbH, Germany). 10 µl deionized pure water was disposed on the samples via the sessile drop method and pictures were captured. The images were characterized through Image J software.

4.4.9. In vitro haemostatic performance

4.4.9.1. Assessment of whole blood clotting time (WBCT)

In vitro coagulation tests, i.e., whole blood clotting time (WBCT), was conducted to evaluate the hemostatic properties of air dried, freeze dried and nanofiber patches. WBCT was estimated by adding an anticoagulant (3.8% sodium citrate) to rabbit blood, following literature [5]. 10 mg of patches were weighed and taken into Eppendorf tubes and placed in a water bath at 37℃ for 15 min. 340 µl of rabbit blood was added into the Eppendorf tube along with 20 µl 0.2 M $CaCl_2$. Eppendorf tubes were inclined towards opposite horizontal positions by a 180° rotation. This procedure was continued till the blood/sample aggregate formed completely and the time was recorded by noted stop watch (EISCO Mechanical Stopwatch, India). WBCT was recorded from the time at the blood addition to the endpoint of coagulation. The control was measured without addition of any patch.

4.4.9.2. Activated partial thromboplastin time (aPTT), Prothrombin time (PT) and Platelet Recalcination Time (PRT)

Fresh rabbit blood was collected and mixed with 3.8% sodium citrate solution at a volumetric ratio of 1.5 ml of anticoagulant to 8.5 ml of blood. The platelet-poor plasma (PPP) was developed by centrifuging the anticoagulated whole blood at a rate of 3000 rpm for 5 min. The test solution was prepared by dispersing 10 mg of patches in 1 ml of normal saline at 37 ℃. To evaluate the activated partial thromboplastin time (aPTT), 50 μL PPP and 50 μL aPTT reagents were added with 10 μL test solution and incubated at 37 ℃ for 3 min. Finally, 50 μL of 0.025 mol/L $CaCl_2$ was combined to this mixture. The aPTT time was recorded as time taken to coagulate under stirring with a fine needle. Solution without any test solution was considered a control. For the Prothrombin time (PT) assay, 10 μL test solution was mixed to 50 μL PPP and incubated at 37 ℃ for 3 min and subsequently mixed with 100 μL of PT reagent. The mixture was agitated until coagulation and PT(s) was recorded. For the measurement of PRT, freshly prepared 300 μL of PPP was incubated at 37 °C with 3 mg patch for 3 min. The plasma recalcification was performed using 30 μL of 0.5 M $CaCl_2$. Fibrin thread formation in PPP was observed subsequently. PRT was calculated from the time of re-calcification to the fibrin thread formation.

4.4.9.3. Platelet adhesion

The interaction between these fabricated haemostat patches and blood platelets was studied at room temperature by taking rabbit blood obtained from animal research centre, West Bengal University of Animal and Fishery Sciences, West Bengal, India. At first, platelet-rich plasma (PRP) was prepared by centrifugation (100 g for 10 min) of anticoagulant-added blood at 4 ℃. The patches (10 mm×10 mm) were washed with the help of deionized water followed by 1X PBS solution. Then, patches were kept in a cell culture well plate with the help of O-rings. 650 μl of PRP sample was gently dropped on the surface of patches. These patches were incubated for 60 min at 37 ℃. The patches were cleaned with 1X PBS to remove plasma protein and non-adhered platelets. After cleaning, the patches were fixed with 2.5% glutaraldehyde (2 h) and then slowly dehydrated using 50%, 60%, 70%, 80%, 90%, and 100% v/v aqueous ethanol. The patches were then dried in a hot air oven at 40 ℃ for 10 min. The platelet adherence on patches was analysed by SEM.

4.4.10. Estimation of hemocompatibility of patch by haemolysis studies

In-vitro hemocompatibility of these fabricated patches was studied by taking rabbit blood as per the procedure from the literature [6]. The collected blood was mixed with 3.8% (w/v) sodium citrate solution at 10:1 to prevent coagulation. In the next step, the anticoagulant-added blood is diluted with normal saline in a ratio of 4:5. The positive control was prepared by taking 0.2 ml of diluted blood in 10 ml of 0.1% Na_2CO_3 solution and a negative control was formulated by taking 0.2 ml diluted blood in 10 ml of normal saline solution. These positive and negative control sample solutions were incubated at 37 °C for 60 min. The patches were dispersed in 10ml saline solution and preserved in an incubator at 37 °C for 30 min. 0.2 ml of diluted blood was taken on each patch, added to the saline solution, and incubated for 60 min at 37°C. All the test tubes were centrifuged at 2100 rpm for 5 min, and the supernatant fluid was carefully moved to a cuvette for optical density measurement in a UV spectrophotometer at 545 nm.

The percentage of haemolysis was calculated from the following **equation (3)**

$$\%\text{ of hemolysis} = \frac{\text{O.D}_{(\text{Test})} - \text{O.D}_{(\text{Negative})}}{\text{O.D}_{(\text{Positive})} - \text{O.D}_{(\text{Negative})}} \times 100\text{-------- } (3)$$

4.4.11. Cell Cytotoxicity tests by MTT Assay

Cell metabolic activity was performed using MTT solution (EZ Count MTT assay kit, Abcam, USA) on Human Adult Dermal Fibroblasts (HADF, CL005) cells. HADF cells were cultured in Hi-glucose Dulbecco’s modified Eagle’s medium (DMEM) with 10% fetal bovine serum and 1% w/v antibiotic solution at 37 °C in a humidified (95%) incubator with 5% CO_2 level for 24 h. The culture was maintained at 80-90% confluency. The fabricated patches were added to DMEM containing 10% fetal bovine serum. After incubation at 37 °C for 48 h, the solutions were filtered through a microporous patch (0.22 μm) to eliminate bacteria and the undissolved part of the sample. This filtered solution was taken in the culture plates where the HADF cells were seeded. This test was performed in 5% CO_2 environment at 37°C in 96 well plate at a density of 10^4 cells per well. The control was prepared by taking HADF cells in DMEM containing 10% FBS. After 24 h, the cultured control and test well medium was replaced with DMEM solution, and the patch added DMEM solution, respectively. After 3 days of culture, 10 μl MTT solution was added to the cell-laden well plate and preserved for 4 h inside the incubator. On addition of MTT, formazan crystal was formed, the amount of formazan crystal formation is directly proportional to the active cell metabolism, indicating cell viability[7]. The crystals were solubilized in DMSO, and the absorbance of each solution was determined using a multi-plate reader (Thermo Scientific Multiskan GO UV-vis spectrophotometric microplate Spectrophotometer, Finland) at 570 nm. These absorbance values were subsequently used to calculate percentage cell viability by **equation (4)**. Measurements were performed in triplicate.

$$\text{Percentage of cell viability} = \frac{\text{Treated-Blank}}{\text{Control-Blank}} \times 100\text{-------- } (\mathbf{4})$$

DAPI staining was done to visualize and measure the number of cells on the nanofiber membranes as well as freeze drying scaffold. HADF cells (1×10^6) were seeded onto the surface of CNF and MSWNF nanofibers and cultured for three days in standard high-glucose DMEM. Membranes were fixed for 15 min with 4% paraformaldehyde (PFA), then incubated for 5 min with DAPI dye. Following rinsing with PBS, images of the scaffolds were taken at 10× magnification using a Nikon eclipse Tí U inverted fluorescence microscope in Japan. Cell numbers were quantified by ImageJ software after capturing images from 10 fields of interest.

4.4.12. Cell Migration assay

This experiment was performed by taking HADF cells in 60 mm Patri dishes, and 80% cell confluency was confirmed initially. A two-dimensional longitudinal cut was made in the confluent zone of cell by the tip of a 200 µl pipette. The debris was removed to smooth the edge of the scratch by washing the cells once with 1 ml of the growth medium and then replace with 5 ml of test solution of hemostatic patches. Close to the scratch, a definite marking was taken as a reference point. The dishes were kept in the tissue culture incubator at 37℃ for 24 h. After the incubation period, the dish was put under a phase-contrast microscope, the reference point was justified, and the photographs were taken.

4.4.13. Drug release study

In vitro TXA and E release from PVA/CS/TXA, PVA/CS/E and PVA/CS/TXA-E patches were determined using a Franz diffusion cell. 4 cm^2 patches (100 mg) were taken and mounted on the upper container. In the receiver chamber, 10 ml PBS solution was stirred continuously (@75 rpm) at 37 ± 1 °C. Aliquots (1 ml) were withdrawn at different time points and replaced with an equal amount of PBS each time. The withdrawn solution was diluted with 10 ml PBS solution. For tranexamic acid release, a diluted solution of 1 ml was reacted with 1% ninhydrin reagent (1 ml) for 2 h at 100℃. The optical density (OD) of resultant solution was measured in a UV/vis spectrophotometer at 575 nm [8], [9]. The drug released per cm^2 for each time point (30 s, 1 min, 2 min, 5 min,10 min, 20 min, 30 min, 1 h, 3 h, 5 h) was calculated.

For Ethamsylate release, patches were placed in 30 ml 0.1 N HCl solution at continuous stir mode/condition @75 rpm [10]. 1 ml fresh 0.1 N HCl solution was added to make up the volume. The study was conducted in triplicate. OD was measured using at 309 nm.

Prior method development and validation was carried out in the range. The regression equation of cumulative drug release was plotted against time and analyzed by different models.

4.4.14. Antibacterial study

The antimicrobial activity of the calcined powder, CNF and MSWNF were assessed using the disk diffusion method, following Kerby-Bauer protocol. Luria Bertani agar plates were made under sterile conditions and inoculated with *Staphylococcus aureus* (MTCC-740) and *Escherichia coli* (MTCC-1687) bacteria. A fresh bacterial culture with a concentration of 10^8 CFU/mL was evenly distributed across agar plates using a sterile spreader. The medium, consisting of agar and Luria-Bertani broth, was prepared and poured into petri dishes. Cut into uniform round pieces (6mm diameter) sponges were incubated alongside the bacterial culture plates for 24 h. The loading was accomplished by weighing the MSW powders and suspended in sterilized 2% w/v acetic acid solution in distilled water at 5 mg/mL, vortexing to obtained uniform slurry, and aliquoting 50 µL of the suspension onto the disks. A separate arrangement was completed for CNF and MSWNF. CNF and MSWNF cut into equal sizes of 6 mm diameter were placed on the agar surface. The positive control used was 1% w/v penicillin, streptomycin, and amphotericin B solution, and the negative control used was 0.2 µm filter paper stored in Eppendorf tubes at 4℃. The agar plates were then incubated at 37℃ for 24 h. After the incubation period, antibacterial activity was determined by measuring the clear zone of inhibition (ZOI) around each disk using ImageJ software.

4.4.15. RT-PCR Analysis

Quantitative reverse transcription polymerase chain reaction (RT-PCR) was performed to assess the expression levels of vascular endothelial growth factor A (VEGF-A), platelet-derived growth factor (PDGF), and interleukin growth factor 1 (IGF-1) gene in HADF cells cultured on different scaffolds, using glyceraldehyde-3-phosphate dehydrogenase (GAPDH) as an internal control. HADF cells were collected from the scaffold surface and Total RNA was extracted using the Trizol method and quantified via Nanodrop. cDNA was synthesized using a reverse transcription kit (Applied Biosystems, USA) and diluted for PCR. Reactions were performed in 20 µL volumes containing SYBR Green PCR Master Mix, cDNA template, specific primers, and nuclease-free water. PCR conditions included initial denaturation (95°C, 10 min), followed by 40 cycles of denaturation (95°C, 15 s), annealing (58°C, 30 s), and extension (72°C, 30 s). Melting curve analysis verified product specificity. Relative gene expression was calculated using the ΔΔCT (relative gene expression fold change) method, normalized to GAPDH.

4.4.16. Haemostatic studies with scaffolds in rabbit injury model

Haemostatic studies with electrospun nanofiber and composite freeze dried sponge were done in rabbit injury model (Total 20 rabbits). A rabbit skin insertion model (14 rabbits) was employed to evaluate the haemostatic efficacy of dual drug loaded scaffold along with CNF and MSWNF. A rabbit femoral artery injury model (6 rabbits) was prepared to examine the efficacy of freeze dried sponge. These both studies adhered to the guidelines for 'Principles of Laboratory Animal Care' and was conducted under the approval of the "Institutional Animal Ethical Committee (IAEC) at West Bengal University of Animal and Fishery Sciences (WBUAFS), West Bengal, India (protocol number 763/G0/Re/SL/03/CPCSEA/21/2021-22)".

Fourteen New Zealand White Rabbits (*Oryctologus cuniculus*), weighing 1.5-1.8 kg of either sex, were anesthetized with intramuscular injections of xylazine hydrochloride (5 mg/kg; Xylaxin, Indian Immunological, India) and ketamine hydrochloride (30 mg/kg; Ketalar, Parke-Davis, India) 15 min before the in vivo experiment. Two animals participated in each group (n=2). The loin region of each animal was prepared for aseptic surgery. A 3-5 mm deep skin incision was made, and bleeding from a superficial vein was induced using a Lister surgical blade. Bleeding from the skin and subcutaneous fascia was observed for 15 s. Following this, membranes (PVA/CS, PVA/CS/TXA, PVA/CS/E, PVA/CS/TXA-E and AbGel) were applied with gentle pressure, and the bleeding time was documented by a digital stopwatch (EISCO Mechanical Stopwatch, India) in **figure 4.9**. Gauge bandages were used as a control. Bleeding was checked at several time intervals. If a membrane was displaced by blood flow, a new sample was applied to the incision site. Bleeding was controlled by membrane application with gentle pressure. Another skin incision experimental procedure was done for CNF and MSWNF nanofibers in **figure 4.10.**

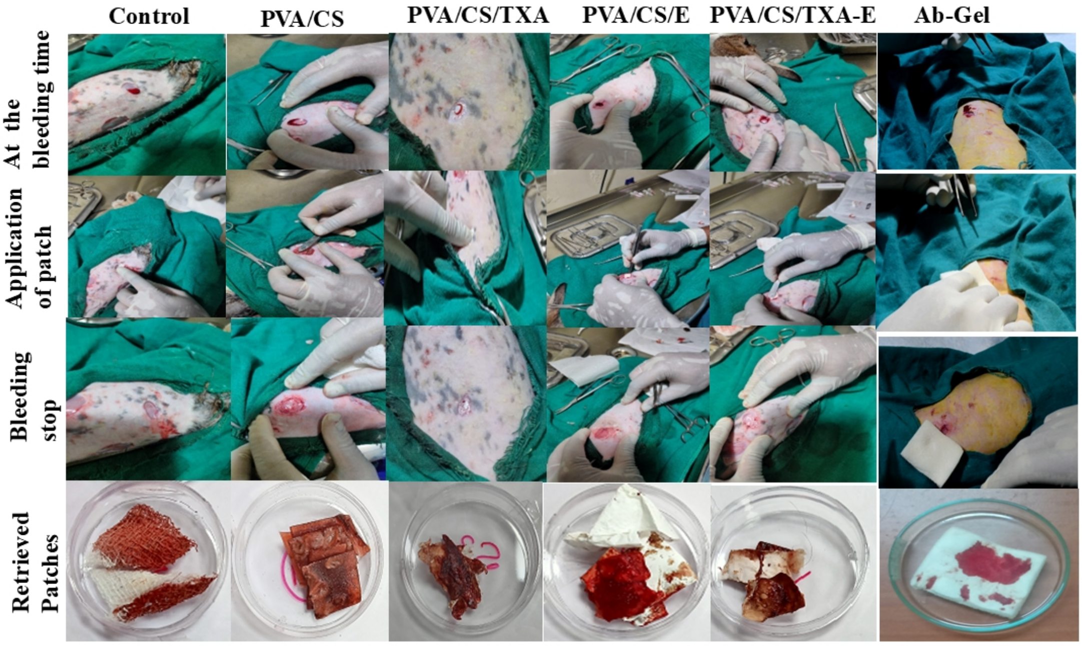

Figure 4. 9 In-vivo assessment of hemostasis performance of dual drug loaded nanofiber studied in skin incision model.

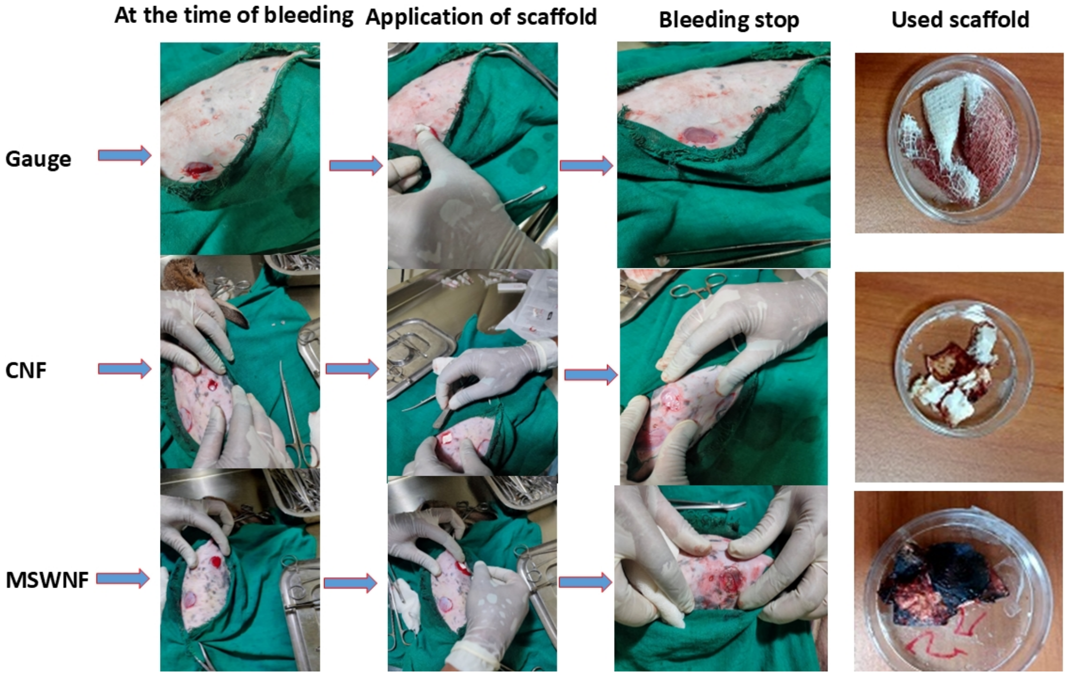

Figure 4. 10 In-vivo rabbit skin incision model for evaluation of marine shell waste nanofiber performance as hemostaic agent depicted by surgical procedure.

These applied membranes were further treated as described in the in vitro platelet adhesion protocol. They were washed with 1X PBS, fixed with 2.5% glutaraldehyde for 2 h, and then slowly dehydrated using an ethanol gradient. The platelet-adhered nanofibers were then analysed by SEM to assess the morphology of the activated platelets on the membranes.

The femoral artery was severed in the rabbit model and the prepared composite sponges (PVA/CS and PVA/CS/MSW-O) were then immediately applied in the wounded area and kept under pressure (n=2). Assessments were made of mean arterial pressure (MAP), time to haemostasis, total amount of blood loss, survival rates, and survival length. For MAP, an oscillometric equipment was used to monitor mean arterial pressure by placing the cuff above the injury area in femoral artery and exclude possibilities of **hypovolemic shock**, which may sometimes accompany a surgical bleeding procedure and alter the normal clotting response. Rectal temperature was continuously monitored through procedure using a digital thermometer. The **MAP and temperature were monitored to control experimental variables and obtain physiologically relevant data** for accurately determining that the outcomes are due to the haemostatic material, and not for other underlying physiological changes. The sponges were placed to the injury site and were changed every 30 s until the bleeding stopped. No additional surgical interventions, such as fluid resuscitation, were permitted during the experimental setup. Total blood loss was measured by computing the difference in the dressing weight before and after the experiment.

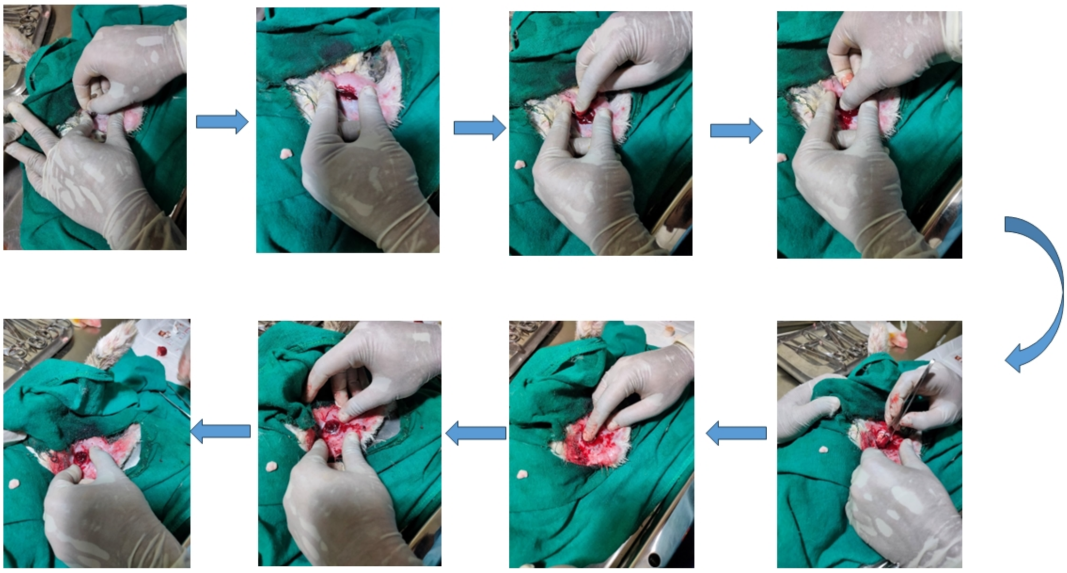

Figure 4. 11 In vivo rabbit femoral artery bleeding model for evaluation of freeze dried PVA/CS/MSW-O sponge.

4.4.17. Histopathology

Histopathology was performed on skin samples from the membrane application site after bleeding was stopped to evaluate microstructural changes in the ruptured blood capillaries. The lesioned skin section was cut with scissors to obtain tissue specimens containing the entire wounded area after 7 days from application. The specimens were preserved in 10% formalin solution for 24 h to prevent damage. Skin samples were then mounted in paraffin blocks (5x5 mm^2) and stained with Hematoxylin and Eosin (H&E) on glass slides. Images were captured using a bright field microscope (Nikon eclipse Ti U, Japan) at 20× magnification.

4.4.18. Statistical analysis

The experiments were done in triplicate unless specified and data are reported as mean ± standard deviation. Statistical significance was made by one-way ANOVA with Tukey's post hoc test. Analyses were conducted using Origin Pro 2022 software, with statistical significance established at $p < 0.05$, wherever relevant, p-values are also reported."

References:

[1] P. Sasmal and P. Datta, “Tranexamic acid-loaded chitosan electrospun nanofibers as drug delivery system for hemorrhage control applications,” *J Drug Deliv Sci Technol*, vol. 52, pp. 559–567, Aug. 2019, doi: 10.1016/j.jddst.2019.05.018.

[2] W. A. Abbas, I. M. Sharafeldin, M. M. Omar, and N. K. Allam, “Novel mineralized electrospun chitosan/PVA/TiO2 nanofibrous composites for potential biomedical applications: Computational and experimental insights,” *Nanoscale Adv*, vol. 2, no. 4, pp. 1512–1522, Apr. 2020, doi: 10.1039/d0na00042f.

[3] E. R. Fischer, B. T. Hansen, V. Nair, F. H. Hoyt, and D. W. Dorward, “Scanning electron microscopy,” *Curr Protoc Microbiol*, no. SUPPL.25, May 2012, doi: 10.1002/9780471729259.mc02b02s25.

[4] D. Massai *et al.*, “Image-based three-dimensional analysis to characterize the texture of porous scaffolds,” *Biomed Res Int*, vol. 2014, 2014, doi: 10.1155/2014/161437.

[5] Y. Zhao *et al.*, “Degradable porous carboxymethyl chitin hemostatic microspheres,” *J Biomater Sci Polym Ed*, vol. 31, no. 11, pp. 1369–1384, Jul. 2020, doi: 10.1080/09205063.2020.1760461.

[6] S. Krishna Samanta and A. Chanda, “Study on the Structure and Properties of Crystalline Pure and Doped β-Tri Calcium Phosphate Ceramics,” in *Materials Today: Proceedings*, Elsevier Ltd, 2018, pp. 2330–2338. doi: 10.1016/j.matpr.2017.09.237.

[7] S. Dasgupta, A. Gope, A. Mukhopadhyay, P. Kumar, J. Chatterjee, and A. Barui, “Chitosan-collagen-fibrinogen uncrosslinked scaffolds possessing skin regeneration and vascularization potential,” *J Biomed Mater Res A*, vol. 111, no. 5, pp. 725–739, May 2023, doi: 10.1002/jbm.a.37488.

[8] M. S. Arayne, N. Sultana, F. A. Siddiqui, A. Z. Mirza, and M. H. Zuberi, “Spectrophotometric techniques to determine tranexamic acid: Kinetic studies using ninhydrin and direct measuring using ferric chloride,” *J Mol Struct*, vol. 891, no. 1–3, pp. 475–480, Nov. 2008, doi: 10.1016/j.molstruc.2008.04.026.

[9] P. Sasmal and P. Datta, “Tranexamic acid-loaded chitosan electrospun nanofibers as drug delivery system for hemorrhage control applications,” *J Drug Deliv Sci Technol*, vol. 52, pp. 559–567, Aug. 2019, doi: 10.1016/j.jddst.2019.05.018.

[10] S. M. El-Masry and S. A. Helmy, “Hydrogel-based matrices for controlled drug delivery of etamsylate: Prediction of in-vivo plasma profiles,” *Saudi Pharmaceutical Journal*, vol. 28, no. 12, pp. 1704–1718, Dec. 2020, doi: 10.1016/j.jsps.2020.10.016.

Chapter 5

RESULTS AND DISCUSSION

5. Results and Discussion

This chapter is divided into different sections as listed below.

A. Extraction of calcium carbonate from marine shell waste and its physical characterization.

B. Physical and mechanical characterization of different forms of haemostatic scaffold prepared by using MSW extract.

C. Biological characterization and in-vitro blood clotting parameters of different forms of haemostatic scaffold.

D. In Vivo characterization of freeze dried and electrospun nanofiber of haemostatic scaffold.

E. Comprehensive report of the comparative performances of scaffolds.

5.A. Extraction of calcium carbonate from marine shell waste and its physical characterization.

Marine Shell Waste (MSW) is calcium rich material, originated in the harbour of Sundarbans Delta, West Bengal, India locally named as “KAKLUS”. It was formed as layer-by-layer depositions of hard scale. It was identified by the Zoological Survey of India, Prani Bigyan Bhavan under Ministry of Environment, Forest and Climate change, Government of India.

Species Name	**Family**	**Specimens**	**Reg. No.**
Magallana Cuttackensis (R.B Newton & E. A. Smith, 1912)	Ostreidae	1	(Voll.-X) M37430

5.A.1. FTIR Spectroscopy analysis

The FTIR spectra displaying the functional group present in synthesized (S0) and calcined specimen of marine oyster shell (S800, S1000, S1200) are shown in **Figure. 5.A.1**. As we can see in S0 spectra, Ca-O was observed at 709 cm^{-1} in plane bending (v1), the peak 872 cm^{-1} revealed the presence of C-O out plane bending (v2) and prominent peak 1405 cm^{-1} exposed the existence of asymmetric stretching vibration (v3) mode of CO_3^{-2} in the calcite form [1], [2], [3]. Similar pattern was observed in the case of calcined powders. For S800, S1000 and S1200, Ca-O peak was found at 710, 712, 699 cm^{-1} and the peak at 866, 857, 853 cm^{-1} was observed for C-O band. In the case of calcined powder some new peaks were found at 3636, 3641, and 3642 cm^{-1} which was absent in S0. These peaks signify to the stretching mode of O-H present in the calcined powder samples which assigned to the -OH of portlandite phase [4],[5]. Particularly, the O-H bond may be related to a low concentration of $Ca(OH)_2$ having a sharp band of 3641-3642 cm^{-1}, that was possibly formed on the S1000 and S1200 samples, because of its hygroscopic property. This revealed that the mixed pattern of calcite ($CaCO_3$) and $Ca(OH)_2$ was observed for the sample calcinated at 1000°C and 1200°C. Therefore, it can be concluded that phase changes occurred due to temperature elevation. Besides the characteristics of overlapped peaks around 1078, 1782, 2352, 2518, 2856, 2922 cm^{-1} are also shown in higher calcinated powder sample. These peaks and assignments are given in **Table 5.A.1**.

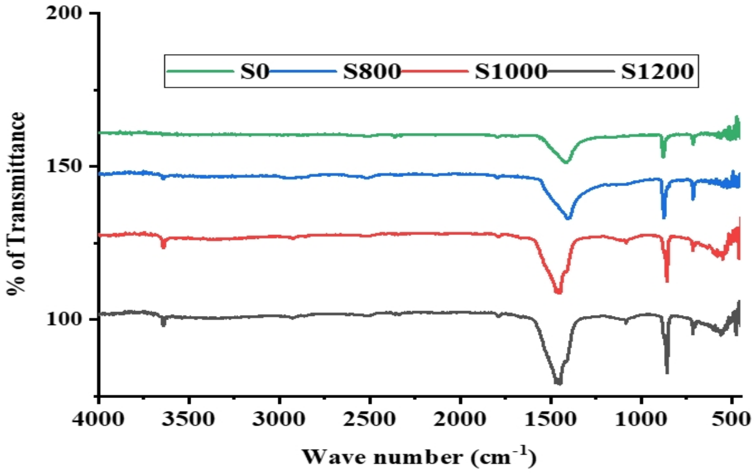

Figure 5.A. 1 FTIR spectra of extracted (S0) and calcinated (S800, S1000, S1200) marine shell waste powder.

Table 5.A.1. FTIR peaks and assignment of extracted and calcined marine shell waste.

S0(MSW-O)	S800	S1000	S1200 (MSW-T)	Assignment
709	710	712	699	In plane bending of CO_3^{-2}
872	866	857	853	Out plane bending of CO_3^{-2}
1092	1064	1081	1078	Vibration frequency for calcite
1403	1401	1455,1469	1447,1468	Asymmetric stretching vibration of CO_3^{-2}
1795	1795	1782	1782	C=O stretching mode of CO_3^{-2}
2509	2508	2525	2518	C–O asymmetric stretching modes of CO_3^{2-}
	2875	2863	2856	CH asymmetric stretching vibration
	2915	2912	2922	C–O symmetric stretching modes of CO_3^{2-}
3400-3600	3636	3641	3642	O-H bond

5.A.2 Energy Dispersive X-ray study of calcined MSW powder

EDX analysis was used for determining the elemental composition of MSW-O and calcined MSW-T. The results showed that MSW-O sample consisted of 28 wt% Ca, 49.5 wt% O_2, and 22.5 wt% C, indicating calcium carbonate as major component. MSW-T samples showed 47.5 wt% of Ca and 51.5 wt% of O_2 respectively, providing low or no evidence of C suggesting the presence of calcium oxide or calcium hydroxide as principal component. **Table 5.A.2** shows atomic % and weight % of synthesized and calcined marine shell waste. Also, MSW-O sample contained 12.7, 33, and 61.7 atomic % of Ca, C and O_2 whereas MSW-T had 26.7 and 72.4 atomic % of Ca, O_2 respectively. Thus, due to calcination, the calcium content increased. Based on the result in EDX peak intensities, the ratio of O/Ca and C/Ca were measured. The ratio of O/Ca were 1.93, 1.08 in MSW-O, MSW-T respectively and the ratio of C/Ca for MSW-O was 0.80. The predominant phase in MSW-T after calcination is likely to be calcium oxide (CaO), which aligns with the findings reported by J.H. Huh and colleagues [6].

Table 5.A.2. Elemental analysis of extracted and calcined marine shell waste.

Element	**MSW-O**		**MSW-T**	
	Weight%	Atomic%	Weight%	Atomic%
C K	22.5	33	----	----
O K	49.2	61.7	51.5	72.4
Ca K	25.4	12.7	47.5	26.7
P K	16.4	10.7	----	----
Mg K	----	----	1.1	1

5.A.3. X-Ray Diffractogram Analysis

To further confirm the phases of MSW, the crystal structure and phase identification was performed by XRD and the diffractogram is shown in the **Figure 5.A.2**. MSW-O showed diffraction peaks at 23, 29, 36, 39, 43 and 49º corresponding to (012) (104), (110), (113), (202), and (116) planes of hexagonal phase of $CaCO_3$ (JCPDS Card No 47-1743) [7]. The observed diffraction peak for calcined MSW-T at $2\theta = 28, 31$ and 53º were attributed to (111), (114) and (110) plane of CaO (JCPDS Card No. 017-0912) [8]. XRD pattern also showed some peak at 17 and 34º which are corresponding to (001) and (011) plane referred to the presence of $Ca(OH)_2$ (JCPDS Card No 01-84-1264) [9]. Two additional peaks at 29 and 47º exhibited to (111) and (011) orientation plane due to the presence of $CaCO_3$. The primary phase in the calcined coral matched with CaO and $Ca(OH)_2$, demonstrating the successful calcination-induced conversion of $CaCO_3$ to CaO and $Ca(OH)_2$ [10]. XRD also revealed the presence of the MgO phase, which may be attributed as trace element in the marine skeleton.

Calcination changed the crystallographic parameter of MSW. The average crystallite size of MSW-O and MSW-T were calculated using Debye-Scherrer's formula from the equation 4 [11]
.

$$D = \frac{0.94\lambda}{\beta cos\theta} \text{ .... } 4$$

The average crystallite size (D) was calculated using the Scherrer equation, where 0.94 represents the Scherrer constant, λ is the CuKα radiation wavelength, β denotes the full width at half maximum (FWHM) in radians, and θ is the peak position. For the hexagonal structures of MSW-O and MSW-T, the lattice parameters "a" and "c" were determined using equation 5.

$$\frac{1}{d^2} = \frac{4(h^2 + hk + k^2)}{3a^2} + \frac{l^2}{c^2} \text{ .... } 5$$

In which $d_{h\ k\ l}$ is the interplanar distance and h,k,l are the Millar indices. The positioning parameter (u) of MSW-O and MSW-T are estimated by equation 6.

$$U = \frac{a^2}{3c^2} + 0.25 \text{................................ } 6$$

Further equation 7 was used to estimate the bond length (l).

$$l = \sqrt{\frac{a^2}{3} + \left(\frac{1}{2} - u\right)^2 \times c^2} \text{ ....}7$$

Moreover equation 8 was used to calculate the volume (V) of the unit cell of MSW-O and MSW-T.

$$A = 0.866 \times a^2 \times c \text{.................... } 8$$

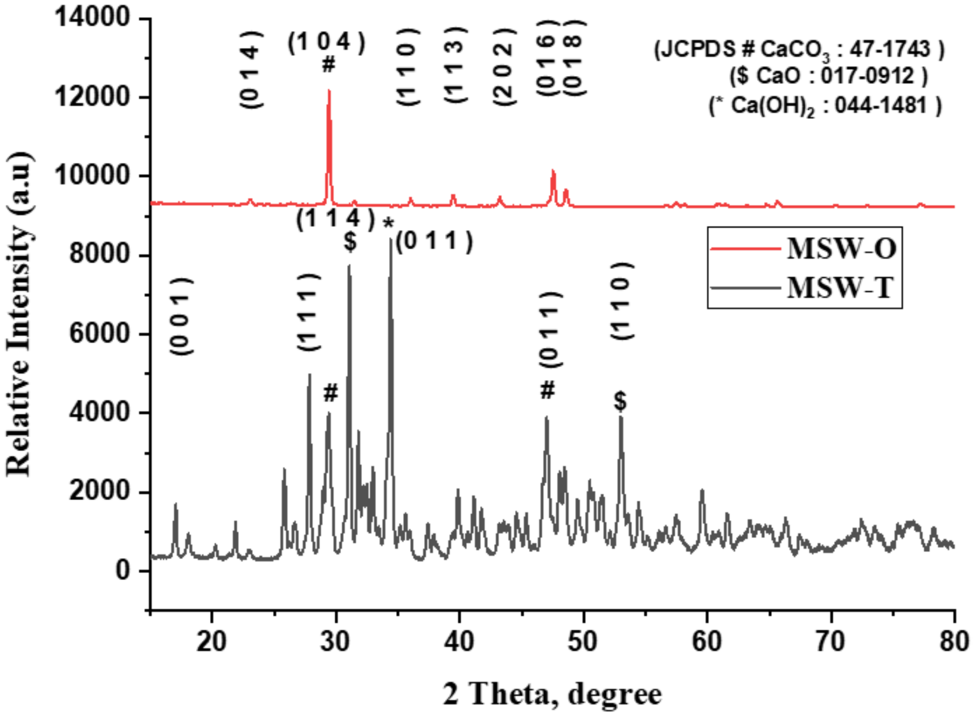

Figure 5.A.2. XRD Characterization of extracted (MSW-O) and calcined marine shell waste (MSW-T)

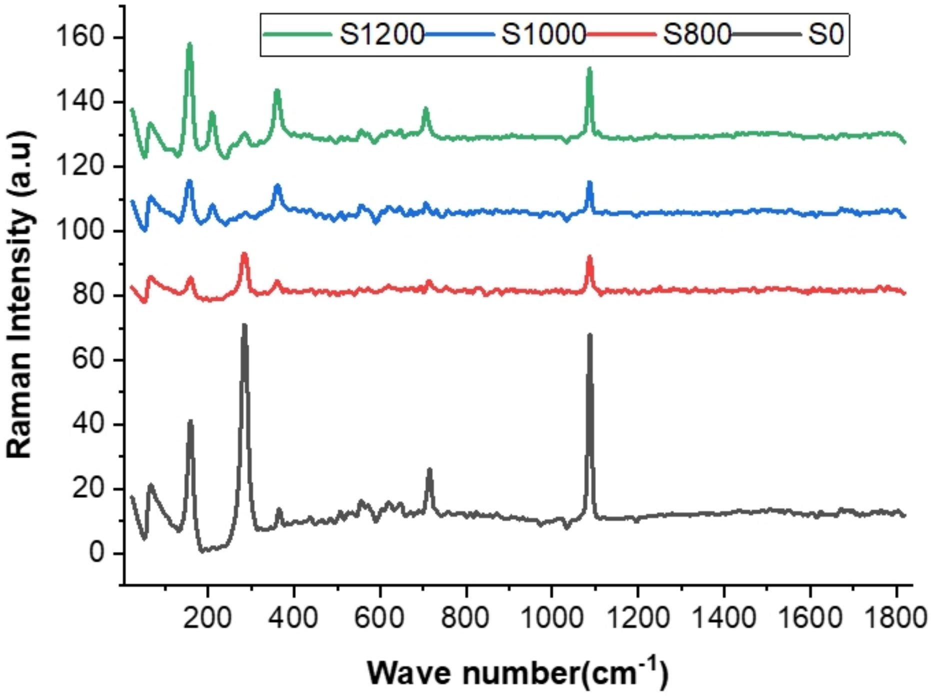

Figure 5.A.3. Raman spectra of extracted (MSW-O) and calcined marine shell waste (MSW-T)

Calcination changed the crystallographic parameter of MSW-O. MSW-O's crystalline size and volume were reduced after calcination, resulting in higher surface area-to-volume ratios, as summarized in **Table 5.A.3.** The small grain size of calcined MSW-T is expected to have higher surface activity and dissolution to elicit superoxide-mediated antibacterial and anti-hemorrhagic activity.

Table 5.A.3 Structural and crystallographic parameters of extracted and calcined marine shell waste.

Sample	**a**	**c**	**c/a**	**Average crystalline size (nm)**	**Positional Parameters (u)**	**Bond length (d)**	**Volume (V)**
MSW-O	4.98	17.06	3.42	180	0.26	3.04	367.76
MSW-T	3.59	4.89	1.37	94.47	0.43	2.52	54.49

5.A.4. Study of Raman Spectroscopy

Raman analysis is a useful method for identifying oxide species. The **Figure. 5.A.3** displays the Raman spectra of synthesized and calcined MSW. It was observed that MSW-O spectra contained signals at 157, 286, 714, 1089 cm^{-1}, representing presence of calcite [12]. The wave number at 157 cm^{-1} corresponds raman spectra of pure $CaCO_3$. The Raman peaks at 714 and 1089 cm^{-1} were ascribed to the out-of-plane bending (v2) and stretching (v1) internal vibration modes of $CaCO_3$ respectively [13]. In MSW-T new peaks were found at 211 cm^{-1} and 356 cm^{-1} which can be attributed to oxide. Also, it was observed that the intensity of 356 cm^{-1} peak was gradually increased and peak at 286 cm^{-1} was decreased in the calcinated sample. The strong Raman signal in MSW-T likely results from its elevated ratio of Ca content. The raman peaks and assignment are given in **Table 5.A.4**.

Table 5.A.4 Raman spectra of Calcinated powder

S0	**S800**	**S1000**	**S1200**	**Assignment**
157	159	155	159	$CaCO_3$
		211	211	CaO
286	286	296	286	$Ca(OH)_2$
367	362	358	365	$Ca(OH)_2$
553		557	557	Calcite
714	720	707	704	$CaCO_3$(v2)
1089	1091	1087	1089	$CaCO_3$(v1)

5.A.5. X-Ray photoelectron spectroscopy analysis

XPS characterization of calcined MSW-T was performed to confirm the presence of calcium oxide. High resolution XPS spectra showed that MSW-T surface chemistry was consistent with the published values for calcium oxide based on binding energies as shown in the survey spectra, **Figure. 5.A.4** [14]. The curve parameters, such as the position of peak and the FHWM of each element were used for curve fitting. Curve fitting was carried out for C-1s, Ca-2p, Cl-2p, Mg-1s, Na-1s, O-1s and Sr-3d spectra set and are presented in the same figure.

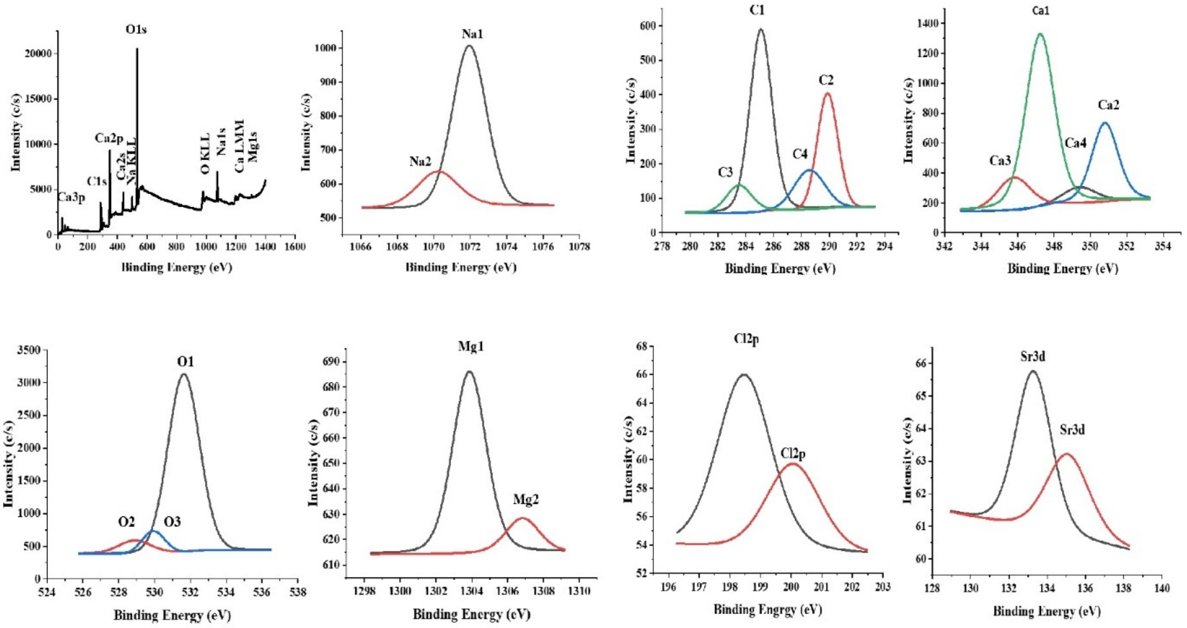

Figure 5.A.4 X- ray photo- electron- spectroscopy (XPS) of marine shell waster extracted and calcined at 1200°C powder (MSW- T) represented by survey spectra of MSW- T powder material and typical curve fitting conducted for Na1s, C1s, Ca2p, O1s, Mg1s, Cl2p, Sr. 3d high resolution XPS spectrum

XPS analysis of the C 1s peak revealed four distinct chemical states of carbon on the sample surface. The spectrum was deconvoluted into components at binding energies of 283.52, 285.09, 288.59, and 289.88 eV. These peaks were attributed to carbon in alkyl chains, C-C and C-H bonds, O-C-O groups, and O-C=O groups, respectively. The lowest binding energy component (283.52 eV) suggested the presence of reduced carbon species, while the highest (289.88 eV) indicated highly oxidized carbon, potentially associated with calcite near the surface [15]. Four Ca 2p peak doublets (i.e., Ca-1, Ca-2, Ca-3 and Ca-4) associated with Ca-incorporated chemical powder materials were defined and fitted to the spectra. It presented two characteristic peaks (Ca-1 and Ca-2) at approximately 345.8ev and 347.24 eV (near to 347.4eV) which correspond to Ca 2p3/2 (Ca in the form of $CaCO_3$) and Ca 2p1/2 ($Ca(OH)_2$), respectively [16]. Using the average of binding energy data from relevant studies, it was assumed that Ca-3 (B.E 349.4eV) and Ca-4 350.9 eV (near to 350.80eV), was present in the form of CaO. O-1s spectra of MSW-T show the presence of three Gaussian components[17]. Two split peaks of O1s at 528.9 eV and 531.69 eV represented asymmetric oxygen states consigned to the lattice oxygen and hydroxyl groups adsorbed on crystalline MSW-T powder from atmospheric moisture respectively [18]. They are attributed to the carbonate $(CO_3)^{2-}$ (B.E. 531.63 eV), to Ca-O (B.E. 529.94 eV), and to hydroxyl group on sample surface (B.E. 528.90 eV). The XPS analysis results, consistent with the XRD and FTIR findings, revealed a peak indicative of calcium oxide on the surface of MSW-T.

5.A.6. Evaluation of pH, Hydrodynamic diameter and Zeta potential

The effect of calcination temperature on S0 was investigated and the results for hydrodynamic particle size in Phosphate Buffer Solution (PBS) measured by Dynamic light scattering particle size distribution analysis (DLS). The hydrodynamic particle size of S0, S800, S1000, S1200 were 1.0095 ±0.287, 1.6673 ±0.189, 2.6553 ±0.62, 4.509 ±1.141 µm respectively. Due to calcination S0 sample exhibited crystal growth and as a result higher particle size obtained in S800, S1000, S1200 samples [19]. Higher hydrodynamic particle size indicates that when particles are dispersed in PBS then form an agglomeration and form clusters of greater size [20].

The variation of zeta potential of S0 with higher calcination temperature (S1200) had presented large value indicating -15.3 ±1.44 to -28.1 ±12.555 respectively. For particles calcinated at 800°C and 1000°C, the zeta potential was observed to be -16.8333 ±1.636 and -22.7367 ±1.614. Higher zeta potential indicating their greater stability in aqueous solutions suggests that the microparticles repelled each other and affected the adsorption or interaction of polar or nonpolar reacting substance depending upon the net surface charges suspended on the surface of the powder sample. A high zeta potential (positive/negative) have the tendency of adsorption rather than agglomeration instantly shows higher ionic concentration (Ca^{++} and HCO_3^-) of $CaCO_3$ in PBS [21], [22], [23]. The effect of calcination temperature on pH, Hydrodynamic Diameter, zeta potential and electrophoric mobility of all samples are shown in the **Table.5.A.5**.

Table 5.A.5 The effect of calcination temperature on pH, Hydrodynamic Diameter, zeta potential and electrophoric mobility of marine shell waste.

Sample	pH	Average pH	Hydrodynamic Diameter(µm)	Average Hydrodynamic Diameter (µm)	Zeta potential	Average Zeta potential	Electrophoretic mobility	Average
S0	9.12	9.12±	0.9886	1.0095	-14.6	-15.3	-1.14	-1.193
	9.18	0.138	0.897	±0.287	-15.5	±1.44	-1.21	±0.109
	9.06		1.143		-15.8		-1.23	
S800	10.76	10.58±	1.584	1.6673 ±0.189	-17.6	-16.833	-1.32	-1.283
	10.52	0.366	1.748		-16.2	±1.636	-1.23	±0.109
	10.46		1.67		-16.7		-1.3	
S1000	11.59	11.557	2.964	2.6553	-22.03	-22.736	-1.71	-1.766
	11.80	±0.60	2.471	±0.62	-22.75	±1.614	-1.77	±0.127
	11.28		2.531		-23.43		-1.82	
S1200	12.51	12.39±	4.498	4.509 ±1.141	-24.1	-28.1	-2.01	-2.186
	12.21	0.371	4.02		-25.9	±12.555	-2.67	±0.977
	12.46		5.009		-34.3		-1.88	

5.A.7. Antibacterial evaluation

Figure. 5.A.5 presents digital photographs of S0, S800, S1000, S1200 showing zones of inhibition against *Staphylococcus. Aureus* contained in a culture plate. Both the S0 and heat-treated powder at 800°C had less zone of inhibition. However, a large zone of inhibition surrounded the thermally treated powder at 1000 and 1200 °C, indicating that S1200 had an excellent antimicrobial activity at the highest treatment temperature showed in **Table. 5.A.6.** Therefore, 1200 °C was chosen as a treatment temperature for powder extracted from oyster shell in preparing bio composites in this study. There was no significant zone of inhibition shown against gram negative bacteria *Pseudomonas. Aeruginosa*.

Table 5.A.6 Zone of inhibition against *Staphylococcus. Aureus* of extracted and calcined marine shell waste.

Sample	Zone of Inhibition (ZOI)	Average (mm)
S0	10.75, 18.848, 15.2, 21.736	16.63±4.111
S800	14.288, 13.528, 19.76, 21.584	17.29±3.45
S1000	16.72, 18.392, 20.672, 16.112	17.974±1.76
S1200	22.496, 15.808, 13.984, 22.648	18.734±3.89

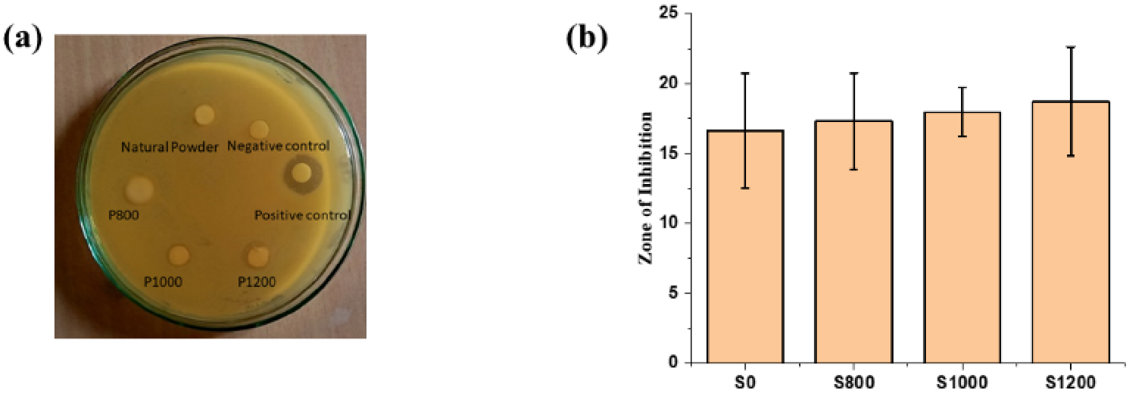

Figure 5.A.5 Antibacterial activity and zone of inhibition of extracted and calcined marine shell waste against *Staphylococcus Aureus*.

5.A.8. In-vitro blood coagulation study

Whole blood was taken from New Zealand white rabbits (*Oryctologus Cuniculus*) in collection tube coated with sodium citrate. 1.5ml blood was collected and 0.25M $CaCl_2$ was mixed to recalcification of blood. 5mg of different powder sample (S0, S800, S1000, S1200) was added to 670µl of rabbit blood and control was taken without powder material. Clotting time (CT) was determined by inversion of tube in every 30 sec and time point which no blood flow was considered as final clotting time for powdered material.

Figure. 5.A.6 shows the visual representation of blood clotting with 5mg different calcined powder (S0, S800, S1000, S1200). Blood clotting S1200 powder demonstrated full clotting within 117 ± 4.8 s, followed by S1000 at 126 ± 7.2 s, S800 showing 130 ± 7.2 s and S0 exhibited at 164 ± 6.6 s with respect to 275 ± 4.2 s for without powder as a positive control represented in the **Table.5.A.7.** Compared with S0, all S800, S1000 and S1200 samples exhibited significant decrease in coagulation time. Calcium ion itself interacts with the platelet activation and aggregation with the simulation of the intrinsic and extrinsic clotting factor pathways.

Table 5.A.7 Clotting time of extracted and calcined marine shell waste.

Sample	Clotting Time
With out powder	275±4 s
5mg S0	164±6 s
5mg S800	130±3 s
5mg S1000	126±7 s
5mg S1200	117±4 s

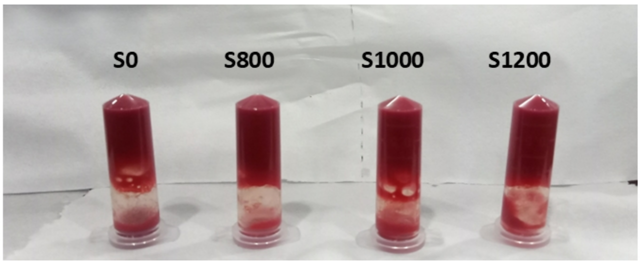

Figure 5.A. 6 The visual representation of blood clotting of extracted and calcined marine shell waste.

Major Observations

- Mixed pattern of calcite and $Ca(OH)_2$ assigned peak was observed in 1000℃ and 1200℃
- Temperature elevation phase changes occurred $CaCO_3$ = CaO +$Ca(OH)_2$. Due to calcination, calcium content was increased and carbon is almost disappeared from EDX peak intensities.
- From XRD crystallographic parameter of MSW changed. Decreased crystalline diameter (180 to 94.47 nm), Decreased bond length (3.04 to 2.52), Decreased volume (367.76 to 54.49).
- Strong raman signal in MSW-T results from its elevated ratio of Ca content.
- A large zone of inhibition surrounded the MSW-T(1200℃), indicate an excellent anti-microbial activity than others.
- Compared to all extracted and calcined MSW, MSW-T exhibited significant decrease in coagulation time.

5.B. Physical and mechanical characterization of different forms of haemostatic scaffold prepared by using MSW extract.

After comprehensive evaluation of air-dried, freeze-dried, and electrospun nanofiber formulations, the drug eluting nanofiber with calcined marine shell waste emerged as the superior haemostatic agent based on multiple performance criteria.

5.B.1. Preparation of electrospun nanofiber by changing parameter

Electrospinning represents an effective technique for creating high quality biopolymer nanofibers, including chitosan. These chitosan nanofibers exhibit biodegradability, biocompatibility, antimicrobial properties, and platelet aggregation making them valuable for haemorrage and wound healing applications. The electrospinning parameters such as solution concentration, applied electric voltage, syringe orifice diameter, temperature, humidity, and flow rate, play a crucial role in determining the nanofiber diameter, morphology, and mechanical properties. In this experiment we worked for smooth, beedless, efficient nanofiber fabrication. Chitosan molecules carry a positive charge in solution, especially under acidic condition that increases the surface tension. The high surface tension and viscosity of chitosan at moderate concentration can lead to a large number bead formation instead of continuous nanofiber. It has rigid structure and forms strong intramolecular hydrogen bonds that leads to less chain entanglement. Electrospinning pure chitosan does not produce nanofibers due to its high molecular weight, limited solubility, and elevated viscosity, which cause bead formation instead of continuous fibers. The strong hydrogen bonding and high viscosity prevent adequate chain entanglement and molecular movement. Blending chitosan with PVA overcomes these limitations by improving solution viscoelasticity, enabling the formation of uniform, bead-free nanofibers. To overcome these challenges, poly vinyl alcohol is added with chitosan to improve electrospinnability showed in **Table 5.B.1**. For this we formulated different ratio of PVA and chitosan polymer in trial-and-error method.

Table 5.B. 1 Electrospinning parameter and respective fiber diameter of different types of poly vinyl alcohol and chitosan formulation.

Sample	Material PVA:CS	Viscosity (CP)	Polymer concentration (g/100mL)	Distance (cm)	Flow rate (ml/hr)	Applied electric voltage (kV)	Temp (°C)	Fiber diameter (nm)
1	PVA:CS (100:0)	1557	12	10-12	1	16-18	27	100-364
2	PVA:CS (90:10)	1326	11	10-12	0.4-0.6	16-20	32	150±17

Sample	Material PVA:CS	Viscosity (CP)	Polymer concentration (g/100mL)	Distance (cm)	Flow rate (ml/hr)	Applied electric voltage (kV)	Temp (°C)	Fiber diameter (nm)
3	PVA:CS (80:20)	1056	10	10-12	0.4-0.6	16-20	32	147±12
4	PVA:CS (70:30)	906	9	10-12	0.7	18-24	37	163±34
5	PVA:CS (60:40)	812	8	10-12	0.5	20-27	38-40	Beeded 180±17
6	PVA:CS (50:50)	724	7	10-12	0.4	20-27	37-42	Beeded 286±63
7	PVA:CS (0:100)	243	2	10-12	0.4-1	20-30	37-42	Not produce
8	PVA:CS (80:20)+ 30mg/mL TXA	1068	10	10-12	0.4	18-20	32-34	247±12
9	PVA:CS (80:20)+ 30mg/mL E	1084	10	10-12	0.4	18-20	32-34	250±17
10	PVA:CS (80:20)+ 30mg/ml txa+30mg/ml E	1012	9.3	10-12	0.4	18-20	32-34	347±22
11	PVA:CS (80:20)+ 30mg/ml txa+30mg/ml E+5mg/ml MSW-T	658	11.7	10-12	0.5	22-27	37-41	152±6

When PVA/CS/Drug/MSW-T fibers were produced, both pore size and fiber diameter showed slight decreases. Pore size refers to the empty spaces that exist between adjacent fibers. During fabrication of MSW-T containing fibers, aggregation occurred at the needle tip. Outlet diameter of needle slightly was decreased by aggregation. The fibre with smaller diameter has larger density and small pore size[24]

5.B.2. Study of vibrational spectroscopy

Figure. 5.B.1(a) depicts the light brown and reddish colours of the air dried PVA/CS (AD1) and PVA/CS/MSW-O (AD2) films, respectively, to the unaided eye. Calcium crosslinked with hydroxyl group of CS and PVA produced an acetal reaction forming a molecule of H-O-H and a novel polymer with an O-C-O bond. The reaction is homogeneous; therefore, chitosan is uniformly distributed in the composite film to prevent high $CaCO_3$ agglomeration. Raman spectroscopy of the AD1 and AD2 films are shown in the **Figure.5.B.1(b)**. In the spectra of PVA powder, the stretching vibration of the C-O group had a peak at 1082 cm^{-1} and the C-C group had a stretching band of 860 cm^{-1}. The spectra of CS exhibited a resonance band at 1114 cm^{-1} representing the saccharide structure and at 1085 cm^{-1} showed the asymmetric stretching vibration of C-O-C glycosidic linkage. The peak of the O-H bond is lower due to involved in the crosslinking reaction. We also observed the Raman peaks of OS powder at 712 and 1090 cm^{-1} assigned respectively to the out-of-plane bending (v2) and stretching (v1) internal vibration mode of $CaCO_3$ [25]. The Raman spectra of AD1 showed an absorption band of 787, 854, 1025, and 1083 cm^{-1} indicating the overlap between CS and PVA. Also, the AD2 film showed the inclusion of OS powder in PVA/CS film.

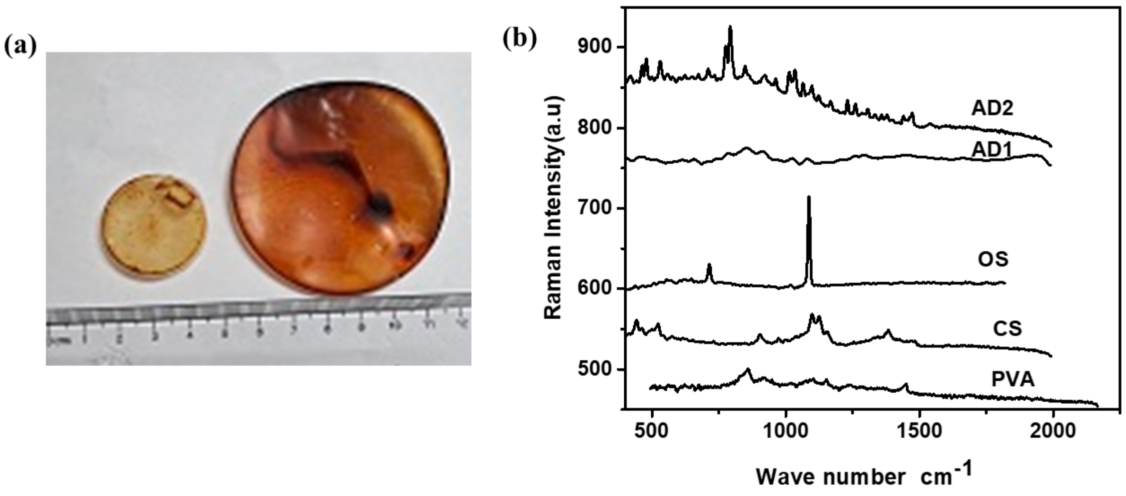

Figure 5.B. 1 Study of air dried film by a. Pictorial image b. Raman spectrum.

The physical properties of the freeze dried PVA-chitosan (PVA/CS) and PVA-chitosan-OS (PVA/CS/MSW-O) sponges represented in **Table 5.B.2.**

Table 5.B. 2 Physical properties of biogenic marine shell waste derived calcium carbonate – chitosan sponges

Samples	Colour	Nature	Density(g/cc)	Porosity (%)	Pore size
PVA/CS	Yellow	Brittle	0.1517	39±8	12.43±1.7
PVA/CS/MSW-O	Brownish	Spongy	0.1245	44±11	5.67±1.3

Sponge PVA/CS exhibited larger pore sizes but the overall pore density was lower. Consequently, the void fraction was reduced, resulting in a higher density compared to the PVA/CS/MSW-O sponge, which was characterized by greater number of smaller pores, increased porosity and lower density. Further, PVA/CS/MSW-O were found to be brownish in colour than PVA/CS, which may be due to Maillard-type self-reaction in chitosan in the presence of calcium ions. This can be prevented by greater pH control towards processing or use of functionalized chitosan preventing access of free amino groups to reducing sugar groups.

Fourier Transform Infrared Spectroscopy (FTIR) analysis confirmed the successful incorporation of $CaCO_3$ into the PVA/CS freeze-dried sponge (**Figure.5.B.2**). The FTIR spectra of the PVA/CS sponge revealed characteristic peaks related to its saccharide structure at 1085 cm^{-1} (C-O deformation vibration), amide bands at 1647, 1543, and 1315 cm^{-1} (corresponding to Amide I, II, and III, respectively), a methylene group peak at 2947 cm^{-1}, and a broad hydroxyl group peak at 3345 cm^{-1}. The weaker amide I, II and III vibrations may be contributed by the N–H bending (in-plane), C–N or C-C stretching of the residual acetamide ($-NHCOCH_3-$) groups from the acetylated parent compound, chitin. The PVA/CS/MSW-O sponge retained all these characteristic peaks with slight diffraction and exhibited additional peaks indicative of $CaCO_3$ incorporation. Peaks related to Ca-O in-plane bending (v1) was observed at 709 cm^{-1}, C-O out-plane bending (v2) at 840 cm^{-1}, and asymmetric stretching vibration (v3) of CO_3^{-2} in calcite at 1416 cm^{-1}. [26] These results comprehensively confirm the presence of both PVA/CS components and the successful integration of $CaCO_3$ in the composite sponge, validating the intended composition of the freeze-dried hemostatic material.

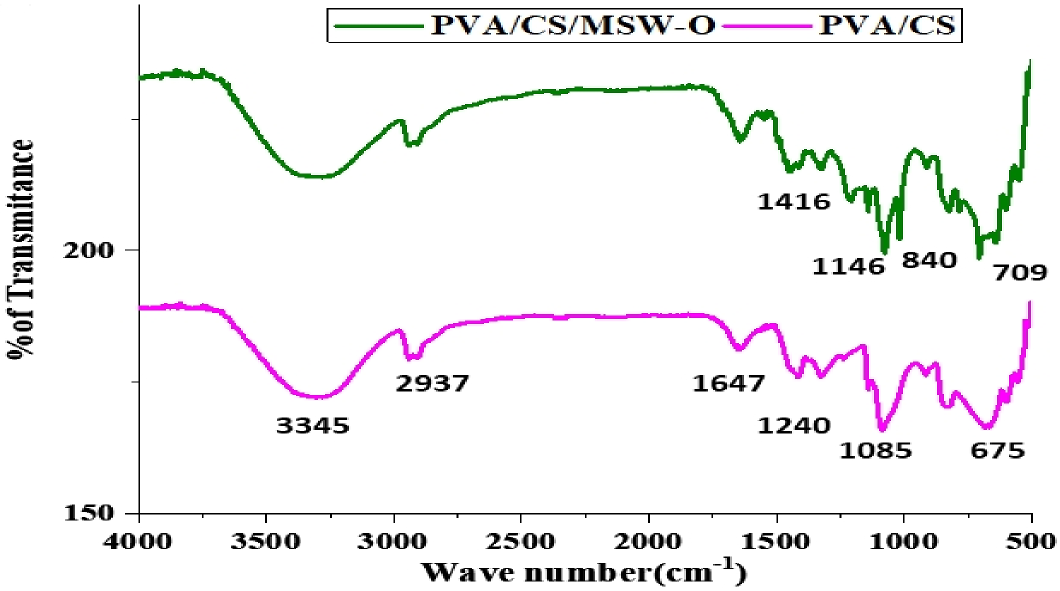

Figure 5.B. 2 FTIR spectra of marine shell waste derived powder incorporated in freeze dried hemostatic sponge.

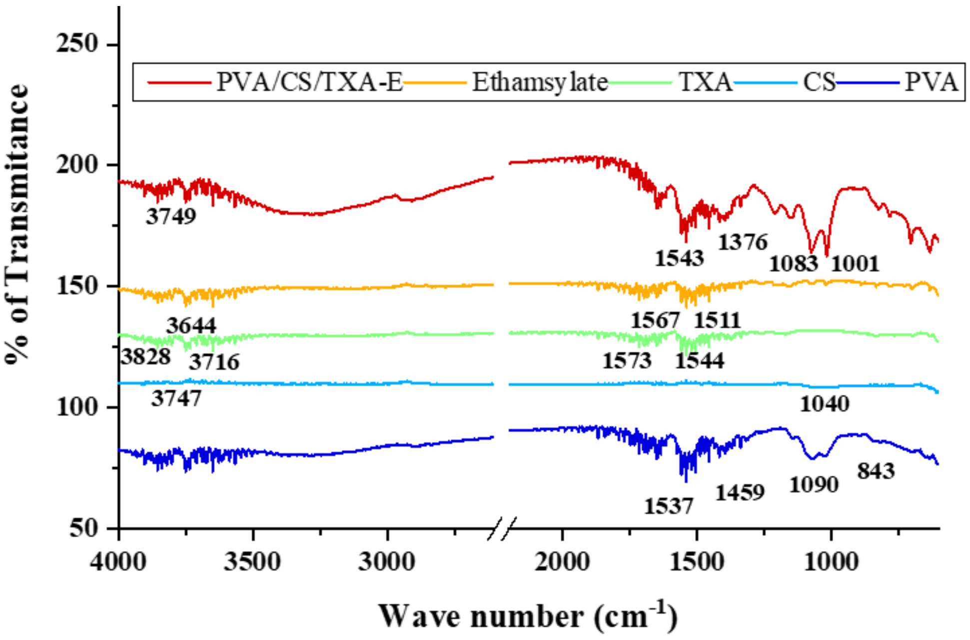

Figure 5.B. 3 FTIR spectra of drug loaded electrospun nanofiber.

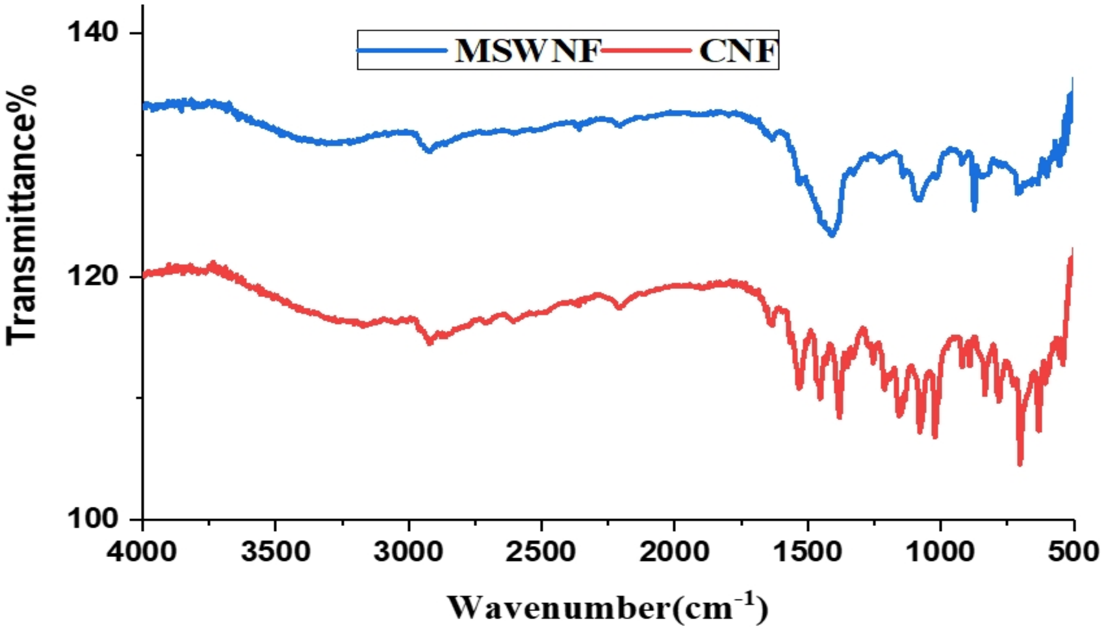

Figure 5.B. 4 FTIR spectra of calcined marine shell waste with drug loaded nanofiber.

Fourier Transform Infrared Spectroscopy (FTIR) analysis confirmed the successful incorporation of active pharmaceutical ingredients (Tranexamic Acid and Ethamsylate) into PVA/CS nanocomposite fibers and MSW-T particles into MSWNF nanofibers, as demonstrated in **Figure 5.B.3 & 5.B.4**. The pure chitosan (CS) spectrum exhibited characteristic peaks associated with its saccharide structure at 888 and 1019 cm^{-1} [27], while strong absorption peaks at 1374, 1542, and 1654 cm^{-1} corresponded to the amide bands (amide III, amide II, and amide I respectively), along with a broad hydroxyl peak at 3317 cm^{-1} and C-H stretching vibrations at 2868 cm^{-1}. The PVA spectrum revealed characteristic vibrations of hydroxyl and acetate groups, specifically showing a broad O-H stretching band at 3296 cm^{-1}, C-H asymmetric stretching of alkyl groups at 2923 cm^{-1}, and distinctive bands at 1084 and 1533 cm^{-1} attributed to acetyl groups and symmetric deformation of the $–NH_3^+$ group. The TXA spectrum displayed characteristic peaks at 1450 cm^{-1} (methylene), 1532 cm^{-1} (carbonyl), and 2858 cm^{-1} (C-H stretching) [28], while ethamsylate showed characteristic peaks at 3750 cm^{-1} (aromatic O-H) and 1022 cm^{-1} (sulfonyl). In the dual drug-loaded PVA/CS/TXA-E (CNF) nanofibers, the presence of both drugs was confirmed by their respective characteristic peaks (ethamsylate: 1147 cm^{-1}, 3742 cm^{-1}; TXA: 1398 cm^{-1}, 2939 cm^{-1}), along with polymer matrix peaks (827, 1076, 1536, 1644 cm^{-1}, and 3300 cm^{-1}) [29]. The absence of new peaks indicating ester, amide, N-glucosamine, or sulfonamide formation, coupled with peak broadening at specific wavelengths, suggested that the drugs were incorporated through hydrogen bonding interactions rather than chemical bond formation. Furthermore, MSWNF nanofibers showed characteristic peaks for Ca-O and -OH functional groups, corresponding to CaO and $Ca(OH)_2$, with C=O peaks at 2864 and 1469 cm^{-1}, and -OH peaks at 841 and 3638 cm^{-1}, which were notably absent in CNF, confirming successful incorporation of MSW-T particles into the MSWNF nanofiber structure [30].

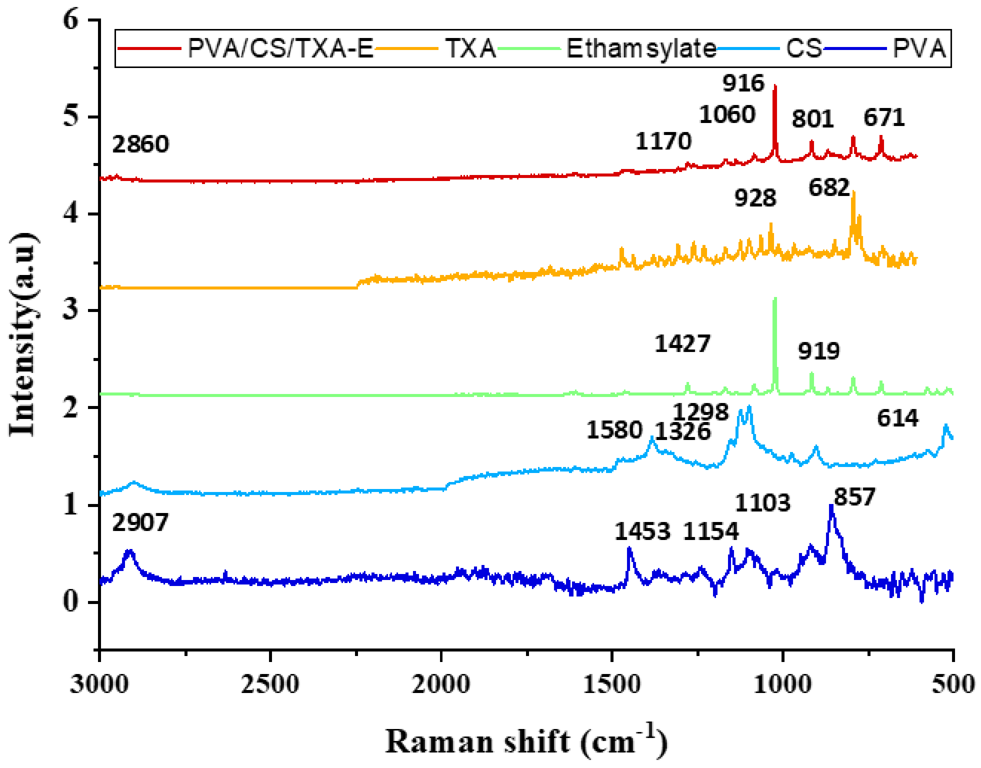

Figure 5.B. 5 Raman spectra of drug loaded nanofiber.

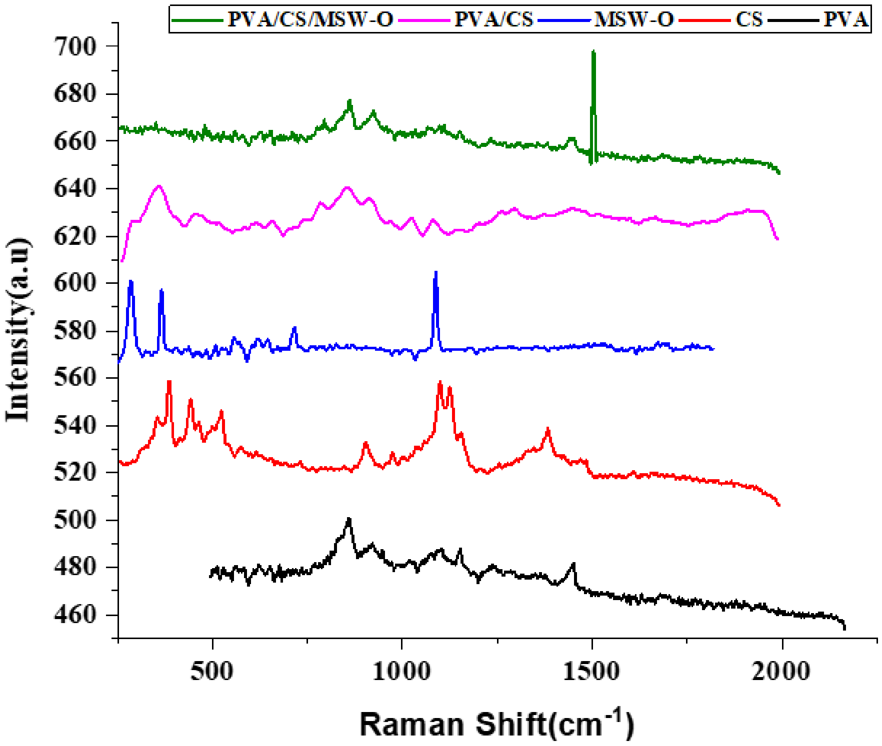

Figure 5.B. 6 Raman spectra of freeze dried sponge.

Raman spectroscopic analysis provided complementary evidence for the successful incorporation of components in PVA/CS/TXA-E and freeze-dried sponge showed in **figure.5.B.5 and 5.B.6**. The PVA powder exhibited characteristic peaks at 1082 cm^{-1} (C-O stretching) and 860 cm^{-1} (C-C stretching bands), while chitosan showed distinctive resonance bands at 1114 cm^{-1} (saccharide structure) and 1085 cm^{-1} (asymmetric stretching of C-O-C glycosidic linkage). The successful incorporation of drugs was confirmed through specific peaks for TXA (1022, 1169, 1469 cm^{-1}) and Ethamsylate (873, 916, 1082, 1155 cm^{-1}). In the case of OS-containing composites, characteristic peaks at 712 and 1090 cm^{-1} were observed, corresponding to the out-of-plane bending (v2) and stretching (v1) internal vibration modes of $CaCO_3$ [25]. The freeze-dried PVA/CS (FD1) film showed characteristic absorption bands at 787, 854, 1025, and 1083 cm^{-1}, indicating successful blending of CS and PVA, while the PVA/CS/MSW-O (FD2) film spectrum further confirmed the incorporation of OS powder through the presence of distinctive $CaCO_3$ peaks alongside the polymer matrix bands. The reduced intensity of O-H bond peaks suggested their involvement in crosslinking reactions.

5.B.3 Mechanical characterization

The mechanical properties of various nanocomposite systems demonstrated significant variations based on their composition and structural characteristics. A suitable material for hemostasis is produced by combining reduced strength and a higher Young's modulus in nanofibers, making them flexible enough to contour wounds but rigid enough for structure. This balance minimizes bleeding by providing a scaffold for clot formation while allowing natural healing. In the air-dried films containing OS (AD2) exhibited superior mechanical performance in **figure.5.B.7** with an ultimate tensile strength (UTS) of 11.6 MPa compared to AD1 (6.4 MPa), and notably higher elongation at break (180% versus 40%). This enhanced elasticity and strength in AD2 was attributed to the incorporation of calcium ions into the PVA/CS matrix, creating a more compact and fracture-resistant structure. This result corroborated with the findings of other researchers. Chitosan exhibits high wetting ability but poor mechanical properties and hence to improve the mechanical properties of the film, CS was mixed with PVA which was a water-soluble polymer with good mechanical properties and biocompatibility [31].

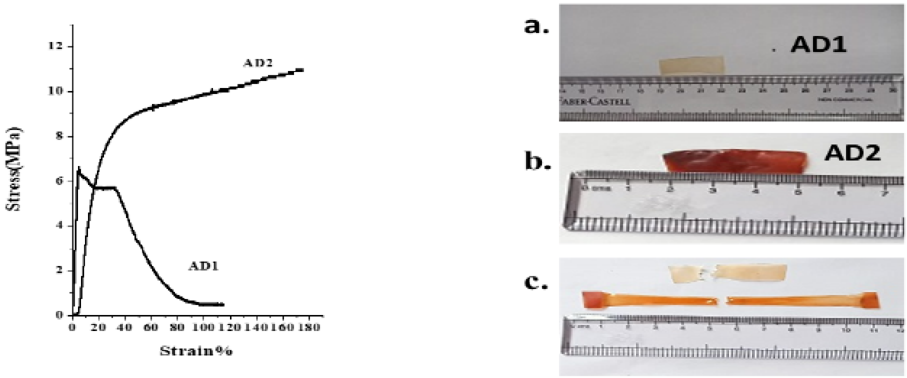

Figure 5.B. 7 Stress-strain graph of air dried film [image acquisition before (a&b) and after (c) measurement]

The PVA/CS nanofibers showed composition-dependent mechanical behaviours in **figure 5.B.8**, where increased chitosan content led to higher brittleness. PC11 mats demonstrated UTS and elongation at break values of 4.2 MPa and 13.5% respectively, while PC32 nanofibers showed 3.78 MPa and 25%. The incorporation of TXA modified these properties, yielding values of 5.2 MPa and 11.4% for PC11T, and 4.64 MPa and 28% for PC32T nanofibers, with an 11% increase in UTS and 48% decrease in elongation upon higher CS content. Literature also suggests that tensile strength (4.2 to 6.5 MPa) increases and elongation of break decreases when CS incorporation increases [32]. The strength also corresponds to the tissue sealants used for bleeding control [33].

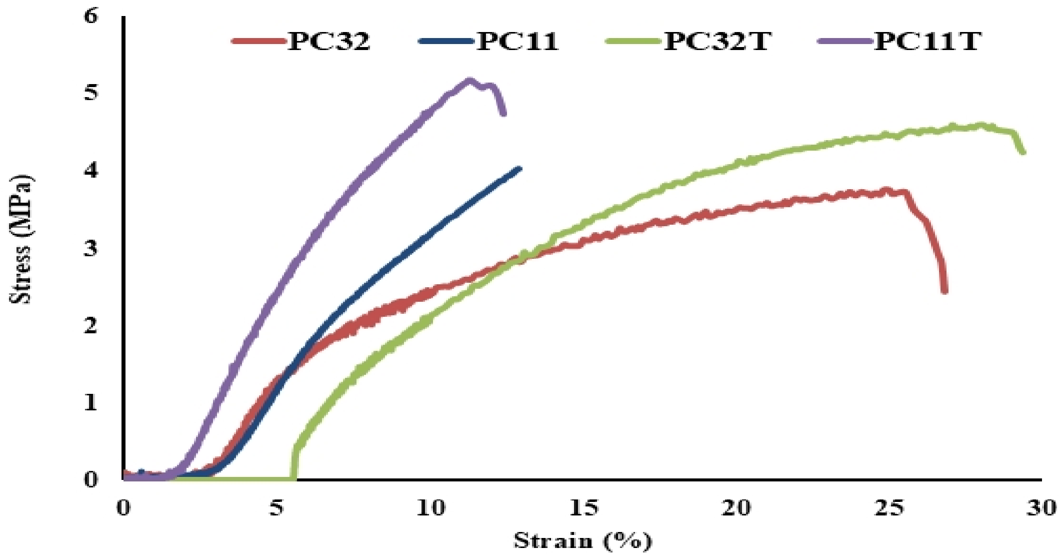

Figure 5.B. 8 Tensile stress-strain behaviour of tranexamic acid incorporated nanofiber with different ratio of polymer composition (PVA/CS:1/1) and (PVA/CS:3/2).

In the case of MSWNF, compared to CNF (UTS: 5.14 MPa, elongation: 11.54%, Young's modulus: 44.54 MPa), it showed an 18% increase in strength and 46% decrease in strain, achieving values of 6.11 MPa, 6.14%, and 99.51 MPa for ultimate stress, elongation at break, and Young's modulus respectively in the **figure 5.B.9(a)**. This enhancement was attributed to calcium oxide incorporation and improved inter-fiber bonding. This aligns with Sambudi et al.'s findings that calcium carbonate inclusion stiffened PVA/CS fiber networks [34]. However, the smooth nature of MSWNF indicated that CaO polymer matrix formed a homogenious composite. Mechanical analysis showed that MSWNF possesses higher stiffness and lower swelling than CNF due to Ca^{2+}- mediated ionic crosslinking with chitosan’s amino groups. While this increases rigidity and dimensional stability, it also results in reduced elongation at break.

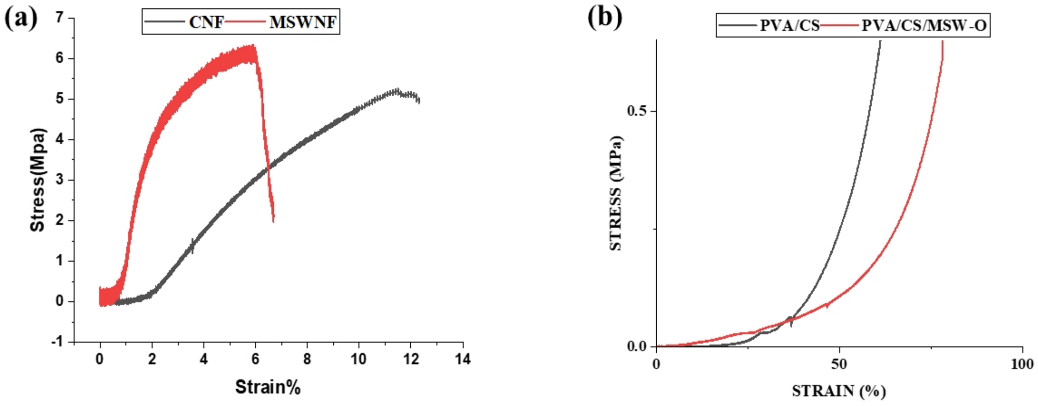

Figure 5.B. 9 Mechanical behaviours characterization by (a) stress-strain curve of marine shell waste nanofiber (b) compression stress-strain of freeze dried sponge.

The compression stress-strain characteristics (**figure. 5.B.9b**) revealed nonlinear behaviour in both PVA/CS and PVA/CS/MSW-O sponges, with initial elastic regions followed by sharp stress increases at higher strains (50% for PVA/CS and 75% for PVA/CS/MSW-O). PVA/CS/MSW-O demonstrated greater initial deformation capacity and enhanced energy absorption due to its higher porosity and softer initial structure, while PVA/CS showed earlier strain hardening due to its denser structure. These mechanical properties align well with the requirements for hemostatic applications, providing suitable strength and flexibility for wound contouring while maintaining structural integrity for effective clot formation.

PVA/CS/MSW-O exhibited greater initial deformation than PVA/CS before stiffening, while PVA/CS demonstrated earlier strain hardening. Compared to PVA/CS, PVA/CS/MSW-O underwent significant compression before densification. The onset of densification in the PVA/CS sponge showed less total deformation capacity, likely due to its denser structure. In contrast, the PVA/CS/MSW-O sponge possessed greater initial porosity with more void space. Its softer initial structure made it more flexible, resulting in lower initial stiffness and enhanced energy absorption capacity. A moderate range of mechanical strengths was previously seen in a number of chitosan composites, such as chitosan-hydroxyapatite-collagen scaffolds (0.06 MPa), alginate/chitosan sponges (0.0043 MPa), and chitosan-collagen sponges (0.013 MPa) [35], [36]. In order to stop blood loss quickly, Patil et al. also found that xerogel composites comprising calcium and silica nanoparticles in chitosan and gelatine have a compressive strength of 2.5 MPa with 89% strain at break [37].

5.B.4 Swelling and degradation study

The swelling and degradation characteristics of various nanocomposite systems demonstrated composition-dependent behaviour crucial for hemostatic applications. In the air dried flim, AD1 showed maximum swelling of 94% after 20 min, while AD2 exhibited higher swelling (107%) after 60 min, with AD1 showing faster degradation compared to AD2. Swelling and degradation results are demonstrated in **figure 5.B.10**. This difference was attributed to calcium's crosslinking effect in AD2's PVA/CS matrix, which restricted faster matrix breakdown.

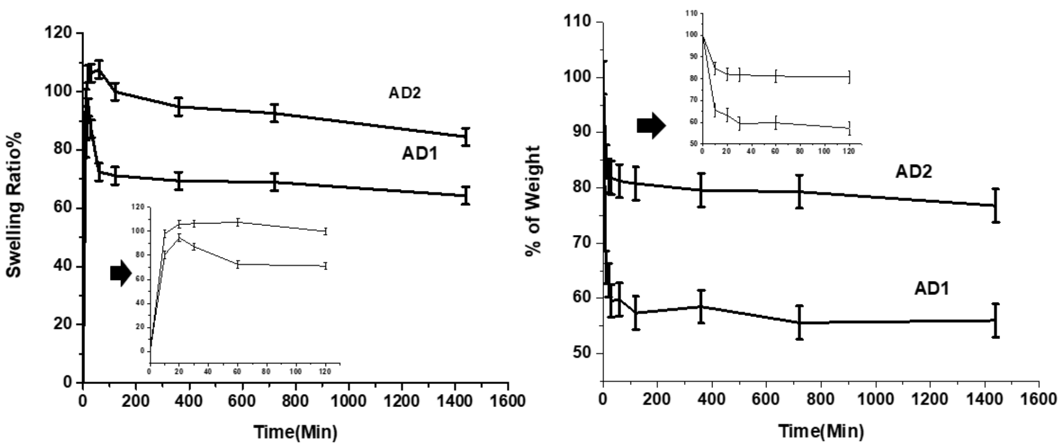

Figure 5.B. 10 Swelling and Degradation study of air dried film.

The PVA/CS sponges demonstrated in **figure 5.B.11** significantly higher swelling capacities, with PVA/CS and PVA/CS/MSW-O reaching 293 ± 5% and 257 ± 5% respectively after 20 minutes, followed by stabilized degradation with remaining mass percentages of 80.76% and 78.57% after 24 h. PVA/CS demonstrated a higher swelling capability compared to PVA/CS/MSW-O. Among the two formulations, PVA/CS initially absorbed phosphate buffer solution (PBS) solution more rapidly, while PVA/CS/MSW-O showed reduced swelling capability due to calcium crosslinking. Swelling is a critical parameter in hemostasis, as it fast absorbs blood and exudates, and subsequently provides a humid environment conducive to cell growth and tissue formation.

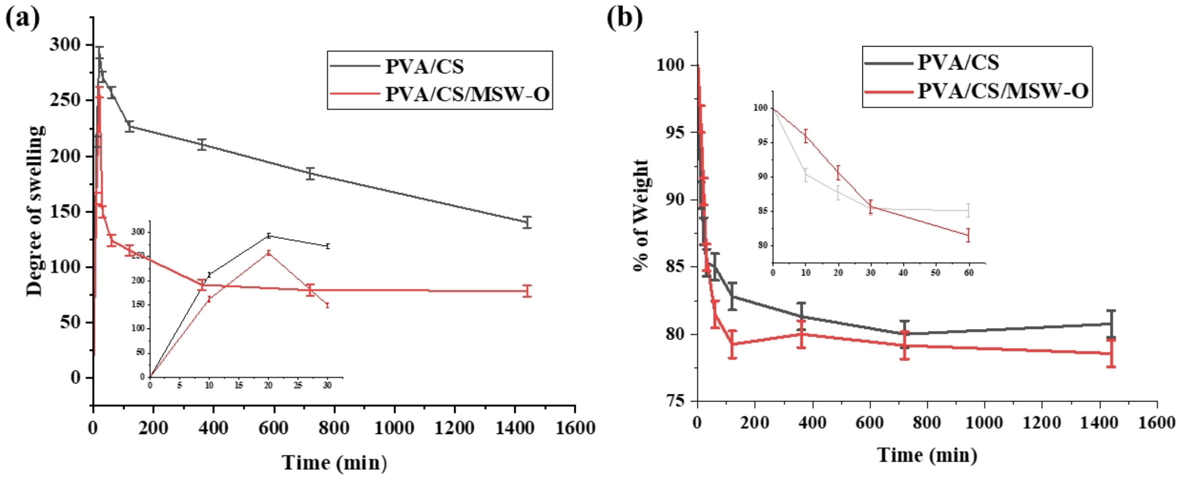

Figure 5.B. 11 Physical characterization of freeze dried sponge by (a) swelling capacity and (b) degradation rate

In the nanofiber systems, PVA/CS matrices loaded with TXA showed varying swelling behaviours, with PC32 exhibiting a swelling ratio of 433% compared to PC11's 410%, attributed to the varying hydrophilic PVA content in the **figure 5.B.12a**. The dual drug-loaded

PVA/CS nanofibers demonstrated rapid swelling in phosphate buffer-saline, achieving saturation within 10 minutes with approximately 500% water absorption while maintaining structural integrity. TXA and E loaded PVA/CS nanofibers showed rapid swelling in phosphate buffer-saline and a saturation swelling ratio of 459% for PVA/CS/TXA, 409% for PVA/CS/TXA-E, 393% for PVA/CS/E, and 366% for PVA/CS was achieved after 10 min of incubation. All the matrices underwent around 500 % water absorption without any structural disintegration. Except, E-loaded nanofibers which showed the least swelling degree was not significantly different amongst the other groups (P value > 0.001). An appreciable swelling is expected from hydrophilic hemostatic patches so that blood components are absorbed onto the surface of the matrix and activate the coagulation cascade. PVA-chitosan based matrices applied for hemostasis applications usually have swelling in the range of 400-800% for adequate performance [38], [39]. The degradation profiles after 25 days showed **figure 5.B.12b** varying mass losses: PVA/CS (47 ± 5%), PVA/CS/TXA (47 ± 4%), PVA/CS/E (69 ± 5%), and PVA/CS/TXA-E (58 ± 3%). Previous literature studies have attempted to optimize degradation rate of hemostat nanofibers to these levels[40] [41]. A balance between degradation rate and efficiency is crucial for topical hemostatic scaffold. Overly rapid degradation raises the possibility of rebleeding, while impaired degradation can interfere with organ regeneration and prolong chronic inflammation phase [42]. It can be suggested that the PVA/CS/TXA-E nanofibers possess the nanofiber diameter, hydrophilicity, morphology, swelling and degradation properties values close to the values reported for satisfactory performance by hemostatic biomaterial patches.

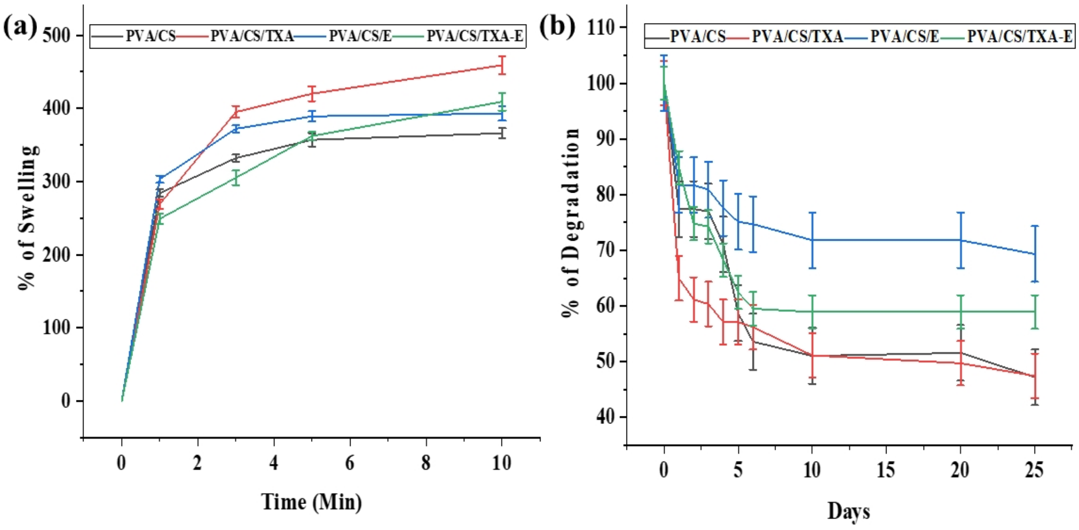

Figure 5.B. 12 Physical characterization of dual drug nanofiber by (a) swelling and (b) degradation study.

A hemostatic nanofiber must strike a balance between structural integrity and its response to blood exposure. Adding MSW-T to CNF nanofiber creates MSWNF, which reduces the hydrophilicity of the nanofiber membrane. This is crucial because hemostatic scaffolds that loosen instantly in the presence of blood or fluid would be ineffective and may flow away from the injured organ. MSWNF demonstrated moderate swelling compared to CNF, with CNF showing peak swelling of 350% after 10 minutes, decreasing to 300% after 1 hour, while MSWNF peaked at 300% after 20 minutes, declining to 220% after 1 hour in the **figure 5.B.13**. This controlled swelling in MSWNF was attributed to chemical interactions between chitosan amine groups, PVA hydroxyl groups, and Ca^{2+} ions from MSW-T. In PBS medium containing monovalent ions like Na^{+}, MSWNF undergoes an ion exchange process between Ca^{2+} and Na^{+} ions, potentially providing a mechanism for controlled nanofiber degradation [43]. These properties align well with hemostatic requirements, where balanced swelling facilitates blood component absorption and coagulation cascade activation, while controlled degradation prevents rebleeding while supporting tissue regeneration.

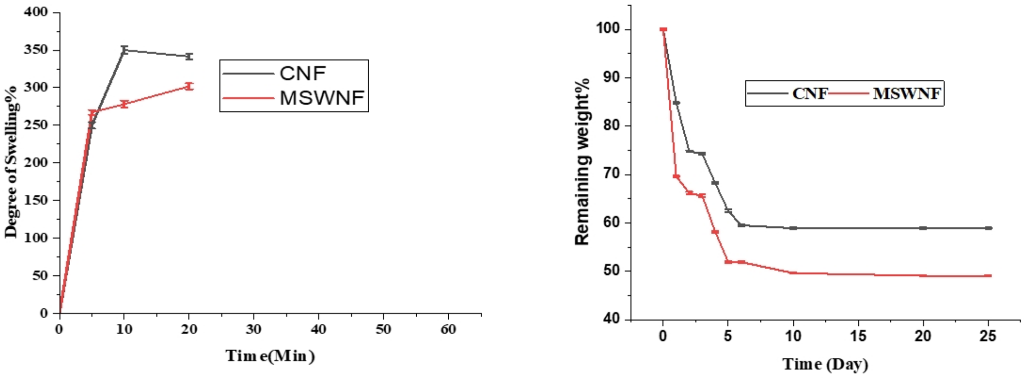

Figure 5.B. 13 Physical characterization of marine shell waste nanofiber by swelling and remaining weight study.

Table 5.B. 3 Swelling contact angle of Hemostatic Scaffold

Physical Parameter	Air Dried		Freeze Dried		Electrospin nanofiber				
	PVA/CS (AD1)	**PVA/CS/MWW-O (AD2)**	**PVA/CS (FD1)**	**PVA/CS/MSW-O (FD2)**	**PVA/CS**	**PVA/CS/TXA**	**PVA/CS/E**	**PVA/CS/TXA-E**	**PVA/CS/TXA-E/MSW-T (MSWNF)**
Swelling	94±3	107±7	257±5	293±5	366±12	459±7	409±12	393±10	300±25
Contact angle	49	60	------	-------	36	36	38	32	37

5.B.5. Contact angle measurement

The contact angle measurements revealed composition-dependent surface wettability across various nanocomposite systems depicted in the **figure 5.B.14**. Surface wettability is crucial for blood coagulation in biomaterials. In the air dried scaffold, AD1 and AD2 films exhibited contact angles of 49.54 ± 0.92° and 59.64 ± 7.71° respectively, with AD1 showing greater hydrophilic behavior. The increased contact angle compared to pure PVA (45.5° ± 1.1°) [44] was attributed to chitosan incorporation, while the higher value in AD2 resulted from calcium carbonate loading. In the drug-loaded nanofiber systems, PVA/CS membranes showed a baseline contact angle of 36 ± 2°. The incorporation of individual drugs maintained similar hydrophilicity, with PVA/CS/TXA and PVA/CS/E showing contact angles of 36 ± 2° and 38 ± 1° respectively. However, the dual drug-loaded system (PVA/CS/TXA-E) demonstrated enhanced hydrophilicity with a significantly reduced contact angle of 32 ± 1° ($P < 0.05$), attributed to the presence of two hydrophilic drugs. In the MSW-T incorporated systems, MSWNF nanofibers showed a slightly increased water contact angle (37 ± 2°) compared to CNF nanofibers (32 ± 1°), maintaining moderate hydrophilicity due to strong hydrogen bonding between PVA and chitosan. These intermediate contact angles (32-60°) are particularly advantageous for hemostatic applications, as they strike a balance between preventing excessive blood loss (unlike superhydrophobic surfaces) while promoting platelet attachment and clot formation (unlike super-hydrophilic matrices with 0° contact angles). The moderate hydrophilicity, combined with nanoporous architecture, supports optimal hemostatic performance through controlled blood absorption and cell adhesion. Both hydrophilic and hydrophobic nanofibers have been explored in hemorrhage control, wherein superhydrophobic surfaces like carbon nanotubes are used to prevent noticeable blood loss but they do not trigger clotting [45]. Contrarily, super hydrophilic matrices like the poly(vinyl pyrrolidone)-calcium chloride-thrombin based matrices with water contact angle of 0° have also been used but they result in appreciable blood loss especially in heavy trauma. The PVA/CS/TXA-E have a contact angle of 32, indicating an intermittent hydrophilicity, which combined with the nanoporous architecture can prevent blood loss and at the same time promote attachment of platelets to form the blood clot. A study with hyperbranched polymers has also shown higher hemostat performance with contact angles in the range of 40º [46][47], [48] [49]. In PVA/CS/TXA-E, incorporation of PVA not only aids in electrospinning process of the crystalline chitosan but also enhances the hydrophilicity required for water absorption. MSWNF (37 ± 2°) nanofibers showed an increased water contact angle compared to CNF nanofibers (32 ± 1°). Both nanofibers exhibited hydrophilic properties, with MSWNF exhibiting a more moderate hydrophobicity due to the incorporation of MSW-T powder, which formed strong hydrogen bonds between PVA and chitosan.

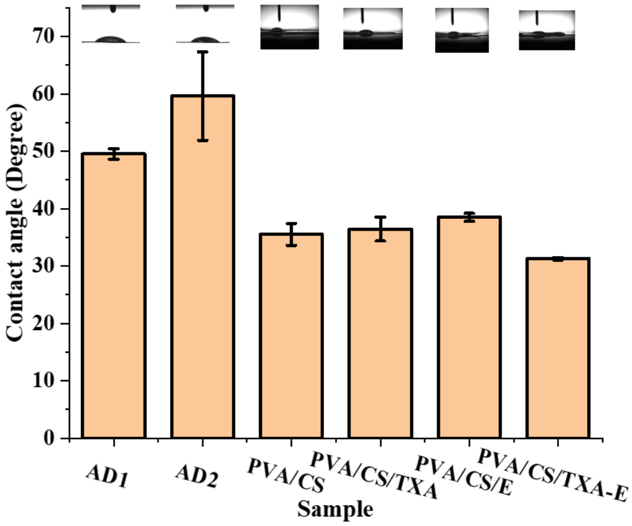

Figure 5.B. 14 Contact angle study of air dried film and electrospun nanofiber.

5.B.6 Scanning electron microscopy study

Scanning electron microscopy (SEM) revealed distinct morphological characteristics across various nanocomposite systems. The PVA/CS and PVA/CS/MSW-O sponges exhibited rough and porous network morphology, with PVA/CS showing larger pore sizes compared to PVA/CS/MSW-O as showed in the **figure 5.B.15**. This may be due to a combination of gas evolution and partial dissolution as calcium carbonate comes in contact with acetic acid, thus acting as a physical template for increasing the pore structure [50]. This porous architecture was designed to facilitate fluid absorption, gas exchange, and blood platelet aggregation, supporting effective clot formation.

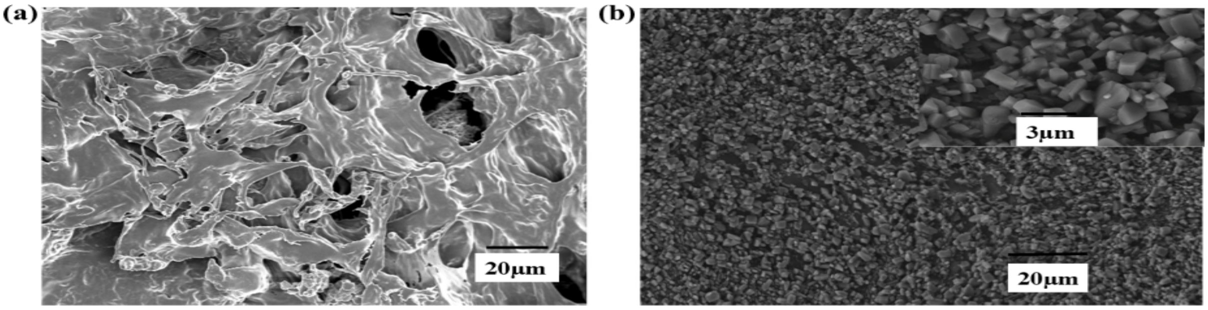

Figure 5.B. 15 SEM micrograph of freeze dried sponges (a) PVA/CS (b) PVA/CS/MSW-O

Figure 5.B.16(a–d) represents SEM micrographs of electrospun PVA-CS-TXA nanofibers. Uniform morphology was seen for both PVA/CS 3:2 and 1:1. After loading the drug, PC32T composition showed uniform beads-free morphology whereas some very small beaded structures could be observed for PC11T. Moreover, drug incorporation showed some flattening of the nanofiber membranes. This may be due to the hygroscopic nature of TXA. Average diameters of membranes were found to be 180, 150, 220 and 160 nm, respectively for PC32, PC11, PC32T and PC11T. Notably, the average diameters were found to decrease due to the addition of CS and found to increase due to addition of TXA. These results are consistent with the values reported in the literatures[51], [52].

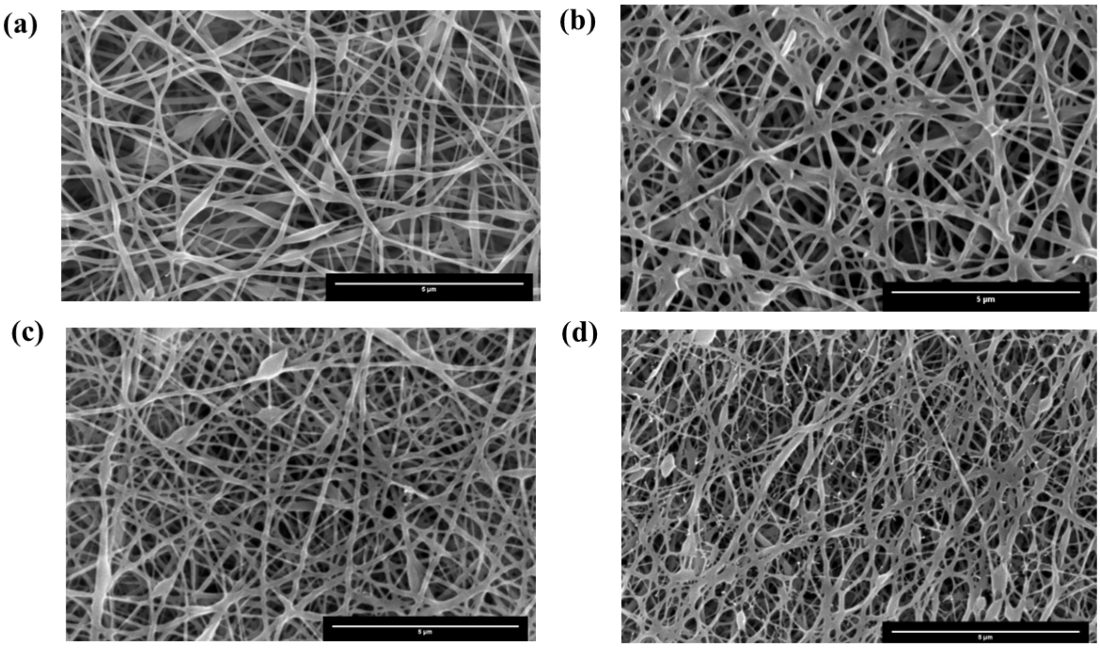

Figure 5.B. 16 SEM micrograph of different polymer composition electrospun nanofiber with tranexamic acid drug loaded (PC32, PC11, PC32T and PC11T)

In the drug-loaded nanofiber systems, the optimal polymer ratio for bead-free fiber formation was established at 20% CS and 80% PVA and showed in the **figure 5.B.17(a-d).** The pristine PVA/CS nanofibers demonstrated good uniformity with regular diameters of approximately 147 nm, while drug incorporation increased fiber diameters to around 400 nm (PVA/CS/E, PVA/CS/TXA, PVA/CS/TXA-E). Upon exposure to water and blood fluid, these nanofibers maintained their structural integrity while exhibiting flattening and thickening to dimensions of 10-15 µm. This fiber diameter range (300-400 nm) aligns with optimal parameters reported for platelet adhesion and water absorption in hemostatic applications [53]. Certain patented dressing composed of chitosan, kaolin and Pluronics^{TM} also employ nanofibers with diameters around or less than 500 nm[54].

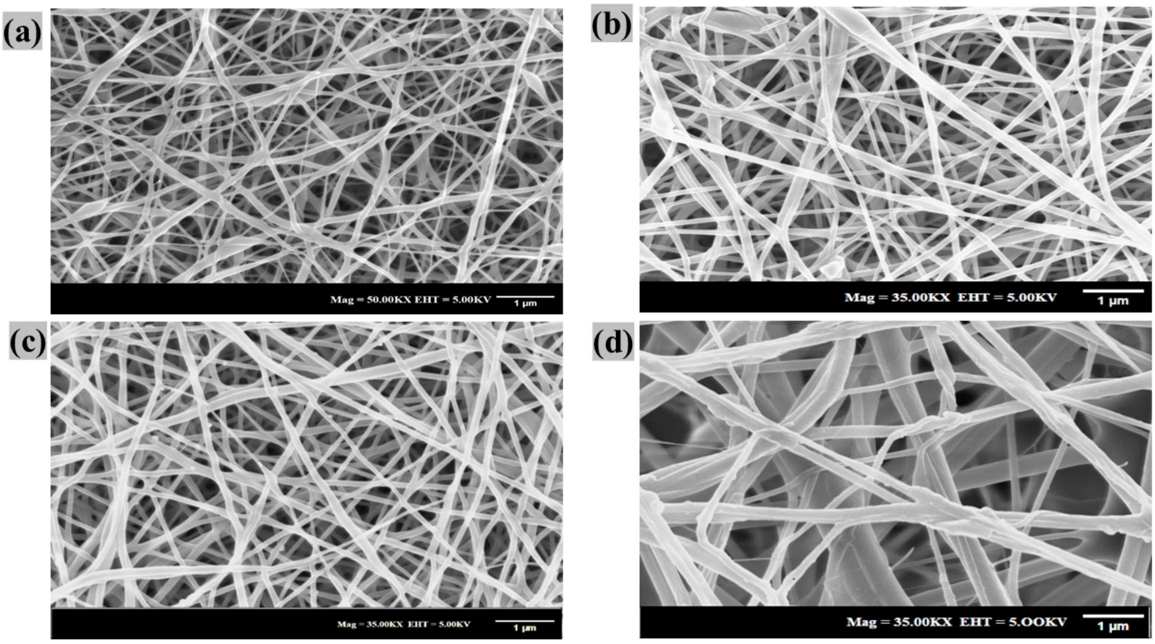

Figure 5.B. 17 SEM picture of drug loaded electrospun nanofiber with same polymer composition (PVA/CS, PVA/CS/E, PVA/CS/TXA, PVA/CS/TXA-E)

The MSWNF system showed successful incorporation of MSW-T particles, with SEM confirming continuous integration of MSW-T microparticles within the nanofiber mesh in **figure 5.B.18(a-b).** CNF nanofibers had an average diameter of 168 ± 38 nm, and the diameter of MSWNF was measured to be 120 ± 20 nm. Macroscopically, the fibrous patches appeared robust, homogeneous, and aesthetically suitable for direct incorporation as kit components, with their morphological characteristics supporting effective haemostatic function through enhanced surface area and platelet interaction capabilities.

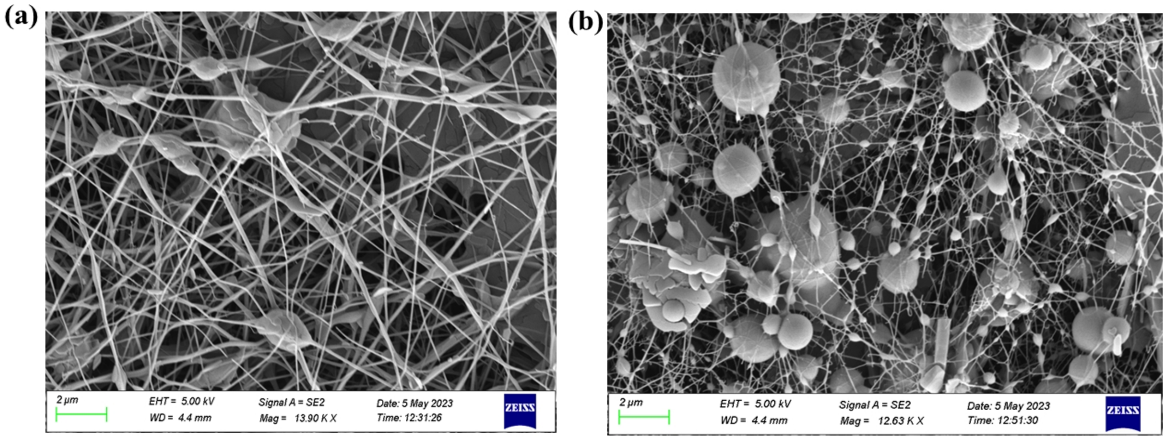

Figure 5.B. 18 (a-b) SEM images of control nanofiber (CNF) and marine shell waste nanofiber (MSWNF).

Major Observations

- PVA/CS sponge exhibited larger pore size and overall pore density was lower.
- PVA/CS/MSW-O was characterized greater number of smaller pores, increased porosity and lower density.
- The fiber formation depends on viscosity of the polymers blend and deacetylation of chitosan. The fiber diameter is proportional to its viscosity.
- The absence of any new peak including ester, amide, N-glucosamine or sulfonamide formation, coupled with peak broadening at specific wave length suggests drug was incorporated through H-bond in PVA/CS/TXA-E nanofiber.
- MSWNF nanofiber showed characteristic peak for CaO and OH functional group conformation of MSW-T incorporation.
- Higher UTS and lower elongation at break was shown in calcium incorporated scaffold. Improved mechanical property when MSW-T was incorporated to chitosan scaffold.
- UTS increase (3.78MPa to 4.2 Mpa) when chitosan incorporation increases. Drug and MSW-T incorporation also increase UTS but decrease in elongation that improve the fiber bonding.
- On compression PVA/CS sponge showed earlier strain hardening due to densar structure. PVA/CS/MSW-O sponge showed grated initial deformation capacity and enhanced energy absorption due to high porosity.
- MSWNF have a contact angle of 32 indicating, an interment hydrophilicity, that bind with nanoporous architecture which prevent blood loss and promote attachment of platelet to from blood clot.
- SEM images show nanofiber diameter increases when viscosity of the solution and concentration increases.
- The controlled swelling in MSWNF was attributed to chemical interaction chitosan amine group, pva hydroxyl group and Ca ion from MSW-T. MSWNF undergoes an ion exchange process between Ca and Na potentially providing a mechanism for control nanofiber degradation.

5.C. Biological characterization and in-vitro blood clotting parameters of different forms of hemostatic scaffold.

5.C.1. Hemocompatibility assessment

The hemocompatibility assessment across various nanocomposite systems demonstrated favourable blood compatibility in accordance with ASTM F756 standards [55]. In the air dried scaffold, AD1 and AD2 films showed minimal hemolysis values of 0.65 ± 0.14% and 1.21 ± 0.2% respectively, well below the 5% ASTM threshold for high hemocompatibility depicted in the **figure 5.C.1a**. The PVA/CS sponge systems exhibited in **figure 5.C.1b** exceptional blood compatibility with hemolysis rates below 0.5%, with PVA/CS/MSW-O showing the lowest hemolysis, attributed to the presence of calcium ions in its matrix which inhibits hemolysis and regulates erythrocyte deformability. This observation can be attributed to the presence of calcium ions within its sponge matrix. Pickering et al. confirmed that an excess of calcium salts inhibits hemolysis [56]. Furthermore, Yalcin et al. emphasized the role of calcium in regulating erythrocyte deformability, noting that increased calcium concentration in the suspending medium impairs RBC deformability [57]. These findings corroborate our conclusion that the reduced hemolysis observed is due to the presence of calcium ions in the PVA/CS/MSW-O matrix, which protects erythrocytes from degradation.

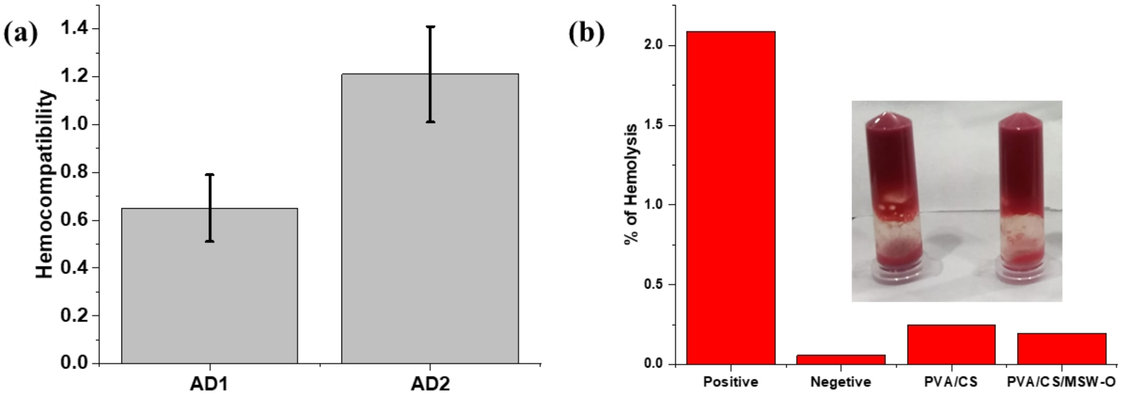

Figure 5.C. 1 Hemocompatibility study of (a) air dried film (b) freeze dried sponge.

In the **figure 5.C.2a** PC32, PC11, PC32T, and PC11T demonstrated hemolysis values of 2.8%, 5.0%, 1.4%, and 3.8% respectively, meeting ISO 10993 requirements (<5%). While chitosan showed slight hemolytic activity, TXA incorporation did not significantly affect hemocompatibility. The MSW incorporated systems showed varying degrees of blood compatibility, with MSW-O and MSW-T powders exhibiting hemolysis percentages of 3.8 ± 0.2% and 0.49 ± 0.24% respectively in the **figure 5.C.2b**. The nanofiber variants, CNF and MSWNF, demonstrated hemolysis percentages of 5 ± 0.3% and 4 ± 0.2% respectively, indicating improved blood compatibility due to the synergistic effect of chitosan and calcined MSW powder. All tested materials maintained hemolysis rates below the 5% confirming their suitability for blood-contacting applications. The consistently low hemolysis rates across all scaffolds suggest minimal risk of complications such as thrombosis or adverse immune reactions, supporting their potential use in various biomedical applications.

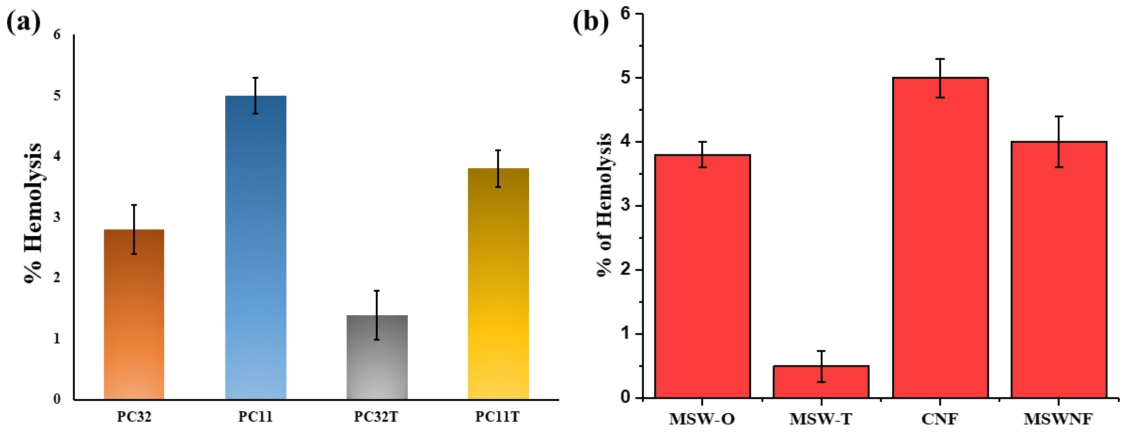

Figure 5.C. 2 Hemocompatibility study of electrospun nanofiber

5.C.2 Antibacterial activity

Various studies have demonstrated enhanced antimicrobial activity with calcium-containing compositions compared to their base counterparts, as evidenced by multiple zone of inhibition (ZOI) measurements in **figure 5.C.3(a,b)**. Studies showed that the ZOI increased from 1.96±0.5 cm^2 to 3.24±0.15 cm^2 when comparing AD1 to AD2, and from 1.74±1 cm^2 to 5.4±0.5 cm^2 for PVA/CS versus PVA/CS/MSW-O in **figure 5.C.3(c,d).** The increased antimicrobial property in AD2 and PVA/CS/MSW-O was noted and this may be due to the addition of Ca ion which can lead to the microbial cell wall rapture and generation of reactive oxygen species (ROS) and free radicals which strongly affects the cell integrity [58]. These study results can be well corroborated with the findings of Egil et al [59] , Their study on antifungal and antibacterial assays revealed that calcium incorporation increased the antimicrobial effects due to the precipitation of $Ca(OH)_2$ on the surface of CaO crystal from the supersaturated liquid phase [60]. Our observation of Ca^{2+} modulation in ROS homeostasis has also been reported by other researchers [61], [62].

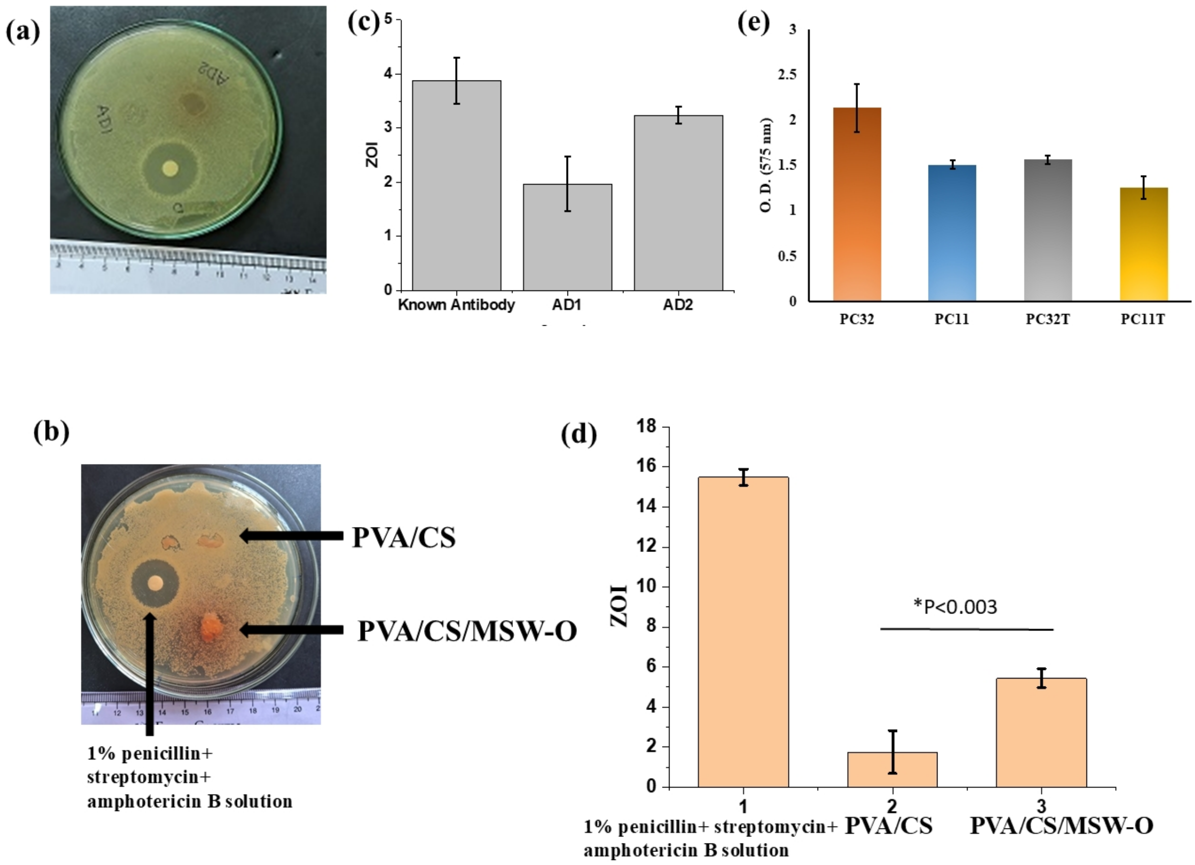

Figure 5.C. 3 Antibacterial assay and zone of inhibition against Staphylococcus aureus in (a,c) air dried and (b,d) freeze dried scaffold (e) anti biofilm activity of PC11T, PC32T

Studies on biofilm formation in the **figure 5.C.3e** revealed that PC32 nanofibers showed an OD@575 of 2.15, while PC11 nanofibers demonstrated 1.5, indicating significant anti-biofilm activity due to CS content. The addition of TXA reduced these values to 1.55 and 1.25 for PC32T and PC11T respectively, suggesting that TXA incorporation did not interfere with the anti-biofilm properties of CS-based nanofibers. Similarly, against S. aureus (**figure 5.C.4**) and E. coli (**figure 5.C.5**), the ZOI increased from 13±1 mm with CNF to 21±1 mm and 26±1 mm with MSWNF, respectively. The presence of CaO endows oyster-shell-derived powders and membranes with antibacterial activities; it is known that Cao shows antibacterial activity through hydration and dissociation in the liquid phase. This leads to an alkaline condition with high pH surrounding the bacteria, the main contributor to its bactericidal activity. Cardiolipin (CL) is the main lipid portion in the cell membrane component of bacteria. It regulates the main dynamic center, including energy metabolism, membrane transport, and cell division. The dissociation of CaO releases Ca^{2+} ions, which have a strong affinity for the negatively charged cardiolipin (CL) in bacterial cell membranes. The resulting Ca^{2+}-CL bonds initiate a cascade of bacterial destabilization processes, including compromised structural integrity, cell wall disruption, and leakage of cellular contents. This sequence ultimately leads to starvation and cell death [63]. The grain dimensions and bond length of calcined MSW-T were reduced after calcination. Finally, Reactive oxygen species (H_2O^+, O_2^-, H_2O_2) formed on the CaO surface disrupt the structural integrity of polyunsaturated phospholipids in microbial cell membranes. Superoxide was produced due to CaO dissociation in the slurry, which was marked as the primary source of active O_2[64]. Thus, MSW-T shows antibacterial activity by combining alkaline pH, Ca^{2+}-CL bonding, and super oxidation (O^{2-}) on the CaO surface, resulting in bacterial cell wall disintegration and cell lysis.

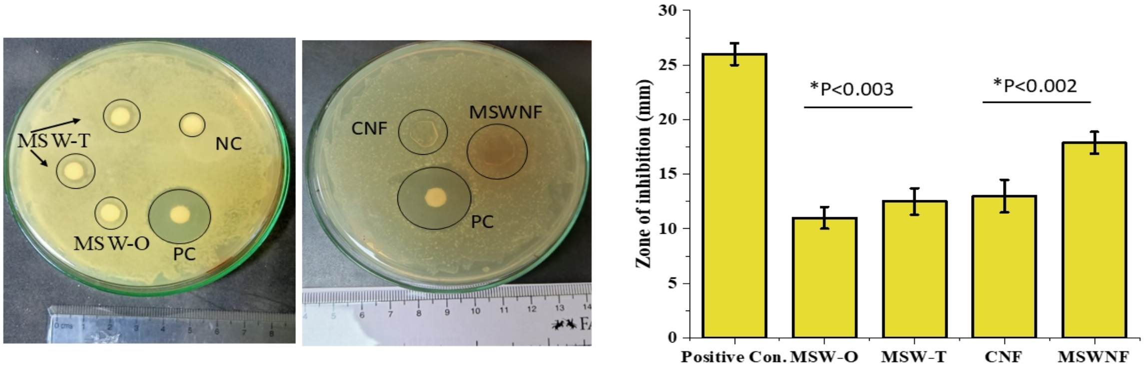

Figure 5.C. 4 Antibacterial activity and zone of inhibition of extracted and marine shell waste powder with electrospun nanofiber against S. Aureus.

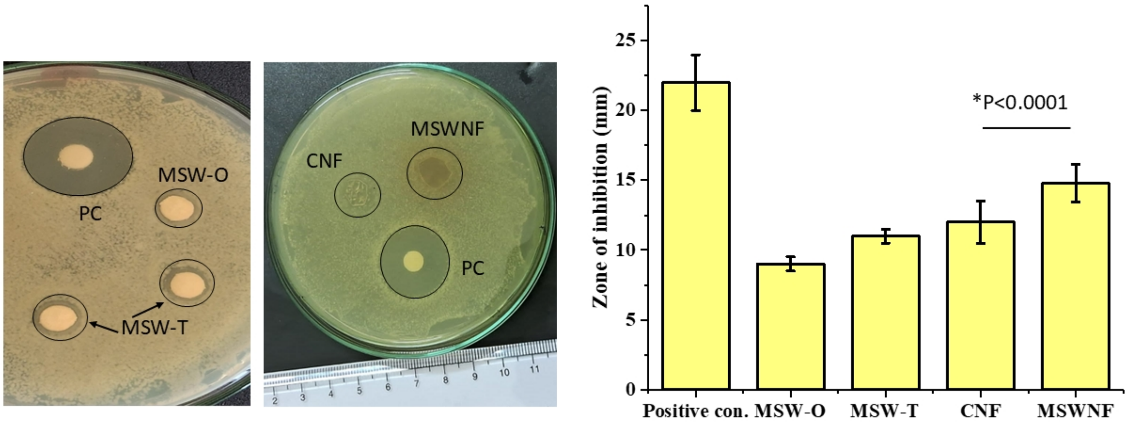

Figure 5.C. 5 Antibacterial activity and zone of inhibition of extracted and marine shell waste powder with electrospun nanofiber against E. Coli bacteria.

Table 5.C. 1 Cell viability and Hemolysis percentage of Saffold.

Biological Parameter	Air Dried		Freeze Dried		Electrospin nanofiber				
	PVA/CS (AD1)	**PVA/CS/MWW-O (AD2)**	**PVA/CS (FD1)**	**PVA/CS/MSW-O (FD2)**	**PVA/CS**	**PVA/CS/TXA**	**PVA/CS/E**	**PVA/CS/TXA-E**	**PVA/CS/TXA-E/MSW-T (MSWNF)**
Cell viability	73±3	76±7	90±5	94±5	83±3	79±2	77±4	85±2	82±4
Hemolysis (%)	0.65±0.1	1.21±0.2	0.25	0.20	5.0	3.18±0.4	7.04±0.8	5±0.3	4±0.2
Antimicrobial (cm^2)	1.96±0.5	3.14±0.15	1.74±1	5.4±0.5	------	-------	-------	4.58±1.5	5.14±1

5.C.3 Cell cytocompatibility and cell migration assay

The cytocompatibility assessment of various materials demonstrated consistently favorable results across different compositions. The MTT assay revealed in the **figure 5.C.6 (a)** that PVA/CS and PVA/CS/MSW-O sponges exhibited excellent cell viability exceeding 90%, with PVA/CS/MSW-O showing the highest confluency in DAPI staining analysis, indicating superior cytocompatibility and cellular proliferation in the **figure 5.C.6 (b&c)** after 3 days**.** Compared to the PVA/CS sponge, fibroblast proliferation on the PVA/CS/MSW-O sponge showed no significant difference at $P<0.05$.

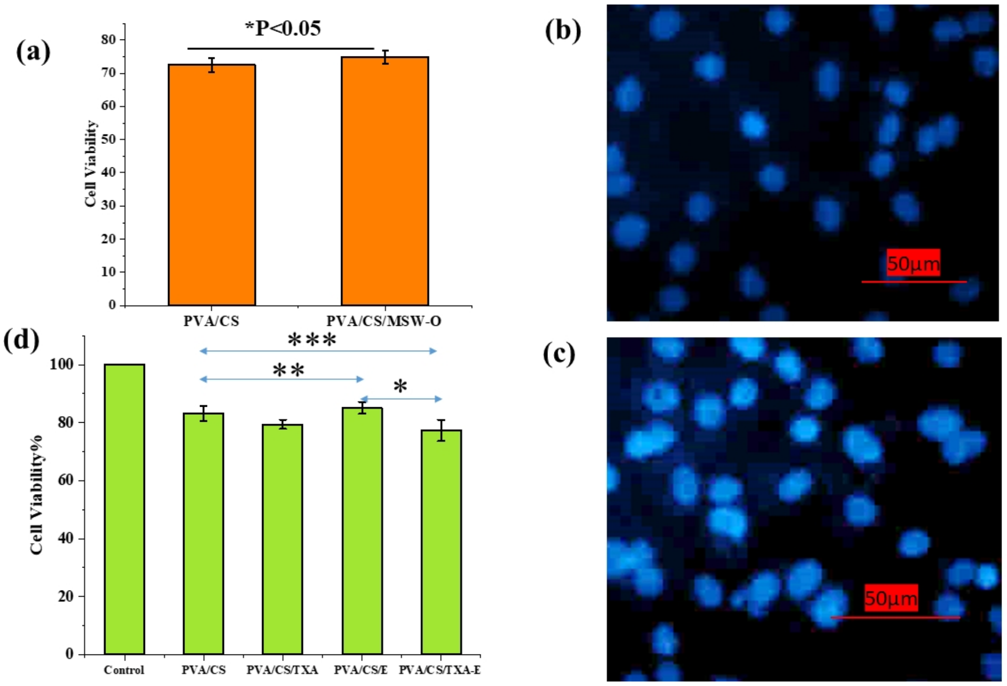

Figure 5.C. 6 Biocompatibility assessment of freeze-dried sponge and dual drug loaded sponge with DAPI

In the evaluation of nanofiber patches, PVA/CS, PVA/CS/TXA, PVA/CS/E, and PVA/CS/TXA-E demonstrated cell viability of 83±3%, 79±2%, 85±2%, and 77±4% respectively after 72 hours of fibroblast cell growth, with PVA/CS/E showing the highest cell viability among the variants in the **Figure 5.C.6(d)**. The influence of hemostatic drug TXA, and E on fibroblast cell migration was studied by scratch assay. Fibroblast cells on either side of the scratch migrated towards each other at higher numbers for PVA/CS/TXA and PVA/CS/TXA-E as compared to that of PVA/CS/E and PVA/CS nanofiber bed showed in the **figure 5.C.7**. Overall, the rate of cell migration was seen to be quite high with all the drug-loaded nanofibers demonstrating near complete gap closure within 24 h. Increase in cell migration suggests the potential for wound healing and higher expression of cell adhesion and growth associated factors, thus proving the regenerative capacity of the nanofibers. A recent report on fibroblast cell migration have shown improved wound healing [65].

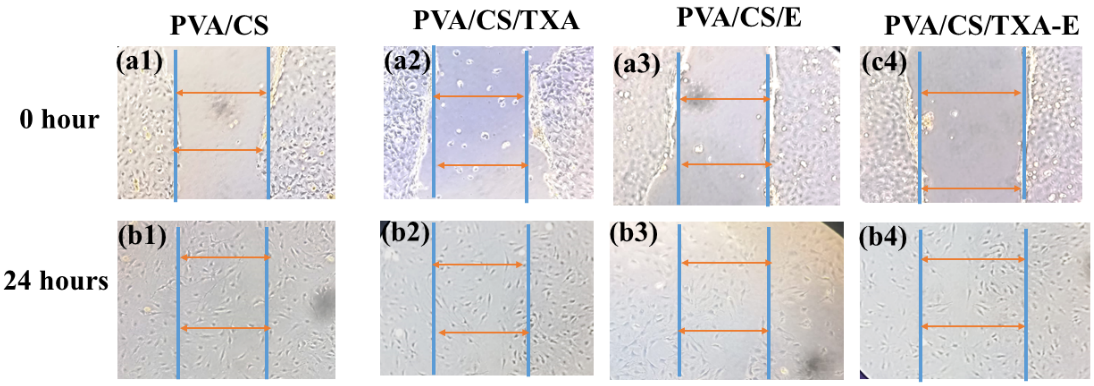

Figure 5.C. 7 Biocompatibility assessment of dual drug-loaded nanofiber patches evaluated by (a1-a4) and (b1-b4) scratch assay for migration of cells at 0 hour and 24 hours.

The powder samples and nanofibers also showed promising results, with MSW-T exhibiting 90% cell viability compared to MSW-O's 81%, while CNF and MSWNF nanofibers achieved 85% and 82% cell viability respectively after three days of cell culture in the **figure 5.C.8a**. The scratch assay revealed enhanced fibroblast cell migration in drug-loaded nanofibers, particularly in PVA/CS/TXA and PVA/CS/TXA-E compositions, demonstrating near-complete gap closure within 24 hours. This increased cell migration suggests strong wound healing potential and elevated expression of cell adhesion and growth-associated factors, confirming the regenerative capacity of the nanofibers. DAPI staining further supported these findings, showing significantly increased cell attachment on MSWNF compared to CNF nanofibers, attributed to the presence of deacetylated chitosan which enhanced biocompatibility (**figure 5.C.8b**). Cell quantity increased significantly on MSWNF (369 ± 10) compared to CNF nanofibers (330 ± 20) or control (310 ± 45).

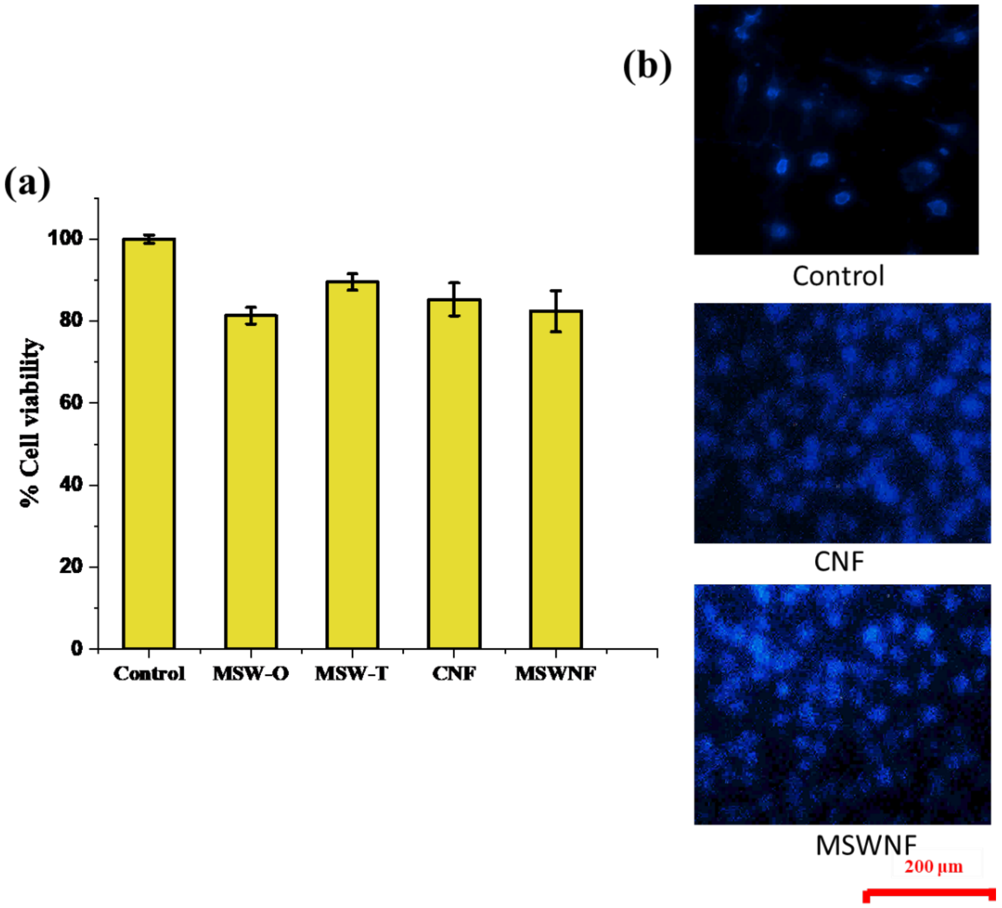

Figure 5.C. 8 Cytocompatibility of marine shell waste powders (extracted and calcined at 1200 °C (MSW-O and MSW-T), PVA/chitosan nanofibers (CNF) and marine shell waste calcined at 1200 °C powder-loaded PVA/chitosan nanofibers (MSWNF) membranes studied by (a) MTT assay and (b) DAPI staining assay.

5.C.4 In-vitro hemostatic properties

The in vitro hemostatic properties of various materials were evaluated through multiple parameters including clotting time (CT), prothrombin time (PT), activated partial thromboplastin time (aPTT), and platelet recalcification time (PRT). Without intervention, blood showed a baseline CT of 464-472 seconds. Calcium-containing compositions consistently demonstrated enhanced hemostatic efficacy compared to their counterparts. For instance, AD2 showed improved CT (280±18s) compared to AD1 (408±12s), while Other confirmatory tests such as PT, APTT, and PRT also confirmed the better performance for AD2 in the **figure 5.C.9(a-d).** The lower PRT of AD2 (62±2s) than AD1(84±4s) showed intrinsic coagulation ability increased. The PT and APTT time off AD2(18±2s & 70±4s) was lower than AD1 (22±1.5s & 96±8s) respectively signifies slower rebleeding ability and higher clotting performances for AD2 film.

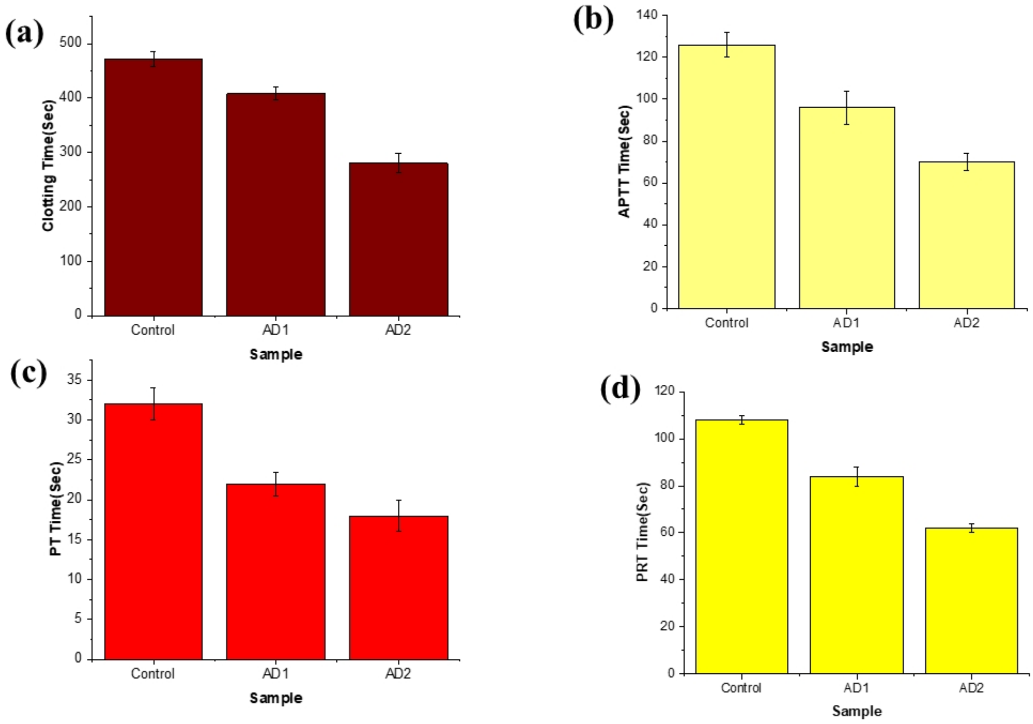

Figure 5.C. 9 In-vitro hemostatic parameters of air dried film.

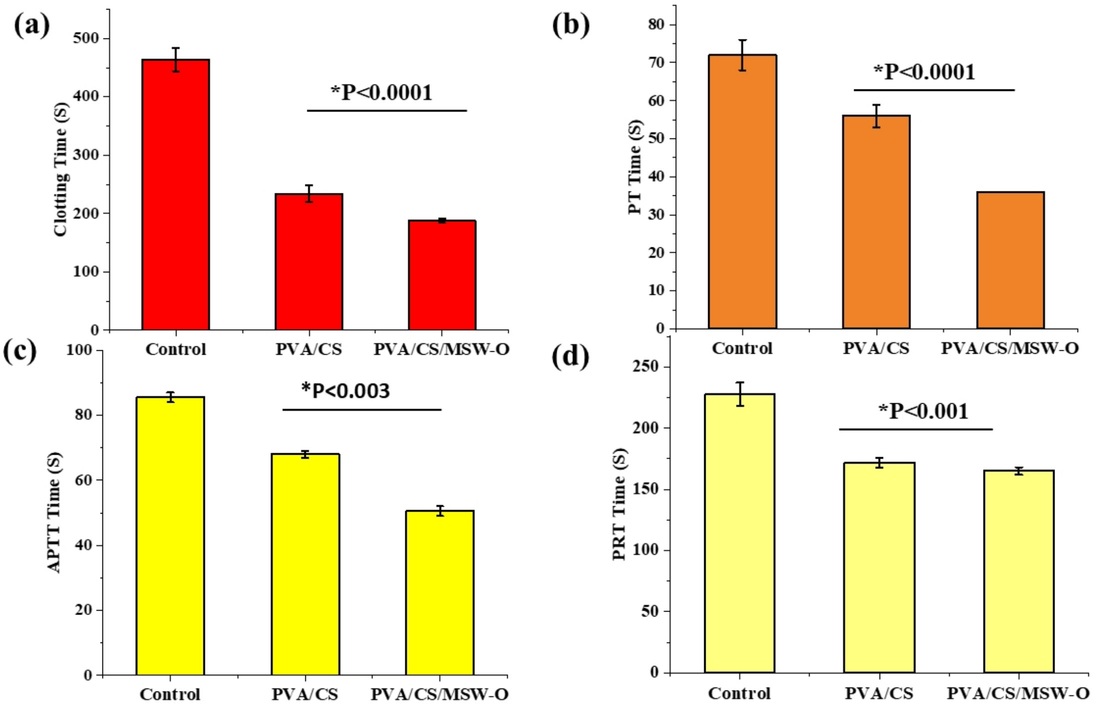

Figure 5.C. 10 In-vitro hemostatic parameters of freeze dried dried film.

The whole blood clotting time (CT) for PVA/CS/MSW-O was 188 ± 4 s, and for PVA/CS it was 234 ± 14 s as represented in **Figure 5.C.10 (a)**. These values represent a significant ($p<0.0001$) reduction to 41% and 50%, respectively, compared to the blank control group with a CT of 464 ± 20 s. In the case of PVA/CS/MSW-O, the CT reduction is attributed to chitosan as well as the sequestration of Ca^{++} ions, which interrupts the blood coagulation pathway and facilitates interaction between the hemostatic materials and the blood samples. Conversely, for PVA/CS, the CT results reflect the presence of porous chitosan microsphere network structures that promote rapid blood absorption and local concentration of blood coagulation factors [66]. The hemostatic efficacy of PVA/CS/MSW-O was higher than that of PVA/CS and the control group. The PT values for PVA/CS/MSW-O and PVA/CS were 36 ± 1 s and 56 ± 3 s, compared to 72 ± 4 s for the blank control group. Similarly, the aPTT times for PVA/CS/MSW-O and PVA/CS were 51 ± 2 s and 68 ± 1 s, respectively, whereas the control group had an aPTT of 86 ± 2 s. These results, illustrated in **Figure 5.C.10(b-c),** indicate significant differences in PT and aPTT parameters among PVA/CS, PVA/CS/MSW-O, and the control group, suggesting that these materials impact the extrinsic and intrinsic coagulation processes. In a previous study, He et al. developed novel porous chitosan/$CaCO_3$ materials via the wet granulation method. They showed reduced in-vitro blood clotting parameters compared to chitosan alone, which accelerates the activation of the intrinsic coagulation system [67]. Additionally, the lower platelet recalcification time (PRT) observed for PVA/CS/MSW-O (58 ± 3 s) and PVA/CS (72 ± 5 s) compared to the control group (96 ± 10 s) indicates an enhancement in intrinsic coagulation ability in the **Figure 5.C.10d**. Both PVA/CS and PVA/CS/MSW-O possess a network structure that facilitates blood absorption and promotes platelet aggregation and adhesion. Furthermore, chitosan, a component of these sponges, contains cationic groups that interact with the anionic phosphate groups on platelets. The superior clotting effect of the PVA/CS/MSW-O sponge can be attributed to the presence of calcium [68]. Notably, PVA/CS/MSW-O exhibits enhanced hemostatic performance, as indicated by reduced clotting and platelet recalcination times. The presence of Ca^{++} in PVA/CS/MSW-O activates the coagulation system by facilitating thrombin formation, promoting the exposure of phosphatidylserine on the platelet surface, and accelerating the coagulation complex formation. Ca^{++} also increases the stiffness of platelet aggregation, thereby aiding in the cessation of bleeding [69]. In the previous study, Zhou et al. confirmed calcium release from a novel acetate chitosan/$CaCO_3$ hydrogel could effectively promote blood coagulation and significantly enhance wound healing of full-thickness skin defects in rats [70].

In chitosan-based systems, PC11T demonstrated superior performance with CT reduced to 65% of control values. The whole blood clotting time of the nanofibers provided the evidence that TXA loading into nanofiber membranes reduced CT. Addition of agents such as gallic acid into chitosan electrospun nanofiber mats has shown a reduction to ~80% of untreated CT in previously reported literature[71]. In our findings, the CT of PC32 and PC32T were lowered to 85 and 82% whereas PC11 and PC11T were 73 and 65% with respect to the control, it signified that the nanofiber formulations developed have potential efficacy. TXA is an analogue of lysine amino acid and inhibits plasmin formation by binding to lysine binding sites on plasminogen. At higher concentrations, a direct inhibition of plasmin is also known for its anti-fibrinolytic activity. In addition, a prolonged release of TXA is also desirable due to its anti-inflammatory actions[72], [73]. On the other hand, CS exerts hemostatic action by enhancing platelet adhesion, which is the primary mechanism of blood coagulation. Therefore, the prominent role of CS in effecting hemorrhage control is explained. However, the combined role of CS and TXA brings about increase in hemostasis performance. Indeed, Bartley proposed quite some time back that CS should be combined with TXA for sinus surgeries, however, the hypothesis was not investigated further[74]. The present study provides an essential support for such an approach as well as shows product development feasibility in form of nanofibers. The whole blood CT was further confirmed with platelet adhesion and PRT, both of which supported the application of developed nanofibers. Even though the effect of TXA on CT was less pronounced compared to CS, this would be anticipated from the mechanism of action of TXA, which is more to stabilize the clot. Sezer et al have also shown that combining gelatin and TXA can provide improved hemostasis performance [75]. Therefore, CS/TXA system would be more suitable to provide prolonged bleeding control. Indeed, investigations performed *in vivo* in future with these delivery systems with measurement of parameters such as thromboelastography would provide more detailed insights.

The incorporation of therapeutic agents further enhanced hemostatic properties, as evidenced by PVA/CS/TXA-E nanofibers showing significantly faster CT (243±3s) compared to single-drug variants PVA/CS/TXA (381±5s) and PVA/CS/E (280±6s) showed in the **figure 5.C.11.** The blood clotting time of the PVA/CS nanofiber was (421 ± 6 s) whereas, without the addition of any test patch, the blood clotting time was (464 ± 35 s). The clotting time was reduced by applying dual drug blended nanofibers ~ 36% and ~13% than either TXA and E loaded nanofiber respectively. Amongst the commercially available hemostats like QuickClot®, a clotting time of about 300 s is known in literature [76]. Chitosan-based nanofibers cause hemostasis by aggregation caused by interaction between positively charged amino groups with negatively charged platelets and erythrocytes [77], [78].. The presence of hydrophilic PVA enhances the interactions. In the dual drug-loaded nanofibers, TXA, a lysine analog, blocks the conversion of plasminogen to plasmin, which is a fibrin mesh cutter. On the other hand, E improves platelet adhesiveness and restores capillary resistance. E mainly binds to the surface receptor in activated platelets and ligands on the endothelial cells, which can signal for patch -p-selectin expression. Several clinical studies have shown improvement in mortality caused by severe hemorrhage by administration of TXA. For example, Elanwar et al. performed a clinical study to investigate the effect of TXA in two different aspects by taking 88 women in each category; one was for a cesarean section and compared it to placental delivery [79]. Their result proved that the administered group showed a significantly lower amount of blood loss (within 2 hours of surgery) than the control group, where no TXA was administered. Another study[80] also revealed less total blood loss up to 2 h postpartum and higher hemoglobin in the TXA-administered group.

Guerra et al. [81] have observed that the patch P selectin expression had increased significantly in the entire blood due to the increase in E concentration. Topically administered E (125 mg/ml) has also reduced the bleeding time in the rat tail bleeding model. According to their observations, the topically administered E is more efficacious than the systemic administration. During hemostasis, TXA and E can complement each other, and their combined intravenous administration produces a synergistic effect on reducing intraoperative and postoperative blood loss. By using this combination, the negative effects of high doses of TXA is avoided [82]. Compared to TXA alone, the combined administration of E and TXA during pediatric heart surgery has been more successful in lowering postoperative blood loss and the need for whole blood transfusions [83]. In a beagle model, E has been shown to reduce intraventricular hemorrhage caused by hemorrhagic hypovolemia [84]. The present study successfully combines the hemostatic performance of chitosan nanofibers with the topical synergistic pharmacological effect of TXA and E.

The hemostasis performance was further validated by studying the activation of intrinsic and extrinsic coagulation pathways using prothrombin time (PT) and activated partial thromboplastin time (aPTT). These results are represented in **Figure 5.C.12**. The PT value of PVA/CS/TXA-E nanofiber patch (21 ± 1 s) was significantly lower than that of PVA/CS (29 ± 2 s) ($P > 0.005$), PVA/CS/TXA (25 ± 1 s) ($P > 0.03$), PVA/CS/E (27 ± 1 s) ($P > 0.003$). There was no statistical difference between PVA/CS and PVA/CS/E. However, PVA/CS/TXA and PVA/CS/TXA/E both exhibited statistically different PT than the other two groups, as well as each other. Similarly, the aPTT value of PVA/CS/TXA-E nanofiber was (79 ± 1 s) which was significantly lower than PVA/CS (98 ± 13 s) ($P > 0.05$), PVA/CS/TXA (86 ± 2 s) ($P > 0.05$), and PVA/CS/E (81 ± 2 s) ($P > 0.01$). In addition, the PT and aPTT values of the blank platelet-poor plasma group were (28 ± 1 s) and (122 ± 3 s), respectively, significantly higher than PVA/CS/TXA-E nanofiber. These results demonstrated that the dual drug-loaded nanofibers synergized and activated the extrinsic and intrinsic blood coagulation pathways. Besides, the PRT value of the PVA/CS/TXA-E nanofiber patch (66 ± 1 s) was significantly lower than that of PVA/CS (94 ± 1 s) ($P < 0.0001$), PVA/CS/TXA (79 ± 0 s) ($P < 0.0001$) and PVA/CS/E (77 ± 3 s) ($P > 0.002$). The PRT value of the blank platelet-poor plasma (PPP) was (111 ± 1 s), which was significantly higher than the dual drug nanofiber. The commercial hemostatic agent Hemcon^{TM} chito gauge's PRT value is approximately 55 s, which is close to the performance of nanofiber patches investigated in the present study. Thus, the drug-loaded PVA/CS nanofibers are expected to provide hemostatic performance without thermal injuries or tissue necrosis due to exothermic reactions observed for QuickClot^{TM} gauzes. Similarly, HemCon^{TM} gauzes rely solely on cell aggregation caused by chitosan-positive charges, which can also cause hemolysis and not provide mechanical compression in many bleeding injuries. However, drug-loaded nanofibers achieve the same performance with lesser chitosan content. Moreover, these gauzes are manufactured by lyophilization process, and it has been shown that scaled-up electrospinning process is a more continuous, high-throughput and cost-effective manufacturing technique compared to lyophilization rendering PVA/CS/TXA-E as an economical product with performance [85], [86].

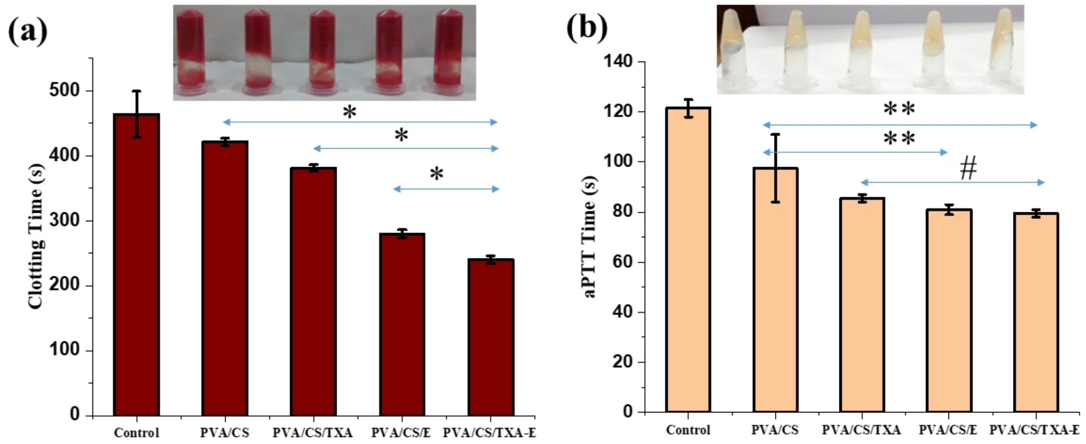

Figure 5.C. 11 In-vitro hemostatic performance of dual drug loaded nanofiber by (a) clotting time (b) activated partial thromboplastin time.

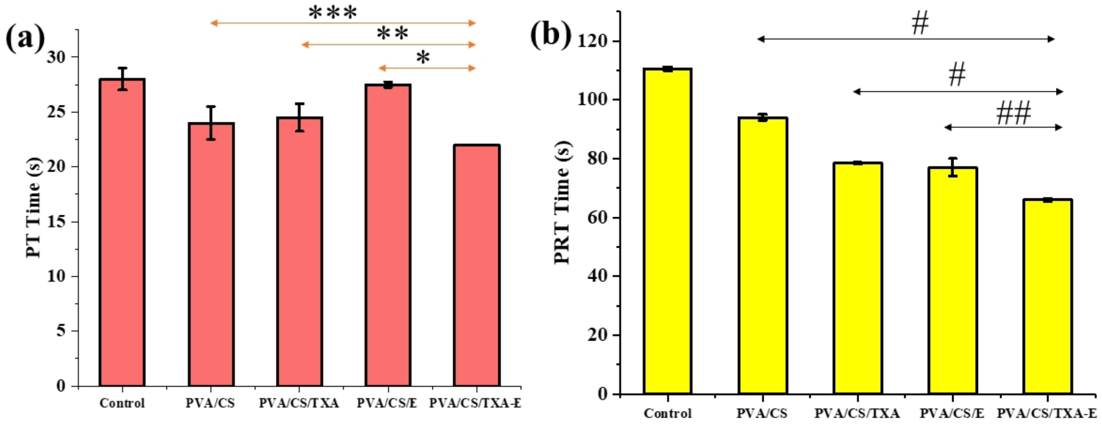

Figure 5.C. 12 In-vitro hemostatic performance of dual drug loaded nanofiber by (a) prothrombin time and (b) platelet recalcination time

The addition of calcined materials like MSW-T significantly improved hemostasis, showing complete clotting in 117±4s compared to MSW-O at 164±6s. The hemostatic mechanism involves multiple pathways, confirmed by PT, aPTT, and PRT measurements. PVA/CS/MSW-O showed improved PT (36±1s) and aPTT (51±2s) compared to PVA/CS (PT: 56±3s, aPTT: 68±1s). Similarly, MSWNF demonstrated enhanced coagulation parameters (CT:168±4s, PT: 22±0.6s, aPTT: 52±6s, PRT: 47±1s) compared to CNF (CT:230±11s, PT: 27±0.4s, aPTT: 58±6.6s, PRT: 76±4s) and was depicted in the **figure 5.C.13**. Li et al shows similar type of clotting time (163 ± 5 s) induced by using Ca incorporated diatom frustules which is comparable to Quikclot® zeolite [87]. The large surface area with respect to volume containing numerous numbers of pores in the MSWNF have a high capacity for absorbing blood which concentrated the coagulation factor and accelerate the blood coagulation cascade reaction. Calcium ion act as a coagulation factor IV, interacts with platelet activation and aggregation with the simulation of the intrinsic and extrinsic clotting factor pathways to form blood coagulation. This aggregation is due to positively charged ion are prone to interact with negatively charged platelet and erythrocytes of blood. In aPTT, the intrinsic coagulation cascade begins with contact system activation and ends with the production of thrombin. The downstream coagulation cascades were blocked by the positive charge on chitosan, which also prevented contact system activation [88]. Furthermore, the intrinsic coagulation pathway was strengthened by the Ca^{2+} release from MSWNF, which acts as coagulation factor IV [89]. Besides that, Platelet Recalcification Time (PRT) was measured the intrinsic coagulation function as well as the action of platelets of the bleeder. PRT is primarily employed in the assessment of platelet capacity to generate thrombi, a crucial function in hemostasis. The coagulation property of MSWNF was greater than CNF due to calcium ion present which simulates an intrinsic coagulation process in vitro and stabilizes the fibrin network by shortening the CT, aPTT, PT and PRT value.

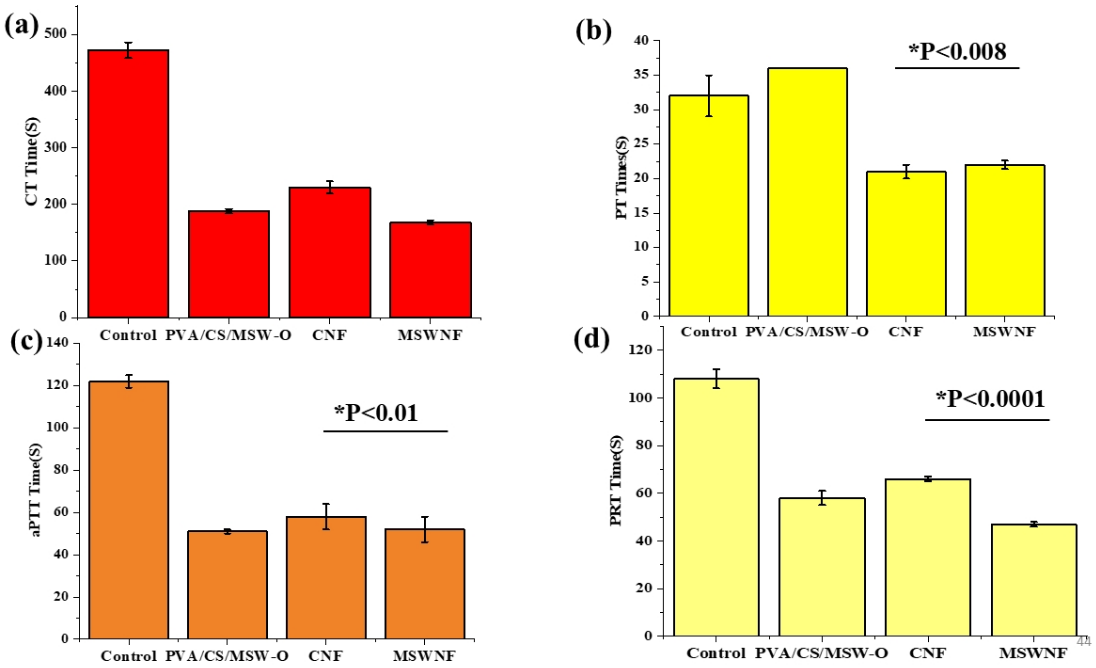

Figure 5.C. 13 In vitro hemostasis performances of control and oyster shell nanofiber evaluated by (a) blood clotting, (b) prothrombin time, (c) activated partial thromboplastin time, (d) platelet recalcification time.

The improved hemostatic performance is attributed to multiple mechanisms: chitosan's cationic groups interact with anionic phosphate groups on platelets, calcium ions activate the coagulation cascade and enhance platelet aggregation, and the nanofiber structure provides high surface area for blood component interactions. SEM analysis confirmed the adhesion of erythrocytes and platelets on nanofiber surfaces, with MSWNF showing superior blood cell binding due to the synergistic effect of chitosan's absorptive properties, nanofiber structural advantages, and calcium-induced biochemical interactions. The presence of therapeutic agents like tranexamic acid and ethamsylate provided additional benefits through complementary mechanisms, with tranexamic acid blocking plasminogen conversion and ethamsylate improving platelet adhesiveness and capillary resistance, resulting in enhanced overall hemostatic performance comparable to commercial products.

Table 5.C. 2 In-vitro Hemostatic Efficacy of the scaffold.

Hemostatic Parameter	Control (Without intervention)	Air Dried		Freeze Dried		Electrospin nanofiber				
		PVA/CS (AD1)	PVA/CS/MSW-O (AD2)	PVA/CS (FD1)	PVA/CS/MSW-O (FD2)	PVA/CS	PVA/CS/TXA	PVA/CS/E	PVA/CS/TXA-E	PVA/CS/TXA-E/MSW-T (MSWNF)
CT(S)	472±14	408±12	280±18	234±14	188±4	421±6	381±4	280±6	230±11	168±4
PT	32±3	22± 1.5	18±2	56±3	36±0	29±1	25±1	27±1	21±1	22±0.6
APTT	122±3	96±8	70±4	68±1	51±1	98±13	86±2	81±2	58±6	52±6
PRT	108±4	84±4	62±2	72±5	58±3	94±1	79±0	77±3	66±1	47±1

5.C.5. RT-PCR analysis of freeze dried sponge and nanofiber patches

IGF, VEGF are key signalling molecules which trigger angiogenesis in wound healing [90]. RT-PCR analysis of growth modulators VEGF-A, PDGF, and IGF-1 reveals that HADF cells cultured on the PVA/CS/MSW-O sponge, PVA/CS/TXA, PVA/CS/E, PVA/CS/TXA-E, and MSWNF nanofiber exhibit greater fold changes in gene expression compared to those cultured on PVA/CS over a 24h period shown in the **Figure. 5.C.14.** Specifically, the fold changes for PDGF in HADF cells on PVA/CS, PVA/CS/MSW-O, PVA/CS/TXA, PVA/CS/E, PVA/CS/TXA-E, and MSWNF nanofiber were 2.1, 2.4, 3.7, 2.84, 3.85 and 4.11 respectively. For IGF-1, the fold changes were 2.8, 3.55, 5.85, 5.85, 7.81, and 8.33 while for VEGF-A, the values were 3.8, 6.73, 4.51, 6.11, 7.21 and 8.45 respectively. These growth factors secreted by fibroblasts play essential roles in wound healing, particularly following haemorrhage. PDGF, released by platelets, initiates the healing process, while the release of Ca^{++} from scaffolds promotes the secretion of these growth factors PDGF, IGF-1, and VEGF-A at the injury site [91]. These factors enhance tissue repair by promoting cell attachment to the extracellular matrix and neighbouring cells [92]. VEGF-A is particularly crucial for angiogenesis, while PDGF and IGF-1 contribute to this process by supporting endothelial cell survival, proliferation, and vessel stabilization. The data suggest that the PVA/CS/MSW-O sponge and MSWNF nanofiber have higher effectiveness in upregulating these growth factors, potentially offering enhanced wound healing. RT- PCR results demonstrated significant upregulation of VEGF- A, PDGF, and IGF- 1, with MSWNF showing the highest expression levels. The enhanced gene activation is attributed to Ca^{2+} ions from calcined shell powder, which are known to accelerate angiogenic and fibroblastic signalling pathways. This confirms that MSWNF functions not only as a hemostatic scaffold but also as a regenerative biomaterial with therapeutic potential.

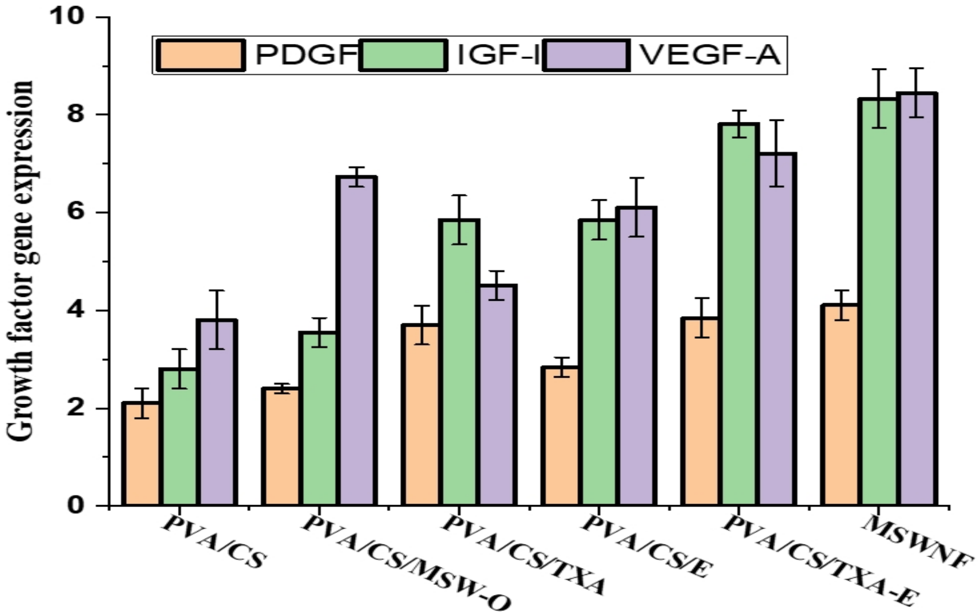

Figure 5.C. 14 Represent growth factor gene expression in HADF cells on the freeze dried sponge and nanofiber for 24h of cell culture.

Table 5.C. 3 Growth factor for gene expression for Freeze dried and Electrospin scaffold

Growth factor gene expression	**Freeze Dried**		**Electrospin nanofiber**			
	PVA/CS (FD1)	**PVA/CS/MSW-O (FD2)**	**PVA/CS/TXA**	**PVA/CS/E**	**PVA/CS/TXA-E**	**PVA/CS/TXA-E/MSW-T (MSWNF)**
PDGF	2.1±0.3	2.4±0.1	3.7±0.4	2.84±0.2	3.85±0.4	4.11±0.3
IGF-I	2.8±0.4	3.55±0.3	5.85±0.5	5.85±0.4	7.81±0.2	8.33±0.6
VEGF-A	3.8±0.6	6.73±0.2	4.51±0.3	6.11±0.6	7.21±0.6	8.45±0.5

5.C.6 In-vitro platelet adhesion

The surface adhesion and morphologies of attached blood cells on nanofiber surfaces (PVA/CS, PVA/CS/TXA, PVA/CS/E, PVA/CS/TXA-E) were visualized by SEM and shown in the **figure**

5.C.15(a-d). The SEM examination confirmed the adhesion of erythrocytes and platelets on the surfaces of all the nanofiber developed [93] and a continuous sheet of platelets with flattened morphology was found on each of the nanofibers.

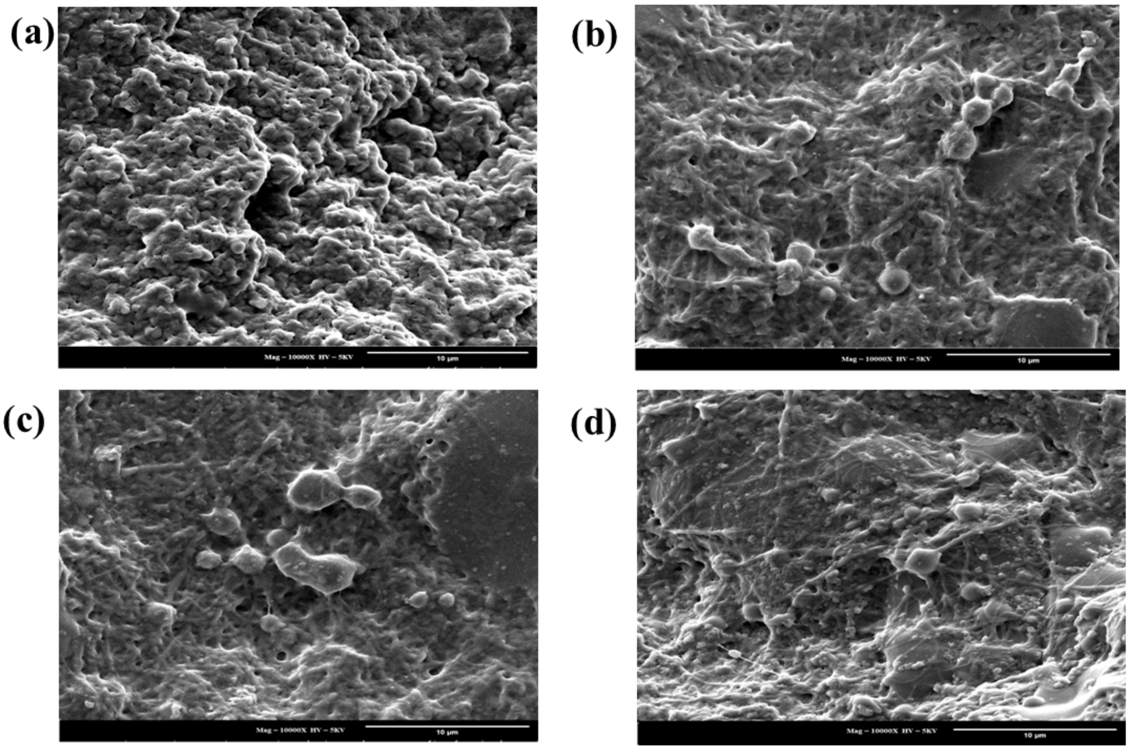

Figure 5.C. 15 Visualization of platelet adhesion on nanofiber patches by SEM images of drug loaded nanofiber (a) PVA/CS (b) PVA/CS/TXA (c) PVA/CS/E and (d) PVA/CS/TXA-E patches.

The binding of blood cells on the surfaces of CNF and MSWNF are depicted in SEM images in **Figure. 5.C.16**. CNF membranes exhibited individual platelets (appearing as spherical or globular structures) adhering to the fibrous matrix to form a more open architecture, with the platelets maintaining their individual morphology while interacting with the underlying network structure. MSWNF displayed a densely packed surface completely covered with small cellular elements indicative of a highly confluent layer of platelets transformed into spread-out morphology. Compared to CNF, MSWNF presented a more uniform, homogeneous surface texture promoting more extensive platelet spreading and aggregation, resulting in a tightly packed layer of platelets that have flattened and covered the entire surface [94]. Platelet adhesion results demonstrate significantly higher platelet binding on MSWNF surfaces compared to CNF due to the rough, mineral- rich Ca^{2+} surface that provides enhanced nucleation sites for platelet anchoring, thereby accelerating plug formation. Invitro platelet activation and adhesion also accelerated to the superior activity in vivo haemostasis (75s bleeding time) observed for MSWNF.

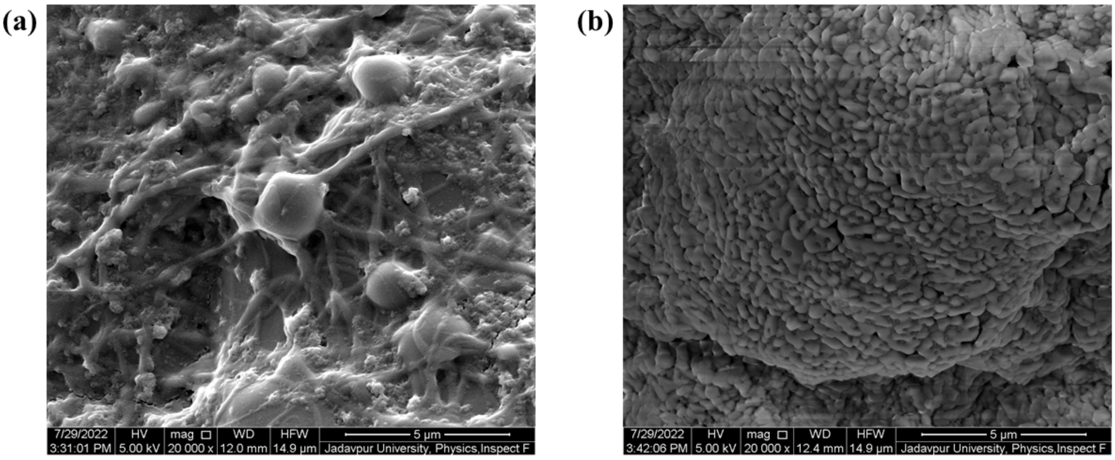

Figure 5.C. 16 platelet adhesion on (a) PVA/chitosan nanofibers (CNF) and (b) marine shell waste calcined at 1200 °C powder-loaded PVA/chitosan nanofibers (MSWNF) membranes.

5.C.7 Drug release assay

The drug release profiles of various nanofiber compositions demonstrated distinct patterns and kinetics. In nanofibers, PC32T exhibited a substantial initial burst release of 37.65% TXA within 3 minutes, while PC11T showed a more controlled initial release of 16.67%, suggesting reduced burst effect in the **figure 5.C.17(a,b).** The difference was attributed to PC32T's higher water uptake capacity. Both formulations achieved approximately 90% drug release within 10 hours, following Korsemeyer-Peppas model kinetics (r^2 = 0.960 for PC11T and 0.923 for PC32T) with n values of 0.139 and 0.275 respectively, indicating Fickian diffusion mechanism. A slight but significant increase in anti-microbial action was established due to incorporation of TXA. TXA and some of its derivatives have been identified with anti-microbial properties [95]. Release of drug within 3-5 min indicated that membranes will be suitable for stabilizing the fibrin to offer efficient hemorrhage control and the revelation of Fickian release mechanism will further allow for controlling the CT or sustaining clotting action as desired for different types of traumas.

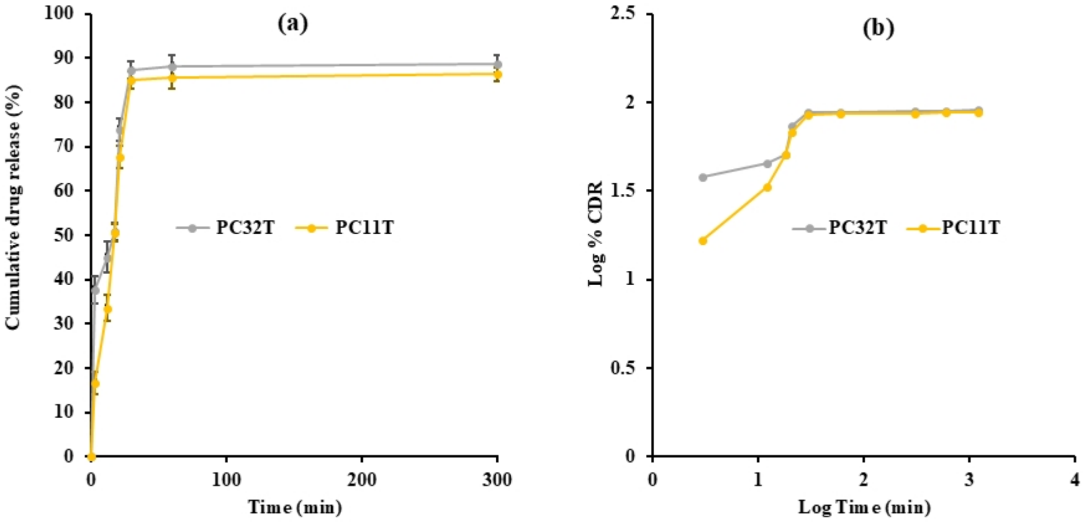

Figure 5.C. 17 (a) In vitro drug release profiles of PC32T and PC11T nanofiber in full range and (b) Korsmeyer Papayas model (n value 0.139 for PC32T and 0.2775 for PC11T) analysis of tranexamic acid release from nanofiber membranes.

The dual-drug loaded systems (PVA/CS/TXA, PVA/CS/E, and PVA/CS/TXA-E) displayed a biphasic release pattern characterized by rapid initial release within 30 minutes followed by sustained release for up to 5 hours showed in the **figure. 5.C.18**. The drug release profile is expected to provide rapid hemorrhage control, stabilize the clot, and prevent rebleeding due to sustained drug release. Kinetics of the drug release process was modeled by using the power law equation ($M/M_\alpha=Kt^n$), where K represents the release constant, n diffusion exponent, t release duration, M/M_α equilibrium concentration, and M_α is the fractional solute concentration. The findings showed TXA release from PVA/CS/TXA and PVA/CS/TXA-E nanofiber best fitted into the Korsmeyer-Peppas model. The n values for these patches were 0.607 and 0.552, respectively ($r^2 = 0.850$ for PVA/CS/TXA and 0.896 for PVA/CS/TXA-E. E drug release from both PVA/CS/E and PVA/CS/TXA-E electrospun nanofibers also followed the Korshmear-Pappas model as the values of the diffusion exponent (n) were 0.735 and 0.553 respectively ($r^2 = 0.988$ for PVA/CS/E and 0.921 for PVA/CS/TXA-E). These values suggested a non-Fickian diffusion for TXA and E release. Thus, both diffusion and polymer chain relaxation were involved in the release of the drug from the patches.

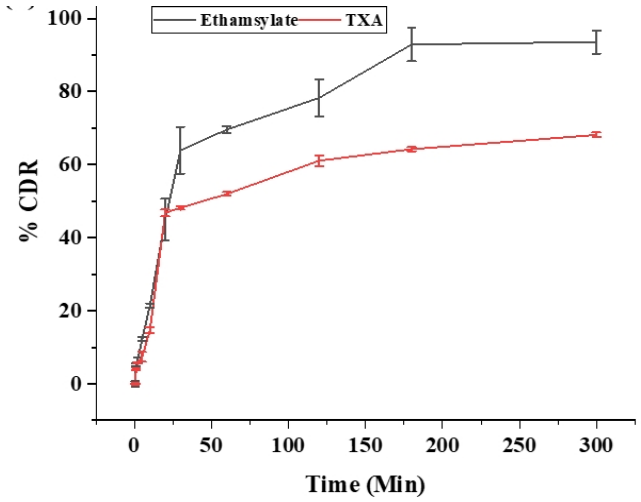

Figure 5.C. 18 Tranexamic acid and ethamsylate drug release profile from dual-drug loaded patches (PVA/CS/TXA-E).

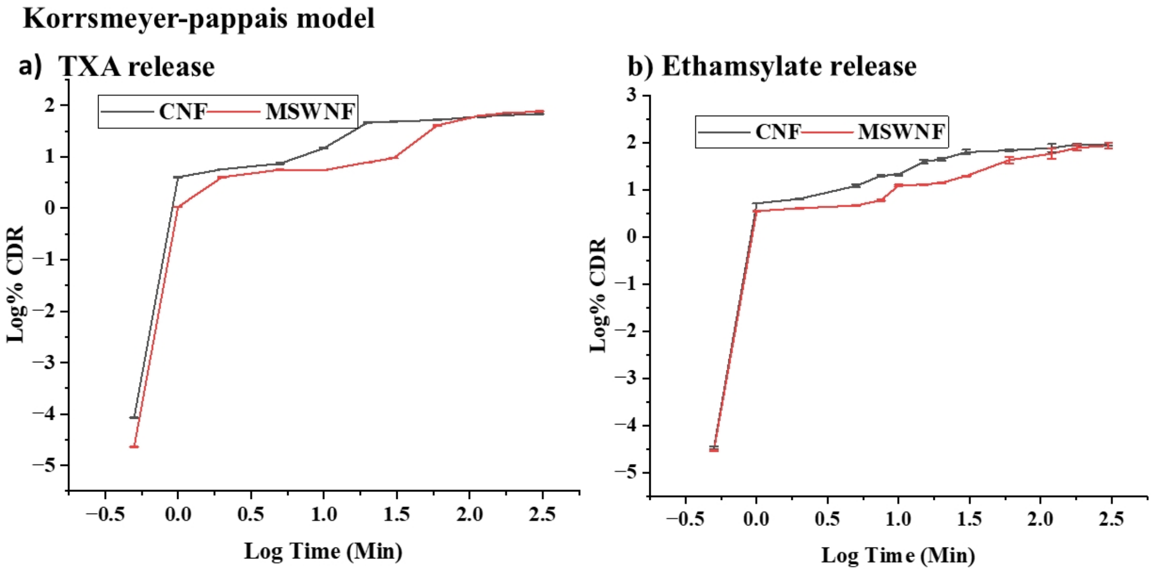

Figure 5.C. 19 Tranexamic acid and ethamsylate drug release profile from control nanofiber and marine shell waste nanofiber (Korsmeyer pappas model).

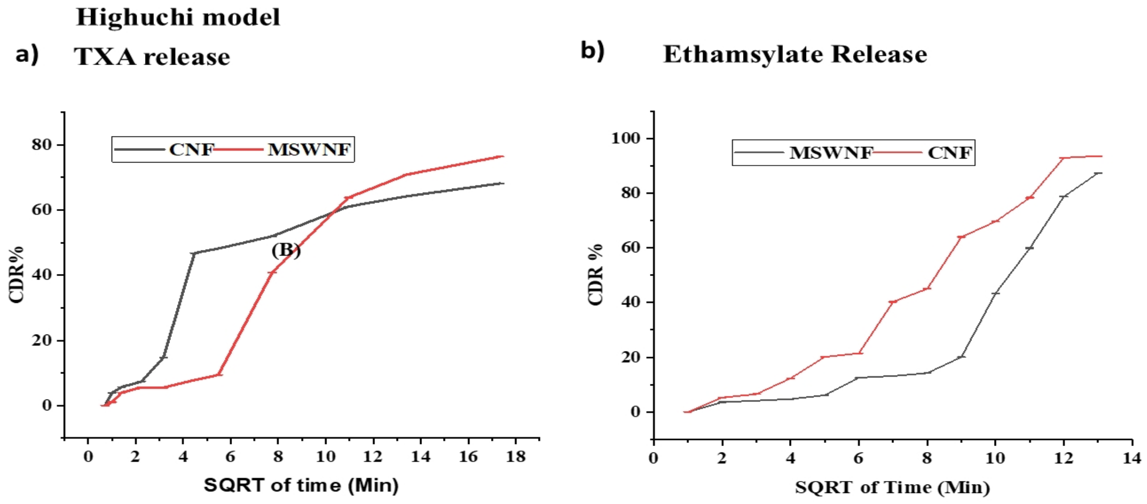

Figure 5.C. 20 Tranexamic acid and ethamsylate drug release profile from control nanofiber and marine shell waste nanofiber (Higuchi model).

In Film-based systems, CNF demonstrated rapid initial release with TXA and ethamsylate reaching 48% and 64% respectively within 30 min due to high porosity and rapid swelling kinetics, followed by sustained release reaching 68% and 94% within 5 h. In contrast, MSWNF showed slower initial release (10% TXA, 20% ethamsylate at 30 min) due to calcium attachment, followed by accelerated release (41% and 43% at 1 h) after calcium dissolution, ultimately achieving 80-90% release within 5 hours as depicted in the **figure 5.C.19 & 5.C.20**. The release kinetics followed the Higuchi model with r² values of 0.935 and 0.978 for TXA and ethamsylate in MSWNF, and 0.80 and 0.87 in CNF, respectively, indicating Fickian diffusion. Drug release kinetics were modulated by calcium presence, with lower ionic concentrations yielding slower initial release due to reduced polymer-solvent interactions at higher ionic strengths. MSWNF exhibited more controlled early-phase drug release than CNF, attributable to Ca^{2+}-chitosan ionic crosslinking that reduces pore size and restricts initial diffusion.

Table 5.C. 4 Tranexamic acid in-vitro drug release with 1% ninhydrin reagent

Formulation	**Zero Order**		**1st order**		**Highuchi model**		**Korshmear pappas model**		
	R^2	K	R^2	K	R^2	K	R^2	k	n
MSWNF	0.76	0.405	0.91	0.676	0.935	7.01	0.59	1.2	1.51
PVA/CS/TXA/E (CNF)	0.59	0.97	0.70	0.59	0.80	6.6	0.52	0.68	1.32

Table 5.C. 5 Ethamsylate in-vitro drug release in 1N HCl solution

Formulation	**Zero Order**		**1st order**		**Highuchi model**		**Korshmear pappas model**		
	R^2	K	R^2	K	R^2		R^2	k	n
MSWNF	0.90	1.006	0.98	1.06	0.9784	6.32	0.54	0.88	1.42
PVA/CS/TXA/E (CNF)	0.67	2.92	0.89	0.96	0.87	7.04	0.49	0.58	1.39

R=Corelation coefficient, K=Release constant, n= Diffusion exponent.

Calcium ion release from MSWNF

We performed EDX characterization to determine the calcium concentration before and after using MSWNF nanofiber in 1X PBS solution for 6 h. After retrieval from PBS, MSWNF nanofiber was heat treated at 40°C for 10 min to prepare a sample for the EDX test. The results are shown in **Figure 5.C.21**. The calcium concentration of MSWNF was 14 and 1.2 in weight percentage before and after the PBS treatment. Similarly, atomic ionic concentration decreased by 200%.

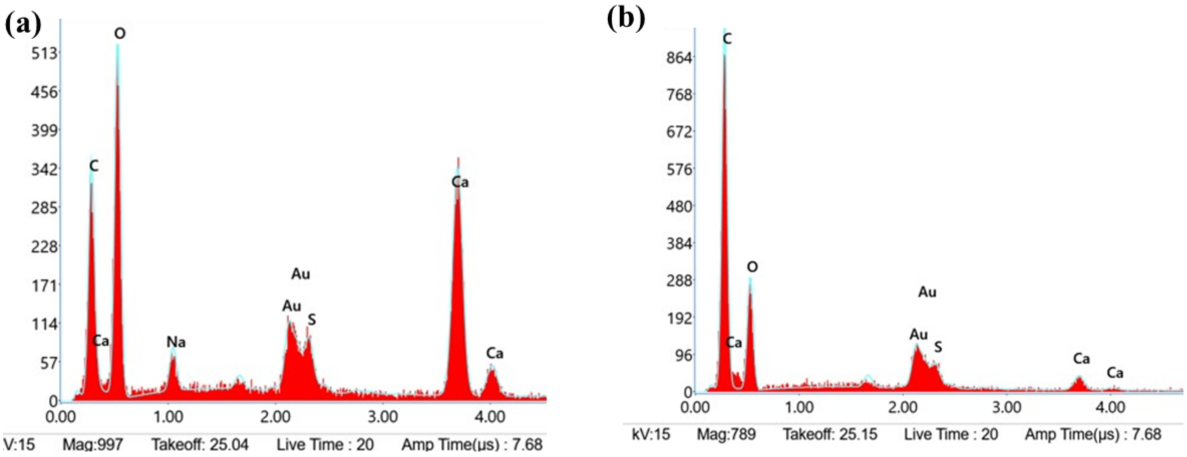

Figure 5.C. 21 EDX spectrum of (a) marine shell waste calcined at 1200 ºC powder-loaded PVA/chitosan nanofibers (MSWNF) and (b) MSWNF after immersion in PBS.

Major Observations

- Hemocompatibility data reveals that all scaffold are highly blood compatible.
- Nontoxic nature of the scaffold in MTT, DAPI, and antibacterial assay.
- MSWNF have significantly slower rebleeding ability and higher clotting performance.
- MSW-T induced powder scaffold have higher effectiveness in upregulating VEGF-A, PDGF, IGF-I in RT-PCR analysis, potentially offering enhanced wound healing.
- The incorporation of therapeutic agents further enhanced hemostatic properties, as evidenced by PVA/CS/TXA-E nanofibers showing significantly faster CT (243±3s) compared to single-drug variants PVA/CS/TXA (381±5s) and PVA/CS/E (280±6s).
- MSWNF demonstrated enhanced coagulation parameters (CT:168±4s, PT: 22±0.6s, aPTT: 52±6s, PRT: 47±1s) compared to CNF (CT:230±11s, PT: 27±0.4s, aPTT: 58±6.6s, PRT: 76±4s).
- Drug release within 3-5 min indicates suitable for stabilising fibrin.

5.D. In-vivo haemostatic study

The haemostatic efficacy of various materials was evaluated using rabbit models through different haemorrhage scenarios. In the femoral artery bleeding model, PVA/CS/MSW-O sponge demonstrated superior haemostatic performance compared to PVA/CS and control groups. The haemostasis time was significantly reduced from 641±22s (control) to 345±15s with PVA/CS/MSW-O, while PVA/CS showed intermediate efficacy at 454±19s shown in the **figure 5.D.1 (a)**. The superior performance of the PVA/CS/MSW-O sponge in reducing hemostasis time was further demonstrated by its impact on blood loss in **Figure 5.D.1 (b).** Blood loss measurements further confirmed this trend, with PVA/CS/MSW-O showing the lowest blood loss (652±13 mg) compared to PVA/CS (772±21 mg) and control groups (889±30 mg). These results suggest that the PVA/CS/MSW-O sponge exhibits enhanced hemostatic efficacy, likely due to its porous microstructure and the presence of calcium derived from natural resources, i.e oyster shells. The interaction between calcium and the CS freeze-dried sponge synergizes to reduce clotting time in the femoral artery injury model. Recent research has shown that nanofibers with high amounts of β-chitosan and $CaCO_3$ demonstrate a similarly fast clotting rate, indicating the potential for enhanced haemostatic efficacy [96]. The reduction in blood clotting time and blood loss observed with the PVA/CS/MSW-O freeze dried sponge may be attributed to the synergistic effects of CS in promoting red blood cell (RBC) and platelet aggregation and Ca in activating the intrinsic, extrinsic, and common pathways of the coagulation cascade, ultimately leading to the formation of a stable fibrin clot. Therefore, the PVA/CS/MSW-O freeze-dried sponge holds the potential to be an effective hemostatic agent.

Table 5.D. 1 Haemostasis-related parameters of marine shell waste derived Ca mineral bound freeze-dried chitosan haemostatic sponge

Sample	**Temperature differences (ºF)**	**Mean arterial pressure (MAP)**	**Survival Duration**
Surgical Gauge	Initial: 102 After: 84	Initial: 64 After: 72	10 ± 2 min
PVA/CS	Initial: 102 After: 86	Initial: 68 After: 74	25 ± 13 min
PVA/CS/MSW-O	Initial: 102 After: 96	Initial: 72 After: 80	126 ± 12 min

Table 5.D. 2 Ex-vivo Haemostatic Efficacy of the scaffold

In vivo Haemostatic Parameter	**Commercial Haemostat AbGel™**	**Control (Gauge)**	**Freeze Dried (Femoral artery incision model)**		**Electrospin nanofiber (Skin incision model)**				
			PVA/CS (FD1)	**PVA/CS/MSW-O (FD2)**	**PVA/CS**	**PVA/CS/TXA**	**PVA/CS/E**	**PVA/CS/TXA-E**	**PVA/CS/TXA-E/MSW-T (MSWNF)**
Bleeding Time(S)	107±15	641±22	454±19	345±15	274±60	130±18	100±25	97±8	75±5
Blood loss(mg)	170±18	889±30	772±21	652±13	380±5	496	224	354±13	121±6

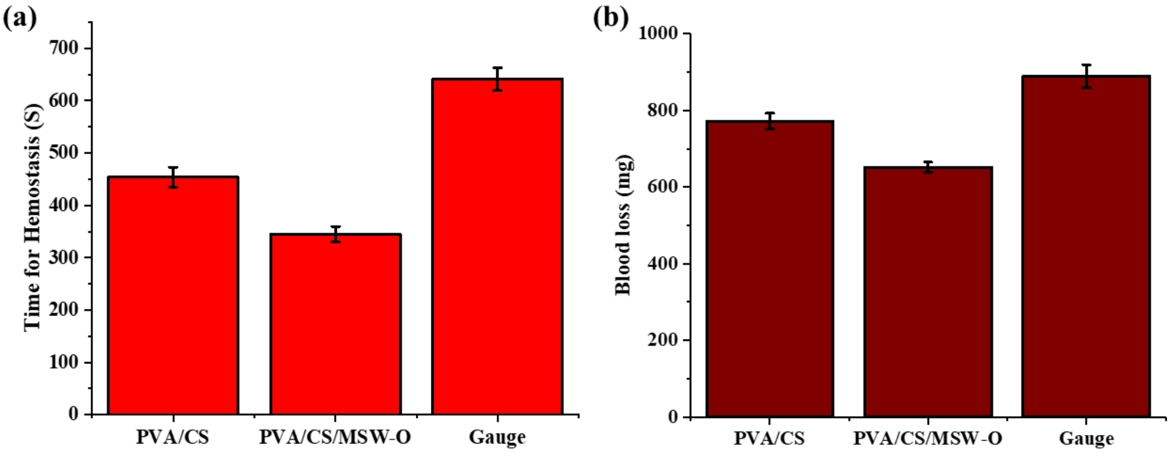

Figure 5.D. 1 In vivo rabbit femoral artery bleeding model for evaluation of freeze dried sponge depicted by (a) In vivo hemostasis time (s), and (b) blood loss (mg).

In skin incision studies, drug-loaded nanofiber patches demonstrated significant improvements in haemostatic efficacy. PVA/CS/TXA-E patches achieved the fastest haemostasis (97±8s) compared to PVA/CS/TXA (130±18s), and PVA/CS/E (100±25s), while the control group required 274±60s and commercial hemostats AbGel™ (107±15s) showed in the **figure 5.D.2**. Similarly, MSWNF showed superior performance with a haemostasis time of 75±5s compared to CNF (97±8s) and control (274±6s). Blood loss measurements reflected this efficacy, with

MSWNF showing minimal blood loss (121mg) compared to CNF (354mg) and control (380mg).

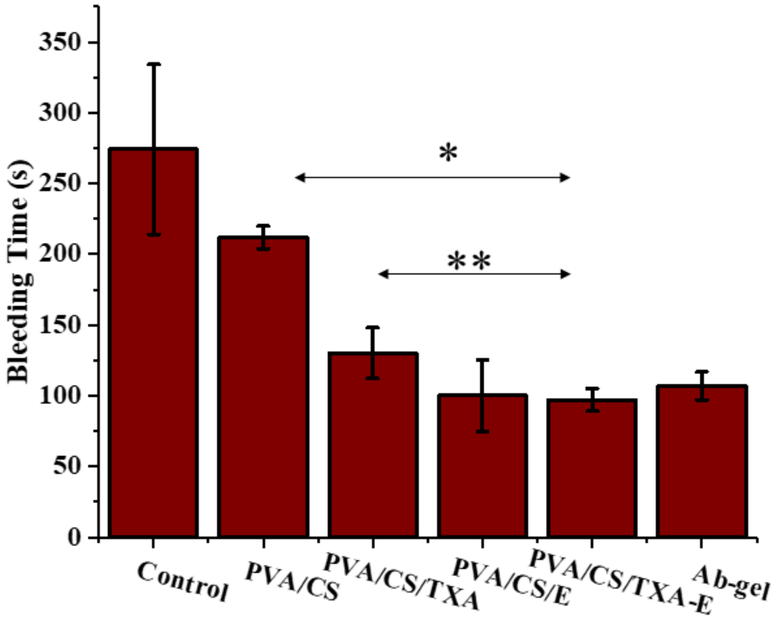

Figure 5.D. 2 Ex-vivo assessment of haemostasis performance of dual drug loaded nanofiber studied bleeding time after application of patches on wounded skin (*p < 0.0001 and **p > 0.01).

SEM analysis of platelet adhesion revealed enhanced blood cell attachment on drug-loaded (PVA/CS/TXA-E) (**figure 5.D.3)** and calcium-containing materials (MSWNF) (**figure 5.D.6**). PVA/CS/TXA-E showed significantly higher platelet and erythrocyte adhesion compared to PVA/CS, while MSWNF demonstrated superior blood cell binding compared to PVA/CS/TXA-E. The activated platelets showed morphological changes and firm adhesion, contributing to fibrin clot development.

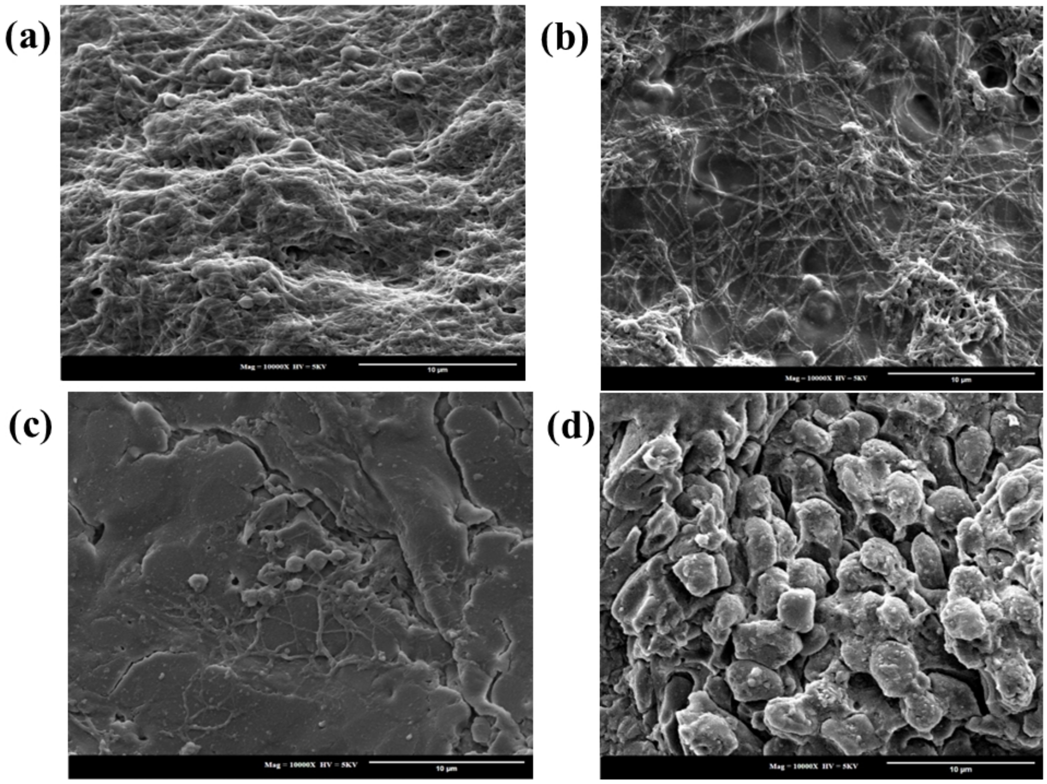

Figure 5.D. 3 Visualization of cellular interaction with dual drug loaded nanofiber patches by SEM images of platelet adhesion on applied patches.

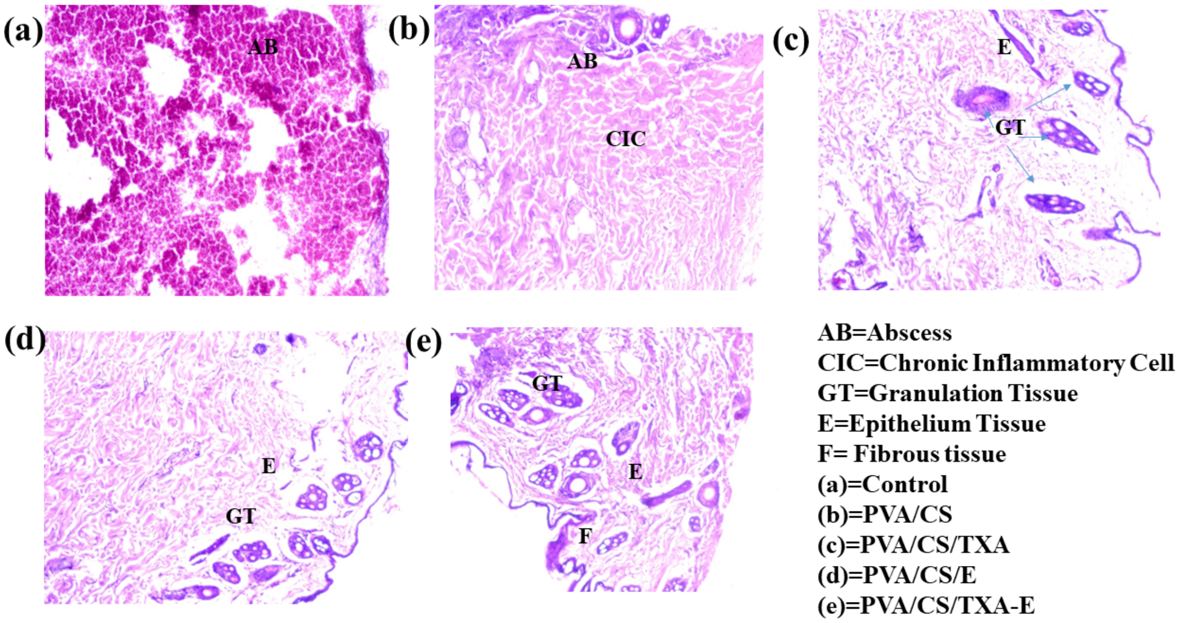

Figure 5.D. 4 Visualization of cellular interaction with dual drug loaded nanofiber patches by Histopathology of rabbit skin after application of patch to arrest bleeding.

A qualitative assessment was done by histopathological examination of the wounded rabbit skin treated with different nanofiber patches and are shown in the **Figure 5.D.4 (a-e).** The lesion skin section of rabbit was cut by the scissor in a way that the tissue specimens contained whole wounded area. In control group, containing only surgical gauge, abscess formation was observed as shown in figure **5.D.4 (a)** without any granulation or capillary tissues. In PVA/CS group moderate number of chronic inflammatory cell and abscess formation were seen. On both PVA/CS/TXA and PVA/CS/E both granulation and fibrous tissue growth was evident. On the dual drug loaded nanofiber, a large number capillaries, granulation tissue and epithelial tissue were visible. Hemostasis is the first stage in the wound healing process. Healthy granulation tissue is pink in colour and that is the indicator of angiogenesis and formation of secondary hemostatic plug. Unhealthy granulation is dark red in colour and often bleeding on contact, it may indicate the development of primary hemostatic plug formation and presence of wound infection. Appearance of pink granulation tissue and bumpy tissue under skin is the notable indication of capillary loop formation tissue with the supply of oxygen and nutrients. Extracellular matrix (ECM) is formed by fibroblasts and proteoglycans to support the development of new blood vessels and collagen. Chitosan-based biomaterials and the degradation products of chitosan have generally been shown to be biocompatible and non-toxic and long-term effect of chitosan products have been satisfactory [97], [98], [99]. ECM also provides strength of tissue elasticity. Fibroblasts change to myofibroblasts to contract and draw the edges of wound together. Fibrin, a robust protein organised in a long fibrous chain, suggests that dual drug-loaded nanofiber patches exhibit rapid blood coagulation. Though rabbits have been the preferred model for assessment of hemostasis performance [100], [101], translation to humans will require further consideration of dose scaling from rabbits to humans, and material design addressing differences in degradation rate of matrices between species along with assessment of biomarkers for wound healing through re-epithelization or cutaneous contraction to account for the inter-species differences in the performance of the materials [102] . To achieve the commercial translation, further studies should be performed with multiple large animal models, examine optimization of dose ratio of the two drugs considering pharmacokinetic-pharmacodynamic modelling, as well as accelerated testing under stress conditions as proposed in certain protocols [103]. Moreover, the drug loaded chitosan formulated in nanoparticulate form or in form nanofiber peanut-form can be extended for the efficient control of internal and surgical bleeding [104], [105].

In the rabbit skin incision, the hemorrhage model, the bleeding time of the control group (274 ± 6 s) was longer than CNF (97 ± 8 s) and MSWNF (75 ± 5 s) ($p<0.0001$)**.** Blood oozing until hemostasis was 0.380 g, 0.354 g, and 0.121 g using a control gauge, CNF, and MSWNF, respectively. These data indicated that MSWNF had more than thrice higher hemostatic effects than CNF or indicator of control. Further, CNF membranes after retrieval showed slight dark coloration, which was more intense for MSWNF. This may be due to the higher number of blood components adhered to the membrane, more extensive fibrin clot formation, or the possible formation of various calcium salts (with various organic or inorganic anions) over time on the membrane surface from blood anions, which further studies should confirm. Calcium ions are released to accelerate the intrinsic pathways of blood coagulation following the topical application of MSWNF nanofiber to the bleeding site. Ca^{2+}, referred to as clotting factor IV, is essential for the orientation and immobilization of clotting enzymes on the surface of fibroblast cells [106]. Moreover, negatively charged platelets or erythrocyte blood cells are drawn to Ca^{2+}. Then, a primary hemostatic plug was formed. Calcium ions play a critical role in blood clotting by facilitating several steps in the coagulation cascade- prothrombin to thrombin conversion, stabilizing the fibrin network, Factor XIII activation, fibrin polymerization, particularly at high-affinity sites in the D-domains, as well as interacting with thromboplastin to activate clotting factors [107], [108].

In-vivo platelet adhesion on CNF and MSWNF nanofiber after applying on rabbit skin hemorrhage to stop bleeding was analyzed by SEM. The images reveal that a small number of platelets and erythrocyte cells adhered to the surface of CNF. In contrast, more blood cells were present on MSWNF, fusing together to form a more uniform, densely packed clot structure. After activation, the platelets were seen to change their sphericity and adhered firmly to the scaffold to develop fibrin clots. Electrospinning creates nanofibers with an exceptionally high surface area-to-volume ratio, providing numerous contact points for blood components and facilitating cell-to-cell interactions [94]. Additionally, the calcium component in MSWNF releases ions upon contact with blood, establishing a positively charged interface that attracts negatively charged blood elements. These calcium ions also serve as crucial cofactors in the coagulation cascade and accelerate fibrin formation. The synergistic effect of chitosan's absorptive properties, the nanofibers' structural advantages, and the calcium-induced biochemical interactions collectively enhance blood cell binding and promote efficient clot formation on the MSWNF nanofiber surface, making it a promising material for advanced wound healing application. Calcium ions are released to accelerate the intrinsic pathways of blood coagulation following the topical application of MSWNF nanofiber to the bleeding site. Moreover, negatively charged platelets or erythrocyte blood cells are drawn to Ca^{2+}. Then, a primary hemostatic plug was formed.

A qualitative assessment was done using the histopathology of the wounded rabbit skin, as shown in **Figure 5.D.5**. In the control group, abscess formation was present, and only a surgical gauge was used to control bleeding. The absence of granulation and capillary tissues was seen in this group. A moderate amount of granulation and epithelial tissue was shown on the skin after treatment with CNF. Many foreign body granulomas in the deep dermis were present on the rabbit skin treated with MSWNF. The presence of fibrous tissues, continued epithelialization, and abundant capillaries in the skin indicated complete blood coagulation. In addition to coagulation, calcium ion-releasing scaffolds play a crucial role in wound healing, as is emphasized by delayed healing and increased incidence of chronic wounds observed in animals with calcium-deficient diets or those consuming calcium-chelating agents. Extracellular calcium mediates epidermal homeostasis through its receptor that regulates calcium signaling to promote keratinocyte adhesion, differentiation, and survival through intracellular calcium signaling and E-cadherin pathways. In contrast, the expression of genes essential for keratinocyte differentiation, such as cytokeratin and transglutaminase, are also regulated by Ca^{2+}. The rapid propagation of calcium ions at the wound site initiates epithelial repair by transcription-independent damage signals. Calcium is a central signaling molecule in pathways regulating angiogenesis as mitogens trigger calcium influx through ion channels or release from the endoplasmic reticulum. Thus, augmenting hemostatic patches with calcium sources can produce dual benefits in hemostasis and subsequent healing [109]. The presence of fibrous tissues, continued epithelialization, and abundant capillaries in the skin indicated complete blood coagulation. Histological examination thereafter confirmed that the developed material promoted wound healing.

MSWNF is, therefore, poised to provide a potential biomaterial therapeutic solution for treating traumatic hemorrhage. agents like Hemcon™, MSWNF has a PRT value of approximately 55 s, similar to the performance of some commercially available hemostatic like HemCon™. However, HemCon™ gauzes rely solely on cell aggregation induced by the positive charges of chitosan, which can lead to hemolysis and fail to provide sufficient mechanical compression in certain bleeding wounds. Certain inorganic hemostatic agents like the QuickClot gauzes comprise kaolin and are known to cause thermal injury or tissue necrosis [110]. As a result, MSWNF represents a more sustainable option with promising performance parameters.

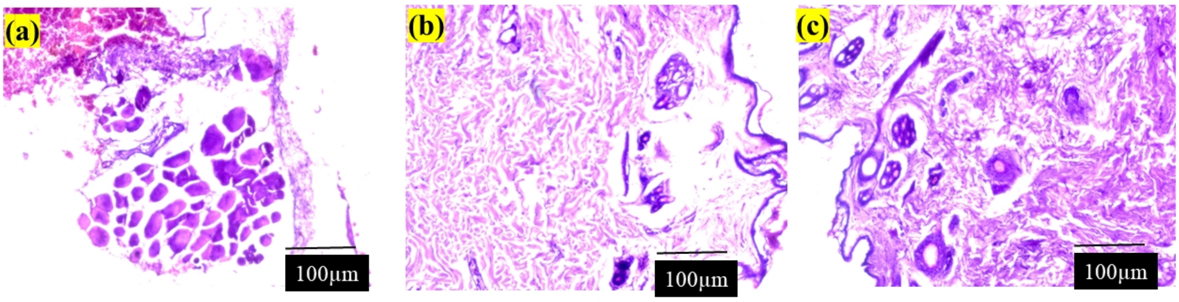

Figure 5.D. 5 Histopathology of wounded skin treated with (a) control, (b) CNF (PVA/chitosan) and (c) MSWNF (PVA/chitosan nanofibers loaded with marine shell waste calcined at 1200 °C powder).

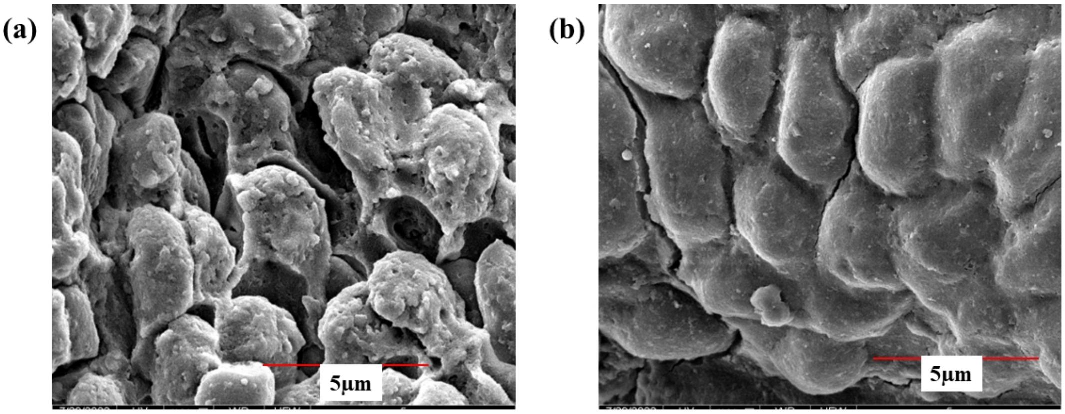

Figure 5.D. 6 Visualization of platelet adhesion in (a) CNF and (b) MSWNF by scanning electron microscopy.

Major Observations

- This research demonstrated that OS waste can be converted into a high value added product suitable for prehospital development.
- Extracted bio-recycled and sustainable MSW was thermally treated to obtain a mixed phase of CaO, $Ca(OH)_2$, confirmed by FTIR, XRD analysis.
- SEM micrograph demonstrated the formation of uniform, bead free flattened nanofiber.
- Mechanically robust but flexible hemostatic biomaterials are produced from natural resources.
- A rabbit skin incision model demonstrated that MSWNF could decrease bleeding time to 75±5s.
- Histopathological assessment shows wounded rabbit skin confirmed the presence of fibrous tissue, continued epithelization, abundance of capillaries after 7 days of application.

5.E. Comprehensive report of the comparative performances of scaffolds.

In PVA/CS nanofiber production, the proportion of each polymer, their viscosity, and concentration play vital roles in **Table 5.E.1**. Despite maintaining consistent total polymer concentration across different CS/PVA ratios, fiber diameter variations directly related to CS content. Increased CS levels enhance solution charge density, causing greater bending in the ejected jet. The strong hydrogen bonds between NH_2 and OH groups in CS chains create high-viscosity solutions unsuitable for electrospinning, making pure chitosan unfavourable for this process. Analysis of electrospun nanofibers showed that PVA/CS mass ratios of 2:8 and 3:7 produced fibers with diameters of 147±12 nm and 163±34 nm respectively. Adding MSW-T powder increased polymer concentration, reducing diameter to 120±20 nm. Optimal polymer viscosity for nanofiber production ranges between 500-1500 CP.

Table 5.E. 1 Fabrication of electrospin nanofiber of polyvinyle alcohol and chitosan formulation

Sample	Material PVA:CS	Viscosity (CP)	Polymer concentration (g/100mL)	Fiber diameter (nm)
1	PVA:CS (100:0)	1557	12	100-364
2	PVA:CS (90:10)	1326	11	150±17
3	PVA:CS (80:20)	1056	10	147±12
4	PVA:CS (70:30)	906	9	163±34
5	PVA:CS (60:40)	812	8	Beeded 180±17
6	PVA:CS (50:50)	724	7	Beeded 286±63
7	PVA:CS (0:100)	243	2	Not produce
8	PVA:CS (80:20)+ 30mg/mL TXA	1068	10	247±12
9	PVA:CS (80:20)+ 30mg/mL E	1084	10	250±17

Sample	Material PVA:CS	Viscosity (CP)	Polymer concentration (g/100mL)	Fiber diameter (nm)
10	PVA:CS (80:20)+ 30mg/ml txa+30mg/ml E	1012	9.3	347±22
11	PVA:CS (80:20)+30mg/ ml txa+30mg/ml E+5mg/ml MSW-T	658	11.7	120±12

In-vitro hemostatic properties of different formulated scaffold were evaluated by measuring blood clotting time (CT), prothrombin time (PT), activated partial thromboplastin time (APTT), platelet recalcination time (PRT) in **Table 5.E.2**. For clotting time analysis both PVA/CS/MSW-O sponge and PVA/CS/TXA-E/MSW-T (MSWNF) nanofiber showed faster blood clotting than air dried scaffold. MSWNF showed excellent clotting time due to presence of hemostatic drug and calcium enriched powder which accelerated the clotting pathway. It also presented a more uniform, homogenious surface texture promoting more extensive platelet spreading and aggregation. For PVA/CS/MSW-O, CT reduction is attributed to porous chitosan microsphere network structure as well as sequestration of Ca ion which promote rapid blood absorption and local concentration of blood clotting factor. In addition, PT and APTT results indicate a higher propensity of MSWNF to interfere with the extrinsic pathway than the intrinsic coagulation pathway than sponge. However, PT values for air dried flim showed lesser due to presence of rich Ca ion. The Prothrombin Time (PRT) decreased for MSWNF because platelets from bleeding individuals interact more effectively with the underlying network structure compared to a sponge. MSWNF nanofibers measured 120 ± 20 nm in diameter positively affect clot formation because their extensive surface area enhances platelet adhesion and clustering, which subsequently influences the development of fiber structures than other nanofibers.

Table 5.E. 2 Comparative study of invitro hemostasis.

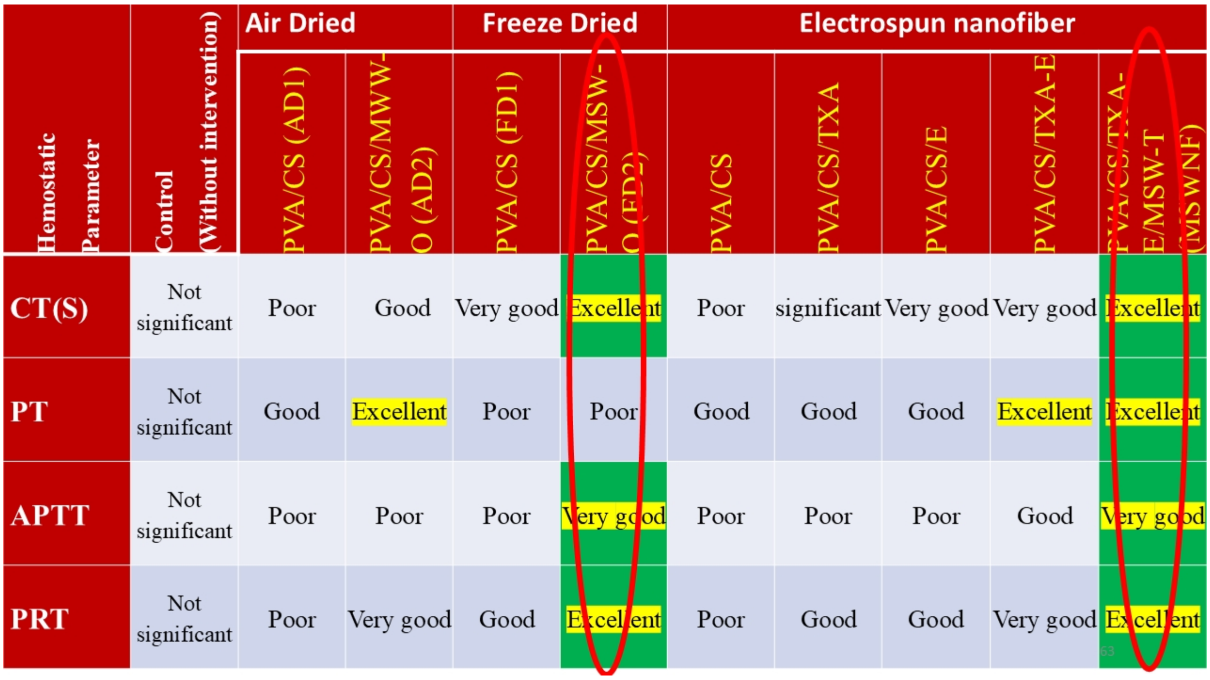

Hemostatic Parameter	Control (Without intervention)	Air Dried		Freeze Dried		Electrospun nanofiber				
		PVA/CS (AD1)	PVA/CS/MWW-O (AD2)	PVA/CS (FD1)	PVA/CS/MSW-O (FD2)	PVA/CS	PVA/CS/TXA	PVA/CS/E	PVA/CS/TXA-E	PVA/CS/TXA-E/MSW-T (MSWNF)
CT(S)	Not significant	Poor	Good	Very good	Excellent	Poor	significant	Very good	Very good	Excellent
PT	Not significant	Good	Excellent	Poor	Poor	Good	Good	Good	Excellent	Excellent
APTT	Not significant	Poor	Poor	Poor	Very good	Poor	Poor	Poor	Good	Very good
PRT	Not significant	Poor	Very good	Good	Excellent	Poor	Good	Good	Very good	Excellent

Table 5.E.3 showed that MSWNF nanofiber demonstrated superior hemostatic effectiveness in the rabbit skin incision model. Blood seepage prior to hemostasis was significantly reduced with MSWNF nanofiber. Upon removal, the material displayed dark coloration, potentially resulting from increased blood component adhesion, more comprehensive fibrin clot development, or calcium salt formation.

Table 5.E. 3 Comparative study of in-vivo hemostasis.

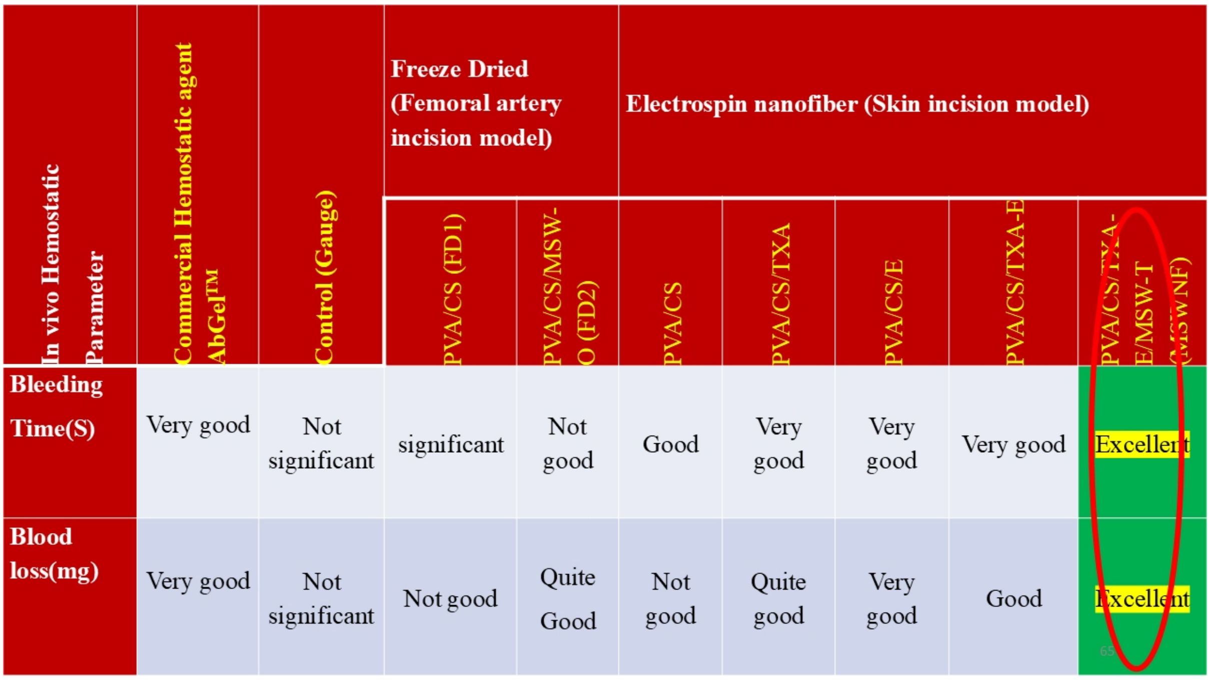

In vivo Hemostatic Parameter	Commercial Hemostatic agent AbGel™	Control (Gauge)	Freeze Dried (Femoral artery incision model)		Electrospin nanofiber (Skin incision model)				
			PVA/CS (FD1)	PVA/CS/MSW-O (FD2)	PVA/CS	PVA/CS/TXA	PVA/CS/E	PVA/CS/TXA-E	PVA/CS/TXA-E/MSW-T (MSWNF)
Bleeding Time(S)	Very good	Not significant	significant	Not good	Good	Very good	Very good	Very good	Excellent
Blood loss(mg)	Very good	Not significant	Not good	Quite Good	Not good	Quite good	Very good	Good	Excellent

The PVA/CS/MSW-T sponge's exceptional ability to reduce hemostasis time was further evidenced by its significant impact on blood loss reduction. These findings indicate that the PVA/CS/MSW-T sponge provides enhanced hemostatic performance, likely attributed to its porous microstructure and the presence of naturally-derived calcium (such as from oyster shell), making it particularly valuable for critical high-pressure emergency situations and trauma care.

References:

[1] X. Inthapanya, S. Wu, Z. Han, G. Zeng, M. Wu, and C. Yang, “Adsorptive removal of anionic dye using calcined oyster shells: isotherms, kinetics, and thermodynamics,” *Environmental Science and Pollution Research*, vol. 26, no. 6, pp. 5944–5954, Feb. 2019, doi: 10.1007/s11356-018-3980-0.

[2] R. K. Blundell and P. Licence, “Quaternary ammonium and phosphonium based ionic liquids: A comparison of common anions,” *Physical Chemistry Chemical Physics*, vol. 16, no. 29, pp. 15278–15288, Aug. 2014, doi: 10.1039/c4cp01901f.

[3] S. W. Lee, Y. N. Jang, K. W. Ryu, S. C. Chae, Y. H. Lee, and C. W. Jeon, “Mechanical characteristics and morphological effect of complex crossed structure in biomaterials: Fracture mechanics and microstructure of chalky layer in oyster shell,” *Micron*, vol. 42, no. 1, pp. 60–70, Jan. 2011, doi: 10.1016/j.micron.2010.08.001.

[4] S. L. Stipp and M. F. Hochella Jr, “Structure and bonding environments at the calcite surface as observed with X-ray photoelectron spectroscopy (XPS) and low energy electron diffraction (LEED),” 1991.

[5] R. Ismail *et al.*, “The potential use of green mussel (Perna Viridis) shells for synthetic calcium carbonate polymorphs in biomaterials,” *J Cryst Growth*, vol. 572, Oct. 2021, doi: 10.1016/j.jcrysgro.2021.126282.

[6] J. H. Huh *et al.*, “The use of oyster shell powders for water quality improvement of lakes by algal blooms removal,” *Journal of the Korean Ceramic Society*, vol. 53, no. 1, pp. 1–6, Jan. 2016, doi: 10.4191/kcers.2016.53.1.1.

[7] D. Render *et al.*, “Biomaterial-Derived Calcium Carbonate Nanoparticles for Enteric Drug Delivery,” *J Nanomater*, vol. 2016, 2016, doi: 10.1155/2016/3170248.

[8] M. Ikram *et al.*, “Facile Synthesis of La- and Chitosan-Doped CaO Nanoparticles and Their Evaluation for Catalytic and Antimicrobial Potential with Molecular Docking Studies,” *ACS Omega*, vol. 7, no. 32, pp. 28459–28470, Aug. 2022, doi: 10.1021/acsomega.2c02790.

[9] S. H. Teo, Y. H. Taufiq-Yap, U. Rashid, and A. Islam, “Hydrothermal effect on synthesis, characterization and catalytic properties of calcium methoxide for biodiesel production from crude Jatropha curcas,” *RSC Adv*, vol. 5, no. 6, pp. 4266–4276, 2015, doi: 10.1039/c4ra11936c.

[10] K. Sadeghi, S. Thanakkasaranee, I. J. Lim, and J. Seo, “Calcined marine coral powders as a novel ecofriendly antimicrobial agent,” *Materials Science and Engineering C*, vol. 107, Feb. 2020, doi: 10.1016/j.msec.2019.110193.

[11] K. Park *et al.*, “Effects of calcination temperature on morphological and crystallographic properties of oyster shell as biocidal agent,” *Int J Appl Ceram Technol*, vol. 18, no. 2, pp. 302–311, Mar. 2021, doi: 10.1111/ijac.13647.

[12] V. Gupta, D. K. Pathak, S. Siddique, R. Kumar, and S. Chaudhary, “Study on the mineral phase characteristics of various Indian biomass and coal fly ash for its use in masonry construction products,” *Constr Build Mater*, vol. 235, Feb. 2020, doi: 10.1016/j.conbuildmat.2019.117413.

[13] T. Schmida and P. Dariz, “Shedding light onto the spectra of lime: Raman and luminescence bands of CaO, Ca(OH)2 and CaCO3,” *Journal of Raman Spectroscopy*, vol. 46, no. 1, pp. 141–146, Nov. 2014, doi: 10.1002/jrs.4622.

[14] G. Vanthana Sree, P. Nagaraaj, K. Kalanidhi, C. A. Aswathy, and P. Rajasekaran, “Calcium oxide a sustainable photocatalyst derived from eggshell for efficient photo-degradation of organic pollutants,” *J Clean Prod*, vol. 270, Oct. 2020, doi: 10.1016/j.jclepro.2020.122294.

[15] P. Ghods, O. B. Isgor, J. R. Brown, F. Bensebaa, and D. Kingston, “XPS depth profiling study on the passive oxide film of carbon steel in saturated calcium hydroxide solution and the effect of chloride on the film properties,” *Appl Surf Sci*, vol. 257, no. 10, pp. 4669–4677, Mar. 2011, doi: 10.1016/j.apsusc.2010.12.120.

[16] H. Maachou, M. J. Genet, D. Aliouche, C. C. Dupont-Gillain, and P. G. Rouxhet, “XPS analysis of chitosan-hydroxyapatite biomaterials: From elements to compounds,” *Surface and Interface Analysis*, vol. 45, no. 7, pp. 1088–1097, Jul. 2013, doi: 10.1002/sia.5229.

[17] P. Ghods, O. B. Isgor, J. R. Brown, F. Bensebaa, and D. Kingston, “XPS depth profiling study on the passive oxide film of carbon steel in saturated calcium hydroxide solution and the effect of chloride on the film properties,” *Appl Surf Sci*, vol. 257, no. 10, pp. 4669–4677, Mar. 2011, doi: 10.1016/j.apsusc.2010.12.120.

[18] G. S. Kamble and Y. C. Ling, “Solvothermal synthesis of facet-dependent BiVO4 photocatalyst with enhanced visible-light-driven photocatalytic degradation of organic pollutant: assessment of toxicity by zebrafish embryo,” *Sci Rep*, vol. 10, no. 1, Dec. 2020, doi: 10.1038/s41598-020-69706-4.

[19] A. H. Shah and M. A. Rather, “Effect of calcination temperature on the crystallite size, particle size and zeta potential of TiO2nanoparticles synthesized via polyol-mediated method,” in *Materials Today: Proceedings*, Elsevier Ltd, 2021, pp. 482–488. doi: 10.1016/j.matpr.2020.10.199.

[20] B. Tryba, M. Piszcz, and A. W. Morawski, “Photocatalytic activity of TiO2 - WO3 Composites,” *International Journal of Photoenergy*, vol. 2009, 2009, doi: 10.1155/2009/297319.

[21] P. Moulin and H. Roques, “Zeta potential measurement of calcium carbonate,” *J Colloid Interface Sci*, vol. 261, no. 1, pp. 115–126, May 2003, doi: 10.1016/S0021-9797(03)00057-2.

[22] D. Alidoust, M. Kawahigashi, S. Yoshizawa, H. Sumida, and M. Watanabe, “Mechanism of cadmium biosorption from aqueous solutions using calcined oyster shells,” *J Environ Manage*, vol. 150, pp. 103–110, Mar. 2015, doi: 10.1016/j.jenvman.2014.10.032.

[23] J.-Y. Gal, J.-C. Bollingerb, H. Tolosa, and N. Gache, “Calcium carbonate solubility: a reappraisal of scale formation and inhibition,” 1996.

[24] J. Y. Park, K. H. Kyung, K. Tsukada, S. H. Kim, and S. Shiratori, “Biodegradable polycaprolactone nanofibres with β-chitosan and calcium carbonate produce a hemostatic effect,” *Polymer (Guildf)*, vol. 123, pp. 194–202, Aug. 2017, doi: 10.1016/j.polymer.2017.07.013.

[25] T. Schmida and P. Dariz, “Shedding light onto the spectra of lime: Raman and luminescence bands of CaO, Ca(OH)2 and CaCO3,” *Journal of Raman Spectroscopy*, vol. 46, no. 1, pp. 141–146, Nov. 2014, doi: 10.1002/jrs.4622.

[26] D. Suflet and others, “Dual Cross-Linked Chitosan/PVA Hydrogels Containing Silver Nanoparticles with Antimicrobial Properties,” *Pharmaceutics*, vol. 13, p. 1461, Sep. 2021, doi: 10.3390/pharmaceutics13091461.

[27] M. Mozafari *et al.*, “Synthesis and characterization of electrospun polyvinyl alcohol nanofibrous scaffolds modified by blending with chitosan for neural tissue engineering,” *Int J Nanomedicine*, p. 25, Jan. 2012, doi: 10.2147/ijn.s25376.

[28] J. Varshosaz, Z. Choopannejad, M. Minaiyan, and A. Z. Kharazi, “Rapid hemostasis by nanofibers of polyhydroxyethyl methacrylate/polyglycerol sebacic acid: An in vitro / in vivo study,” *J Appl Polym Sci*, vol. 138, no. 5, Feb. 2021, doi: 10.1002/app.49785.

[29] S. Muthu and A. Prabhakaran, “Vibrational spectroscopic study and NBO analysis on tranexamic acid using DFT method,” *Spectrochim Acta A Mol Biomol Spectrosc*, vol. 129, pp. 184–192, Aug. 2014, doi: 10.1016/j.saa.2014.03.050.

[30] K. Park *et al.*, “Effects of calcination temperature on morphological and crystallographic properties of oyster shell as biocidal agent,” *Int J Appl Ceram Technol*, vol. 18, no. 2, pp. 302–311, Mar. 2021, doi: 10.1111/ijac.13647.

[31] J. Guo, Q. Liu, J. Cheng, X. Fu, Y. Zhang, and H. Yang, “Hemostatic cotton based on biocompatible poly(vinyl alcohol)/soluble starch-fish skin collagen composites,” *Mater Today Commun*, vol. 32, Aug. 2022, doi: 10.1016/j.mtcomm.2022.103812.

[32] A. T. Hang, B. Tae, and J. S. Park, “Non-woven mats of poly(vinyl alcohol)/chitosan blends containing silver nanoparticles: Fabrication and characterization,” *Carbohydr Polym*, vol. 82, no. 2, pp. 472–479, Sep. 2010, doi: 10.1016/j.carbpol.2010.05.016.

[33] L. Lacaze *et al.*, “Tensile strength of biological fibrin sealants: A comparative study,” *Journal of Surgical Research*, vol. 176, no. 2, pp. 455–459, Aug. 2012, doi: 10.1016/j.jss.2011.11.1017.

[34] N. S. Sambudi, M. G. Kim, and S. Bin Park, “The formation of web-like connection among electrospun chitosan/PVA fiber network by the reinforcement of ellipsoidal calcium carbonate,” *Materials Science and Engineering C*, vol. 60, pp. 518–525, Mar. 2016, doi: 10.1016/j.msec.2015.11.079.

[35] P. Arpornmaeklong, P. Pripatnanont, and N. Suwatwirote, “Properties of chitosan-collagen sponges and osteogenic differentiation of rat-bone-marrow stromal cells,” *Int J Oral Maxillofac Surg*, vol. 37, no. 4, pp. 357–366, Apr. 2008, doi: 10.1016/j.ijom.2007.11.014.

[36] N. K. Sari, D. J. Indrani, C. Johan, and J. E. M. Corputty, “Evaluation of chitosan-hydroxyapatite-collagen composite strength as scaffold material by immersion in simulated body fluid,” in *Journal of Physics: Conference Series*, Institute of Physics Publishing, Aug. 2017. doi: 10.1088/1742-6596/884/1/012116.

[37] G. Patil, A. Torris, P. R. Suresha, S. Jadhav, M. V. Badiger, and V. Ghormade, “Design and synthesis of a new topical agent for halting blood loss rapidly: A multimodal chitosan-gelatin

xerogel composite loaded with silica nanoparticles and calcium," *Colloids Surf B Biointerfaces*, vol. 198, Feb. 2021, doi: 10.1016/j.colsurfb.2020.111454.

[38] Y. F. Zhao *et al.*, "Synthetic poly(vinyl alcohol)-chitosan as a new type of highly efficient hemostatic sponge with blood-triggered swelling and high biocompatibility," *J Mater Chem B*, vol. 7, no. 11, pp. 1855–1866, 2019, doi: 10.1039/C8TB03181A.

[39] G. Patil, R. Pawar, S. Jadhav, and V. Ghormade, "A chitosan based multimodal 'soft' hydrogel for rapid hemostasis of non-compressible hemorrhages and its mode of action," *Carbohydrate Polymer Technologies and Applications*, vol. 4, Dec. 2022, doi: 10.1016/j.carpta.2022.100237.

[40] Q. Y. Yuan, L. Yang, T. T. Li, B. C. Shiu, C. W. Lou, and J. H. Lin, "Study on the regulation of degradation performance of polyethylene glycol nanofiber membranes by urushiol," *Polym Test*, vol. 128, Nov. 2023, doi: 10.1016/j.polymertesting.2023.108240.

[41] V. Deineka *et al.*, "Hemostatic and tissue regeneration performance of novel electrospun chitosan-based materials," *Biomedicines*, vol. 9, no. 6, 2021, doi: 10.3390/biomedicines9060588.

[42] H. Herliana, H. Y. Yusuf, A. Laviana, G. Wandawa, and A. Cahyanto, "Characterization and Analysis of Chitosan-Gelatin Composite-Based Biomaterial Effectivity as Local Hemostatic Agent: A Systematic Review," Feb. 01, 2023, *MDPI*. doi: 10.3390/polym15030575.

[43] S. Droge and K. U. Goss, "Effect of sodium and calcium cations on the ion-exchange affinity of organic cations for soil organic matter," *Environ Sci Technol*, vol. 46, no. 11, pp. 5894–5901, Jun. 2012, doi: 10.1021/es204449r.

[44] H. Wu *et al.*, "Preparation and Properties of Biocomposite Films Based on Poly(vinyl alcohol) Incorporated with Eggshell Powder as a Biological Filler," *J Polym Environ*, vol. 28, no. 7, pp. 2020–2028, Jul. 2020, doi: 10.1007/s10924-020-01747-2.

[45] Z. Li *et al.*, "Superhydrophobic hemostatic nanofiber composites for fast clotting and minimal adhesion," *Nat Commun*, vol. 10, no. 1, Dec. 2019, doi: 10.1038/s41467-019-13512-8.

[46] P. Yu and W. Zhong, "Hemostatic materials in wound care," 2021, *Oxford University Press*. doi: 10.1093/burnst/tkab019.

[47] Y. Zheng, J. Wu, Y. Zhu, and C. Wu, "Inorganic-based biomaterials for rapid hemostasis and wound healing," Nov. 30, 2022, *Royal Society of Chemistry*. doi: 10.1039/d2sc04962g.

[48] M. Mecwan *et al.*, "Recent advances in biopolymer-based hemostatic materials," 2022, *Oxford University Press*. doi: 10.1093/rb/rbac063.

[49] Z. Li *et al.*, "Superhydrophobic hemostatic nanofiber composites for fast clotting and minimal adhesion," *Nat Commun*, vol. 10, no. 1, Dec. 2019, doi: 10.1038/s41467-019-13512-8.

[50] X. Hu, L. Long, T. Gong, J. Zhang, J. Yan, and Y. Xue, "Enhanced alginate-based microsphere with the pore-forming agent for efficient removal of Cu(II)," *Chemosphere*, vol. 240, Feb. 2020, doi: 10.1016/j.chemosphere.2019.124860.

[51] Nasikhudin, A. Kusumaatmaja, M. Diantoro, A. Kusumaatmaja, and K. Triyana, “Effect of blend ratio on morphology and swelling properties of PVA/chitosan nanofibers,” in *Materials Science Forum*, Trans Tech Publications Ltd, 2017, pp. 79–84. doi: 10.4028/www.scientific.net/MSF.901.79.

[52] M. Koosha and H. Mirzadeh, “Electrospinning, mechanical properties, and cell behavior study of chitosan/PVA nanofibers,” *J Biomed Mater Res A*, vol. 103, no. 9, pp. 3081–3093, Sep. 2015, doi: 10.1002/jbm.a.35443.

[53] I. Greenfeld, X. Sui, and H. D. Wagner, “Stiffness, Strength, and Toughness of Electrospun Nanofibers: Effect of Flow-Induced Molecular Orientation,” *Macromolecules*, vol. 49, no. 17, pp. 6518–6530, Sep. 2016, doi: 10.1021/acs.macromol.6b01204.

[54] “WO2018080692A1”.

[55] “Designation: F 756-00 Standard Practice for Assessment of Hemolytic Properties of Materials 1.” [Online]. Available: www.astm.org

[56] J. W. Pickering and F. E. Taylor, “Blood coagulation, anti-coagulants and hæmolysis,” *Proceedings of the Royal Society of London. Series B, Containing Papers of a Biological Character*, vol. 97, no. 680, pp. 1–19, Oct. 1924, doi: 10.1098/rspb.1924.0040.

[57] O. Yalcin, B. Eglenen, M. Turkay, G. Yavas, E. Ugurel, and P. Connes, “The role of calcium in active regulation of erythrocyte deformability,” *The FASEB Journal*, vol. 30, no. S1, Apr. 2016, doi: 10.1096/FASEBJ.30.1_SUPPLEMENT.947.4.

[58] Y. C. Chen, C. L. Lin, C. T. Li, and D. F. Hwang, “Structural transformation of oyster, hard clam, and sea urchin shells after calcination and their antibacterial activity against foodborne microorganisms,” *Fisheries Science*, vol. 81, no. 4, pp. 787–794, Jul. 2015, doi: 10.1007/s12562-015-0892-5.

[59] A. C. Egil, B. Ozdemir, S. K. Gunduz, M. Altıkatoglu-Yapaoz, Y. Budama-Kilinc, and E. Mostafavi, “Chitosan/calcium nanoparticles as advanced antimicrobial coating for paper documents,” *Int J Biol Macromol*, vol. 215, pp. 521–530, Aug. 2022, doi: 10.1016/J.IJBIOMAC.2022.06.142.

[60] E. Ferraz, J. A. F. Gamelas, J. Coroado, C. Monteiro, and F. Rocha, “Recycling Waste Seashells to Produce Calcitic Lime: Characterization and Wet Slaking Reactivity,” *Waste Biomass Valorization*, vol. 10, no. 8, pp. 2397–2414, Aug. 2019, doi: 10.1007/s12649-018-0232-y.

[61] A. Görlach, K. Bertram, S. Hudecova, and O. Krizanova, “Calcium and ROS: A mutual interplay,” Dec. 01, 2015, *Elsevier B.V.* doi: 10.1016/j.redox.2015.08.010.

[62] Y. Yan, C. L. Wei, W. R. Zhang, H. P. Cheng, and J. Liu, “Cross-talk between calcium and reactive oxygen species signaling,” Jul. 2006. doi: 10.1111/j.1745-7254.2006.00390.x.

[63] S. Thanakkasaranee, K. Sadeghi, I. J. Lim, and J. Seo, “Effects of incorporating calcined corals as natural antimicrobial agent into active packaging system for milk storage,” *Materials Science and Engineering C*, vol. 111, Jun. 2020, doi: 10.1016/j.msec.2020.110781.

[64] A. Roy, S. S. Gauri, M. Bhattacharya, and J. Bhattacharya, “Antimicrobial activity of CaO nanoparticles,” *J Biomed Nanotechnol*, vol. 9, no. 9, pp. 1570–1578, Jan. 2013, doi: 10.1166/jbn.2013.1681.

[65] F. Wang *et al.*, “Cytotoxicity and Effect of Topical Application of Tranexamic Acid on Human Fibroblast in Spine Surgery,” *World Neurosurg*, vol. 153, pp. e380–e391, Sep. 2021, doi: 10.1016/j.wneu.2021.06.125.

[66] M. Lootsik, R. Bilyy, M. Lutsyk, R. S.-B. Acta, and undefined 2015, “Preparation of chitosan with high blood clotting activity and its hemostatic potential assessment,” *cyberleninka.ru*, doi: 10.15407/biotech8.06.032.

[67] W. He *et al.*, “CaCO3–Chitosan Composites Granules for Instant Hemostasis and Wound Healing,” *Materials*, vol. 14, no. 12, p. 3350, Jun. 2021, doi: 10.3390/ma14123350.

[68] M. Świerczyńska *et al.*, “Blood Coagulation Activities and Influence on DNA Condition of Alginate—Calcium Composites Prepared by Freeze-Drying Technique,” *Mar Drugs*, vol. 22, no. 9, p. 415, Sep. 2024, doi: 10.3390/md22090415.

[69] Y. Zhang, Y. Qiu, … A. B.-P. of the, and undefined 2018, “Platelet integrins exhibit anisotropic mechanosensing and harness piconewton forces to mediate platelet aggregation,” *National Acad Sciences*, vol. 111, no. 40, pp. 14430–14435, Oct. 2014, doi: 10.1073/pnas.1322917111.

[70] Y. Zhou *et al.*, “Acetate chitosan with CaCO3 doping form tough hydrogel for hemostasis and wound healing,” *Polym Adv Technol*, vol. 30, no. 1, pp. 143–152, Jan. 2019, doi: 10.1002/pat.4452.

[71] N. D. Sanandiya, S. Lee, S. Rho, H. Lee, I. S. Kim, and D. S. Hwang, “Tunichrome-inspired pyrogallol functionalized chitosan for tissue adhesion and hemostasis,” *Carbohydr Polym*, vol. 208, pp. 77–85, Mar. 2019, doi: 10.1016/j.carbpol.2018.12.017.

[72] H. J. Robertshaw, “An anti-inflammatory role for tranexamic acid in cardiac surgery?,” Jan. 16, 2008. doi: 10.1186/cc6210.

[73] Y. Teng, C. Feng, Y. Liu, H. Jin, Y. Gao, and T. Li, “Anti-inflammatory effect of tranexamic acid against trauma-hemorrhagic shock-induced acute lung injury in rats.”

[74] J. Bartley, “Should chitosan and tranexamic acid be combined for improved hemostasis after sinus surgery?,” *Med Hypotheses*, vol. 81, no. 6, pp. 1036–1038, Dec. 2013, doi: 10.1016/j.mehy.2013.09.027.

[75] U. Aydemir Sezer *et al.*, “Combination of gelatin and tranexamic acid offers improved haemostasis and safe use on internal hemorrhage control,” *RSC Adv*, vol. 6, no. 97, pp. 95189–95198, 2016, doi: 10.1039/c6ra16790j.

[76] A. K. Gaharwar *et al.*, “Shear-thinning nanocomposite hydrogels for the treatment of hemorrhage,” *ACS Nano*, vol. 8, no. 10, pp. 9833–9842, Oct. 2014, doi: 10.1021/nn503719n.

[77] Y. W. Wang *et al.*, “Biological effects of chitosan-based dressing on hemostasis mechanism,” *Polymers (Basel)*, vol. 11, no. 11, Nov. 2019, doi: 10.3390/polym11111906.

[78] Y. Xia, R. Yang, H. Wang, Y. Li, and C. Fu, “Application of chitosan-based materials in surgical or postoperative hemostasis,” Aug. 31, 2022, *Frontiers Media S.A.* doi: 10.3389/fmats.2022.994265.

[79] A. Alanwar, S. Akl, S. El-Mekawi, and M. M. Gamal, “Tranexamic Acid and Ethamsylate for Reducing Blood Loss in Patient Undergoing Lower Segment Cesarean Section at High Risk for Post-Partum Hemorrhage: A Pilot Study,” *Open J Obstet Gynecol*, vol. 10, no. 09, pp. 1340–1350, 2020, doi: 10.4236/ojog.2020.1090123.

[80] D. T Deeksha, M. A. Kumar, and G. Suresh, “A Comparative Study of Tranexamic Acid and Ethamsylate in Dysfunctional Uterine Bleeding,” *Indian Journal of Pharmacy Practice*, vol. 14, no. 3, pp. 205–210, Aug. 2021, doi: 10.5530/ijopp.14.3.40.

[81] M. Alvarez-Guerra, M. Rosa Hernandez, G. Escolar, C. Chiavaroli, R. P. Garay, and P. Hannaert, “The hemostatic agent ethamsylate enhances P-selectin membrane expression in human platelets and cultured endothelial cells.”

[82] P. L. Mccormack and P. J. Zufferey, “Tranexamic Acid A Review of its Use in the Treatment of Hyperfibrinolysis.”

[83] I. I. Abd El Baser, H. M. ElBendary, and A. ElDerie, “The synergistic effect of tranexamic acid and ethamsylate combination on blood loss in pediatric cardiac surgery,” *Ann Card Anaesth*, vol. 24, no. 1, pp. 17–23, Jan. 2021, doi: 10.4103/aca.ACA_84_19.

[84] L. R. Ment, W. B. Stewart, and C. C. Duncan, “PROSTAGLANDINS BEAGLE PUPPY MODEL OF INTRAVENTRICULAR HEMORRHAGE: ETHAMSYLATE STUDIES.”

[85] P. Vass *et al.*, “Continuous alternative to freeze drying: Manufacturing of cyclodextrin-based reconstitution powder from aqueous solution using scaled-up electrospinning,” *Journal of Controlled Release*, vol. 298, pp. 120–127, Mar. 2019, doi: 10.1016/j.jconrel.2019.02.019.

[86] R. Cassano *et al.*, “Chitosan Hemostatic Dressings: Properties and Surgical Applications,” Jul. 01, 2024, *Multidisciplinary Digital Publishing Institute (MDPI)*. doi: 10.3390/polym16131770.

[87] Q. Li, Z. He, H. E. Rozan, C. Feng, X. Cheng, and X. Chen, “An improved blood hemorrhaging treatment using diatoms frustules, by alternating Ca and light levels in cultures,” *Mar Life Sci Technol*, vol. 5, no. 3, pp. 316–325, Aug. 2023, doi: 10.1007/s42995-023-00180-3.

[88] Q. He *et al.*, “Positive charge of chitosan retards blood coagulation on chitosan films,” *J Biomater Appl*, vol. 27, no. 8, pp. 1032–1045, May 2013, doi: 10.1177/0885328211432487.

[89] F. Chen, X. Cao, X. Chen, J. Wei, and C. Liu, “Calcium-modified microporous starch with potent hemostatic efficiency and excellent degradability for hemorrhage control,” *J Mater Chem B*, vol. 3, no. 19, pp. 4017–4026, May 2015, doi: 10.1039/c5tb00250h.

[90] C. Miele, J. J. Rochford, N. Filippa, S. Giorgetti-Peraldi, and E. Van Obberghen, “Insulin and insulin-like growth factor-I induce vascular endothelial growth factor mRNA expression via different signaling pathways,” *Journal of Biological Chemistry*, vol. 275, no. 28, pp. 21695–21702, Jul. 2000, doi: 10.1074/jbc.M000805200.

[91] C.-H. Heldin and B. Westermark, “Role of Platelet-Derived Growth Factor in Vivo,” *The Molecular and Cellular Biology of Wound Repair*, pp. 249–273, 1988, doi: 10.1007/978-1-4899-0185-9_7.

[92] G. F. Pierce, T. A. Mustoe, B. W. Altrock, T. F. Deuel, and A. Thomason, “Role of platelet-derived growth factor in wound healing,” *J Cell Biochem*, vol. 45, no. 4, pp. 319–326, 1991, doi: 10.1002/JCB.240450403.

[93] W. Ye *et al.*, “Fabricating bio-inspired micro/nano-particles by polydopamine coating and surface interactions with blood platelets,” *Appl Surf Sci*, vol. 351, pp. 236–242, Oct. 2015, doi: 10.1016/j.apsusc.2015.05.108.

[94] X. Yu, Z. Gao, J. Mu, H. Lian, and Z. Meng, “Gelatin/calcium chloride electrospun nanofibers for rapid hemostasis,” *Biomater Sci*, vol. 11, no. 6, pp. 2158–2166, Jan. 2023, doi: 10.1039/d2bm01767a.

[95] A. A. El-Habeeb and M. S. Refat, “Synthesis, structure interpretation, antimicrobial and anticancer studies of tranexamic acid complexes towards Ga(III), W(VI), Y(III) and Si(IV) metal ions,” *J Mol Struct*, vol. 1175, pp. 65–72, Jan. 2019, doi: 10.1016/j.molstruc.2018.07.099.

[96] J. Y. Park, K. H. Kyung, K. Tsukada, S. H. Kim, and S. Shiratori, “Biodegradable polycaprolactone nanofibres with β-chitosan and calcium carbonate produce a hemostatic effect,” *Polymer (Guildf)*, vol. 123, pp. 194–202, Aug. 2017, doi: 10.1016/j.polymer.2017.07.013.

[97] T. Kean and M. Thanou, “Biodegradation, biodistribution and toxicity of chitosan,” Jan. 31, 2010. doi: 10.1016/j.addr.2009.09.004.

[98] H. Kim, C. H. Tator, and M. S. Shoichet, “Chitosan implants in the rat spinal cord: Biocompatibility and biodegradation,” *J Biomed Mater Res A*, vol. 97 A, no. 4, pp. 395–404, Jun. 2011, doi: 10.1002/jbm.a.33070.

[99] C. Schmitt *et al.*, “Long-term pre-clinical evaluation of an injectable chitosan nanocellulose hydrogel with encapsulated adipose-derived stem cells in an ovine model for IVD regeneration,” *J Tissue Eng Regen Med*, vol. 15, no. 7, pp. 660–673, Jul. 2021, doi: 10.1002/term.3216.

[100] “Patent Application Publication Dec,” 2015.

[101] S. A. Mousa, “Hemostasis Models: Bleeding Models,” in *Drug Discovery and Evaluation: Pharmacological Assay, Fourth Edition*, Springer International Publishing, 2015, pp. 783–787. doi: 10.1007/978-3-319-05392-9_14.

[102] J. da C. Carvalho-Júnior, F. Zanata, A. C. Aloise, and L. M. Ferreira, “Acellular dermal matrix in skin wound healing in rabbits – histological and histomorphometric analyses,” *Clinics*, vol. 76, 2021, doi: 10.6061/CLINICS/2021/E2066.

[103] S. Omer *et al.*, “Development of innovative electrospun nepafenac-loaded nanofibers-based ophthalmic inserts,” *Int J Pharm*, vol. 647, Nov. 2023, doi: 10.1016/j.ijpharm.2023.123554.

[104] S. Mukherjee *et al.*, “Spatiotemporally Controlled Release of Etamsylate from Bioinspired Peptide-Functionalized Nanoparticles Arrests Bleeding Rapidly and Improves Clot Stability in a Rabbit Internal Hemorrhage Model,” *ACS Biomater Sci Eng*, vol. 10, no. 8, pp. 5014–5026, Aug. 2024, doi: 10.1021/acsbiomaterials.4c00743.

[105] S. Chen, M. A. Carlson, Y. S. Zhang, Y. Hu, and J. Xie, “Fabrication of injectable and superelastic nanofiber rectangle matrices (‘peanuts’) and their potential applications in hemostasis,” *Biomaterials*, vol. 179, pp. 46–59, Oct. 2018, doi: 10.1016/j.biomaterials.2018.06.031.

[106] S. Pourshahrestani, E. Zeimaran, I. Djordjevic, N. A. Kadri, and M. R. Towler, “Inorganic hemostats: The state-of-the-art and recent advances,” *Materials Science and Engineering C*, vol. 58, pp. 1255–1268, Jan. 2016, doi: 10.1016/j.msec.2015.09.008.

[107] S. Singh *et al.*, “Structure functional insights into calcium binding during the activation of coagulation factor XIII A,” *Sci Rep*, vol. 9, no. 1, Dec. 2019, doi: 10.1038/s41598-019-47815-z.

[108] M.Furlan, C. Steinmann, and M. Jungo, “Binding of calcium ions and their effect on clotting of fibrinogen Milano III, a variant with truncated A alpha-chains,” *Blood coagulation and fibrinolysis*, vol. 7, pp. 331–335, 1996, Accessed: Apr. 15, 2025. [Online]. Available: 10.1097/00001721-199604000-00007

[109] T. Subramaniam, M. B. Fauzi, Y. Lokanathan, and J. X. Law, “The role of calcium in wound healing,” Jun. 02, 2021, *MDPI*. doi: 10.3390/ijms22126486.

[110] A. E. Pusateri, A. V. Delgado, E. J. Dick, R. S. Martinez, J. B. Holcomb, and K. L. Ryan, “Application of a granular mineral-based hemostatic agent (QuikClot) to reduce blood loss after grade V liver injury in swine,” *Journal of Trauma - Injury, Infection and Critical Care*, vol. 57, no. 3, pp. 555–562, Sep. 2004, doi: 10.1097/01.TA.0000136155.97758.CD.

Chapter 6

CONCLUSION AND FUTURE PROSPECTS OF WORK

6. Conclusions & Future Prospects of the work

Conclusions of the work

Various aspects were systematically explored throughout this study h to identify the most effective combination for achieving reliable haemostasis. By evaluating multiple parameters, materials, and experimental conditions, this study aimed to determine an optimal approach that can enhance haemostatic performance and address the challenges associated with current methods.

Firstly, an affordable air-dried film was made from PVA and chitosan (CS) combined with marine shell waste (MSW) powder for bleeding control. Its Raman spectroscopy confirmed that the MSW powder was successfully integrated into the PVA/CS film structure. The film containing MSW powder (AD2) showed superior mechanical properties with a tensile strength of 11.6 MPa and 180% elongation, significantly outperforming the film without oyster shell powder (AD1), which had a tensile strength of 6.4 MPa and only 40% elongation. Both films are hemocompatible, have an antimicrobial nature, and exhibit significant swelling ability (For AD1=94% and AD2=107%). The haemostatic activity of AD2 was more effective than AD1 as confirmed by CT, PRT, APTT, and PT time observation. CT for AD2 (280±18s) was lower than AD1(408±12), showing that Ca^{++} has enhanced the clotting factor to reduce the bleeding time. All these findings conclude that MSW power incorporated PVA/CS film with haemostatic performance and antibacterial activity will be a promising biomaterial to reduce haemorrhage for designing wound dressings in clinical application and in emergency situations.

Secondly, a new type of freeze-dried sponge was made from chitosan and MSW powder, designed to stop bleeding faster. The sponge demonstrated impressive material properties, including a high swelling capacity of 250-300% within 20 min, cytocompatibility with human dermal fibroblasts, and antimicrobial activity against *Staphylococcus aureus*. Notably, the 3%CS- 12%PVA-$CaCO_3$ (FD2) composite exhibited enhanced haemostatic performance compared to the 3%CS-12%PVA (FD1) sponge, showing improved blood clot formation in aPTT, PT, and PRT assays. The sponge works by absorbing fluid, concentrating clotting factors, and releasing calcium ions through its porous design and the positively charged components in chitosan. In-vivo testing using a rabbit femoral artery injury model further validated these findings, with the composite sponge achieving rapid and stable clot formation in the shortest time and minimal blood loss compared to a control gauze.

Finally, a successful development of multifunctional hemostatic scaffold was derived from natural polymers and sustainable calcined marine shell waste. An electrospun nanofibre loaded with tranexamic acid (TXA) and Ethamsylate (E) was prepared based on Chitosan and PVA matrix. The FTIR and FT-Raman confirmed the absence of any chemical interaction between the drug and polymer blends. At the same time, SEM micrographs demonstrated the formation of uniform and bead-free flattened nanofibers. The nanofibers had a water contact angle of 32º, showing moderate hydrophillicity. The patches were able to release 48% and 64% of loaded TXA and E within 30 min, respectively, while the patches degraded by more than 25% after 48 h. The kinetic analysis of drug release fitted the Korsmeyer-Peppas model and showed a non-Fickian diffusion. Dual drug-loaded nanofiber patches showed a decrease in whole blood clotting time, PRT, and aPTT time by 30 ± 12%, 20 ± 7%, and 11 ± 6 % over the clotting times observed for a single drug-loaded patch or only polymeric patch. An in vivo study of rabbit skin incision demonstrated more platelet aggregation and better control over rapid blood loss by dual drug-loaded patch than a single drug-loaded patch. The results indicate the potential of tranexamic acid and E-loaded chitosan patches as a topical hemostatic patch suitable for both military as well as civilian injury kits.

A biogenic approach has been made to develop a highly effective material by incorporating MSW-T powder into nanofiber wound dressings through electrospinning technology. MSW-T showed a large zone of inhibition surrounding it and had an excellent antibacterial activity against *Staphylococcus Aureus*. This enhanced antibacterial activity at elevated calcination temperature results from the thermal conversion of calcium carbonate ($CaCO_3$) into calcium oxide (CaO) and calcium hydroxide ($Ca(OH)_2$). MSW-T particles and MSWNF nanofiber demonstrated significant blood clotting (measured by CT, aPTT, PT, and PRT tests) properties. Swelling, degradation, and contact angle measurements of nanofiber dressings showed moderate hydrophilicity and swelling properties, whereas the incorporation of MSW-T powder increased Young's nanofiber modulus by 123%. Furthermore, a rabbit skin incision in vivo model demonstrated that MSWNF could decrease bleeding time to 75 ± 5 s. Histopathological assessment of the wounded rabbit skin confirmed the presence of fibrous tissue, continued epithelialization, and an abundance of capillaries, indicating complete blood coagulation.

These studies collectively demonstrate the successful development of innovative biomaterials for haemorrhage control using natural polymer chitosan, two drug molecules ethamsylate, tranexamic acid, and sustainable marine resources, particularly oyster shell waste. The research showed that MSW-O and MSW-T into various delivery formats (air-dried films, freeze-dried sponges, and electrospun nanofibers) significantly enhanced haemostatic performance. The molecular integrity of all components was maintained in the composite materials, as all findings confirmed that each component preserved its original structural properties and functional characteristics within the blended materials.

Among all the fabricated formulations, the biogenic calcium-loaded nanofiber scaffold (MSWNF) emerged as the most effective, offering rapid hemostasis, improved platelet adhesion, controlled therapeutic release, and superior tissue-regenerative potential. The Ca^{2+} ions derived from marine shell waste were found to play a crucial role in accelerating the coagulation cascade, enhancing fibroblast activity, and strengthening the scaffold’s mechanical integrity. Additionally, the dual-drug contributed to enhanced clot stability and reduced bleeding tendency. Findings from the in vivo studies further validated the scaffold’s suitability as a rapid and reliable prehospital intervention for traumatic hemorrhage. Overall, this research establishes marine shell waste as a valuable bio-based hemostatic component, aligning with sustainability and bioeconomy principles while offering clinically relevant performance in conjunction with pharmacotherapeutics agents.

Future prospects of the work

Based on our progress thus far, we plan to scale up the haemostatic dressing production, generate more comprehensive data, and optimize the composition for enhanced clinical performance. The future of haemostatic agents for challenging trauma haemorrhage lies in developing smart, multifunctional, and personalized solutions that address the complex nature of severe bleeding across diverse healthcare settings. This development requires careful balancing of clinical efficacy with affordability, storage stability, and ease of use to ensure accessibility in resource-limited environments.

Key innovations driving this field forward include responsive materials that activate based on specific bleeding conditions or patient physiological parameters, enhancing effectiveness while minimizing complications. The integration of imaging guidance with haemostatic delivery devices enables precise placement of patient-specific materials in deep, non-compressible wounds, while point-of-care systems capable of rapidly formulating personalized haemostatic agents based on real-time wound assessment represent the ultimate goal of individualized haemorrhage control.

Furthermore, the development of haemostatic agents with integrated analgesic components represents a significant advancement in wound care technology, simultaneously addressing bleeding control and pain management to improve patient outcomes while reducing treatment complexity. Our approach has been validated through in-vivo haemorrhage experiments using large animal models, which demonstrated long-term biocompatibility and safety profiles essential for clinical translation.

From a manufacturing perspective, energy-efficient fabrication methods represent a convergence of sustainability goals and innovation, offering pathways to reduce environmental impact while maintaining critical performance characteristics. Complementing these advances, the mechanical and rheological optimization of blood clots after haemorrhage provides a sophisticated approach to improving haemostatic outcomes through precise control of clot physical properties, ensuring optimal performance across varied clinical scenarios.

Together, these interconnected developments create a comprehensive framework for next-generation hemostatic solutions that are effective, accessible, sustainable, and tailored to individual patient needs.